Effects of Strain on Mass Transport in CsPbBr3; Insights from Kinetic Modelling

Smolders, Thijs

Award date:
2022

Awarding institution:
University of Bath

Effects of Strain on Mass Transport in $CsPbBr_3$; Insights from Kinetic Modelling

submitted by

Thijs Josephus Adrianus Maria Smolders

for the degree of Doctor of Philosphy

of the

University of Bath

Department of Physics

July 19, 2022

Declaration

The material presented here for examination for the award of a higher degree by research has not been incorporated into a submission for another degree. Moreover, I am the author of this thesis, and the work described therein was carried out by myself personally.

Access to this thesis/portfolio in print or electronically is restricted until .....

Signed on behalf of the Doctoral College .....

Caesium
Hot-headed firebrand
whose violent behaviour
hides a softer side.

Lead
Lecherous plumber
with an appetite for both
acids and bases.

Bromine
The shame of your name
now lost except to the Greeks.
No need to still fume.

Mary Soon Lee [1]

Abstract

Lead-halide perovskites (LHPs) have attracted much attention for their favourable optoelectronic properties, which in combination with their ease of fabrication justifies them being dubbed as the "poor man's high-performance semiconductors". Indeed, they have been used successfully in various technologies, including photovoltaics, LEDs and photocatalysis. Thus far, the large-scale commercialisation of such devices has been hindered by the limited stability of the LHP layers therein.

Generally, the instability is observed as a decomposition of the ABX_3 perovskite to the BX_2 precursor salt. Although an atomic understanding of the exact decomposition mechanisms is still under development, it seems likely that such decomposition is facilitated by mass transport in the perovskite layer. Indeed, there has been a wealth of evidence indicating that LHPs exhibit significant ionic conduction, in addition to their favourable electronic conduction. In particular, the X-site anion has been shown to be rather mobile, though ionic migration of the A-site cation has also been observed.

In some cases, the stressors responsible for the observed instabilities can be mitigated using encapsulation, for example in the case of instabilities towards moisture and oxygen. In many other cases, for example in the case of instabilities towards heat and illumination, the stressors are naturally present under operation and cannot be avoided. Recently, a strong correlation between strain and stability has been observed. Several studies have shown that tensile strain can worsen the LHP degradation, while compressive strain has been linked to improved stability.

These observations beg the question to what extent ionic migration is influenced by strain, for which an atomistic understanding is equally elusive. This thesis has therefore been dedicated to unravel the effects of strain on the ionic migration in LHPs. We do so by looking at three representative types of strain in one, two and three dimensions, and compute the ionic mobility for both caesium (the A-site cation) and bromide (the X-site anion) in $CsPbBr_3$, which we consider as a representative material for the larger class of LHPs. We find that for both ions the directionality and magnitude of the mobility can change dramatically with strain, in particular for the A-site cation. In this thesis, we identify strain states that should be avoided experimentally and suggest more desirable strain states to reduce the ionic mobility, and potentially reduce the material instability under strain.

Samenvatting

Lood-halide perovskieten (in het vervolg simpelweg perovskieten) hebben veel aandacht gekregen omwille van hun gunstige opto-elektronische eigenschappen, die ze, in combinatie met de eenvoud van hun fabricatie, met recht de naam van "hoogwaardige hafgeleiders voor alleman". Ze zijn daarom ook gebruikt in verschillende toepassingen, zoals photovoltaïsche, maar ook in LEDs en photokatalyse. Hun productie en gebruik op grote schaal wordt echter tot op heden beperkt door de beperkte stabiliteit van de perovskietlagen in deze apparaten. De instabiliteit komt in het algemeen tot uiting als een ontleding van de ABX_3 structuur tot het precursorzout BX_2. Hoewel het begrip van deze ontleding op atomaire schaal nog steeds onder ontwikkeling is, is het zeer waarschijnlijk dat deze samenhangt met het transport van atomen in de perovskietlaag. Er is namelijk een grote hoeveelheid bewijs dat perovskieten naast elektronen ook sterk ionen geleiden. Met name het anion op de X-positie is erg mobiel, al is ook migratie van het kation op de A-positie opgemerkt.

In sommige gevallen kunnen de aanleidingen voor de instabiliteit verlicht worden met behulp van inkapseling, bijvoorbeeld voor instabiliteit als gevolg van vocht en zuurstof. In veel andere gevallen, te denken aan instabiliteit tengevolge van hitte en verlichting, kunnen de aanleidingen niet ontweken worden omdat ze inherent bijdragen aan de werking van het apparaat. Er is recent een sterke correlatie tussen de vervorming en de stabilteit van de perovskietlagen ontdekt. Wanneer de laag uitgerekt wordt, wordt deze minder stabiel en vice versa voor ineendrukking.

Deze ontdekkingen wekken de vraag op of de beweging van ionen ook wordt beïnvloed door de vervorming van de perovskietlaag, waarvoor een begrip op atomaire schaal ook zeer beperkt is. Dit proefschrift is er daarom op gericht om te achterhalen van de effecten van vervorming van de perovskietlaag op de beweging van ionen zijn. We kijken daarbij naar drie representatieve uitingen van vervormingen, in een, twee en drie dimensies, en berekenen de mobiliteit van zowel caesium (het kation op de A-positie) als ook bromide (het anion op de X-positie) in het materiaal $CsPbBr_3$, wat we gebruiken als representatief materiaal voor de grotere groep perovskieten. We ontdekken dat zowel de richting als de grootte van de mobiliteit sterk wordt beïnvloed door vervorming, met name voor het kation op de A-positie. In deze scriptie raden we bepaalde vervormingen af en bevelen we andere vervormigen aan om de mobiliteit van de ionen te beperken, om op die manier hopelijk de perovskietlagen stabieler en daarmee duurzamer te maken.

Contents

1 Introduction and Background **1**

1.1 General Properties of the Perovskite Crystal Structure 2

2 Literature Review **7**

2.1 Ion Migration in LHPs 8

2.1.1 Experimental Evidence for Ionic Migration in LHPs 8

2.1.2 Ionic Migration in $CsPbBr_3$ 11

2.1.3 Comparison to Other LHPs 14

2.2 Strain and Strain Engineering of LHPs 16

2.2.1 Softness of the Perovskite Lattice 16

2.2.2 Origins of Strain 19

2.3 Stability 25

2.3.1 External Factors Towards Instability 25

2.3.2 Intrinsic Factors Towards Instability 26

2.4 Interplay between Ion Migration, Strain and Stability 27

2.4.1 Links between Strain and Stability 28

2.4.2 Links between Strain and Ionic Migration 29

2.4.3 Links between Ionic Migration and Stability 31

3 Computational Techniques **33**

3.1 Density Functional Theory 33

3.1.1 Decoupling the Nuclear and Electronic Degrees of Freedom 34

3.1.2 Resolving the Electronic Wavefunction; Hartree-Fock Theory 35

3.1.3 Exchange-Correlation Energy 36

3.1.4 Hohenberg-Kohn Theorems 37

3.1.5 Kohn-Sham Equations 38

3.1.6 Exchange-Correlation Functionals 40

3.1.7 Plane Wave Basis Set 43

3.1.8 Pseudopotentials . . . 44
3.2 Kinetic Model . . . 44
3.2.1 Derivation of the Master Equation . . . 44
3.2.2 Equilibrium Conditions . . . 45
3.2.3 Vineyard's Rate Equation . . . 46
3.3 (Climbing Image) Nudged Elastic Band Method . . . 51
3.4 Dimer Method . . . 53
3.4.1 Evaluating the Rotation Angle . . . 54
3.4.2 Evaluating the Translation . . . 56
3.5 Computation of the Vibrational Frequencies . . . 57
3.6 Computation of the Mobility Tensor . . . 58
3.7 Elasticity theory . . . 59
3.7.1 Elasticity Theory - Bulk . . . 60
3.7.2 Elasticity Theory - Point Defect . . . 60
3.7.3 Ion Migration Activation Enthalpy . . . 62

4 Development of the General Methodology; Ionic Mobility in the Pristine Structure 63
4.1 Introduction . . . 63
4.2 Preliminary Testing . . . 65
4.2.1 Convergence of the Plane Wave Basis Set . . . 65
4.2.2 Choice of XC Functional . . . 67
4.3 Connectivity of the Sublattices in the Orthorhombic Phase with Space Group *Pnma* . . . 73
4.3.1 Connectivity of the Bromide Sublattice . . . 74
4.3.2 Connectivity of the Caesium Sublattice . . . 76
4.4 Migration Enthalpies . . . 78
4.4.1 Bromide Migration . . . 78
4.4.2 Caesium Migration . . . 80
4.5 Attempt Frequencies . . . 81
4.6 Setting Up the Kinetic Model . . . 82
4.6.1 Details of the Calculations . . . 83
4.7 Mobility Tensor Results . . . 84
4.7.1 Bromide Mobility . . . 84
4.7.2 Caesium Mobility . . . 85
4.7.3 Sanity Checks . . . 86
4.8 Conclusion . . . 89

5 Effect of Hydrostatic Pressure on Ionic Mobility **90**
5.1 Introduction . . . 90
5.2 Structural Response . . . 91
5.2.1 Additional Set of SEPS . . . 92
5.3 Anion Vacancy Migration under Hydrostatic Pressure . . . 97
5.3.1 Convergence of the Activation Enthalpies . . . 99
5.3.2 Attempt Frequencies for Bromide Vacancy Hops . . . 101
5.3.3 Mobility . . . 102
5.4 Additional Analysis . . . 102
5.4.1 Convergence of the Mobility Tensor with Respect to the Number of Paths . . . 102
5.4.2 Effective Dipole Approaches . . . 105
5.5 Caesium Vacancy Migration under Hydrostatic Pressure . . . 112
5.5.1 Activation Enthalpies . . . 112
5.5.2 Attempt Frequencies . . . 112
5.5.3 Mobilities . . . 113
5.6 Conclusion . . . 115

6 Effect of Biaxial Strain on Ionic Mobility **117**
6.1 Introduction . . . 117
6.2 Structural Response to Strain . . . 120
6.3 Bromide Migration under Biaxial Strain . . . 123
6.4 Caesium Migration Under Biaxial Strain . . . 128
6.5 Conclusion . . . 130

7 Effect of Uniaxial Strain on Ionic Mobility **131**
7.1 Introduction . . . 131
7.2 Structural Response to Strain . . . 132
7.3 Bromide Migration under Uniaxial Strain . . . 136
7.4 Caesium Migration under Uniaxial Strain . . . 140
7.5 Conclusion . . . 142

8 Migration Barrier Analysis **143**
8.1 Bromide Migration . . . 143
8.1.1 Intersite Distance Approach . . . 143
8.1.2 Critical Radius Analysis . . . 151
8.1.3 Metal-Anion Bond Order . . . 153
8.1.4 Predictions from Elasticity Theory . . . 155

8.1.5 Other Methods 159
8.2 Caesium Migration 159
8.2.1 Intersite Distance Approach 159
8.2.2 Halide Aperture Approach 162
8.2.3 Linear Response Predictions 174

9 Insights **177**

10 Acknowledgements **182**

Bibliography **189**

A Appendix **227**
A.1 Organic Cation Perovskites 227
A.1.1 Organic Cation Perovskites; Bromide Perovskites 227
A.1.2 Organic Cation Perovskites; Iodide Perovskites 227
A.2 Inorganic Cation Perovskites 229
A.2.1 Inorganic Cation Perovskites; Bromide Perovskites 229
A.2.2 Inorganic Cation Perovskites; Iodide Perovskites 229
A.2.3 Comparison between I- and Br-based LHPs 229

Chapter 1

Introduction and Background

Over the past decade, lead-halide perovskites (LHPs) have emerged as promising materials for optoelectronic applications, because of their excellent optoelectronic properties, including sharp optical absorption onsets, low nonradiative recombination and low effective masses of charge carriers [2]. This is remarkable given the fact that LHPs are generally solution-processed at low temperatures, which are typically assumed to give rise to high concentrations of grain boundaries and point defects which negatively affect the material quality and diminish the optoelectronic properties. The optoelectronic performance of LHPs however remains largely unaffected, and this apparent defect-tolerance has been the inspiration for many studies in the field [3–5]. As a result, LHPs have been dubbed as the "poor man's high-performance semiconductors" [6] as they combine facile processing with excellent optoelectronic properties. This has allowed them to be explored in various optoelectronic applications. For example $CsPbBr_3$, which is the main material under consideration in this work, has emerged as a particularly versatile material, finding applications not only in photovoltaics [7–9], but also in LEDs [10–13], photon detectors [14–16], photocatalysis [17–19], water splitting [20, 21], transistors [22–24] and batteries [25, 26].

In addition to the aforementioned electronic conduction, LHPs have also been shown to exhibit significant ionic conduction [27], indicating the presence at least one type of mobile defect. This mixed ionic-electronic conductivity has been implicated as the underlying cause for several typical observations in LHP-based devices, such as the current-voltage hysteresis [28–30]. More crucially, it has been linked to the relative instability of LHP-based devices [31–35], which remains the key impediment to large-scale commercialisation of these systems [36–40]. Several approaches have been taken to mitigate ionic migration in LHPs, including surface passivation [9, 41], passivation by introducing potassium [42, 43], the addition of organic spacer molecules to create so-called 2D perovskites [44–46] and

compositional engineering [47, 48].
More recently, strain engineering has been investigated as an additional means of tuning the properties of LHPs [49–51]. This is a particularly fruitful approach, given that LHPs are several orders of magnitude [2, 52] softer than more typical inorganic semiconductors [53–56]. The effects of strain on the optoelectronic properties have been studied experimentally [49, 57–62], and several theoretical studies have been carried out to extract an atomistic understanding of the processes involved [63–68]. However, despite a number of recent studies indicating that the ionic conductivity of LHPs is significantly affected by stress [69–73], a similarly detailed atomistic understanding of the effects of stress and the resulting strain on ionic migration is largely lacking.
In this thesis, we address this gap by modelling the effects of different types of stress, and their resulting strain, on the ionic migration in $CsPbBr_3$, which we consider as a model system for the larger class of LHPs. In particular, we focus on the strain induced by hydrostatic pressure, biaxial stress and uniaxial stress, being the most reasonable experimentally relevant sources of three-, two- and one-dimensional stresses. Specifically, we use DFT calculations to compute rates for vacancy-mediated hopping, and use these rates to compute the ionic mobility tensor. We find that the stress can strongly affect both the magnitude and directionality of the ionic mobility, which is altered differently for the different types of stress. Finally, we aim to also give some atomistic understanding regarding why the mobility changes more in certain cases than in others.
Since our findings are closely linked to the structural anisotropy of the perovskite structure in its low-temperature phase, we first wish to introduce the perovskite structure and its phase transitions below.

1.1 General Properties of the Perovskite Crystal Structure

In 1839, a German scientist named Gustav Rose was the first to discover $CaTiO_3$, which he coined perovskite in honour of the Russian mineralogist Lev Perovski. The general class of materials that adopt the same crystal structure as $CaTiO_3$ is commonly referred to as perovskites. They all share the same ABX_3 stoichiometry, and are composed of corner-sharing octahedra of X-site anions, with B-site metals at their centres and A-site cations in the voids between them. A schematic representation of the perovskite in its so-called aristotype is shown in Figure 1-1. In the class of the halide perovskites, the A-site site is typically occupied by methylammonium (MA), formamidinium (FA) or caesium (Cs), the B-site is typically occupied by lead (Pb), or in some cases tin (Sn), while the X-site is typically occupied by iodide (I), bromide (Br) or in a few cases even chloride (Cl). In our

study, we choose $CsPbBr_3$ as a model system, because it is structurally representative of the larger class of LHPs while being easier to model since it includes no organic molecule with an associated dipole, though we note that the best-performing perovskite compositions in terms of photovoltaic properties typically have more exotic mixtures of components at the A- and X-sites, i.e. $Cs_{0.05}(FA_{0.95}MA_{0.05})_{0.95}Pb(I_{0.95}Br_{0.05})_3$ [74, 75].

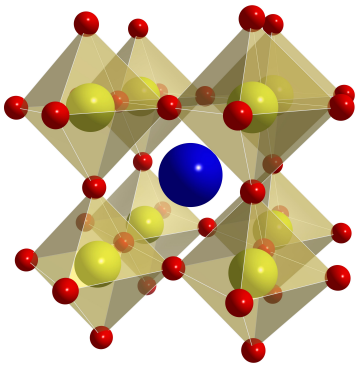

Figure 1-1: Representation of the ABX_3 perovskite crystal structure in the cubic (α) phase. The X (red) atoms form octahedral cages, filled by the B (yellow) atom. The structure is stabilised by the A (blue) atom, which sits in between the octahedral cages. Shade has been added to represent the 3D visualisation.

Whether a generic material with an ABX_3 stoichiometry is likely to adopt the perovskite structure can be tested by computing the so-called Goldschmidt tolerance factor t [76]:

$$t = \frac{(R_\mathrm{A} + R_\mathrm{X})}{\sqrt{2}\,(R_\mathrm{B} + R_\mathrm{X})},$$

in which R_i denotes the ionic radius of component i. This geometric factor gives an indication as to how well the A-site cation fits in the void between the octahedra. A value of $t = 1$ indicates a perfect fit, meaning that the material will likely exhibit a perovskite structure. For values of $t > 1$ the A-site cation is too large, and the perovskite structure is unlikely to form. For values of $t < 0.7$, the A-site cation is too small, and the perovskite structure is unlikely to form. For values of $0.7 < t < 1$, the A-site cation is also too small to completely fill the void, though materials with such tolerance factors are still likely to adopt the perovskite structure. In such cases, the small size of the A-site cation can be compensated by octahedral tilting.

In the 1970s, Glazer developed a classification scheme to formalise the octahedral tilting in

perovskites [77, 78]. In his formalism, the octahedral tilting is described as a linear combination of rotations about the three crystallographic axes of the aristotype. Along any one of these three directions, only two types of tilting are allowed, being either in-phase or out-of-phase tilting. For in-phase tilting, subsequent octahedra are tilted in the same direction by the same angle, while for out-of-phase tilting, subsequent octahedra are tilted in opposite directions, but again with the same angle. A schematic representation of these tilts is shown in Figure 1-2. For each of these tilts, a periodicity of two unit cells of the cubic aristotype is assumed, which limits the number of distinct tilting patterns to 15, each of which can be expressed by a unique notation in the Glazer notation. An illustrative example of a tilting pattern in the Glazer notation is $a^0b^+c^-$, which indicates a lack of tilting (0), an in-phase tilt (+) and out-of-phase tilt (-) with distinct tilting angles along the [100], [010] and [001] directions respectively. For tilting patterns where tilting angles along different crystallographic directions are the same, the same letter is used, e.g. $a^0b^+b^+$.

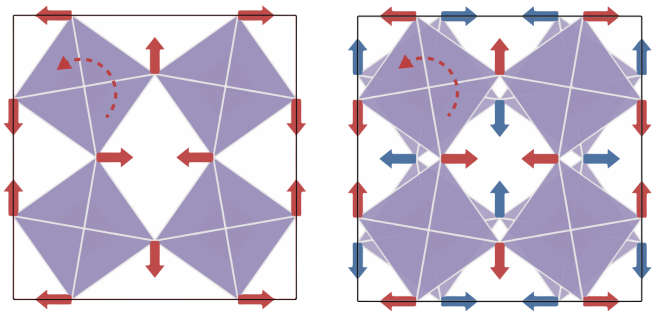

Figure 1-2: Schematic representation of in-phase tilting (left) and out-of-phase tilting (right). Reprinted Figure with permission from Reference 79. Copyright 2018 by the American Physical Society.

Two decades later, Stokes and Howard published a group-theoretical analysis of the different perovskite phases based on the tilting patterns described within the Glazer classification scheme. In group-theory nomenclature, the octahedral tilting can expressed by the irreducible representations R4+ and M3+. This description facilitates the group-subgroup relationships between the different perovskite phases, an overview of which is shown in Figure 1-3, with a particular emphasis on the phases that many LHPs, including $CsPbBr_3$, adopt.
The Glazer notation facilitates the description of the different perovskite phases, and the phase transitions between them. At high temperatures, $CsPbBr_3$ adopts a cubic structure with space group $Pm\bar{3}m$, which is often denoted as the α or cubic phase, with a corresponding $a^0a^0a^0$ tilting pattern. It then undergoes a phase transition at 130°C to a tetragonal structure with space group $P4/mbm$, which is often denoted as the β or tetragonal phase, with a corresponding $a^0a^0c^+$ tilting pattern. Finally, it undergoes another (and final) phase transition to an orthorhombic structure with space group $Pnma$, which is often denoted

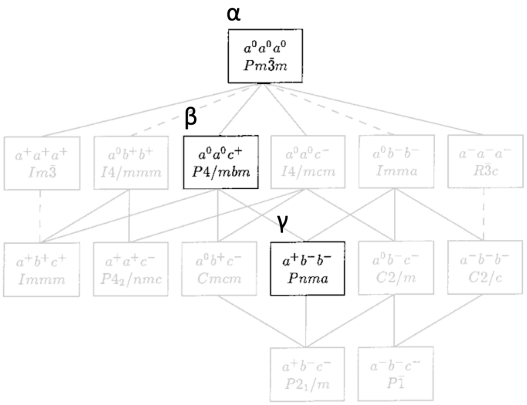

Figure 1-3: Perovskite tilting systems, reproduced with permission of the International Union of Crystallography [80].

as the γ or orthorhombic phase, with a corresponding $a^-b^+a^-$ tilting pattern. We note that in the orthorhombic phase with space group $Pnma$, the in-phase direction is along the [010] direction. If it were along the [001] direction, as it is in the tetragonal phase, it would correspond to a $Pbnm$ space group. These space groups are often interchanged in the literature, which was pointed out rather nicely by Marsh [81], though they indicate a different permutation of the crystal lattice. The $\alpha \rightarrow \beta$ phase transition can be described as a $a^0a^0a^0 \rightarrow a^0a^0c^+$ tilting in the Glazer notation. Likewise, the $\beta \rightarrow \gamma$ phase transition can be described as a $a^0a^0c^+ \rightarrow a^-b^+a^-$ tilting in the Glazer notation. A visual representation of the α, β and γ phases, along with the phase transition temperatures for $CsPbBr_3$, are shown in Figure 1-4.

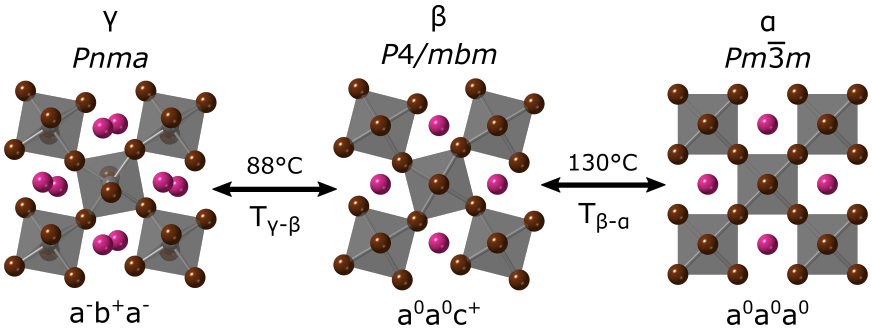

Figure 1-4: Phase transition temperatures for $CsPbBr_3$.

Many LHPs exhibit a similar series of phase transitions, though in some cases the intermediate phase corresponds to a tetragonal structure with space group $I4/mcm$, which corresponds to a tilting pattern of $a^0a^0c^-$, thus having an out-of-phase tilt instead of an in-phase tilt along one of the three crystallographic axes. Moreover, the phase transition tempera-

tures of most other LHPs are lower than those of $CsPbBr_3$. For instance, the prototypical methylammonium lead triiodide ($MAPbI_3$) has already gone through a phase transition at room temperature, adopting a tetragonal structure with space group $I4/mcm$ [82].
The exact nature of the phase transitions is still under some debate. Though the rather sharp onset of the phase transitions suggests a displacive nature of these phase transitions [83], there is also ample theoretical evidence that higher symmetry phases such as the α and β phases only exist as dynamical averages of the lower symmetry γ phase [84, 85], which could explain the gradual reduction of the intensity of diffraction peaks with increasing temperature [82]. The potential energy surface of $CsPbBr_3$ as a function of in- and out-of-phase tilts is shown in Figure 1-5. The four local minima correspond to translational and rotational variants of the γ-phase. In this picture, the phase $\gamma \rightarrow \beta$ phase transition can thus be interpreted in terms of oscillations between these local minima through the β-phase, as a result of which the structure might appear to be in the β-phase, because these fluctuations occur at timescales faster than can be resolved experimentally. At high temperatures, the structure has sufficient thermal energy to probe all local minima, resulting in an apparent transition to a structure which adopts the cubic symmetry on average.

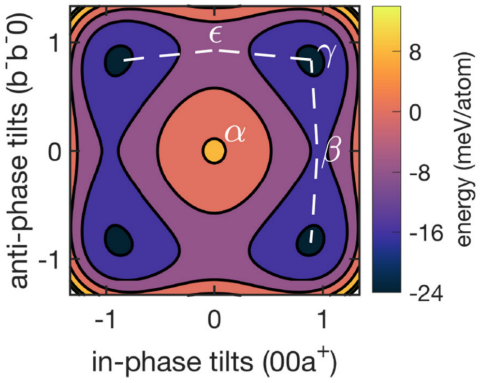

Figure 1-5: Potential energy surface of $CsPbBr_3$ as a function of octahedral tilting angles. Reprinted Figure with permission from Reference 85. Copyright 2019 by the American Physical Society.

Chapter 2

Literature Review

In the following chapter, we will present an overview of the relevant background literature on ionic migration and strain, in relation to the overarching theme of the effects of strain on mass transport in lead-halide perovskites in general, and $CsPbBr_3$ in particular. While we will focus mostly on the background literature on ion migration and strain, we note that to do so without also introducing the background literature on stability in LHPs would be a missed opportunity since the three different subjects are strongly related, as exemplified by the following timely citation:

'Vacancies and strain in the perovskite lattice are considered as the major sources of instability against both intrinsic and extrinsic factors.' [86]

The trinity of these subjects is illustrated schematically below. In the remainder of this chapter, we will first introduce the necessary background of each seperate topic, in order of ion migration, strain and finally stability, after which we will touch upon the current understanding of the interplay between each of these topics.

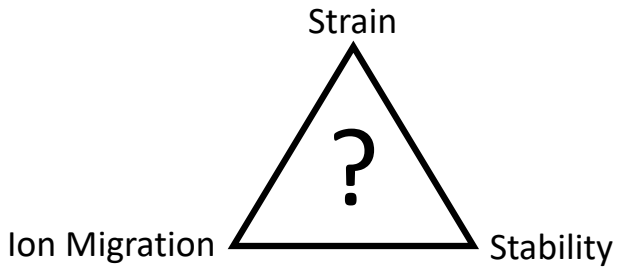

2.1 Ion Migration in LHPs

Over the last decade, LHPs have been widely studied for their favourable optoelectronic properties. It was however understood very early on that in addition to being good electronic conductors, they also exhibit significant ionic conduction [87–89]. Ever since, there has been a large number of studies on ionic migration in LHPs, as evidenced by a large number of reviews on the topic [90–93]. Below we will highlight some important observations, both experimental and theoretical, to give a background on the current level of understanding of ionic migration in LHPs.

2.1.1 Experimental Evidence for Ionic Migration in LHPs

2.1.1.1 Hysteresis

This mixed electronic-ionic conduction was suspected early on from anomalous behaviour in J-V measurements, which are standard measurements for any solar cell device, in which the applied voltage is swept and the output current is measured. From such a measurement, critical device parameters such as the open-circuit voltage (V_{OC}), the short-circuit current (J_{sc}) and power conversion efficiency (PCE) at the maximum power point (MPP) can be derived. Typically such a J-V curve is measured for a forward and a reverse sweep, where the applied voltage is swept from an open-circuit applied voltage (V_{OC}) to short-circuit (0 V) and then back to V_{OC} again. Early on, it was observed that the current profile as a function of voltage was different between the forward and reverse sweep, a phenomenon which was dubbed as 'hysteresis' [94]. Three possible origins were suggested to explain this anomalous behaviour, namely charge trapping and detrapping at the interface of the perovskite layer and the charge transport layers, polarisation of the (potentially ferroelectric) perovskite layer, or mobile ions that drift under the applied field and migrate to the interface, effectively screening the applied potential.
The timescale associated with the anomalous behaviour in the J-V curve was of the order of several seconds, and thus concluded to be incommensurate with both charge (de)trapping and polarisation of the perovskite layer [95]. Instead, theoretical efforts confirmed the hypothesis of mobile ions being responsible for the anomalous behaviour; based on a computed activation enthalpy of 0.58 eV for iodide vacancy migration in $MAPbI_3$ [87], drift-diffusion modelling was able to perfectly reproduce the observed anomalous behaviour [96]. In particular, the model is able to correctly reproduce the observed level as a function of the scan rate, the rate of change in the bias voltage over time [30]. Experiments show that the level

of hysteresis is low for slow scan rates, because the ions remain in a steady-state distribution with no effective ionic mobility, while for fast scan rates the level of hysteresis is equally low, since the ions are unable to move on such a fast timescale. The hysteresis is however most pronounced for intermediate scan rates, typically on the order of 0.1 V/s, in between these two extremes. This behaviour is perfectly reproduced by the drift-diffusion model based on mobile halide ions [30].
The hypothesis of mobile ions was also consistent with other experimental observations, most notably from impedance spectroscopy, an excellent overview of which is given in Reference 97, through which activation energies of 0.55 and 0.68 eV were derived for the mid-frequency and low-frequency signals for $MAPbI_3$ [88]. The lower of these two values was attributed to halide vacancy migration, since it agreed well with the theoretically value predicted by DFT. The higher activation energy was suggested to be linked to A-site cation migration, since the activation enthalpy of V_{MA}^{-} was calculated to be 0.84 [87], while the activation enthalpy of V_{Pb}^{2-} migration was computed at 2.31 eV and thus deemed too high.

2.1.1.2 Ion Exchange

Another observation which suggests that ionic species are mobile in LHPs is the observation that ions can be exchanged between nanocrystals and films of different composition, an excellent review of which is given in Reference 98. Evidence of such ion-exchange was shown in an early study through the synthesis of nanocrystals (NCs) of $CsPbX_3$ (X = Cl, Br, I) through partial or complete anion-exchange, the range of which is shown in Figure 2-1 [99]. As can be seen, a wide range of compositions can be accessed through anion-exchange, both through anion exchange with a halide-rich solution or directly between NCs with different compositions. The grown nanocrystals retain narrow emission linewidths throughout, indicating the overall crystallinity is retained during the exchange reaction. These exchanges were very fast (on a timescale of several seconds or minutes), at a temperature of only 40°C, highlighting the relatively facile migration of halides in LHPs. Similarly rapid halide exchange was also observed in $MAPbX_3$ (X = Cl, Br, I) [100]. All exchanges were shown to be facile apart from the bromide to iodide exchange, which was slow and incomplete. Interestingly, $MAPbI_3$ and $MAPbBr_3$ NCs synthesised through ion exchange with $MAPbCl_3$ show enhanced photoluminescence compared to the NCs precipated from pristine solution. Efforts have been made to suppress the extent of anion exchange. For example, capping of the NCs with $PbSO_4$-oleate has been shown to succesfully suppress the anion exchange between $CsPbBr_3$ and $CsPbI_3$ [101].

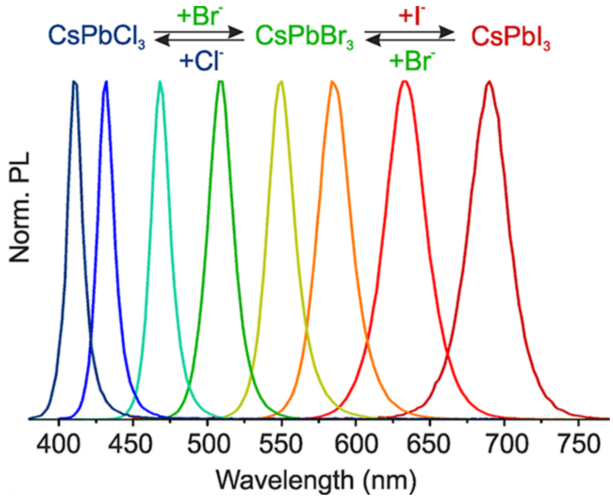

Figure 2-1: Formation of mixed-halide Cs-based perovskite nanocrystals through halide mixing. Copied from Reference 99.

Though most studies have focussed on the anion exchange in LHPs, there is also ample evidence for cation exchange. In the first of these studies, films of $MAPbI_3$ and $FAPbI_3$ were able to take up either FA or MA from solution, with a full conversion possible even at room temperature [102]. In a subsequent study, the resulting $MA_{1-x}FA_xPbI_3$ film was shown to lack any indication of the presence of the non-perovskite δ-phase [103], highlighting the possibility of using ion exchange as a way to stabilise the perovskite composition. The exchange rates for cations and anions were measured for a range of hybrid perovskite $APbX_3$ compositions (A = MA, FA; X = Cl, Br, I) [104]. The interchange was shown to exhibit an exponential dependence, as shown through the exponential decay and increase of the Bragg peak intensity in the XRD spectra. The characteristic decay time constants associated with the interchange between $MAPbI_3$ and $MAPbCl_3$ was measured to vary over a range of 6 to 86 s, while the exchange from $FAPbBr_3$ to $MAPbBr_3$ and $MAPbI_3$ to $FAPbI_3$ had decay times of 709 and 718 s, respectively, suggesting a much slower exchange of cations compared to the halide ions. Though exchange reactions in tin-based perovskites have not been studied in as much detail experimentally, theoretical free energy calculations do indicate that mixing of the A-site cation and the halide should also be favoured in all-inorganic tin based perovskites [105].

Temperature-dependent studies were performed to extract an effective activation energy for ion exchange in LHPs. Most of these have looked at the exchange kinetics of halide anions. Activation energies were found to be in the range of 0.75–0.77 eV for iodide-bromide interdiffusion in between $CsPbBr_3$ and $CsPbI_3$ NCs [106, 107] and 0.53 eV for iodide-bromide interdiffusion in thin films of mixed $MAPbBr_{3-x}I_x$ composition, with diffusion coefficients

in the range 10^{-12}–10^{-8} cm^2s^{-1} [108]. The interdiffusion between $CsPbBr_3$ nanowires and $CsPbCl_3$ nanoplates revealed an apparant activation energy of 0.44 eV associated with the interdiffusion of the halide species [109]. In contrast, similar experiments with $CsPbBr_3$ nanowires and nanoplates of $MAPbI_3$ and $FAPbBr_3$ revealed very limited iodide-bromide and A-site cation exchange. A-site cation was also not observed for a system of $CsPbBr_3$ and $MAPbBr_3$ [109]. In a different study however, $Cs_{1-x}FA_xPbI_3$ was succesfully synthesised through cation exchange between $CsPbI_3$ and $FAPbI_3$ NCs [110]. The activation energy for the apparent miscibility was measured to be 0.65 eV, interestingly in a very similar regime to the activation energy for halide interdiffusion. This suggests that a similar thermally-activated process might be responsible for the observed temperature-behaviour which is different from simple halide or cation migration in the bulk.
Though the exchange between NCs is brought to completion fairly rapidly, this is not always the case for exchange in films, for which complete exchange can take several hours [100]. Several studies have made attempts to elucidate the kinetics of interdiffusion between the surfaces and the bulk. A particularly nice visualisation of such a study is shown in Figure 2-2. It clearly shows the rapid exchange at the nanocrystal surfaces, after which bulk interdiffusion is visible only at a later stage. Such differences between surface and bulk diffusion have resulted in several studies designing mixed $CsPbBr_{3-x}I_3$ and $MAPbBr_{3-x}I_3$ with a halide anion gradient throughout the film [111–113].
Though the activation energies for ion migration in interdiffusion processes might differ from those related to ion migration in single crystals or thin films of a single compositions, they nevertheless indicate the high mobility of ionic species in LHPs.

2.1.2 Ionic Migration in $CsPbBr_3$

2.1.2.1 Experimental evidence

The first quantitative measurements of ionic migration were derived from the temperature-dependence of the conductivity, which was shown to increase with increasing temperature, thus indicating a thermally activated process for which the corresponding activation energy can be derived from the slope of the temperature-dependence. Impedance measurements on single crystals of $CsPbBr_3$ at temperatures of 150 °C and above, yielded an activation energy of 0.25 eV [115]. Conductivity measurements of multicrystalline samples at similarly high temperatures yielded an activation energy of 0.17 eV, whereas this increased to 0.21 eV for temperatures below 90 °C, commensurate with the low-temperature orthorhombic phase [116].
Moreover, the nature of the mobile species was derived from a so-called Tubandt-method

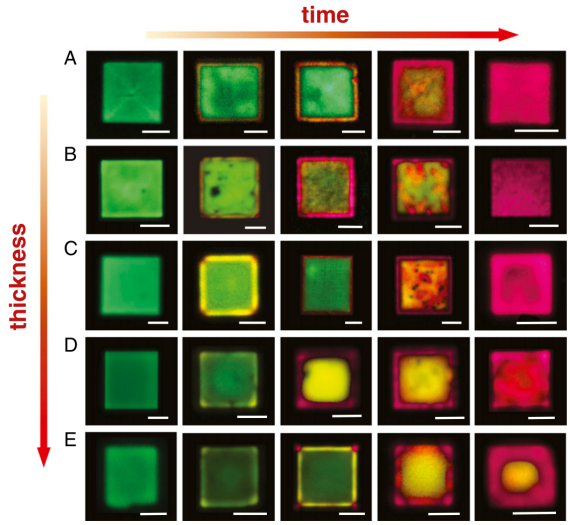

Figure 2-2: Formation of mixed-halide Cs-based perovskite nanocrystals through halide mixing. Reproduced with permission from Reference 114.

measurement [115]. A DC-current was applied to a Pb/$CsPbBr_3$/AgBr electrochemical cell with Pb as the positive electrode, and the individual components were weighed before and after the measurement. After the application of the DC-bias, the authors found an increase in the weight of the Pb/$CsPbBr_3$, consistent with the migration of Br^-, which the authors speculate occurs through vacancy-mediated transport rather than interstitialcy-based transport.

A more recent NMR study yielded an activation energy of 0.49 eV [117]. Another measure of bromide migration was obtained through temperature-dependent transient response measurements on single crystals of $CsPbBr_3$. In these measurements, a DC bias was applied, and the resulting current was measured, which was shown to exponentially decay to a constant value as a result of the build-up of ions at the interfaces, screening the DC bias. Subsequently, the DC bias was removed, and again a current was measured resulting from the electric field induced by the non-homogeneous distribution of mobile ions. This current was shown to exponentially decay to zero as a result of the diffusion of the mobile ions, leading to a homogeneous distribution. The time constants of both these processes were measured as a function of temperature, yielding activation energies of 0.13 [118] and 0.16 eV [119]. Finally, an interesting qualitative observation was made based on impedance measurements on $CsPbBr_3$ powder samples, which showed that the characteristic low-frequency arc typically attributed to long-range ionic migration and observable at ambient pressure, was lost for pressures above 2.3 GPa, suggesting ionic migration is quenched at elevated pressures [69]. This observation inspired our work on hydrostatic pressure, which is discussed later in this

thesis.

2.1.2.2 Theoretical studies

Though ionic migration in the hybrid LHPs has been studied extensively through computation, only a few studies have investigated ionic migration in $CsPbBr_3$ using computational methods. For instance, *ab initio* molecular dynamics (MD) simulations were performed on $APbX_3$ systems, with A={MA,Cs} and X={I,Br}, and the activation energies for hopping were extracted in order to interpret experimental observations on $MAPbI_3$, [120]. In this study, simulations of $CsPbBr_3$ were performed using a simulation cell adopting the tetragonal phase, which we have previously discussed is only stable for temperatures between 88 and 130 °C. Because of the reduced symmetry of the tetragonal phase with respect to the cubic phase, the halide sites can be grouped in two different sets which are denoted as apical and equatorial, such that the activation energy now depends on the direction of the hop, i.e. the apical direction is parallel to the rotation axis corresponding to the octahedral tilting, while the (two) equatorial directions span the plane perpendicular to the rotation axis. For V_{Br}^{+} migration, an activation energy of 0.27 eV is reported for a hop between two equatorial bromide sites, and an activation energy of 0.29 eV is reported for a hop from an equatorial to an apical site, whereas the reverse hop has an activation energy of 0.16 eV. For V_{Cs}^{-} migration, activation energies of 0.7 and 1.2 eV are reported for hops in the equatorial and apical directions, respectively. For V_{Pb}^{2-} migration, activation energies of 0.94 and 1.22 eV are reported for hops in the equatorial and apical directions, respectively. In another study, ion migration was studied using molecular dynamics based on a set of interatomic potentials [121], yielding an activation energy of 0.3 eV for bromide vacancy migration, and 1.25 eV for caesium vacancy migration.
Other studies have used density functional theory (DFT) to compute the activation energies for vacancy hopping. Calculations of $CsPbBr_3$ in the cubic phase yielded activation enthalpies of 0.33 [70] and 0.65 [122] eV for V_{Br}^{+} hopping. Calculations of $CsPbBr_3$ adopting an orthorhombic phase resulted in activation enthalpies of 0.51 and 0.8 eV, for hopping in the [010] direction of V_{Br}^{+} and V_{Cs}^{-} respectively [123], though we note that this does not fully specifiy the hop in the orthorhombic phase because of the low symmetry with respect to the cubic aristotype. The ramifications of the lower symmetry were addressed in a different study, where the authors found activation enthalpies in a range of 0.19–0.26 eV for V_{Br}^{+} in the orthorhombic phase, higher than the activation enthalpy of 0.12 eV that was computed for the cubic phase [124]. The authors find that the activation enthalpy is increased when the surrounding octahedra are kept fixed, concluding that freely rotating octahedra facili-

tate ionic migration in LHPs, suggesting that experimental approaches that lock octahedral tilting should be pursued in order to mitigate ionic migration. Finally, DFT calculations were performed for vacancies at and near surfaces of $CsPbBr_3$ adopting the cubic phase, yielding activation enthalpies for hopping in the range 0.26–0.40 eV depending on the surface termination and the distance to the surface [122].

2.1.3 Comparison to Other LHPs

Since we use $CsPbBr_3$ as a model system, the question remains to what extent the activation energies differ with composition. In other words, is the activation energy similar for bromide and iodide vacancy migration, and is there an influence of the A-site cation? The results of several studies looking at activation energies for halide migration in LHPs are compiled below. These results are visualised in the form of histograms, as depicted in Figure 2-3, in which the occurences of migration barriers in a certain range are grouped together in bins of 0.25 eV. The studies on which these histograms are based are tabulated in Tables A.1 to A.4.

Interestingly, these histograms clearly show that the majority of the activation energies that were measured and calculated fall below a value of 0.5 eV. Such values are relatively low, and are consistent with experimental observations that have been observed on the second/minute timescale, such as the widely observed current-voltage hysteresis and the existence of features in the corresponding frequency range when performing impedance spectroscopy measurements.

Because there is a large variety of both experimental and theoretical techniques, the studies that look at both iodide and bromide migration using the same methodology (being computational in all cases) in a single study are shown in Table A.5. Since the differences between the measured and computed activation energies are small, these results suggest no major indication that bromide migration is substantially different from iodide migration. As such, our work on bromide migration should be a good proxy to understanding halide migration in LHPs more generally.

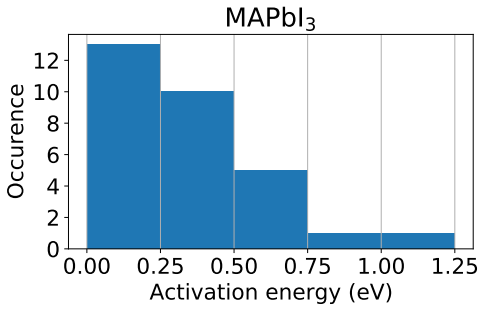

(a) Histogram of the activation energies of $MAPbI_3$.

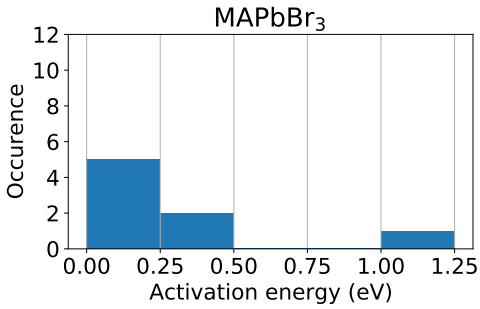

(b) Histogram of the activation energies of $MAPbBr_3$.

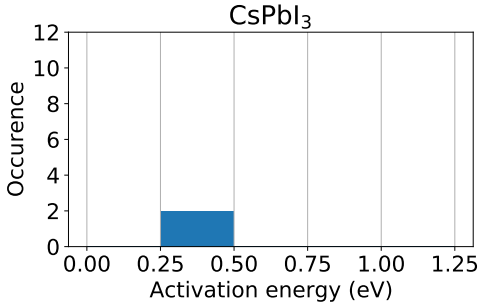

(c) Histogram of the activation energies of $CsPbI_3$.

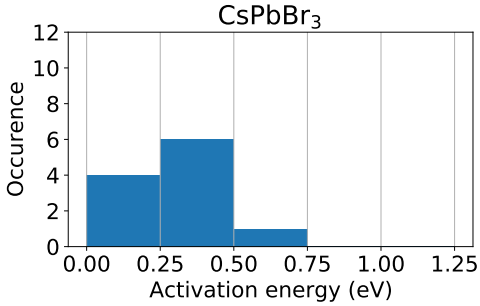

(d) Histogram of the activation energies of $CsPbBr_3$.

Figure 2-3: Histograms of the activation energies of halide migration for $MAPbI_3$, $MAPbBr_3$, $CsPbI_3$ and $CsPbBr_3$, grouped in bins of 0.25 eV each.

2.2 Strain and Strain Engineering of LHPs

In general, strain (deformation) results from a stress being applied to the crystal lattice. Strain can be induced through external stresses such as hydrostatic pressure, but it is also inherently present in LHP-based devices, for example due to lattice mismatch between the perovskite layer and the substrate, or through bending or stretching of the perovskite layer. Given the soft nature of MHPs [125], substantial deformations can be accessed through moderate levels of stress. Hence strain engineering has recently been suggested as a means to control the properties of LHP layers in perovskite-based devices [49–51, 62, 126, 127]. Interestingly, strain is also being increasingly looked at as an important parameter affecting the ionic migration in the wide class of energy materials [128]. Indeed, the high levels of ionic migration observed in LHPs have been linked to the fact that lead-halide perovskites are relatively soft materials [121, 129].
In this section, we wish to provide a general understanding of the origins of stress and strain in LHPs, and how they correlate through the elastic constants.

2.2.1 Softness of the Perovskite Lattice

The relationship between stress and strain was first published by Robert Hooke. The original formulation was cryptically included in the following statement: "The true Theory of Elasticity or Springiness, and a particular Explication thereof in several Subjects in which it is to be found: And the way of computing the velocity of bodies moved by them, *ceiiinosssttuu*." [130] In a later publication, he explained the meaning of this anagram, "About two years since I printed this Theory in an Anagram at the end of my Book of the Descriptions of Helioscopes, viz. *ceiiinosssttuu*, id est, Ut tensio, sic vis; That is, The Power of any Spring is in the same proportion with the Tension thereof." [131].
This can be paraphrased to a statement like as the extension, so is the force, meaning that a linear relationship between stress and strain exists. More formally, such a relationship can be expressed using elastic moduli. Several such examples exist, including Young's modulus (E), the bulk modulus (B) and the shear modulus (G).
Young's modulus (E) describes the lengthwise deformation ϵ resulting from a lengthwise tensile or compressive stress σ

$$E = \frac{\sigma}{\epsilon}. \tag{2.1}$$

The bulk modulus (B), also sometimes denoted by K, describes the volumetric compression (ΔV) resulting from hydrostatic pressure (P)

$$B = -V\frac{dP}{dV} \approx -\frac{P}{\Delta V}. \tag{2.2}$$

Finally, the shear modulus (G) describes the shear strain (γ) resulting from a shear stress (τ) in a given direction

$$G = \frac{\tau_{xy}}{\gamma_{xy}}. \tag{2.3}$$

These expressions can be related to each other by using the Poisson ratio ν, which is a measure of the deformation in a direction transverse to the direction of stress, i.e.

$$\nu = -\frac{d\epsilon_{\text{trans}}}{d\epsilon_{\text{axial}}}. \tag{2.4}$$

With this expression, the elastic moduli (assuming an isotropic system) can be expressed in terms of one another via

$$E = 2G\,(1+\nu) = 3B\,(1-2\nu)\,. \tag{2.5}$$

An overview of the elastic moduli for several commercially interesting metal-halide perovskites are given in Table 2.1. These values have been computed using DFT calculations of the structures in the orthorhombic unit cell with space group $Pnma$ [55]. As can be seen, the bulk and Young's moduli of these materials are within a range of 15–31 GPa. Both the bulk and Young's moduli for $CsPbBr_3$ fall towards the lower end of this range, with values of 20.7 and 19.9 GPa, respectively.

Other DFT calculations of the bulk modulus of $CsPbBr_3$ in a cubic phase with space group $Pm\bar{3}m$ find bulk moduli in a range 17.2–23.5 GPa [132–137], similar to the values obtained for $CsPbBr_3$ in the orthorhombic phase. Similarly low values are found experimentally through nano-indentation of single-crystal $CsPbBr_3$ in the orthorhombic phase, with values of 15.8 and 15.5 GPa for Young's and the bulk modulus, respectively [138]. In a separate experiment, a bulk modulus of 18.1 GPa is measured for single-crystal $CsPbBr_3$ by fitting the cell volume as a function of pressure to a second-order Birch–Murnaghan equation of state [123]. Other experimental studies on $CsPbBr_3$ nanocubes find values for the bulk moduli in a range of 16.9–17.7 GPa [63, 139]. In comparison, the bulk moduli of oxide perovskites are about an order of magnitude larger, with respective values of 177 and 258 GPa for $CaTiO_3$ [140] and $MgSiO_3$ [141].

Table 2.1: Values reported (in GPa) for the elastic moduli of various common halide perovskites compositions in the $Pnma$ phase [55].

Material	E	B	G	ν
$MAPbI_3$	20.5	19.0	7.8	0.32
$MAPbBr_3$	24.8	22.9	9.4	0.32
$MAPbCl_3$	26.1	25.6	9.8	0.33
$CsPbI_3$	18.4	16.0	7.0	0.31
$CsPbBr_3$	20.7	19.9	7.8	0.33
$CsPbCl_3$	21.9	23.2	8.1	0.34
$MASnI_3$	23.3	19.1	9.0	0.30
$MASnBr_3$	25.8	23.4	9.8	0.32
$MASnCl_3$	30.8	27.9	11.7	0.32
$CsSnI_3$	19.3	17.1	7.3	0.31
$CsSnBr_3$	20.9	20.8	7.9	0.33
$CsSnCl_3$	24.5	25.4	9.2	0.34

The elastic moduli discussed above are useful for describing isotropic materials, but in order to describe anisotropy we wish to introduce the elasticity tensor $\boldsymbol{C}$, which can be used to link the strain and stress tensors $\boldsymbol{\epsilon}$ and $\boldsymbol{\sigma}$ as

$$\boldsymbol{\sigma}_{ij} = \boldsymbol{C}_{ijkl}\boldsymbol{\epsilon}_{kl}. \tag{2.6}$$

The notation of the individual components of this elasticity tensor can be simplefied using Voigt notation which maps the tensor indices to reduce its order. The standard mapping is as follows;

$$\begin{aligned} ij &\Rightarrow \alpha \\ 11 &\Rightarrow 1 \\ 22 &\Rightarrow 2 \\ 33 &\Rightarrow 3 \\ 23, 32 &\Rightarrow 4 \\ 13, 31 &\Rightarrow 5 \\ 12, 21 &\Rightarrow 6 \end{aligned} \tag{2.7}$$

The relevant components of the elasticity tensor are shown for several perovskite compositions in Table 2.2. Among the three components $C_{11},\ C_{22}$ and C_{33}, the elastic component is highest along the [010] direction (corresponding to C_{22}) for all compositions, meaning that the perovskite is least deformable along this direction. Whether it is lowest along [100] or [001] depends on the composition, as can be seen in Table 2.2.

Table 2.2: Values reported (in GPa) for the components of the elasticity tensor of various common halide perovskites compositions, obtained from DFT calculations on structures in the $Pnma$ phase [55].

Material	C_{11}	C_{22}	C_{33}	C_{44}	C_{55}	C_{66}	C_{12}	C_{13}	C_{23}
$MAPbI_3$	25	41	31	6	10	5	8	16	13
$MAPbBr_3$	29	48	35	7	14	6	11	20	16
$MAPbCl_3$	34	53	40	7	13	7	14	20	20
$CsPbI_3$	31	34	17	6	11	7	9	17	9
$CsPbBr_3$	33	40	21	7	14	8	12	20	13
$CsPbCl_3$	35	46	24	7	16	8	15	23	17
$MASnI_3$	24	42	33	7	11	6	7	15	13
$MASnBr_3$	33	48	38	7	13	7	12	19	16
$MASnCl_3$	42	54	43	9	16	9	16	23	17
$CsSnI_3$	27	36	21	6	12	7	9	16	10
$CsSnBr_3$	32	43	23	7	15	7	12	21	14
$CsSnCl_3$	35	49	31	8	17	8	14	25	18

2.2.2 Origins of Strain

The origin of strain in LHP layers has been the subject of a large number of studies. For example, the so-called photostriction effect, which is defined as a change in the strain state resuling from irradation, and which is of interest for devices such as microsensors, was investigated for $MAPbI_3$ [142] and $MAPbBr_3$ [143]. For both materials, the crystal was found to compress under illumination, with photostrictive coefficients of $5 \times 10^{-8}\,m^2W^{-1}$ and $2.08 \times 10^{-8}\,m^2W^{-1}$ for $MAPbI_3$ and $MAPbBr_3$, respectively. Authors verified that these strains did not result from thermal effects. These observations were linked to strong coupling of the molecular rotation modes to the irradiation. In a different study, $MAPbI_3$ was shown to exhibit photostriction but expand under illumination, as did $CsPbBrI_2$, while no photostriction was observed for $FAPbI_3$ [144].

Interestingly, compressive lattice strain was also shown to result from an applied voltage bias, with strain values of -1% measured for voltages of $\pm$3.7 $V\mu m^{-1}$ [145]. The authors suggest that such behaviour is not a result of piezoelectricity, but rather results from the formation of defects under applied bias. In a study on $MAPbI_3$, authors found that a combination of illumination and an applied field led to induced strain, which was attributed to lateral motion of the MA-cation [146].

Other studies have focussed on the residual strain which remains after the crystallisation stage [147]. Such strains can manifest themselves on various lengthscales, ranging from tens of nanometers (sub-grain) to tens of micrometers, which is much larger than a single grain [59]. While such strains near grain boundaries and even subgrain strain fields have

been linked to instabilities [60,148], we now wish to shift our focus to slightly different forms of stress and strain which are very relevant to LHP-based devices both under production and operation. Below we will discuss origins the most relevant origins of triaxial, biaxial and uniaxial strain. We nonetheless note that insights into the effects of these macroscopic types of strain can also aid the understanding of the effects of other types of strain.

2.2.2.1 Triaxial Strain

Many studies have aimed to induce triaxial strain through the application of hydrostatic pressure, as exemplified by various reviews on the topic [58, 61, 149–151]. Hydrostatic pressure is typically exerted using a diamond anvil cell with the perovskite submerged in a pressure transmitting medium, which ensures that the pressure is exerted on the perovskite uniformly [51, 61, 152].

Most studies have focussed on the effects of hydrostatic pressure on the optoelectronic properties, most notably the band gap. Experimentally, it has been found that the response of the band gap on applied stress, in particular hydrostatic pressure, is quite non-linear but of the order of 17-100 meV/GPa and exhibits both blueshifts and redshifts depending on the level of stress [61].

There have been a lot of efforts in developing an atomistic understanding of the structural change that induces the change in the band gap. In general, the dependence on the band gap on mechanical strain has been rationalised based on variations in the coupling of atomic orbitals. To summarise the consensus (with a focus on $CsPbBr_3$); the VBM is composed of antibonding states resulting from interactions between the Pb s-orbital (6s) and the bromide 4p-orbital (3p for chloride, 5p for iodide), while the CBM is mainly composed of non-bonding Pb 6p states. As a result, variations in the band gap are dominated by changes in the coupling between the Pb 6s orbitals and the bromide 4p orbitals [64]. Shortening of the Pb-Br bond-length increases the coupling between the orbitals, widening the valence band and pushing the VBM up, leading to a decrease in the band gap, and vice versa for bond lengthening. The coupling strength is also determined by the Pb-Br-Pb bond angle. Octahedral rotations reduce the bond angle from the maximal value of 180°, reducing the coupling between the Pb- and Br-orbitals, reducing the VBM and resulting in a increased band gap.

Under low hydrostatic pressures ($<$5 GPa), octahedral tilting is claimed to be dominant [57], though the delicate trade-off between these two competing effects makes the behaviour of the band gap as a function of stress hard to predict *a priori*. As a result, many individual studies have been performed on various perovskites, as shown in the reviews highlighted

before [58, 61].

The structural and optoelectronic properties of $CsPbBr_3$ have been studied under a pressure range up to 2.0 GPa. It is found that for low pressures the band gap decreases, being 2.28 eV at 1.0 GPa compared to an initial value of 2.32 eV, after which it increases up to a value of 2.33 eV at 2.0 GPa. At 1.0 GPa, the band gap shows a very clear discontinuity, going from a linear decrease to a linear increase in the band gap as function of pressure. XRD and Raman results however do not indicate any change in the lattice symmetry, and the phase transition is concluded to be isostructural.

Also the effects of pressure on the charge carrier dynamics have been studied both theoretically and experimentally. To the best of our knowledge, the charge carrier dynamics of $CsPbBr_3$ have been studied only in pristine samples, and find charge carrier mobilities in the range of about 10-2000 $cm^2V^{-1}s^{-1}$ [153–159]. It is worth mentioning that in one of these studies, experiments were performed on a single crystal with dimensions of 3 cm in diameter and 10 cm in length, which indicates the viability of single crystal design of $CsPbBr_3$ [160]. To understand the effects of pressure on charge carrier dynamics we therefore look at other LHPs. In-situ high-pressure femtosecond transient absorption spectroscopy measurements were performed on $MAPbBr_3$ to study the excited-state carrier dynamics as a function of pressure [161]. The authors find that the optical-acoustic phonon scattering and Auger recombination can be modified using pressure, thereby changing the lifetimes for charge carrier relaxation. These lifetimes are initially shown to increase with pressure from 130 ps up to 450 ps at a pressure of 0.3 GPa, after which point the lifetime drops to 275 ps at 0.4 GPa as a result of a pressure-induced phase transition from the cubic $Pm\bar{3}m$ to the cubic $Im\bar{3}$ phase. Up to 1.6 GPa the lifetime further decreases with pressure, and after a small increase as a result of another pressure-induced phase change to the orthorhombic $Pnma$ phase it continues to decrease with increasing pressure.

2.2.2.2 Biaxial Strain

Another type of stress that has been regularly observed in layered perovskite-based devices, is that resulting from the mismatch in thermal expansion coefficient (TEC) of the perovskite and substrate [71] layers. This stress due to a mismatch in TECs ($\sigma_{\Delta T}$) can be estimated by

$$\sigma_{\Delta T} = \frac{E_{\mathrm{p}}}{1-\nu_{\mathrm{p}}} \left(\alpha_{\mathrm{s}} - \alpha_{\mathrm{p}}\right) \Delta T, \tag{2.8}$$

where E_{p} is the perovskite Young's modulus, ν_{p} is the Poisson's ratio of the perovskite layer, α_{s} and α_{p} are the TECs of the substrate and perovskite layers respectively, and finally ΔT

is the difference between the annealing temperature and operating temperature [73, 162]. Typical TEC values are shown in Figure 2-4 for several substates, electron transporting layers (ETLs), perovskites and hole transporting layers (HTLs) that are commonly used in PSCs. As can be seen the TEC of most substrates and ETLs is significantly lower than those of the perovskite layers. Based on the lower TEC value of substrates and ETLs compared to the perovskite layer, Equation (2.8) predicts the perovskite layer to exhibit tensile strain. XRD studies show that these strains are highest directly at the interface, and become lower with increasing depth, though they are still noticeable 500 nm from the surface [49]. Several

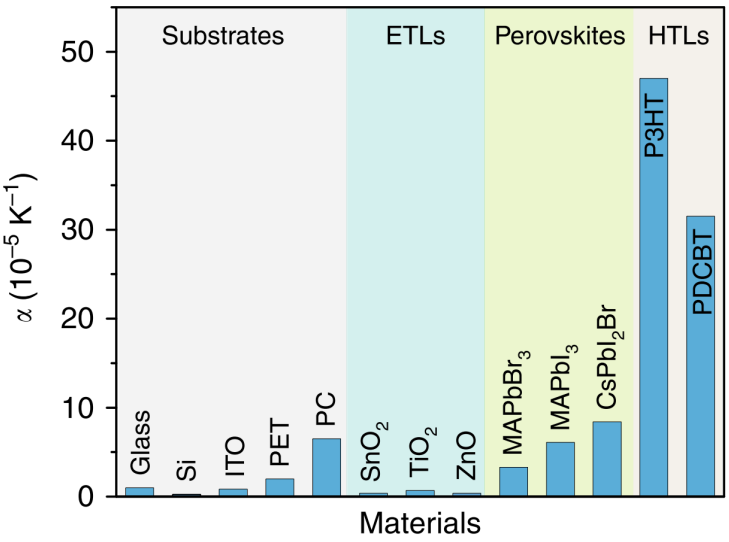

Figure 2-4: Thermal expansion coefficients (TECs) of several commonly used substrates, ETLs, perovskite layers and HTLs in PSCs. Reproduced from Reference 73.

approaches have been explored to mitigate the tensile strain in the perovskite layer. One straightforward approach is to use substrates with a higher TEC, which has indeed been shown to significantly reduce the stress induced in the perovskite layer [162]. For example, devices were fabricated with polyethylene terephthalate (PET) (TEC $\approx 6.5 \times 10^{-5}$ K^{-1}) and polycarbonate (PC) (TEC $\approx 2.0 \times 10^{-5}$ K^{-1}) as substrates [162]. These devices showed superior stability to humidity and temperature. Interestingly, the stress on the perovskite layer was found to be independent of the ETL for a glass substrate. This was rationalised because the glass substrate is typically orders of magnitude thicker than the ETL layer such that it dominates the induced stress in the perovskite layer. This suggest that the TEC mismatch between perovskite and substrate layer is the most important parameter to optimise in layered devices, though typically these layers are not in direct contact. Interestingly, the correlation between stress and annealing temperature was found to be independent of

perovskite formulation, deposition method and anti-solvent used, and can thus be linked purely to the annealing stage. In a separate study, a WS_2/$CsPbBr_3$ heterostructure was designed, with the idea that the interaction between the perovskite and the substrate is reduced, such that it can contract upon cooling [72]. Indeed, the authors do find that the perovskite film in the presence of WS_2 exhibits less tensile strain and shows improved PCEs, when compared to the film in the absence of WS_2 as an interlayer.

In another study, $MAPbI_3$ (4–16 $\times 10^{-5}\,K^{-1}$) was deposited on a Kapton substrate (3–11 $\times 10^{-5}\,K^{-1}$) with PEDOT:PSS ($\approx 5 \times 10^{-5}\,K^{-1}$) and PMMA (5–10 $\times 10^{-5}\,K^{-1}$) as charge transport layers [163]. Though the TECs of all these layers are all relatively similar, significant strains of the order -0.37–0.8% were still observed in the $MAPbI_3$ layer as observed through grazing incidence wide angle X-ray scattering (GIWAXS) measurements, and which were linked to the presence of ferroelastic domains, i.e. the spontaneous formation of subgrain domains of differing orientation.

Another approach to minimise lattice strain from mismatch in TECs that was explored was to compensate the tensile stress from the substrate with compressive stress from the HTL [73]. To achieve such strain-compensation, HTLs should have a higher TEC than the perovskite layer, have a strong interaction with the perovskite layer in order to achieve strain offset and should be able to withstand and be coated at high temperatures. For this purpose PDCBT, with a measured TEC of 31.5 $\times 10^{-5}\,K^{-1}$, was used as a HTL layer in a glass/ITO/TiO_2/$CsPbI_2Br$/PDCBT/MoO_x/Au device. It was found through XRD measurements that for coating temperatures of about 80 °C the tensile strain in the perovskite layer was effectively compensated, while for higher temperatures (homogeneous) compressive strain was induced in the perovskite layer, such that strains of almost 2% were induced for a coating temperature of 120 °C. Interestingly, the devices with compressively strained perovskite layers showed significantly increased stability in terms PCE, as shown in Figure 2-5.

Finally, reducing the annealing temperature of the perovskite layer to reduce ΔT reduces the level of strain in the perovskite layer, which effectively becomes strain-free at annealing temperatures around room temperature [71].

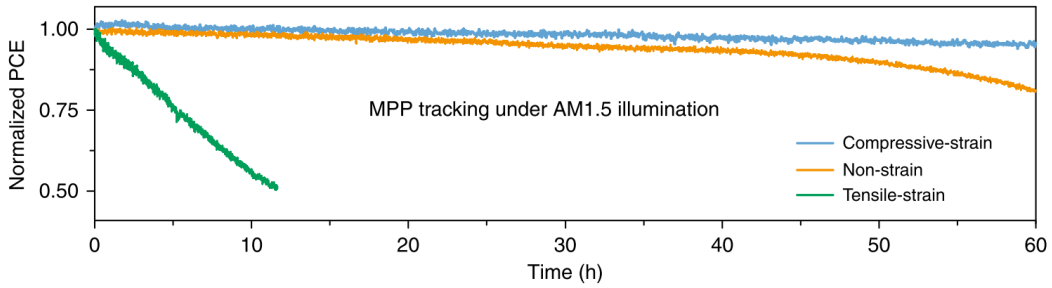

Figure 2-5: PCE stability of PSCs with different HTL coating temperatures, such that the perovskite layer is under tensile, no and compressive biaxial strain. Tensile biaxial strain is shown to reduce devic stability, while compressive strain improves it. Reproduced from Reference 73.

2.2.2.3 Uniaxial Strain

Yet another form of strain can result from conceptually simple stresses along a single dimension, such as stretching and bending. An understanding of the effects of uniaxial strain are therefore clearly important, in particular when LHPs are deposited on flexible substrates, e.g. to create flexible solar cells [164–168]. Such devices are under strain during production, for example when using roll-to-roll deposition methods [168, 169]. Moreover, being specifically designed for applications in flexible conditions, they are continuously being bent during operation, such that the LHP layers are continuously exposed to uniaxial strain.

To mimic such conditions, flexible solar cells are bent around cylinders of a certain radius R, which depending on the thickness z of the solar cell device results in an effective strain that can be approximated by $z/2R$. This process is often done repeatedly to study the stability of the perovskite layer over many bending cycles.

In one example, $MAPbI_3$ was deposited on flexible polyethylene terephtalate (PET) substrates after which the full stack was bent around cylinders with radii of 6 and 12 mm [162]. Both tensile and compressive strain could be induced using this approach, depending on the orientation of the perovskite layer and the substrate. Interestingly, other authors were also able to bend stacks of perovskite layers deposited on top of glass substrates [71]. In both studies, strong correlations between strain and stability were observed, with tensile strain driving enhanced degradation and compressive strain improving the stability. Importantly, the stress-strain response was shown to be non-linear for multicrystalline samples of $MAPbI_3$ [163]. This non-linearity was attributed to the formation of twin walls or boundaries, which correlated strongly with defect formation and degradation of the LHP films.

Such deterioration of both the film quality and performance is linked to cracking of the perovskite layer [170], allowing for the ingress of H_2O and O_2 [166]. Several approaches

have been taken to mitigate some of the negative effects of such continuous bending. In one such case, a conductive polymer was glued between the indium tin oxide and perovskite layers [171]. This approach, termed bionic as it was inspired by the continuous bending of vertebrae, was shown to facilitate oriented crystallisation, and act as an adhesive between the ITO and perovskite layers, enhancing the stability. In another study, a thin layer of 2D perovskites, which have large organic cations at the A-site acting as spacers, was used as a capping layer on the active perovskite layer [172]. This approach boosted the stability over many bending cycles, with the enhanced efficiency being attributed to an effective sealing of the surface flaws and cracks in the active layer.

2.3 Stability

Over the years, LHPs have seen a remarkable improvement in their power conversion efficiency (PCE), which is now similar to those of more established photovoltaic technologies, such as silicon solar cells. However, their limited stability has thus far hindered their large-scale commercialisation [37–39,86], despite a large number of studies dedicated to this issue, as exemplified by a large number of reviews on the topic [173–176]. In these studies, many drivers towards instability have been elucidated, some of which are a result of extrinsic factors, such as humidity and oxygen, while others are a result of more intrinsic factors, such as the phase stability. Both of these groups of factors will be discussed in the sections below.

2.3.1 External Factors Towards Instability

Two of the most pervasive environmental factors affecting the stability of LHP solar cell devices are humidity and the presence of oxygen [174]. For instance, though the presence of a small amount of water may favour nucleation and crystallisation of the perovskite layer, it has a strong negative impact on the long-term stability of LHP-based solar cells as it can result in device degradation over a few hundreds of hours, or in some cases even less [177]. The current understanding of such humidity-induced degradation is that water molecules are able to penetrate the perovskite structure, where it can then form hydrogen bonds with the organic cation, loosening its hydrogen bonds to the lead-halide framework and making it more volatile [178]. Moreover, it can protonate the halide species, resulting in the formation of volatile HX [179]. Such enhanced volatility then facilitates mass transport and finally material degradation.

The presence of oxygen has also been identified as an important cause towards material instability. In particular in combination with other factors such as illumination or bias, the

presence of oxygen has been linked to rapid degradation on the order of several hours, while such instabilities are largely absent when the perovskite films are tested in an atmosphere of N_2 [180, 181]. The ingress of oxygen has been shown to occur rapidly and to be facilitated by halide vacancies both at the surface and in the bulk of perovskite crystallites, leading to a uniform distribution throughout the film [182]. The common understanding is that through electron capture, the oxygen species then form a highly reactive superoxide species, which causes the material instability.
The main approach to mitigate the negative effects of these extrinsic factors has been to enclose the devices within an impermeable layer of encapsulation, in the first place to keep moisture and oxygen away, but also to prevent the perovskite components, such as the volatile A-site cation but more importantly the lead, from leaking out [183,184]. Though encapsulation has been shown to dramatically boost the overall stability of LHP-based devices, many issues such as delamination under strain and heat still exist, such that the development of encapsulation techniques is still a very active area of research, as exemplified by several recent reviews [185–187].

2.3.2 Intrinsic Factors Towards Instability

While the effects of extrinsic factors towards instability can be largely mitigated through encapsulation, several intrinsic drivers towards material instability remain. One such case is that of thermal instability, which is detrimental to solar cell operation and which typically occurs at elevated temperatures of 60–70°C and above. Thermal instabilities can be observed through changes in various material properties even under inert conditions, i.e. with no exposure to either moisture or oxygen [188]. For example, heat induces changes in the absorption spectra that indicate a loss of the perovskite and the formation of precursor lead halide PbX_2. Over time, such changes also become apparent through changes in the film structure, which can be observed using scanning electron microscopy (SEM) or Kelvin probe force microscopy (KPFM). These also indicate a degradation of the perovskite structure into the precursor salts, in particular PbX_2. The film structure evolution under heat, as shown via SEM imaging, is shown in Figure 2-6. Interestingly, the inorganic halide perovskites exhibit a much higher tolerance to heat instabilities than their hybrid organic-inorganic lead-halide perovskite counterparts, which have been linked to the volatility of the organic molecule [173].
Another cause of material instability is a result of the spontaneous transition from the black perovskite phase to a yellow non-perovskite phase. This is an issue particularly for $CsPbI_3$, which, similar to $CsPbBr_3$, adopts a cubic phase with space group $Pm\bar{3}m$ at elevated temperatures, in the case of $CsPbI_3$ at temperatures of 360° and above. With decreasing

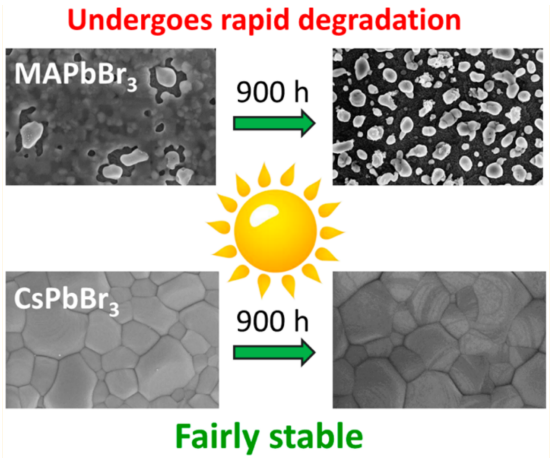

Figure 2-6: Relative stability of $MAPbBr_3$ and $CsPbBr_3$ towards heat. Reprinted with permission from Reference [188]. Copyright 2017 American Chemical Society.

temperature, it then undergoes a series of phase transitions, first to a tetragonal phase with space group $P4/mbm$ at 260°C and then to an orthorhombic structure with space group $Pnma$ at 175°C [189]. Over time however, the black phase transitions to the true ground state, which corresponds to a different orthorhombic phase, also with space group $Pnma$. Despite having the same stoichiometry, this structure is not a perovskite; instead of having corner-sharing octahedra, the octahedra are edge-sharing, and the resulting structure is not photoactive.

Though such thermodynamic instabilities are challenging to address, several studies have nonetheless been directed at stabilising the black perovskite phase relative to the yellow non-perovskite phase. Interestingly, strain engineering has successfully been used for this purpose [190, 191]. Tensile biaxial strain was shown to kinetically trap the black perovskite phase by increasing the energy barrier for going from the perovskite to the non-perovskite phase. In contrast, compressive biaxial strain was shown to reduce the energy of the cubic phase with respect to the non-perovskite phase. Additionally, the surface energy of the non-perovskite phase was found to be higher than that of the perovskite phase, such that the perovskite phase could also be stabilised by reducing the nanoparticle size, thereby increasing the surface-to-volume ratio.

2.4 Interplay between Ion Migration, Strain and Stability

Having introduced the background into the each of the separate we now want to shift our attention towards the interplay between the various topics. In particular, the link between

strain and stability has been widely studied, and the evidence for this link will be provided first. Though there is also some evidence of links between strain and ion migration, and ion migration and stability, the general understanding of these links is much less advanced, making our work on the effects of strain on the ionic migration in $CsPbBr_3$ very relevant.

2.4.1 Links between Strain and Stability

Many reports have suggested a link between the level of strain and stability of the perovskite layer. One such example is that of a $MAPbI_3$ film, which was bent in convex and concave ways, with approximate levels of strain out of the plane estimated at 0.2% and 0.67%, respectively [71]. Such conditions mimic in-service strains of perovskite layers in flexible PSCs. After 500h of illumination, the convex film exhibited large yellow areas, indicative of degradation of the perovskite layer into the precursor PbI_2. In contrast, an unstrained film showed only minor signs of degradation, whereas no signs of any PbI_2 formation were observed for the concave films. From conductivity measurements, the activity energies for ion migration were measured to be 0.29, 0.39 and 0.53 eV in the case of convex, flat and concave films, suggesting that higher levels of ion migration under tensile strain accelerate degradation. Interestingly, the authors observed that when the strain was removed before illumination, it had no clear effect on the degradation.
Similar results were obtained for $MAPbI_3$ on a PET substrate, for which the concave (i.e. compressively strained) films showed very little signs of degradation, which was much more severe in films that were in a convex bent state [162]. Similar observations were made for $MAPbI_3$ on a Kapton substrate, where clear signs of PbI_2 formation were found for films with convex bending, in contrast to films with concave bending for which no formation of PbI_2 was observed [163]. On such flexible substrates, fracturing of the perovskite layer is an important aspect to consider. Studies of $CsPbBr_3$ and $MAPbI_3$ on (PEDOT:PSS)-coated PES substrates indicate that the fracture energy can be increased with compressive biaxial strain during thin film formation, such that it is respectively 260 and 161% higher in the flat film during operation compared to a film that was coated in the absence of strain [192]. Tensile strain during thin film formation was conversely shown to decrease the fracturing energy.
The level of strain in the perovskite layer has also been shown to be of importance in terms of the PSC performance. By tuning the level of strain in the perovskite layer through changing the coating temperature of the HTL, Xue et al [73] showed that the PCE could retain 95 and 81% of its initial value after 60 hours of maximum power point (MPP) tracking when the perovskite layer was under compressive strain and when the strain was mitigated, respectively. In contrast, the PCE of the PSC with the perovskite layer under tensile strain

dropped to 50% after only ten hours of MPP tracking. In a separate study, pressure was applied during the annealing of $Cs_xFA_{3-x}I_3$ films using so-called confined pressure annealing [193]. The authors find that annealing under pressure significantly enhances the thin film quality, even after the pressure is removed. Moreover, even without any encapsulation, the PCE is shown to maintain 75% of its initial value after 500 hours of exposure in humidity, while this is only 80 hours for the control film. This indicates the role of stress and strain not only under operation, but also during device preparation.
Strain engineering has also been used to influence the phase stability of perovskites. $CsSnI_3$, which typically adopts an orthorhombic phase at room temperature, was deposited on KCl and shown to adopt a tetragonal phase [66]. The black perovskite phase of $CsPbI_3$, whose stable phase at room temperature is the non-perovskite δ-phase, was shown to be stabilised by substrate clamping through inducing tensile strain in the perovskite layer [190]. The photoactive perovskite phase of $FAPbI_3$, which also suffers from phase instability towards the non-perovskite phase, was stabilised through epitaxial growth on a lattice-mismatched $MAPbCl_xBr_{3-x}$ perovskite underlayer, generating compressive strains as high as -2.4% [62]. Remarkably, the thin $FAPbI_3$ film was shown to retain the dark perovskite phase for 360 days under strain, while degradation into the non-perovskite yellow phase occured within a day in the absence of strain.
Other observations of effects of strain include the stabilisation of a crystal phase with significant Rashba-splitting in $CsPbI_3$ and $MAPbI_3$ [194]. Moreover, tensile strain was shown to stabilise a ferroelectric phase in cubic $CsPbI_3$ [195], however with the knowledge that the thermodynamically stable phase $CsPbI_3$ is a non-perovskite phase, great care must be taken with the interpretation of these results. For $CsSnI_3$, both compressive and tensile strains were shown to stabilise ferroelectric phases [196].

2.4.2 Links between Strain and Ionic Migration

Using impedance spectroscopy, the dependence of ionic migration on external pressure was studied for $FAPbBr_3$ [197] and $CsPbBr_3$ [69]. In the measurements on $FAPbBr_3$, the electronic resistivity was shown to decrease with increasing pressure up to 0.5 GPa at which point it is about two orders of magnitude lower than the pristine value. This pressure marks a pressure-induced phase transition, and at higher pressures, the ionic resistivity increases again, such that at 3.4 GPa it is about five orders of magnitude higher than at 0.5 GPa. The ionic resistivity was observed as an inductive loop for low frequencies, and linked to migration of the organic FA cation. It was measured to be about two to three orders of magnitude lower than the electronic resistivity, but to follow a similar trend.

Similar experiments on $CsPbBr_3$ did not observe an inductive loop, though the ionic resistivity is again two orders of magnitude lower than the electronic resistivity over a range of pressures spanning 0–2.9 GPa, suggesting $CsPbBr_3$ is a mixed ionic-electronic conductor in this full pressure range before amorphisation takes place at 2.9 GPa. Similar to $FAPbBr_3$, both the ionic and electronic resistivities decrease for low pressures up to 1.2 GPa, at which pressure an isostructural phase transition takes place and after which both resistivities increase with pressure. In contrast to $FAPbBr_3$, variations in the resistivities are within one order of magnitude. In combination with the absence of an inductive loop in the impedance spectra, this suggests that this response is perhaps linked to halide migration, for which the dependence on pressure is still significant, but much less so than for the A-site cation in $FAPbBr_3$. Interestingly, the authors find that the ionic diffusivity in $CsPbBr_3$ increases by a factor of three up to a pressure of 1.2 GPa, after which it decreases up to a pressure of 2.9 GPa, at which point no ionic conduction is observed. These findings highlight the role of pressure in tuning the ionic conduction in MHPs, and $CsPbBr_3$ in particular.

In another study, the effect of pressure on the phase segregation in $MAPb(Br_xI_{1-x})_3$ was studied [70]. The authors used pressure-dependent transient absorption spectroscopy to track the phase segragation in the material, since the Br- and I-rich regions have different band gaps. The authors find that the phase segregation rate is reduced by two orders of magnitude when applying a pressure of 0.3 GPa, corresponding to an increase in the effective activation energy for halide migration by a factor of three. To verify whether such changes in ionic migration barriers can be induced through similar levels of stress, the authors calculate halide vacancy migration barriers in cubic $CsPbBr_3$ and $CsPbI_3$, and find that these increase by about 50% at 2.0 GPa of externally applied hydrostatic pressure. Though the variations found computationally are not as large as suggested experimentally, these results indicate that indeed ionic migration barriers can increase with hydrostatic pressure.

Strain was also shown to enhance light-induced halide segragation in mixed $MAPb(Br_xI_{1-x})_3$ [198]. The authors show that while for compositions with Br concentrations below <50% no light-induced halide segregation is initially present, such light-induced halide segregation can be induced by uniaxial compressive stress. They also show that this can be suppressed by releasing the strain using additives or by choosing a substrate with a more suitable lattice constant.

The hypothesis that ion migration is enhanced by tensile strain and linked to degradation was further explored for the $WS_2/CsPbBr_3$ heterostructure [72]. Through energy-dispersive X-ray spectroscopy (EDS) mapping the elemental distribution was measured along the cross-section of the device. For the device without the WS_2 interlayer, the Br distribution is rather disperse after ageing, with significant amounts of bromide noticeable throughout the device, particularly in the carbon HTL. In contrast, the bromide distribution remains much more

confined to the $CsPbBr_3$ layer after ageing when a WS_2 interlayer is used, though some bromide can be observed to have entered the carbon stack.
In another study activation barriers for halide vacancy migration in $CsPbI_2Br$ were computed using nudged elastic band (NEB) calculations [73]. Compared to a value of 0.667 eV in the unperturbed lattice, the migration barrier is shown to increase substantially to almost 1.0 eV at -3% biaxial strain, while it decreases to below 0.4 eV for +3% tensile strain. Sadly, the authors do not specify which specific vacancy they consider, nor in which phase the calculations are performed, nor whether the out-of-plane lattice is allowed to relax or kept fixed, complicating the interpretation of these results.
In yet another study, activation energies of iodide vacancy migration in $MAPbI_3$ were computed under both compressive and tensile triaxial and biaxial strain [199]. In both cases, activation energies were shown to increase with compressive strain, and decrease with tensile strain. The effect was much more severe in the case of triaxial strain however, with the activation energy doubling from 0.45 to 0.90 eV at 4% compressive triaxial strain, while the increase was limited to 0.05 eV in the case of 4% compressive biaxial strain. For tensile strain, the differences between the two types of strain were smaller, with a decrease of about 0.25 and 0.20 V for 4% triaxial and biaxial tensile strain, respectively.
Migration barriers were also measured in $MAPbI_3$ using conductivity measurements [71]. The activity energies for ion migration were measured to be 0.29, 0.39 and 0.53 eV in the case of convex, flat and concave films, which were bent to induce such strains.
In yet another study, samples of $CsPbI_{3-x}Br_x$ were aged over 12h, over which time the XRD-peaks shifted significantly [200]. These shifts were attributed to strain release. Interestingly, the aged sample, thus assumed to have released some of its strain, showed significantly lower amounts of hysteresis, which was linked to a reduction in the levels of ionic migration.

2.4.3 Links between Ionic Migration and Stability

Though ionic migration has very often been named as one of the primary drivers for towards instabilities, this link is predominantly speculative as direct experimental evidence is hard to obtain. Nonetheless, several studies have shown a direct link between ion migration and degradation. One such example was observed in a study on the role of the gold metal contact [201]. At an elevated temperature of 70°C, the authors observed significant diffusion of Au atoms through the HTL and into the perovskite layer, as evidenced by ToF-SIMS measurements. This Au diffusion was shown to cause severe reductions in both the open-circuit voltage and the short-circuit current of the devices. The authors however showed that such diffusion could be mitigated by adding a chromium interlayer.

In a different study, the conversion from $MAPbI_3$ into PbI_2 was studied using solid-state electrochemical reactions [202]. Two threads of $MAPbI_3$ were connected by a thread of PbI_2. The authors showed that under bias, the relative sizes of the two threads of $MAPbI_3$ could be altered which was visible through an electrically driven shift of the PbI_2 thread in between the two threads of $MAPbI_3$. Because no mass is lost or added during the application of the field, this experiment provides direct evidence of mass transport being responsible for the conversion between $MAPbI_3$ and the precursor PbI_2, which is the general reaction typically observed under degradation.

Chapter 3

Computational Techniques

3.1 Density Functional Theory

Density Functional Theory (DFT) has emerged as a versatile and robust quantum mechanical method based on first principles for computing defect calculations [203]. Its formal derivation was published in 1964 in a seminal paper by Walter Kohn and Pierre Hohenberg [204], the theorems derived in which provide the foundation for modern density functional theory. This accomplishment, in combination with other developments, was acknowledged in the form of a Nobel Prize in Chemistry, which was awarded to Walter Kohn in 1998. The essential elements to understanding DFT are described below, in which we closely follow Reference 205.

From our current understanding of the theory of matter, the physical and chemical properties of matter can be derived from a quantum-mechanical treatment of the interactions between the nuclei and their respective clouds of electrons. More formally, such interactions are described by a Hamiltonian operator $\widehat{H}$

$$\begin{aligned}\widehat{H} =& -\sum_{I=1}^{P}\frac{\hbar^2}{2M_I}\nabla_I^2 - \sum_{i=1}^{N}\frac{\hbar^2}{2m}\nabla_i^2 \\ &+ \frac{e^2}{2}\sum_{I=1}^{P}\sum_{J\neq 1}^{P}\frac{Z_I Z_J}{\left|\vec{R}_I - \vec{R}_J\right|} + \frac{e^2}{2}\sum_{i=1}^{N}\sum_{j\neq 1}^{N}\frac{1}{|\vec{r}_i - \vec{r}_j|} \\ &- e^2\sum_{I=1}^{P}\sum_{i=1}^{N}\frac{Z_I}{\left|\vec{R}_I - \vec{r}_i\right|} \\ =& \widehat{T}_n + \widehat{T}_e + \widehat{U}_{nn} + \widehat{U}_{ee} + \widehat{U}_{ne},\end{aligned} \tag{3.1}$$

in which $\vec{R}_I$ and $\vec{r}_i$ describe the nuclear and electronic coordinates, respectively, Z_I and M_I describe the charge and mass of the nuclei, respectively, and e and m describe the charge and mass of the electrons. These terms can be conceptualised as the kinetic energy terms of the nuclei $\left(\widehat{T}_n\right)$ and electrons $\left(\widehat{T}_e\right)$, the electrostatic interactions of the nuclei $\left(\widehat{U}_{nn}\right)$ and electrons $\left(\widehat{U}_{ee}\right)$ and the electrostatic interactions between the nuclei and the electrons $\left(\widehat{U}_{ne}\right)$. In principle, the many-body time-independent Schrödinger equation

$$\widehat{H}\Psi_i\left(\vec{R},\vec{r}\right) = E_i\Psi_i\left(\vec{R},\vec{r}\right) \tag{3.2}$$

can then be solved to find the eigenstates and eigenenergies of the system, from which the physical and chemical properties can be derived. Analytic solutions to this set of equations however only exist for a few particular cases, In practice, even numerical solutions are generally intractable for almost any system of interest due to the large number of coupled degrees of freedom. Several approximations are therefore typically made to cast this problem into a more readily solvable one.

3.1.1 Decoupling the Nuclear and Electronic Degrees of Freedom

A first approximation that is generally applied is the so-called Born-Oppenheimer or adiabtatic approximation [206]. This approximation is based on the observation that the timescales of motion of the nuclei are orders of magnitude lower than those of the electrons as a result of their much larger mass. The electrons can thus be assumed to instantaneously follow the motion of the nuclei, and as a result, the wave function of the system can be factorised as

$$\Psi\left(\vec{R},\vec{r},t\right) = \Theta_m\left(\vec{R},t\right)\Phi_m\left(\vec{R},\vec{r}\right), \tag{3.3}$$

in which $\Phi_m\left(\vec{R},\vec{r}\right)$ describes the mth electronic wave function with corresponding eigenenergy $\epsilon_m\left(\vec{R}\right)$, and Θ_m describes the mth nuclear wave function, which can be resolved using either the time-dependent

$$i\hbar\frac{\partial\Theta_m\left(\vec{R},t\right)}{\partial t} = \left[\widehat{T}_n + \widehat{U}_{nn} + \epsilon_m\left(\vec{R}\right)\right]\Theta_m\left(\vec{R},t\right) \tag{3.4}$$

or the time-independent Schrödinger equation

$$\left[\widehat{T}_n + \widehat{U}_{nn} + \epsilon_m\left(\vec{R}\right)\right]\Theta_m\left(\vec{R}\right) = E_m\Theta_m\left(\vec{R}\right). \tag{3.5}$$

A full quantum-mechanical solution to Equations (3.4) and (3.5) is still intractable, and the dynamics of the nuclei is therefore often treated classically using

$$M_I \frac{\mathrm{d}^2 \vec{R}_I}{\mathrm{d}t^2} = -\nabla E_m \left(\vec{R}_I \right). \tag{3.6}$$

3.1.2 Resolving the Electronic Wavefunction; Hartree-Fock Theory

The problem how to resolve the many-body wavefunction of the N interacting electron in the system remains. A first approximation, suggested by Hartree in 1928 [207], was to rewrite the full N-body electronic wavefunction as a product of one-electron wavefunctions $\phi_i(\vec{r}_i)$

$$\Phi_m \left(\vec{R}, \vec{r} \right) = \prod_i \phi_i \left(\vec{r}_i \right), \tag{3.7}$$

with each of the one-electron wavefunctions obeying a one-electron Schrödinger equation

$$\left(-\frac{\hbar^2}{2m} \nabla^2 + V_{\text{eff}}^{(i)} \left(\vec{R}, \vec{r} \right) \right) \phi_i \left(\vec{r} \right) = \epsilon_i \phi_i \left(\vec{r} \right) \tag{3.8}$$

including an effective potential V_{eff} which includes a mean-field interaction with the other electrons in the system

$$V_{\text{eff}}^{(i)} \left(\vec{R}, \vec{r} \right) = V \left(\vec{R}, \vec{r} \right) + \int \frac{\sum_{j \neq i}^{N} \rho_j \left(\vec{r}\,' \right)}{|\vec{r} - \vec{r}\,'|} d\vec{r}\,', \tag{3.9}$$

in which $\rho_j(\vec{r})$ describes the electron density of electron j

$$\rho_j \left(\vec{r} \right) = \left| \phi_j \left(\vec{r} \right) \right|^2. \tag{3.10}$$

To avoid counting electron-electron interactions twice, the sum of eigenenergies needs to be corrected in order to obtain the Hartree energy E_H of the system

$$E_H = \sum_{n=1}^{N} \epsilon_n - \frac{1}{2} \sum_{i \neq j}^{N} \iint \frac{\rho_i \left(\vec{r} \right) \rho_j \left(\vec{r}\,' \right)}{|\vec{r} - \vec{r}\,'|} d\vec{r} d\vec{r}\,'. \tag{3.11}$$

This set of N coupled equations can be solved self-consistently by computing the electronic densities from Equation (3.10), and casting them back into Equation (3.9) in order to solve Equation (3.8) while minimising the energy until the change in the wavefunction or the effective potential gets below a certain threshold. This procedure is called the self-consistent Hartree approximation.

This approach however treats the electrons as distinguishable particles, and neglects their fermionic character. An exact way to make the wavefunction antisymmetric upon particle exchange is to include a description of the electron spin σ_i and write the electron wavefunction as a Slater determinant [208, 209]

$$\Phi\left(\vec{R},\vec{r}\right)=\frac{1}{\sqrt{N!}}\begin{vmatrix}\phi_1\left(\vec{r}_1,\sigma_1\right) & \phi_1\left(\vec{r}_2,\sigma_2\right) & \cdots & \phi_1\left(\vec{r}_N,\sigma_N\right)\\ \phi_2\left(\vec{r}_1,\sigma_1\right) & \phi_2\left(\vec{r}_2,\sigma_2\right) & \cdots & \phi_2\left(\vec{r}_N,\sigma_N\right)\\ \vdots & \vdots & \ddots & \vdots\\ \phi_N\left(\vec{r}_1,\sigma_1\right) & \phi_N\left(\vec{r}_2,\sigma_2\right) & \cdots & \phi_N\left(\vec{r}_N,\sigma_N\right)\end{vmatrix}. \tag{3.12}$$

This method is generally described as Hartree-Fock (HF), and can again be solved self-consistently to find the optimal Slater determinant to minimise the energy of the system.

3.1.3 Exchange-Correlation Energy

The necessity to have the wavefunction adopt the form of a Slater determinant is however quite a severe limitation. In general, we wish to find an N-electron wavefunction $|\Phi\rangle$ so as to minimise the energy

$$E=\langle\Phi|\,\widehat{T}_e+\widehat{V}_e+\widehat{U}_{ee}\,|\Phi\rangle\,. \tag{3.13}$$

The main drawback to directly solving the above equation is the term that describes the electron-electron interactions

$$\langle\Phi|\,\widehat{U}_{ee}\,|\Phi\rangle=\langle\Phi|\,\frac{1}{2}\sum_{i=1}^{N}\sum_{j\neq i}^{N}\frac{1}{|\vec{r}_i-\vec{r}_j|}\,|\Phi\rangle \tag{3.14}$$

which can be expressed as

$$\langle\Phi|\,\widehat{U}_{ee}\,|\Phi\rangle=\iint\frac{\rho_2\left(\vec{r},\vec{r}\,'\right)}{|\vec{r}-\vec{r}\,'|}d\vec{r}d\vec{r}\,', \tag{3.15}$$

in which

$$\rho_2\left(\vec{r},\vec{r}\,'\right)=\frac{1}{2}\sum_{\sigma,\sigma'}\langle\Phi|\,\Psi_\sigma^\dagger\left(\vec{r}\right)\Psi_{\sigma'}^\dagger\left(\vec{r}\,'\right)\Psi_{\sigma'}\left(\vec{r}\,'\right)\Psi_\sigma\left(\vec{r}\right)|\Phi\rangle \tag{3.16}$$

describes the two-body density matrix with Ψ and $\Psi^\dagger$ the creation and annihilation operators for electrons, respectively. By defining a two-body correlation function $g\left(\vec{r},\vec{r}\,'\right)$

$$\rho_2\left(\vec{r},\vec{r}\,'\right)=\frac{1}{2}\rho\left(\vec{r},\vec{r}\right)\rho\left(\vec{r}\,',\vec{r}\,'\right)g\left(\vec{r},\vec{r}\,'\right) \tag{3.17}$$

in which the one-body density matrix $\rho(\vec{r},\vec{r}')$ is defined as

$$\begin{aligned}\rho(\vec{r},\vec{r}) &= \sum_{\sigma}\rho_{\sigma}\left(\vec{r},\vec{r}'\right)\\ \rho_{\sigma}\left(\vec{r},\vec{r}'\right) &= \langle\Phi|\,\Psi_{\sigma}^{\dagger}(\vec{r})\,\Psi_{\sigma}\left(\vec{r}'\right)|\Phi\rangle\end{aligned} \tag{3.18}$$

and in which the diagonal elements represent the real-space electronic density $\rho(\vec{r}) = \rho(\vec{r},\vec{r})$, the energy contribution of the electron-electron interaction can be written as

$$\langle\Phi|\,\widehat{U}_{ee}\,|\Phi\rangle = \frac{1}{2}\iint\frac{\rho(\vec{r})\,\rho(\vec{r}')}{|\vec{r}-\vec{r}'|}d\vec{r}d\vec{r}' + \frac{1}{2}\iint\frac{\rho(\vec{r})\,\rho(\vec{r}')}{|\vec{r}-\vec{r}'|}\left[g(\vec{r},\vec{r})-1\right]d\vec{r}d\vec{r}'. \tag{3.19}$$

The first term in the right-hand side of the equation describes the purely classical electrostatic interaction, while the second term includes quantum mechanical interactions and is more commonly referred to as the exchange-correlation energy. The correlation energy includes correlation effects that penalise the presence of two nearby electrons beyond simple Coulomb repulsion, while the exchange energy describes the repulsive contribution based on the Pauli exclusion interaction.

3.1.4 Hohenberg-Kohn Theorems

An early inspiration towards the formal development of DFT came from Thomas and Fermi, who in 1927 postulated that the energy of the electronic part of the Schrödinger equation could be expressed solely in terms of the electron density [210, 211]. These concepts were later derived more formally by Hohenberg and Kohn, in the form of two theorems often referred to as the Hohenberg-Kohn theorems which would usher in the dawn of the DFT formalism [204]. These Hohenberg-Kohn theorems describe the relation between a system of electrons with a fixed inter-electron interaction and under the influence of an external potential.

Hohenberg-Kohn Theorem I. *The external potential is a uniquely determined by the electron density, apart from an arbitrary constant.*

This can be proved through *reductio ad absurdum*. Let Ψ be the ground state wavefunction and $E_0 = \langle\Phi|\,\widehat{H}\,|\Phi\rangle = \langle\Phi|\,\widehat{T}+\widehat{U}+\widehat{V}\,|\Phi\rangle$ its corresponding ground-state energy. Now let Ψ' represent a different wavefunction with corresponding ground-state energy $E_0' =$

$\langle\Phi|\,\widehat{H}'\,|\Phi\rangle = \langle\Phi|\,\widehat{T}+\widehat{U}+\widehat{V}'\,|\Phi\rangle$. By invoking the variational principle, we can show that

$$\begin{aligned} E_0 < \langle\Psi'|\,\widehat{H}\,|\Psi'\rangle &= \langle\Psi'|\,\widehat{H}'\,|\Psi'\rangle + \langle\Psi'|\,\widehat{H}-\widehat{H}'\,|\Psi'\rangle \\ &= E_0' + \int \rho\left(\vec{r}\right)\left[\widehat{V}\left(\vec{r}\right)-\widehat{V}'\left(\vec{r}\right)\right]d\vec{r}, \end{aligned} \tag{3.20}$$

though the opposite statement must be equally true

$$\begin{aligned} E_0' < \langle\Psi|\,\widehat{H}'\,|\Psi\rangle &= \langle\Psi|\,\widehat{H}\,|\Psi'\rangle + \langle\Psi|\,\widehat{H}'-\widehat{H}\,|\Psi\rangle \\ &= E_0 - \int \rho\left(\vec{r}\right)\left[\widehat{V}\left(\vec{r}\right)-\widehat{V}'\left(\vec{r}\right)\right]d\vec{r}. \end{aligned} \tag{3.21}$$

By summing Equations (3.20) and (3.21), we obtain that $E_0 + E_0' < E_0 + E_0'$, which is clearly a contradiction and hence we prove that no two distinct external potentials can give rise to the same electron density.

Hohenberg-Kohn Theorem II. *The functional that delivers the ground-state energy of the system gives the lowest energy if and only if the input density is the true ground-state density.*

Let $\rho\left(\vec{r}\right)$ correspond to the ground state electron density, and let $\tilde{\rho}\left(\vec{r}\right)$ correspond to a different electron density normalised to the same number of electrons. Then

$$\begin{aligned} E\left[\tilde{\rho}\right] &= \langle\Psi\left[\tilde{\rho}\right]|\,\widehat{T}+\widehat{U}\,|\Psi\left[\tilde{\rho}\right]\rangle + \int \tilde{\rho}\left(\vec{r}\right)V\left(\vec{r}\right)d\vec{r} \\ &\geq E\left[\rho\right] = E_0 = \langle\Psi\left[\rho\right]|\,\widehat{H}\,|\Psi\left[\rho\right]\rangle, \end{aligned} \tag{3.22}$$

where the inequality is introduced by invoking Rayleigh-Ritz's variational principle. Provided that the functional expression is explicitly known, these two theorems provide the formal grounds for finding the ground state of a system in a variational approach.

3.1.5 Kohn-Sham Equations

Another hurdle towards explicitly computing the ground state is the fact that the kinetic energy of the system also includes a correlation term. This problem was addressed by Kohn and Sham in 1965, when they proposed to replace the system of interacting electrons by an equivalent system of non-interacting electrons whose ground state density equals that of the interacting system [212]. The ground state density can then be written in terms of

single-particle orbitals $\phi_{i,s}(\vec{r})$ as

$$\rho(\vec{r}) = \sum_{s=1}^{2} \sum_{i=1}^{N} |\phi_{i,s}(\vec{r})|^2 . \tag{3.23}$$

These orbitals, also referred to as Kohn-Sham orbitals, obey the self-consistent Kohn-Sham equations

$$\left[-\frac{\nabla^2}{2} + V_{\text{eff}}(\vec{r}) \right] \phi_{i,s}(\vec{r}) = \epsilon_{i,s} \phi_{i,s}(\vec{r}) , \tag{3.24}$$

in which the effective potential V_{eff} is given by

$$V_{\text{eff}}(\vec{r}) = V(\vec{r}) + \int \frac{\rho(\vec{r}\,')}{|\vec{r} - \vec{r}\,'|} d\vec{r}\,' + \mu_{XC}[\rho(\vec{r})] , \tag{3.25}$$

and where the exchange-correlation potential μ_{XC} is the derivative of the exchange-correlation energy E_{XC}

$$\mu_{XC} = \frac{\partial E_{XC}[\rho(\vec{r})]}{\partial \rho}, \tag{3.26}$$

which differs from the previous expression in Equation (3.19) because correlation effects of the kinetic energy operator have now been moved to the exchange-correlation functional part of the Hamiltonian. This can be taken into account by varying the electron-electron interaction in the Hamiltonian $\widehat{H} = \widehat{T} + \widehat{V} + \lambda \widehat{U}_{ee}$ and by averaging over the corresponding correlation function $g_\lambda(\vec{r} - \vec{r}\,')$ such that

$$E_{XC}[\rho] = \frac{1}{2} \iint \frac{\rho(\vec{r})\,\rho(\vec{r}\,')}{|\vec{r} - \vec{r}\,'|} \left[\tilde{g}(\vec{r}, \vec{r}\,') - 1 \right] d\vec{r} d\vec{r}\,', \tag{3.27}$$

in which

$$\tilde{g}(\vec{r}, \vec{r}\,') = \int_0^1 g_\lambda(\vec{r} - \vec{r}\,') . \tag{3.28}$$

By defining the so called exchange-correlation hole $\tilde{\rho}_{XC}(\vec{r}, \vec{r}\,') = \rho(\vec{r}\,')[\tilde{g}(\vec{r}, \vec{r}\,') - 1]$, the exchange-correlation energy can be written as

$$E_{XC}[\rho] = \frac{1}{2} \iint \frac{\rho(\vec{r})\,\tilde{\rho}_{XC}(\vec{r}, \vec{r}\,')}{|\vec{r} - \vec{r}\,'|} d\vec{r} d\vec{r}\,'. \tag{3.29}$$

This exchange-correlation hole describes the hole that an electron digs for itself around its position $\vec{r}$ and indicates the probability of finding another electron at $\vec{r}\,'$, and should always integrate to -1

$$\int \tilde{\rho}_{XC}(\vec{r}, \vec{r}\,')\, d\vec{r}\,' = \int \tilde{\rho}_{XC}(\vec{r}, \vec{r}\,')\, d\vec{r} = -1. \tag{3.30}$$

In principle, the Kohn-Sham equations defined in this way are still exact and the self-consistent solution can be found by an iterative procedure, given that we know the expression for E_{XC}. In practice however, the exact expression for E_{XC} is not known, and approximations to it are used.

3.1.6 Exchange-Correlation Functionals

The accuracy and computational expense of solving the Kohn-Sham equations to a large extent depend on the level of approximation of the exchange-correlation functional. The different levels of approximations are often denoted as rungs on the so-called Jacob's ladder [213], after verses 10-12 from chapter 28 of the book of Genesis:

"Jacob left Beer-sheba and went toward Haran. He came to a certain place and stayed there for the night, because the sun had set. Taking one of the stones of the place, he put it under his head and lay down in that place. And he dreamed that there was a ladder set up on the earth, the top of it reaching to heaven; and the angels of God were ascending and descending on it." Interestingly, this scene is also depicted in the exterior design of the Bath Abbey, a picture of which is shown in Figure 3-1. In this analogy, higher rungs correspond to more accurate approximations, and go up towards an ultimate goal of obtaining exact accuracy, which is currently yet unreached. However, higher rungs come at the cost of lower computational efficiency, and for this reason many calculations are still performed with exchange-correlation functionals corresponding to the lower rungs of this ladder, of which we will discuss the first three in particular.

3.1.6.1 Local Density Approximation

The first rung of Jacob's ladder corresponds to the local density approximation (LDA), which is a local functional in the sense that only the local charge density determines the exchange-correlation energy, which can be expressed in general terms as

$$E_{XC}^{\mathrm{LDA}}[\rho] = \int f(\rho)\,. \tag{3.31}$$

More specifically, it treats the generally inhomogeneous electronic density as if it were locally homogeneous. The corresponding exchange-correlation hole $\tilde{\rho}_{XC}^{\mathrm{LDA}}(\vec{r},\vec{r}\,')$, which can be computed exactly using Quantum Monte Carlo methods, can be used to define an exchange-

Figure 3-1: Picture of Jacob's ladder, as ornamentation on Bath Abbey.

correlation hole energy density $\epsilon_{XC}^{\mathrm{LDA}}[\rho]$

$$\epsilon_{XC}^{\mathrm{LDA}}[\rho] = \frac{1}{2}\int \frac{\tilde{\rho}_{XC}^{\mathrm{LDA}}(\vec{r},\vec{r}\,')}{|\vec{r}-\vec{r}\,'|}d\vec{r}\,', \tag{3.32}$$

using which the exchange-correlation energy in the LDA approximation can be expressed as

$$E_{XC}^{\mathrm{LDA}}[\rho] = \int \rho(\vec{r})\,\epsilon_{XC}^{\mathrm{LDA}}[\rho]\,d\vec{r}. \tag{3.33}$$

In the LDA approximation, the energy density is thus a local functional of the electron density. This makes it easy to compute, and in many cases it gives reasonable geometries, though it typically tends to overbind both molecules and solids. Being the cheapest to use, it was the most used approximation for a long time.

3.1.6.2 Generalised Gradient Approximation

Several approaches have been taken to improve the performance of the exchange-correlation functional description. Some of the most successful, yet computationally efficient, ap-

proaches have looked at semilocal functionals that expand $E_{XC}[\rho]$ as a function of the electron density and its gradients. These approaches constitute the second rung on Jacob's ladder, and are commonly referred to as generalised gradient approximation (GGA). As said, they take into account the first derivative of the electron density, such that the corresponding exchange-correlation energy can be expressed as

$$E_{XC}^{\mathrm{GGA}}[\rho] = \int f(\rho, \nabla\rho). \tag{3.34}$$

Several such GGA functionals have been developed over the years. Of these, the PBE exchange-correlation functional [214], developed by Perdew, Burke an Ernzerhof, and its analogous PBEsol functional [215], optimised specifically for solids, have been used abundantly in many solid state calculations. The exchange-correlation energy in the PBE approximation can be expressed as

$$E_{XC}^{\mathrm{PBE}}[\rho] = \int \rho(\vec{r})\,\epsilon_{XC}[\rho(\vec{r})]\,d\vec{r} + \int F_{XC}[\rho(\vec{r}), \nabla\rho(\vec{r})]\,d\vec{r}, \tag{3.35}$$

in which the function F_{XC} can be tuned, given several conditions. The GGA functional offer a significant improvement over the use of LDA, though it typically tends to slightly underbind many both molecules and solids.

3.1.6.3 Meta-GGA

Approaches that also take into account the second derivative of the density are denoted as meta-GGA, and constitute the third rung on Jacob's ladder. In general, the exchange correlation energy can thus be expressed as

$$E_{XC}^{\mathrm{mGGA}}[\rho] = \int f(\rho, \nabla\rho, \tau), \tag{3.36}$$

in which τ describes the positive orbital kinetic energy densities $\tau = \sum_s \sum_i \frac{1}{2} |\nabla\phi_{i,s}|^2$, with $\phi_{s,i}$ describing the Kohn-Sham orbitals. One such implementation is the Strongly Constrained and Appropriately Normed (SCAN) semilocal density functional [216]. It was designed to obey all 17 of the constraints known for a meta-GGA functional, which are described in more detail in the supplementary information of Reference 216, in addition to the functional form which is too extensive to copy here. In contrast, PBE only satisfies 11 of these constraints.
SCAN shows excellent performance at a very reasonable cost, yielding more accurate geome-

tries compared to both LDA and GGA [217]. More recently, the family of SCAN functionals has been extended, and now includes revised SCAN (rSCAN) [218], which does not obey all 17 contstraints, but is numerically more stable. Its successor, r2SCAN, also shows an improved numerical stability, while obeying all 17 exact constraints.
The exchange-correlation functional can be further improved by the inclusion of dispersion corrections, also often described as van der Waals-interactions, which take into account long-range attractive interactions resulting from instantaneous charge fluctuations in the electron density. Several recent developments have aimed to add dispersion corrections to the r2SCAN functional, such as the r2SCAN-c3 [219] and r2SCAN-D4 [220] functionals.

3.1.7 Plane Wave Basis Set

Finally, in order to solve the Kohn-Sham equations, the one-electron wavefunctions need to be described in terms of a basis set. Typically, either one of two approaches is used, one constructing a basis set of plane waves and one using Gaussian functions to form a basis set. Some advantages of using a plane wave basis set are that the basis set is orthogonal by definition, that the accuracy is systematically improvable and that the basis set size does not scale with the number of electrons. However, the basis set size does scale with the simulation volume and basis sets are usually quite large. In contrast, Gaussian basis sets are not typically orthogonal and it is not always possible to systematically improve the accuracy. Though it does scale with the number of electrons, it does not scale with the system volume and also the system can be modelled with varying accuracy, so interesting regions can be probed with a higher accuracy, which is not possible when adopting plane-wave basis sets. Many DFT software suites, including VASP, adopt a plane wave approach. The one-electron wavefunctions can then be described by plane waves of the form

$$\psi_{\vec{k}}\left(\vec{r}\right) = e^{i\vec{k}\cdot\vec{r}} u_{\vec{k}}\left(\vec{r}\right), \tag{3.37}$$

in which the Bloch functions $u_{\vec{k}}\left(\vec{r}\right)$ can be written as a linear combination of a finite number of plane waves

$$u_{\vec{k}}\left(\vec{r}\right) = \sum_{m} c_{\vec{k},m} e^{i\vec{G}_m\cdot\vec{r}}, \tag{3.38}$$

in which $c_{\vec{k},m}$ are the expansion coefficients corresponding to the reciprocal lattice vector $\vec{G}_m$. Thus, the one-electron wavefunctions can be written as

$$\psi_{\vec{k}}\left(\vec{r}\right) = e^{i\vec{k}\cdot\vec{r}} \left(\sum_{m} c_{\vec{k},m} e^{i\vec{G}_m\cdot\vec{r}} \right) = \sum_{m} c_{\vec{k},m} e^{i\left(\vec{k}+\vec{G}_m\right)\cdot\vec{r}}. \tag{3.39}$$

In principle, both the number of k-points as well as the number of reciprocal lattice vectors are infinite. In practice, the k-point mesh is typically interpolated using the Monkhorst-Pack scheme [221]. Additionally, the number of reciprocal lattice vectors is typically truncated by setting a cutoff value for which

$$\left|\vec{k}+\vec{G}\right| < \vec{G}_{\mathrm{cut}}, \tag{3.40}$$

in which

$$E_{\mathrm{cut}} = \frac{\hbar^2}{2m}\vec{G}_{\mathrm{cut}}^2. \tag{3.41}$$

The choice of both k-point mesh and the cutoff energy are to some degree arbitrary, and the user should always verify that convergence of the geometry structure with respect to both of these parameters is reached.

3.1.8 Pseudopotentials

Finally, to be computationally efficient, DFT is typically used in conjunction with so-called pseudopotentials or projector augmented wave potentials. These are used to smoothen out the rapidly fluctuating potentials around the nuclei which improves numerical convergence.

3.2 Kinetic Model

In the following section, we will introduce the background theory on the kinetic model, which we use to relate microscopic models of atomic movements to macroscopic phenomenological coefficients. It closely follows the derivation of the formalism of kinetic theories from the seminal work of Allnatt and Lidiard [222].

3.2.1 Derivation of the Master Equation

Kinetic theories are based on the assumption that the motion of atoms can be divided into (i) thermal vibrations around defined lattice sites and (ii) jumps or hops between these well-defined sites, and that the average time of stay at these lattice sites is much longer than the time of flight during a hop. This is equivalent to stating that for such hops to occur, sufficiently large energy barriers have to be overcome such that these hops must be thermally activated and are therefore relatively infrequent compared to the thermal vibrations around the lattice sites. Because the residence time of atoms at the lattice sites is much longer

than the time-of-flight between these sites, the thermal vibrations at the lattice sites may be averaged out, and hops may be assumed to occur effectively instantaneously.
We now consider the states $i, j, k, ...$ of the system to correspond to a vacancy occupying a certain lattice site $i, j, k, ...$ We denote the rate that corresponds to a transition from state i to state j as Q_{ji} (in this notation, the final state is indexed before the initial state). The system is assumed to be Markovian, i.e. the thermal vibrations around the lattice site erase the memory of the transition, such that the rates depend only on the initial and final states of the transition. By considering an ensemble of identical systems, we can derive average properties of the entire ensemble, such that the average probability for the system to occupy a state i, which can evolve with time t, can be denoted as $p_i(t)$.
The time evolution of the occupation probability can then be described as

$$\frac{\mathrm{d}p_i}{\mathrm{d}t} = -\sum_{j\neq i} Q_{ji}p_i + \sum_{j\neq i} Q_{ij}p_j, \tag{3.42}$$

in which the first term on the right side of the equation corresponds to transitions from state i to other states, while the second term corresponds to transitions from other states to state i. In matrix form, this can be written as

$$\frac{d\vec{p}}{dt} \;=\; \mathbf{Q}\vec{p}, \tag{3.43}$$

in which $\vec{p}$ is the *probability vector*, each element p_j of which is the probability of a vacancy occupying site j, and $\mathbf{Q}$ is the *transition rate matrix*, each element Q_{ij} $(i \neq j)$ of which is the rate (probability per unit time) for a vacancy at site j to hop to site i, with the diagonal elements set to $Q_{ii} = \sum_{j\neq i} Q_{ji}$. Equation (3.43) is more commonly known as the master equation. From the definition of the transition rate matrix $\mathbf{Q}$ it can be easily seen that

$$\sum_j Q_{ji} = 0 \;\forall\; i, \tag{3.44}$$

i.e. that all columns of $\mathbf{Q}$ sum to zero so as to preserve normalisation of $\vec{p}$.

3.2.2 Equilibrium Conditions

To illustrate some of the properties of $\mathbf{Q}$ and $\vec{p}$ we consider them in the special case of thermal equilibrium, in which case the transition rate matrix and the probability vector are

denoted as $\mathbf{Q}^{(0)}$ and $\vec{p}^{(0)}$. In equilibrium, the occupation probabilities are given by

$$p_i^{(0)} = \frac{\exp\left(-E_i^{(0)}/k_{\mathrm{B}}T\right)}{\sum_j \exp\left(-E_j^{(0)}/k_{\mathrm{B}}T\right)}, \tag{3.45}$$

with $E_i^{(0)}$ the energy of the system when it is in state i, k_{B} the Boltzmann constant and T the temperature. At equilibrium, also detailed balance must be obeyed, which can be expressed as

$$Q_{ji}^{(0)}\vec{p}_i^{(0)} = Q_{ij}^{(0)}\vec{p}_j^{(0)} \;\forall\; i \neq j, \tag{3.46}$$

and which implies microscopic reversibility, i.e. that at equilibrium forward and backward transitions (the product of the transition rate and the occupation probability) are exactly equal. From Equations (3.45) and (3.46) we find that at equilibrium the ratio of the rates can be expressed as

$$\frac{Q_{ji}^{(0)}}{Q_{ij}^{(0)}} = \exp\left(E_i^{(0)} - E_j^{(0)}\right)/k_{\mathrm{B}}T, \tag{3.47}$$

thus obeying Boltzmann statistics.

3.2.3 Vineyard's Rate Equation

In the formalism derived in the previous paragraphs, the transition rate matrix plays a crucial part in describing the dynamics of the system, and it will again be critical in the calculation of phenomenological parameters at the macroscopic scale. Already back in 1957, Vineyard derived an elegant expression of the transition rates based on the change in free energy by going from the initial to the transition state [223]. An overview of the steps in this derivation that are relevant to our model wil be summarised below.

Ionic hops can be described as thermally activated processes, with transitions from an initial to a final state going through a first-order energetic saddle point, which is defined as the transition state. Such hopping events can be characterised by an activation energy, which is defined as the difference in (free) energy between the transition and initial state, and an attempt frequency ν, which describes the frequency of vibrations in the initial state in the direction of the transition state. Within the standard formalism of the transition state theory [224–226], jump rates Q_{ji} (we reiterate that the final state is indexed first) are assumed to depend exponentially on the activation energy:

$$Q_{ji} = A_{ji}e^{\frac{-\Delta G_{ji}}{k_{\mathrm{B}}T}}, \tag{3.48}$$

with ΔG_{ji} the activation (free) energy, which describes the change in (here: Gibbs) free energy for a transition from state i to the transition state corresponding to the transition from state i to state j, A_{ji} is a prefactor with a unit of frequency, k_{B} is the Boltzmann constant and T is the temperature. These transitions are thus implicitly assumed to be purely classical and any quantum effects are neglected. Though the rates effectively describe the hop of a single atom, the problem is one of many bodies, though this is readily incorporated in discussing the states of the system, which include the relaxation of the lattice in the initial, final and transition states. The underlying asssumptions are that these initial, transition and final states are well-defined.

We now wish to define these initial, transition and final states more rigorously. To do so, we consider a crystal with a vacancy at one of its lattice sites and let the crystal contain $N/3$ atoms, such that there are N degrees of freedom, $x_1\ x_2\ \cdots\ x_{\mathrm{N}}$. Combined with the mass m associated with each of these degrees of freedom, a set of coordinates $y_1\ y_2\ \cdots\ y_{\mathrm{N}}$ can be formulated, with $y_{\mathrm{i}} = \sqrt{m}x_{\mathrm{i}}$. The potential energy Φ of the system can then be described as a function of $\vec{y}$. For visual purposes, a schematic representation of the potential energy surface (PES), which is a 2-dimensional cross-section of the N-dimensional hypersurface $\Phi\left(\vec{y}\right)$, is shown in Figure 3-2.

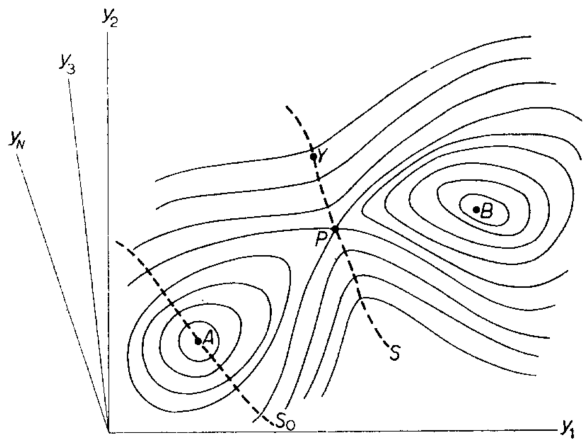

Figure 3-2: Schematic 2D representation of the potential energy surface (PES) as a cross-section of the N-dimensional potential energy hypersurface. Reprinted from [223], Copyright 1957, with permission from Elsevier.

In Figure 3-2, two local minima of the potential energy Φ are shown and denoted as states A and B, both of which correspond to a vacancy occupying two adjoining lattice sites, with all the other atoms relaxed. A 2D schematic representation of contours of constant Φ are shown around states A and B, though again we state that more generally these correspond to N-1 dimensional hypersurfaces. The first order saddle point, having a negative curvature

along the direction of the transition and positive curvatures in all other N-1 directions, between states A and B is shown as P in Figure 3-2, and corresponds to the transition state associated with a transition between states A and B.
A unique hypersurface, denoted as S in Figure 3-2, can now be defined as the hypersurface that passes through P and is otherwise perpendicular to the contours of Φ, thus creating a well-defined surface that separates regions around states A and B. Any point in the region around A and reaching S with a finite velocity is assumed to enter B. It is thus implicitly assumed that no re-crossing events occur, which might lead to an overestimation of the overall transition rate from A to B.
The overall transition rate Q_{BA} (previously described as Q_{ji}) can then be expressed as a ratio of the number of points I_{BA} on S crossing from the region around A to the region around B per unit time, relative to the number of points in the region around state A, defined as Ω_A. This ratio, which can also be interpreted as an inverse lifetime τ_{BA}, can thus be described as

$$Q_{BA} = \frac{1}{\tau_{BA}} = \frac{I_{BA}}{\Omega_A}. \tag{3.49}$$

Ω_A can be described as an integral of a characteristic density in configuration space $\rho(\vec{y}) = \rho_0 e^{-\Phi(\vec{y})/k_B T}$ over the confined region around A:

$$\Omega_A = \rho_0 \int_A e^{-\Phi(\vec{y})/k_B T} dV, \tag{3.50}$$

with ρ_0 a normalisation constant.
I can be calculated as an integration of an effective density of the points Y on S with hypervelocity $\mathscr{V} = \{\dot{y}_1 \cdots \dot{y}_N\}$ (not to be confused with the volume V), in the range $d\mathscr{V} = d\dot{y}_1 \cdots d\dot{y}_N$ as follows:

$$\rho(Y, \mathscr{V})\, d\mathscr{V} = \rho_1 e^{-\Phi(Y)/k_B T} e^{-\mathscr{V}^2/2k_B T} d\dot{y}_1 \cdots d\dot{y}_N, \tag{3.51}$$

with

$$\rho_1 = \rho_0 (2\pi k_B T)^{-N/2}. \tag{3.52}$$

The flux dI across S at a specific point Y on S can then be calculated by direct integration over the multiplication of $dS = dS_1 \cdots dS_N$ with the hypervelocity $\mathscr{V}$

$$dI = dS \cdot \int \mathscr{V} \rho(Y, \mathscr{V})\, d\mathscr{V}, \tag{3.53}$$

with the integration over all $\mathscr{V}$ such that

$$dS \cdot \mathscr{V} > 0. \tag{3.54}$$

This condition can be met by rotating the axes, such that one of them, y_1 for simplicity, is parallel to dS at the point Y. Then the flux can be expressed as

$$\begin{aligned} dI &= \rho_0 \left(2\pi k_B T\right)^{-N/2} e^{-\Phi(Y)/k_B T} dS_1 \times \int_0^\infty \dot{y}_1 e^{-\dot{y}_1^2/2k_B T} d\dot{y}_1 \\ &\prod_{j-2}^{N} \int_{-\infty}^{\infty} e^{-\dot{y}_j^2/2k_B T} d\dot{y}_j \\ &= \rho_0 \sqrt{kT/2\pi} e^{-\Phi(Y)/k_B T} dS_1. \end{aligned} \tag{3.55}$$

The total flux I can then be computed as

$$I = \int dI = \rho_0 \sqrt{kT/2\pi} \int_S e^{-\Phi(Y)/k_B T} dS_1, \tag{3.56}$$

with the integration over the full hypersurface S.
By including the expressions for Q_A and I from Equations (3.50) and (3.56), Equation (3.49) can be rewritten as

$$Q_{BA} = \sqrt{\frac{k_B T}{2\pi}} \frac{\int_S e^{\Phi/k_B T} dS_1}{\int_A e^{\Phi/k_B T} dV}. \tag{3.57}$$

This equation describes the transition rate as a ratio between two partition functions, which account for all degrees of freedom.
To cast Equation (3.57) in a more computationally tractable expression, the harmonic approximation is invoked - this is the reason the current method is often referred to as harmonic transition state theory. In the harmonic approximation, Φ can be expanded to second order by a Taylor series. Near point A this leads to an expression of Φ of

$$\Phi \cong \Phi\left(A\right) + \sum_{j=1}^{N} \frac{1}{2} \left(2\pi\nu_j\right)^2 q_j^2, \tag{3.58}$$

with $q_1 \cdots q_N$ the normal coordinates and $\nu_1 \cdots \nu_N$ the normal frequencies of vibrations around point A. A similar expression can be derived for Φ near P at the dividing surface S

$$\Phi \cong \Phi\left(P\right) + \sum_{j=1}^{N-1} \frac{1}{2} \left(2\pi\nu_j'\right)^2 q_j'^2, \tag{3.59}$$

with $q'_1 \cdots q'_N$ the normal coordinates and $\nu'_1 \cdots \nu'_N$ the normal frequencies of vibrations around point P, where the (imaginary) vibrational mode along dS is removed from the summation.
The partition functions in Equation (3.57) can then be expressed as

$$\prod_{j=1}^{N-1} \left(\frac{\sqrt{2\pi k_B T}}{2\pi \nu'_j} \right) e^{-\Phi(P)/k_B T} \tag{3.60}$$

and

$$\prod_{j=1}^{N} \left(\frac{\sqrt{2\pi k_B T}}{2\pi \nu_j} \right) e^{-\Phi(A)/k_B T} \tag{3.61}$$

for the numerator and denominator, respectively.
Finally, the transition rate can be expressed as

$$Q_{BA} = \left(\frac{\prod_{j=1}^{N} \nu_j}{\prod_{j=1}^{N-1} \nu'_j} \right) e^{-(\Phi(P)-\Phi(A))/k_B T} \tag{3.62}$$

In general, the transition rate can thus be expressed as the product of an attempt frequency

$$\nu_{BA} = \left(\frac{\prod_{j=1}^{N} \nu_j}{\prod_{j=1}^{N-1} \nu'_j} \right) \tag{3.63}$$

and an activation exponential, with an activation enthalpy of

$$\Delta H_{BA} = -\left(\Phi\left(P\right) - \Phi\left(A\right)\right)/k_B T. \tag{3.64}$$

The attempt frequency is thus expressed as the ratio of the product of N normal frequencies when the system is in its initial configuration A and the $N-1$ normal frequencies when the system is constrained to the transition state P.
Equation (3.62) can also be decomposed in a slightly different way to clarify the origin of the attempt frequency and activation energy

$$Q_{BA} = \tilde{\nu}_{BA} e^{\Delta S_{BA}/k_B} e^{-\Delta H_{BA}/k_B T}, \tag{3.65}$$

in which $\tilde{\nu}_{BA}$ is an effective attempt frequency excluding the contribution of the entropy change ΔS_{BA}, and ΔH_{BA} is stated more explicitly as the change in the enthalpy of the system in going from the initial state to the transition state. It can be shown that the expression $\tilde{\nu}_{BA} e^{\Delta S_{BA}/k_B}$ can be rewritten to reproduce our previous expression of the attempt

frequency

$$\nu_{BA} = \left(\frac{\prod_{j=1}^{N} \nu_j}{\prod_{j=1}^{N-1} \nu'_j} \right), \tag{3.66}$$

which thus includes an expression of the migration entropy of the system, defined as the change in entropy through the transition from state A to the transition state P.

3.3 (Climbing Image) Nudged Elastic Band Method

Over the last few decades, developments to the implementation of the Nudged Elastic Band (NEB) method have made it one of the standard tools to obtain activation enthalpies from atomistic calculations [227–229]. Below we will provide the background theory for the NEB method, after which we will discuss the development of the climbing image nudged elastic band method (CI-NEB).

The Nudged Elastic Band (NEB) method is designed to find to the minimum energy path (MEP) on a potential energy surface [227]. Similar to other elastic band methods, the MEP is found by generating a series of images between the initial and final state of a transition. These images are then connected by artificial springs that act like elastic bands, and ensure that the path is continuous and that the images do not slide down and collapse onto the (stable) initial and final states. This band of images can then be optimised to align with the MEP, which thus enables one to find the transition state and activation energy of an associated transition.

During the optimisation, both the true force and the spring force are decomposed into components parallel and perpendicular to the path. What distinguishes the NEB method from other elastic band methods is that only the perpendicular component of the true force on the image and only the parallel component of the spring force are used to optimise the path. This force projection is referred to as 'nudging', giving the NEB method its name.

We now wish to introduce the NEB method, a schematic representation of which is shown in Figure 3-3, more rigorously. To do so, we consider an elastic band with $N+1$ images $\vec{R}_0, \vec{R}_1, \cdots \vec{R}_N$ which are fully described by the positions of all atoms [227]. The end points $\vec{R}_0$ and $\vec{R}_N$ describe the initial and final state of a transition and remain fixed throughout the optimisation.

As discussed above, the total force acting on image i $\left(\vec{F}_i^{\mathrm{NEB}}\right)$ is composed of the true force $F_i^{\perp}$ perpendicular to the local tangent and the spring force parallel $\left(\vec{F}^{\,S\parallel}\right)$ to the local tangent

$$\vec{F}_i^{\mathrm{NEB}} \;=\; F_i^{\perp} + \vec{F}^{\,S\parallel}, \tag{3.67}$$

in which the perpendicular true force is expressed as

$$F_i^{\perp} = \nabla E\left(\vec{R}_i\right) - \left(\nabla E\left(\vec{R}_i\right) \cdot \widehat{\tau}_i\right) \widehat{\tau}_i, \tag{3.68}$$

in which E is the energy of the system and $\vec{\tau}_i$ is the normalised local tangent at image i. The spring force $\vec{F}^{S\,\|}$ can be expressed as

$$\vec{F}^{S\|} \;=\; k\left(\left|\vec{R}_{i+1} - \vec{R}_i\right| - \left|\vec{R}_i - \vec{R}_{i-1}\right|\right) \widehat{\tau}_i. \tag{3.69}$$

Upon convergence, one can then interpolate the images to guess the transition state. A

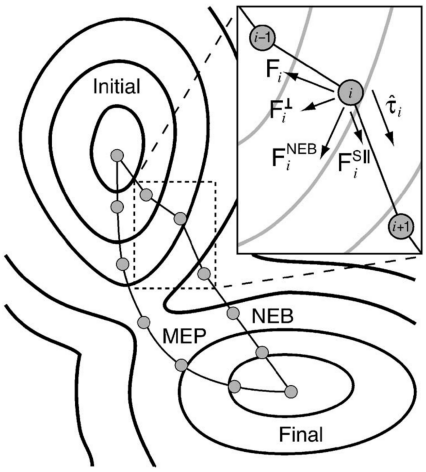

Figure 3-3: Schematic representation of a NEB calculation, showing the optimisation of the nudged elastic band (NEB) towards the minimal energy pathway (MEP). The nudged elastic band force acting on image i, F_i^{NEB}, is composed of two terms; the spring force $F_i^{S\|}$ along the tangent vector τ_i towards the next image, and the projection perpendicular to this tangent of the force due to the overall potential $F_i^{\perp}$. Reprinted from Reference 228, with the permission of AIP Publishing.

more robust approach is to use the Climbing Image Nudged Elastic Band (CI-NEB) method. In this method, the force $\vec{F}_l^{\,\mathrm{CI}}$ on the image l with the highest energy is expressed as

$$\vec{F}_l^{\,\mathrm{CI}} = \vec{F}_l - 2\left(\vec{F}_l \cdot \vec{\tau}_l\right) \vec{\tau}_l, \tag{3.70}$$

such that it has no contribution of the spring forces. Instead, the projection of the force along the tangent is reversed, such that instead of going down the hill, the image moves up the hill towards the transition state.

3.4 Dimer Method

Another method that can be used to find the transition state is the dimer method [230–233], which is a local transition state search algorithm that makes use only of first derivatives and is thus computationally feasible even for large systems. The transition state predicted by NEB or CI-NEB calculations can be used as an initial guess for the dimer calculation. The following derivation closely follows that of Reference 230.
The dimer is composed of a pair of images, which are described by their respective coordinates $\vec{R}_1$ and $\vec{R}_2$, and which are very similar but slightly displaced with respect to one another. A schematic description of the dimer is shown in Figure 3-4a.

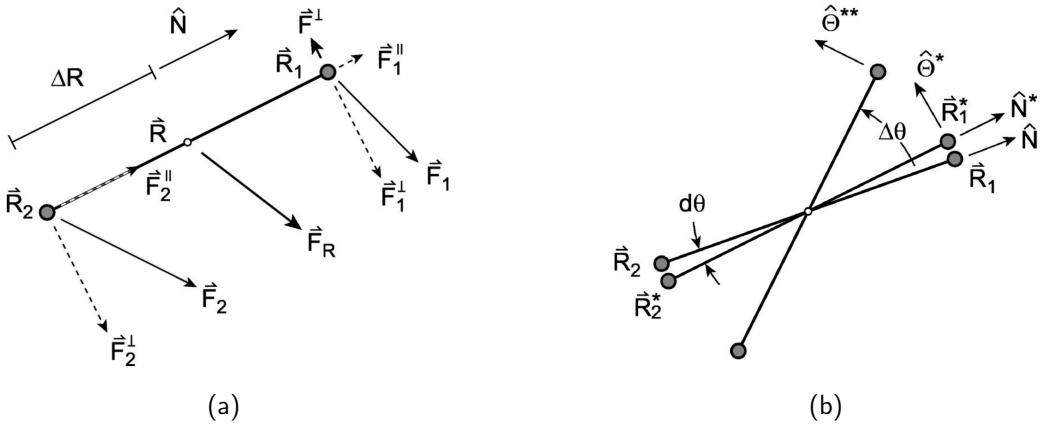

Figure 3-4: Schematic representation of a dimer calculation. Reprinted from Reference 230, with the permission of AIP Publishing.

The pair of images are shown with respect to a common midpoint $\vec{R}$. Their position vectors can be generated from this common midpoint by adding and subtracting a displacement of length ΔR in a direction $\widehat{N}$ resulting in the following expression for $\vec{R}_1$

$$\vec{R}_1 = \vec{R} + \Delta R\widehat{N} \tag{3.71}$$

and $\vec{R}_2$

$$\vec{R}_2 = \vec{R} - \Delta R\widehat{N}. \tag{3.72}$$

The saddle point search algorithm consists of two steps; first, the dimer is rotated to align with the lowest curvature mode at $\vec{R}$, after which it is translated by a certain step-length along $\widehat{N}$ (which has been updated during the rotation) towards the saddle point.

3.4.1 Evaluating the Rotation Angle

Instead of computing the curvature from the Hessian, which is a relatively expensive calculation and includes computation of the second derivatives, the curvature C_N along $\widehat{N}$ is approximated by

$$C_N \approx \frac{\left(\vec{F}_2 - \vec{F}_1\right)^{\intercal} \cdot \widehat{N}}{2\Delta R} \approx \frac{E_1 + E_2 - 2E_0}{(\Delta R)^2}, \tag{3.73}$$

in which E_1 and E_2 and $\vec{F}_1$ and $\vec{F}_2$ denote the energies and the forces acting on images 1 and 2, respectively. It is evident from Equation (3.73) that a minimisation of the curvature is equivalent to a minimisation of the sum $E = E_1 + E_2$. To minimise the curvature, a rotation can be performed in a rotational plane spanned by $\widehat{N}$ and a vector $\widehat{\Theta}$ orthogonal to $\widehat{N}$. In the modified Newton method the normalised vector $\widehat{\Theta}$ is along the rotational force $\vec{F}^{\intercal} = \vec{F}_1^{\intercal} - \vec{F}_2^{\intercal}$, where

$$\vec{F}_{1,2}^{\intercal} \equiv \vec{F}_{1,2} - \left(\vec{F}_{1,2} \cdot \widehat{N}\right) \widehat{N}. \tag{3.74}$$

Image 1 can now be rotated by an angle $d\theta$, in the plane spanned by $\widehat{N}$ and $\widehat{\Theta}$, to a new configuration described by $\vec{R}_1^*$

$$\vec{R}_1^* = \vec{R} + \left(\widehat{N}\cos(d\theta) + \widehat{\Theta}\sin(d\theta)\right)\Delta R. \tag{3.75}$$

A new dimer direction $\widehat{N}^*$ based on the new position $\vec{R}_1^*$ can be computed, with which the new configuration $\vec{R}_2^*$ for image 2 can be derived. Subsequently, the forces $\vec{F}_1^*$ and $\vec{F}_2^*$ are calculated. The scalar rotational force F can be expressed as

$$F = \vec{F}^{\intercal} \cdot \widehat{\Theta}/\Delta R, \tag{3.76}$$

in which the division by ΔR scales F such that it is independent of the dimer separation. The change in the rotational force F as a function of $d\theta$ is then given by

$$F' = \frac{F}{d\theta} \approx \left|\frac{\vec{F}^* \cdot \widehat{\Theta}^* - \vec{F} \cdot \Theta}{d\theta}\right|_{\theta = d\theta/2}, \tag{3.77}$$

in which $\vec{F}^* = \vec{F}_1^* - \vec{F}_2^*$ and in which the approximation is most accurate at the midpoint $\theta/2$. The optimal rotation angle $\Delta\theta$ (not to be confused with the 'probe' $d\theta$, for more clarification, see Figure 3-4) can then be approximated using

$$\Delta\theta \approx \frac{\vec{F} \cdot \widehat{\Theta} + \vec{F}^* \cdot \widehat{\Theta}^*}{-2F'} \tag{3.78}$$

It was however discovered that the proposed method generally overestimates the rotation angle $\Delta\theta$. An improvement to the general method was proposed, based on an expression of the potential hyperplane $U(\vec{R})$ in terms of a Taylor expansion near $\vec{R}_0$. This plane is described in terms of two normal modes $\widehat{x}$ and $\widehat{y}$ which are defined for the two-dimensional plane spanned by $\widehat{N}$ and $\widehat{\Theta}$. Including terms up to second order, this potential energy can be expressed as

$$U = E_0 - (F_x x + F_y y) + \frac{1}{2}\left(c_x x^2 + c_y y^2\right), \tag{3.79}$$

in which the forces F_x and F_y are $-\partial U/\partial x$ and $-\partial U/\partial y$, respectively, with x and y distances along $\widehat{x}$ and $\widehat{y}$. The terms c_x and c_y indicate the curvatures of the potential along $\widehat{x}$ and $\widehat{y}$. The dimer energy within this quadratic approximation can then be expressed as a function of θ as

$$E = 2E_0 + (\Delta R)^2\left[c_x \cos^2(\theta - \theta_0) + c_y \sin^2(\theta - \theta_0)\right], \tag{3.80}$$

in which θ_0 is a reference angle and which can be rewritten using a trigonometric identity as

$$E = 2E_0 + \frac{1}{2}(\Delta R)^2\left[(c_x - c_y)\cos(2(\theta - \theta_0)) + (c_x + c_y)\right]. \tag{3.81}$$

The derivative F of this potential can then be expressed as

$$F = \frac{dE}{d\theta} = A\sin(2(\theta - \theta_0)), \tag{3.82}$$

in which $A = -(\Delta R)^2(c_x - c_y)$. From Equation (3.82) it can be deduced that θ_0 corresponds to the rotation angle at which the rotation force F is zero. It is therefore useful to find the expression in which the rotational force is minimised with respect to θ, by evaluating the first derivative of F with respect to θ

$$F' = \frac{dF}{d\theta} = 2A\cos(2(\theta - \theta_0)). \tag{3.83}$$

Since both F and F' are evaluated for some orientation of the dimer, we can set this orientation to correspond to $\theta = 0$ and denote the corresponding force F and its first derivative F' as F_0 and F_0', respectively. Their ratio can then be expressed as

$$\frac{F_0}{F_0'} = \frac{1}{2}\tan(-2\theta_0), \tag{3.84}$$

from which a simple expression for the rotation angle $\Delta\theta$ can be deduced

$$\Delta\theta = \theta_0 = -\frac{1}{2}\arctan\left(\frac{2F_0}{F_0'}\right), \tag{3.85}$$

which was shown to have improved behaviour with respect to Equation (3.85) in the limits of $F \to 0$ and $F' \to 0$.

3.4.2 Evaluating the Translation

After the dimer has been rotated towards its direction of minimum curvature, the evaluation of the subsequent translation is relatively straightforward. Without any modification, the net force acting on the center of the dimer $\vec{F}_R$ draws it to a local minimum. In analogy to the calculation of the force for the CI-NEB method, cfr. Equation (3.70), the force in the direction of $\widehat{N}$, which we denote as $\vec{F}^{\parallel}$, is reversed to make sure it moves uphill towards a saddle point, such that the modified force $\vec{F}^{\dagger}$ can be expressed as:

$$\vec{F}^{\dagger} = \vec{F}_R - 2\vec{F}^{\parallel}. \tag{3.86}$$

This is schematically shown in Figure 3-5. However, this equation only holds when the local curvature is indeed negative, as desired. If this is not the case, the modified force is directed against the the parallel component of F. The expression for the modified force $\vec{F}^{\dagger}$ can thus be summarised by

$$\vec{F}^{\dagger} = \begin{cases} -F^{\parallel} & \text{if } C > 0 \\ \vec{F}_R - 2\vec{F}^{\parallel} & \text{if } C < 0 \end{cases}. \tag{3.87}$$

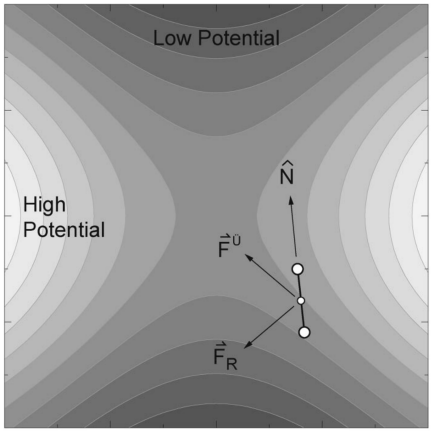

Figure 3-5: Schematic representation of the translation step in a dimer calculation. Reprinted from Reference 230, with the permission of AIP Publishing.

3.5 Computation of the Vibrational Frequencies

In order to obtain the attempt frequencies as discussed in Equation (3.63), we need to compute the vibrational frequencies of the system. In crystals, such lattice vibrations act as quasi-particles, with a well-defined frequency and direction. They are more commonly referred to as phonons, which are used to describe various material properties, such as heat or sound transmission through a solid. Thanks to the rapid progress of *ab initio* codes over the last few decades, phonon properties can now be routinely obtained from standard DFT calculations [234]. We will introduce the relevant background below, closely following the derivation in References [234, 235].

In crystals, atoms are assumed to move around equilbrium position $\vec{r}(lk)$ with displacements $\vec{u}(lk)$, with the labels l and k describing the unit cell index and index for each atom in the cell, respectively. The potential energy Φ can then be expressed as a series expansion around the equilbrium position in terms of these displacements;

$$\begin{aligned}\Phi = \Phi_0 &+ \sum_{lk}\sum_{\alpha}\Phi_\alpha(lk)\vec{u}_\alpha(lk) \\ &+ \frac{1}{2}\sum_{ll'kk'}\sum_{\alpha\beta}\Phi_{\alpha\beta}(lk,l'k')\vec{u}_\alpha(lk)\vec{u}_\beta(l'k') \\ &+ \frac{1}{3!}\sum_{ll'l''kk'k''}\sum_{\alpha\beta\gamma}\Phi_{\alpha\beta\gamma}(lk,l'k'',l'k'')\vec{u}_\alpha(lk)\vec{u}_\beta(l'k')\vec{u}_\beta(l''k'') + \cdots,\end{aligned} \tag{3.88}$$

in which α, β, $\cdots$ describe the Cartesian coordinates, such that the expansion coefficients Φ_0, $\Phi_\alpha(lk)$, $\Phi_{\alpha\beta}(lk,l'k')$ and $\Phi_{\alpha\beta\gamma}(lk,l'k'',l'k'')$ can be interpreted as the zeroth, first,

second and third order force constants, respectively. In the harmonic approximation, the first order term is assumed to be negligible, and the expansion can be truncated after the second-order force constant, such that the potential energy can be written as

$$\Phi = \Phi_0 + \frac{1}{2}\sum_{ll'kk'}\sum_{\alpha\beta}\Phi_{\alpha\beta}(lk,l'k')\vec{u}_\alpha(lk)\vec{u}_\beta(l'k'). \tag{3.89}$$

By defining the force as $F_\alpha(lk) = -\frac{\partial\Phi}{\partial\vec{u}_\alpha(lk)}$, the second order force constants can now be readily computed as

$$\Phi_{\alpha\beta}(lk,l'k') = -\frac{\partial F_\beta(l'k')}{\partial\vec{u}_\alpha(lk)} = \frac{\partial^2\Phi}{\partial\vec{u}_\alpha(lk)\partial\vec{u}_\beta(l'k')}. \tag{3.90}$$

Two common approaches to calculate the second-order force constants can be distinguished; one using the finite displacement method [236, 237] and the other using density functional perturbation theory [238, 239].
Regardless of how the second-order force constants are obtained, they can then be used to define the so-called dynamical matrix $D(\vec{q}$, the entries of which can be computed as

$$D^{\alpha\beta}_{kk'}(\vec{q}) = \sum_{l'}\frac{\Phi_{\alpha\beta}(0k,l'k')}{\sqrt{m_k m_{k'}}}e^{i\vec{q}\cdot[\vec{r}(l'k')-\vec{r}(0k)]}, \tag{3.91}$$

with $\vec{q}$ the wave vector, m_k the mass of atom k. Finally, the dynamical matrix can be diagonalised as

$$D(\vec{q})\vec{e}_{\vec{q}j} = \omega^2_{\vec{q}j}\vec{e}_{\vec{q}j} \tag{3.92}$$

to obtain of the vibrational frequencies $\omega_{\vec{q}j}$ and modes $\vec{e}_{\vec{q}j}$.

3.6 Computation of the Mobility Tensor

Now that we have discussed the necessary background on computing the activation enthalpies and attempt frequencies, we finally move on to a discussion on how to calculate macroscopic transport properties from these atomistic data. In this work, we focus on the mobility tensor, $\boldsymbol{\mu}$, which is defined by

$$\vec{v}_\mathrm{d} = \boldsymbol{\mu}\vec{E}. \tag{3.93}$$

In Equation 3.93, $\vec{v}_\mathrm{d}$ is the drift velocity of the bromide vacancies under an electric field $\vec{E}$. Therefore the influence of an electric field must be incorporated into the kinetic scheme.

This is done by considering the activation enthalpy $(H_{\mathrm{a}})_{ji}$ for each hop of a vacancy from site i to site $j \neq i$ as the sum of two terms:

$$\Delta H_{ij}^{\ddagger}(\vec{E}) = \Delta H_{ji}^{\ddagger}(0) + q\left(\vec{r}_{ji}^{\ddagger} - \vec{r}_i\right) \cdot \vec{E}, \tag{3.94}$$

where the first term, $\Delta H_{ji}^{\ddagger}(0)$, is the (zero-field) activation enthalpy obtained from our DFT calculations. The second term, which takes into account the work done by, or against, the electric field in attaining the transition state, follows from the single-ion approximation such that it is equal to the difference between the position vector of the moving ion in the transition state, and the position vector of the same ion in the initial state, multiplied by its charge q. We note that this approach, which is essentially the same as that originally adopted by Mott and Gurney [240], is valid only in the low-field regime, and for stronger electric fields non-linear effects must be taken into account [241, 242].
The mobility is a steady state quantity, so we need to solve the steady state version of Equation 3.43:

$$\frac{d\vec{p}}{dt} = \vec{0} = \mathbf{Q}\vec{p}. \tag{3.95}$$

If vacancy–vacancy interactions are neglected, corresponding to the dilute limit, then $\mathbf{Q}$ does not depend on the state of the system, and is therefore constant in time. This renders the problem sufficiently simple that Equation 3.95 can be solved directly by finding the eigenvector of the transition rate matrix with eigenvalue 0, which corresponds to the stationary distribution $\vec{\pi}$. In general, the number of hops of a vacancy from site j to i per unit time (the flux) is $Q_{ij}p_j$, and the steady state drift velocity, $\vec{v}_{\mathrm{d}}$, is simply the sum of the steady state fluxes multiplied by the displacement vectors associated with each hop, $\vec{r}_i - \vec{r}_j$:

$$\vec{v}_{\mathrm{d}} = \sum_i \sum_{j \neq i} Q_{ji}\pi_i(\vec{r}_j - \vec{r}_i). \tag{3.96}$$

By computing the drift velocity vector for electric fields along three orthogonal directions, all nine components of the mobility tensor can be generated.

3.7 Elasticity theory

Linear elasticity theory of point defects, an excellent account of which is given in [243], describes the interaction between point defects and stress. A very comprehensive review is given on account of Clouet et al [244], the main points of relevance of which will be summarised below.

3.7.1 Elasticity Theory - Bulk

Elasticity theory describes the deformation of solid bodies as a result of forces exerted on them, be it internal or external. The deformation $\vec{u}$ is described by the displacement of a point in the unstrained body $\vec{R}$ to a new point in the strained body $\vec{r}$, given by

$$\vec{u}(\vec{R}) = \vec{r} - \vec{R}. \tag{3.97}$$

The central quantity that describes the change in size and shape of a solid body is the symmetric and dimensionless strain tensor, $\boldsymbol{\epsilon}_{ij}$, which is defined by

$$\boldsymbol{\epsilon}_{ij}(\vec{R}) = \frac{1}{2}\left(\frac{\partial \vec{u}_i}{\partial \vec{R}_j} + \frac{\partial \vec{u}_j}{\partial \vec{R}_i} + \frac{\partial \vec{u}_n}{\partial \vec{R}_i}\frac{\partial \vec{u}_n}{\partial \vec{R}_j}\right), \tag{3.98}$$

in which typically only the two leading terms are kept when assuming a small deformation, as is a common assumption in linear elasticity. To leading order, the energy E as a function of strain can be described as

$$E(\epsilon) = E_0 + \frac{1}{2}\boldsymbol{C}_{ijkl}\boldsymbol{\epsilon}_{ij}\boldsymbol{\epsilon}_{kl}, \tag{3.99}$$

where E_0 is the energy of unstrained body, and the elastic constants $\boldsymbol{C}_{ijkl}$ are defined by

$$\boldsymbol{C}_{ijkl} = \frac{\partial^2 E}{\partial \boldsymbol{\epsilon}_{ij}\partial \boldsymbol{\epsilon}_{kl}}. \tag{3.100}$$

This fourth-rank tensor obeys minor and major symmetries, viz. $\boldsymbol{C}_{ijkl} = \boldsymbol{C}_{jikl} = \boldsymbol{C}_{ijlk} = \boldsymbol{C}_{klij}$, such that it has at most 21 independent coefficients, which can be further reduced depending on the symmetry of the system. This expression leads to the more familiar relation between stress and strain, originally summarised by Robert Hooke as *Ut tensio, sic vis*

$$\sigma_{ij} = \boldsymbol{C}_{ijkl}\boldsymbol{\epsilon}kl. \tag{3.101}$$

3.7.2 Elasticity Theory - Point Defect

The introduction of a point defect in an otherwise periodic solid will lead to a force distribution, $\vec{f}(\vec{r}) = \sum_{q=1}^{N} \vec{F}^q \delta(\vec{r} - \vec{a}^q)$, consisting of N forces $\vec{F}^q$ acting on position $\vec{a}^q$, with the defect located at the origin. Another representation which fully characterises the point defect within elasticity theory is the second rank (and symmetric) elastic dipole tensor, defined

as

$$\boldsymbol{P}_{ij} = \sum_{q=1}^{N} \vec{F}_j^q \vec{a}_k^q. \tag{3.102}$$

The related point-defect relaxation volume can be expressed as

$$\Delta V = \boldsymbol{S}_{iikl} \boldsymbol{P}_{kl}, \tag{3.103}$$

where the elastic compliances S_{ijkl} are the inverse of the elastic constants, i.e. $S_{ijkl}C_{klmn} = \frac{1}{2}(\delta_{im}\delta_{jn} + \delta_{in}\delta_{jm})$. Arguably, the most important quantity of interest is the interaction energy between a point defect and an external strain field, which is expressed as

$$E^{\text{int}} = -\boldsymbol{P}_{ij} \boldsymbol{\epsilon}_{ij}^{\text{ext}}(\vec{0}), \tag{3.104}$$

and described as the workhorse of the modelling of point defects within linear elasticity. The name of the elastic dipole tensor is based on it being analogous in nature to the electric dipole, as it locally distorts the strain field in the crystal [245].
Consider now a simulation box of volume V, the equilibrium volume of the pristine bulk material. Upon the introduction of a point defect, the variation of the energy can be described by

$$E(\epsilon) = E_0 + E_{\text{def}} + \frac{V}{2} \boldsymbol{C}_{ijkl} \boldsymbol{\epsilon}_{ij} \boldsymbol{\epsilon}_{kl} - P_{ij} \boldsymbol{\epsilon}_{ij}, \tag{3.105}$$

with E_0 the energy of the pristine box, and E_{def} the (unstrained) defect energy, which can include both electrostatic and elastic interactions with its periodic images. The residual stress on the simulation box is expressed as

$$\begin{aligned} \langle \boldsymbol{\sigma}_{ij}(\boldsymbol{\epsilon}) \rangle &= \frac{1}{V} \frac{\partial E}{\partial \boldsymbol{\epsilon}_{ij}}, \\ &= \boldsymbol{C}_{ijkl} \boldsymbol{\epsilon}_{kl} - \frac{1}{V} \boldsymbol{P}_{ij}, \end{aligned} \tag{3.106}$$

where the average is taken over different configurations/orientations of the point defect. In the case where the lattice vectors are kept fixed ($\boldsymbol{\epsilon} = 0$) the elastic dipole tensor can be derived from the residual stress

$$\boldsymbol{P}_{ij} = -V \langle \boldsymbol{\sigma}_{ij} \rangle . \tag{3.107}$$

Care should be taken that the unstrained box has no residual stress, if it does, this needs to be corrected for such that the residual stress in the above expression is solely due to the introduction of the point defect. In the opposite situation, where a homogeneous strain $\bar{\boldsymbol{\epsilon}}$ has been applied to cancel the residual stress, the elastic dipole tensor can be derived from

the residual strain

$$\boldsymbol{P}_{ij} = V\boldsymbol{C}_{ijkl}\bar{\boldsymbol{\epsilon}}_{kl}. \tag{3.108}$$

Generally, keeping the lattice parameters fixed is the desired approach, since $\sigma = 0$ calculations require an increased number of force calculatios and an increased precision of the calculations for *ab initio* calculations. A final point worth mentioning, is that the elastic dipole tensor can itself depend on an external elastic field $\boldsymbol{\epsilon}^{\mathrm{ext}}$, such that the total elastic dipole can be expressed as

$$\boldsymbol{P}_{ij}\left(\boldsymbol{\epsilon}^{\mathrm{ext}}\right) = \boldsymbol{P}^{0}_{ij} + \boldsymbol{\alpha}_{ijkl}\boldsymbol{\epsilon}^{\mathrm{ext}}_{kl}, \tag{3.109}$$

in which $\boldsymbol{P}^{0}_{ij}$ is the elastic dipole tensor in the absence of external strain, and $\boldsymbol{\alpha}_{ijkl}$ is the so-called point defect diaelastic polarisability. This equation not only describes the behaviour of the elastic dipole tensor under an externally applied strain, but it also describes the elastic interaction between a point defect and the strain fields generated by its periodic images. The second term scales as $\frac{1}{r^3}$ and hence the unperturbed elastic dipole tensor $\boldsymbol{P}^{0}_{ij}$ can be extrapolated from a fit of $\boldsymbol{P}_{ij}$ as a function of the simulation box volume.

3.7.3 Ion Migration Activation Enthalpy

We describe the dependence of the ion migration activation enthalpy as a function of strain, based on Reference 246, and the dependence on stress, based on Reference [247]. Following Equation 3.104, the activation enthalpy H_a for migration as a function of applied strain can simply be expressed as

$$\begin{aligned} H_a &= H^0_a - (\boldsymbol{P}^{\ddagger}_{ij} - \boldsymbol{P}_{ij})\boldsymbol{\epsilon}_{ij}, \\ &= H^0_a - \Delta\boldsymbol{P}_{ij}\boldsymbol{\epsilon}_{ij}, \end{aligned} \tag{3.110}$$

in which H^0_a is the activation enthalpy for migration of a point defect in the absence of strain, and $\boldsymbol{P}$ and $\boldsymbol{P}^{\ddagger}$ are the elastic dipole tensors in the initial and transition state respectively. The dependence of the activation enthalpy H_{a} as a function of stress can be described by

$$\Delta H_{\mathrm{a}} = -\Delta\mathbf{V}_{kl}\boldsymbol{\sigma}_{kl}, \tag{3.111}$$

in which $\boldsymbol{\sigma}$ describes is the stress tensor, and $\Delta\mathbf{V}$ is the migration volume tensor, the components of which are computed as

$$\Delta\mathbf{V}_{kl} = \Delta\mathbf{P}_{ij}\mathbf{S}_{ijkl} \tag{3.112}$$

Chapter 4

Development of the General Methodology; Ionic Mobility in the Pristine Structure

4.1 Introduction

Based on our interpretation of the background literature on ionic migration, strain and stability in Chapter 2, we argue that the effects of strain on the level of ionic migration in LHPs remain poorly understood. To address this gap in the literature, we will develop a methodology in the remainder of this chapter that can be used to link the results from atomistic calculations to a macroscopically observable quantity that can be compared to experiment. Specifically, we focus on the computation of the ionic mobility tensor, since LHPs are predominantly used in applications in which they are exposed to a bias voltage, i.e. when used as active layers in solar cell [248] and LED [249] devices. We do however note that such fields can be screened by the build-up of charged defects at the interfaces in such devices [30].

In this thesis, we model the ionic mobility in $CsPbBr_3$, which we consider as a representative material for the larger class of LHPs. While it is structurally representative of the larger class of LHPs, it lacks the structural complexity of the asymmetric organic molecule at the A-site, such that effects as hydrogen bonding and dipole interactions can be neglected. Though its bandgap of 2.3 eV is substantially higher than those of its hybrid counterparts [250], it boasts a superior stability compared to other LHPs [86, 188]. An atomistic understanding of the relative stability of $CsPbBr_3$ can thus be used to improve the stability of other LHP compositions.

An additional benefit of taking $CsPbBr_3$ as a model system, is that it adopts the low-

temperature orthorhombic phase with space group $Pnma$ up to a temperature 88°C, such that this phase is retained for a large range of operating temperatures. The results we obtain from DFT simulations, effectively performed at 0 K, should thus be representative for the behaviour at operating conditions. In contrast, most other LHPs undergo at least one phase transition even before room temperature [251, 252]. Nevertheless, several studies have suggested that the higher symmetry phases adopted by LHPs at operating temperatures are in fact dynamical averages of the orthorhombic phase with space group *Pnma* [79, 85, 253]. As a result, the relevant phase to consider will depend on the frequency of ionic hops relative to the frequency of transitions between the various orthorhombic structures. Preliminary results from our work, presented later in this thesis, as well as theoretical evidence published elsewhere [85], suggest that the energy barriers for transitions between orthorhombic structures are of the order of several tens of meV per atom, while the energy barrier for vacancy hopping is of the order of several hundred meV, thus an order of magnitude larger. This suggests that vacancy hops should occur on a longer timescale compared to transitions between different orthorhombic structures. However, regardless of which way this balance tips, we anticipate that the insights obtained from this larger study can be used to improve the stability of generic LHP compositions.

Finally, we restrict our study to the migration of caesium and bromide, occupying the A- and X-sites respectively, since the migration barrier of lead was previously shown to be significantly higher [87, 254], and which we therefore assume to be effectively immobile. Halide migration has been studied very widely, and the halide is generally considered to be the most mobile defect in LHPs [90, 255]. Migration of the A-site cation is considered much less frequently, and though its migration is considered to be slower than that of the halide species [256], it has previously been linked to both reversible- and non-reversible performance losses [35, 257] in LHP-based devices. We will therefore focus our study on the computation of both the bromide and caesium mobility tensors.

In the remainder of this chapter, we will introduce the tools we have developed and used to compute these mobility tensors. The general methodology is the main workhorse that will be exploited under different conditions in Chapters 5 to 7. A general overview of the steps taken in this approach are condensed in a flowchart and shown in Figure 4-1. We suggest that the reader refers back to the flowchart whilst reading the rest of this chapter, and perhaps even subsequent chapters, to improve their understanding of how each section fits in the larger methodology.

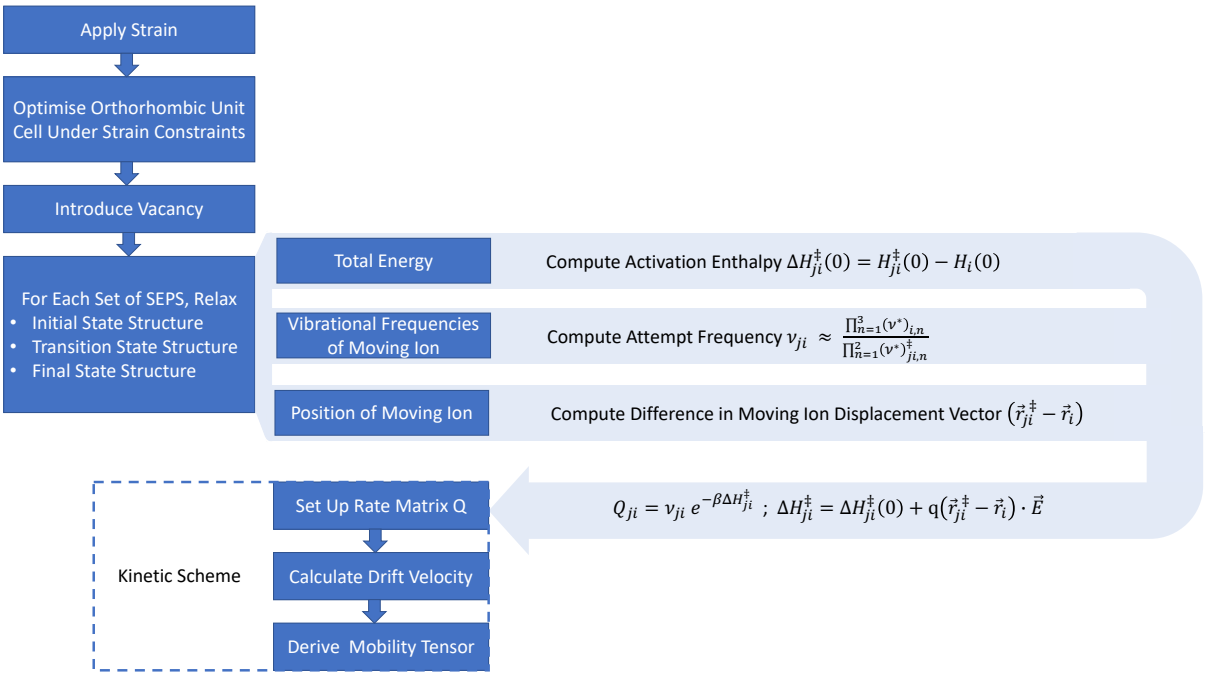

Figure 4-1: Flowchart of the general steps taken to compute the ionic mobility tensor, the methodology of which is critical for the work in subsequent Chapters 5 to 7.

4.2 Preliminary Testing

4.2.1 Convergence of the Plane Wave Basis Set

The accuracy of the results obtained from DFT calculations depends on the choice of both k-point mesh and the cutoff energy, as discussed in Section 3.1.7, and the user should always verify that convergence of the geometry structure with respect to both of these parameters is reached.

Below, we show a compilation of the convergence of both the total energy (a/b) and the lattice parameter (c/d) as a function of the cut-off energy and the k-point mesh density. These results are obtained for $CsPbBr_3$ in the cubic structure with space group $Pm\bar{3}m$, which gives similar insight into the convergence but for which the convergence tests are cheaper to perform in comparison to the orthorhombic structure with space group $Pnma$. Firstly, we note that the total energy can be seen to converge poorly with the cut-off energy, as observed in Figure 4-2a. This is a fairly standard observation and does not pose an issue, since DFT is typically used to compute total energy differences between structures, which for a given cut-off energy are generally well-converged. In contrast, Figure 4-2c shows that the lattice parameter does converge with increasing cut-off energy, as an apparent plateau is

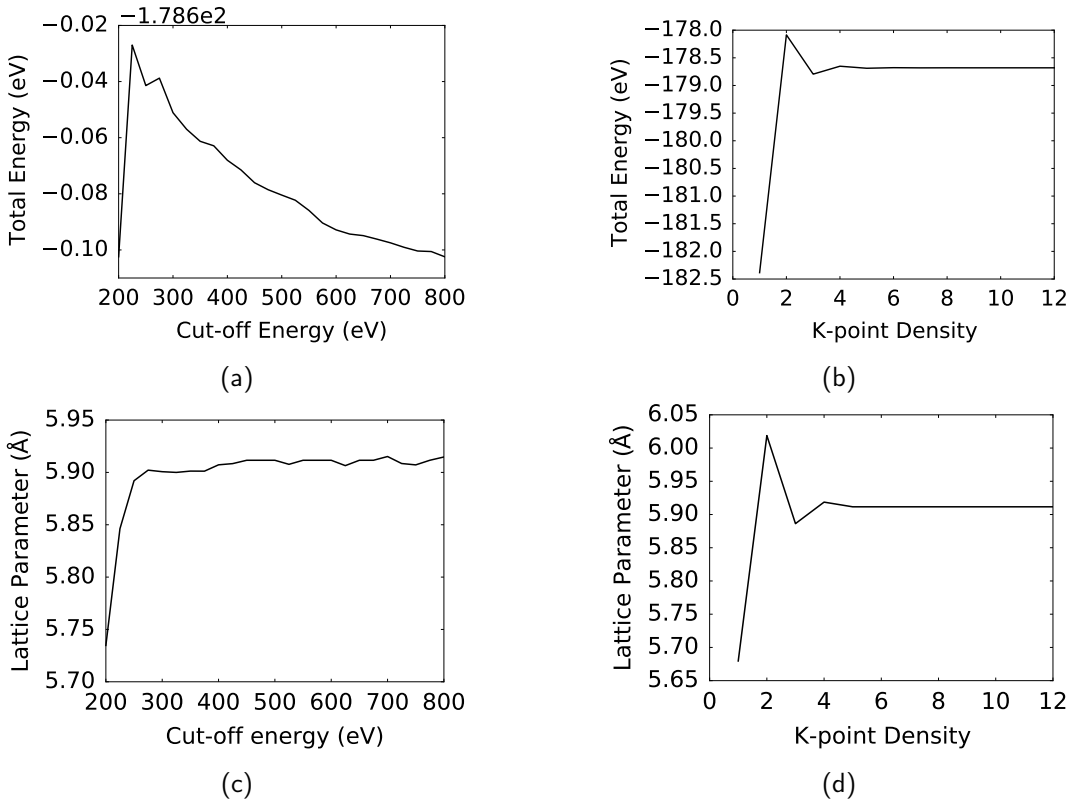

Figure 4-2: Convergence tests of the computed total energy as a function of cut-off energy (a) and k-point mesh density (b), and the computed lattice parameter as a function of cut-off energy (c) and k-point mesh density (d) of cubic $CsPbBr_3$ using the SCAN functional. Convergence tests of varying cut-off energy are performed for a k-point mesh density of 8×8×8, while convergence tests of varying k-point mesh density are performed using a cut-off energy of 500 eV.

reached for a cut-off energy of about 250 eV. As can be observed from Figures 4-2b and 4-2d, both the total energy and lattice parameter give well-converged values from a k-point mesh density upwards of 6×6×6.

The cut-off energy does not depend on the system size but rather on the chemical composition. The threshold value for the cubic structure can thus be used for the orthorhombic structure to obtain equal accuracy. In contrast, the necessary k-point mesh density does scale with system size. However, the values obtained for the cubic structure can be related to those of the orthorhombic structure by using the inverse relationship between the reciprocal and the real-space lattice, i.e. when the length of a certain lattice vector is increased by a factor of two, the corresponding number of k-points sampled along that direction can be halved, thus obtaining a similar k-point mesh density.

The unit cell of the orthorhombic structure with space group is roughly $\sqrt{2}$ as large in the

[100] and [001] directions, and twice as long in the [010] direction in comparison to the lattice vector of the cubic unit cell with space group $Pm\bar{3}m$. For each value of pressure and strain considered in this thesis, optimisation of both the lattice parameters and the atomic coordinates of the bulk unit cell of the orthorhombic structure with space group $Pnma$ was performed until the changes in both the total energy and the Kohn–Sham eigenvalues between two self-consistent cycles were below 10^{-8} eV, and the magnitudes of the forces on the ionic cores were below 0.001 eV Å^{-1} using a cut-off energy of 600 eV and a k-point mesh density of 8×6×8, generated automatically according to the Monkhorst–Pack scheme [221], and corresponding to a k-point mesh density of 12×12×12 for the cubic structure with space group $Pm\bar{3}m$. These values are by and large on the safe side of caution, and give credibility towards the convergence of the lattice parameters and fractional coordinates. Subsequent calculations of the fractional coordinates of the vacancy structures in the initial and transitions states are performed using supercells generated by the application of a [[2,0,2], [0,2,0], [-2,0,2]] scaling matrix to the optimised $Pnma$ unit cells at a cut-off energy of 300 eV, while the Brillouin zone is only sampled at the Γ-point. This corresponds to a k-point mesh density of 4×4×4 in the cubic cell, which is towards the lower end of the convergence threshold. However, taking a higher k-point mesh density becomes compuationally unfeasible. We do note that in particular the energies (the lattice parameters are not optimised for these calculations) seem sufficiently well-converged to give credibility towards our results.

4.2.2 Choice of XC Functional

We previously stated that the accuracy and computational expense of solving the Kohn-Sham equations to a large extent depends on the level of approximation of the exchange-correlation functional, as discussed in more detail in Section 3.1.6.

In this thesis, the recently developed SCAN (strongly constrained and appropriately normed) meta-GGA (generalised gradient approximation) exchange–correlation functional [216] is employed, as it has been shown to outperform other commonly used exchange–correlation functionals in terms of the lattice parameters of perovskites [258], the local potential energy surface [259], the pressure-induced phase transitions [260], the geometry and enthalpies of defects [261] and lattice formation enthalpy [262]. Below we verify that the SCAN functional gives reasonable results in terms of the optimised lattice parameters of the pristine unit cell, the elasticity tensor and the phase stability of the unit cell with space group $Pnma$.

4.2.2.1 Lattice Parameters

First, we compute the lattice parameters of the pristine unit cell of the orthorhombic structure with space group $Pnma$, and compare the results to experimental values and to values obtained using the more established PBE [214] and PBEsol [215] exchange–correlation functionals, both of which are GGA functionals. The results of this comparison are shown in Figure 4-3, in which the values obtained using the different XC-functionals are shown as red dots, and experimental values from References 263, 153 and 264 are shown using dashed blue, black and green lines, respectively.

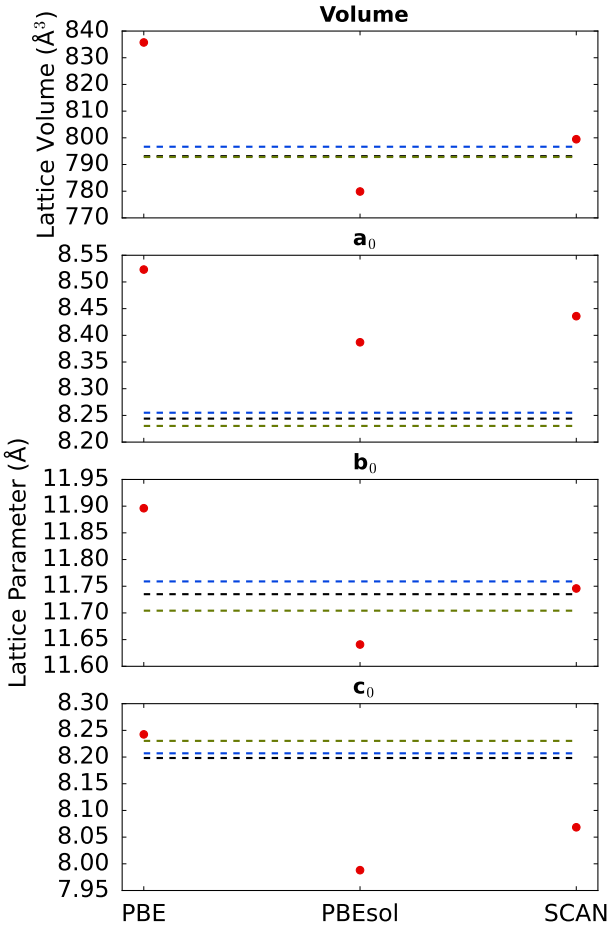

Figure 4-3: Comparison of lattice parameters and volume of $CsPbBr_3$ in the orthorhombic *Pnma* phase for the PBE, PBEsol and SCAN functionals, compared to experimental values from References 263, 153 and 264, shown using dashed blue, black and green lines, respectively.

As can be seen in the top panel, the volume predicted using the PBE functional is approximately 5% higher than the experimentally measured value, which is a sign of underbinding, i.e. making the chemical bonds too long. In contrast, the PBEsol functional predicts a volume that is approximately 2% too low, which is an indication of slight overbinding. The experimentally observed lattice volume is most accurately reproduced by the SCAN functional, being only fractionally higher than those observed in experiment.

We observe similar trends in the individual lattice parameters, where the PBE functional consistently yields the highest values and PBEsol the lowest. In particular, the length of $\boldsymbol{b}$ in the pristine structure, which we denote as b_0, is predicted particularly well by the SCAN functional, while it is too high for PBE and too low for PBEsol. The values for a_0 and c_0 predicted by the SCAN functional are further from the experimental values, being 2% too high and 2% too low, respectively. A similar trend is observed for the PBEsol functional, which suggests that this might not be an issue with the SCAN functional, but rather a result of the DFT approximation, which operates effectively at 0 K. At such temperatures, the anisotropy of the equatorial plane, spanned by $\boldsymbol{a}$ and $\boldsymbol{c}$ seems to be higher than that observed at higher temperatures at which thermal motion can potentially lead to averaging of a_0 and c_0. All in all, we conclude that the SCAN functional yields reasonable results for the lattice parameters, although the anisotropy in the equatorial plane is significantly enhanced.

Values from several computational studies 3, 265–267 of the lengths of the lattice vectors of $CsPbBr_3$ in the $Pnma$ phase are shown in Table 4.1, along with the experimental values reported in Figure 4-3. Similar to what we observed previously, we observe that the PBE functional tends to strongly overbind, with values of a_0, b_0 and c_0 all larger than the experimentally observed values. The values obtained using the PBEsol functional are much closer to the experimental values. Interestingly, Reference [265] also observes a strong anisotropy of the equatorial plane spanned by **a** and **c**, similar to our own work, while Reference 266 observes a more or less isotropic equatorial plane, similar to experiment. The differences could be a result of the fact that the values from the latter study were obtained using the WIEN2K software package [268], while those from Reference 265 were obtained using the ABINIT software package [269] and ours were obtained using VASP. While all three of these software packages employ plane waves to represent the electronic wavefunction, it is unclear which of these yields the most accurate results, though generally VASP is considered to be one of the more reliable codes.

Table 4.1: Values reported for the lengths of the lattice vectors (a_0, b_0 and c_0) of $CsPbBr_3$ in the $Pnma$ phase in the absence of strain. Values from experimental studies are labelled 'Exp.' while density functional theory studies are labelled according to the exchange–correlation functional.

Study	Method	a_0 (Å)	b_0 (Å)	c_0 (Å)
Rodova *et al.* [263]	Exp.	8.26	11.76	8.21
Stoumpos *et al.* [153]	Exp.	8.24	11.74	8.20
Xue *et al.* [264]	Exp.	8.23	11.70	8.23
This work	SCAN	8.42	11.76	8.07
Sadok *et al.* [265]	PBEsol	8.39	11.64	7.98
Ghaithan *et al.* [266]	PBEsol	8.16	11.62	8.12
Kang *et al.* [3]	PBE	8.50	11.89	8.23
Tomanova *et al.* [267]	PBE	8.53	11.97	8.26
Ghaithan *et al.* [266]	PBE	8.56	12.19	8.51

4.2.2.2 Phase Stabilty

As was discussed in more detail in Section 1.1, perovskite structures typically exhibit significant octahedral tilting with respect to the cubic aristotype. The various different tilting patterns were classified by Glazer [77, 78], and an overview of these tilting pattern was shown in Figure 1-3, in which the tilting patterns that correspond to the phases adopted by $CsPbBr_3$ were highlighted.

The total energies corresponding to these different tilting patterns have previously been computed using the PBE functional, and the variation in total energies of these different tilting patterns was shown to be quite small, with differences no larger than 50 meV per formula unit, apart from the cubic aristotype, the total energy of which was shown to be at least 50 meV per formula unit higher than the tilted structures [79]. To verify these results, we recomputed the relative energies using the PBE XC-functional and compare our results to the literature values, as shown in Figure 4-4a. Apart from relatively small deviations, our computed values agree well with those reported in the literature, indicating that the structures we have used are indeed correct.

We then compare the total energy differences obtained from calculations using either the PBE or the SCAN XC-functional, the results of which are shown in Figure 4-4b. The relative ordering of the different phases is very similar for both functionals. In particular, the orthorhombic structure with space group $Pnma$ has the lowest energy, along with the orthorhombic structure with space group $P2_1/m$. The tilting pattern of the structure with space group $Pnma$ is $a^+b^-b^-$, while that of the structure with space group $P2_1/m$ is $a^+b^-c^-$. The similar energies indicate that the additional degree of freedom, i.e. the additional tilting angle, does not further stabilise the structure and confirms that the structure

with space group $Pnma$ is indeed the ground state structure, regardless of the choice of functional. For many LHPs, the tetragonal β-phase corresponds to tilting about one of the three principal lattice directions. For in-phase tilting, the tilting pattern can be written as $a^0a^0b^+$ with corresponding space group $P4/mbm$, while for out-of-phase tilting, the tilting pattern can be written as $a^0a^0b^-$ with corresponding space group $I4/mcm$. Interestingly, the structure with space group $I4/mcm$ is predicted to have a lower energy than the structure with space group $P4/mbm$ for both functionals, while experimentally the structure with space group $P4/mbm$ is observed at intermediate temperatures, suggesting that at such temperatures it has a lower free energy than the structure with space group $I4/mcm$. A result for this discrepancy could be that at elevated temperatures also entropic contributions need to be considered, while our results only account for enthalpy contributions. Moreover, it could also be an indication of a lower transition barrier for transitions that average out the in-phase tilts, rather than the out-of-phase tilts, thus resulting in slightly different forms of dynamical averaging over the lower-symmetry orthorhombic structures with space group $Pnma$, though this hypothesis is not confirmed by calculations shown previously in Figure 1-5. Overall, these results nonetheless confirm the feasability of using the SCAN XC-functional in modelling the orthorhombic unit cell with space group $Pnma$ of $CsPbBr_3$.

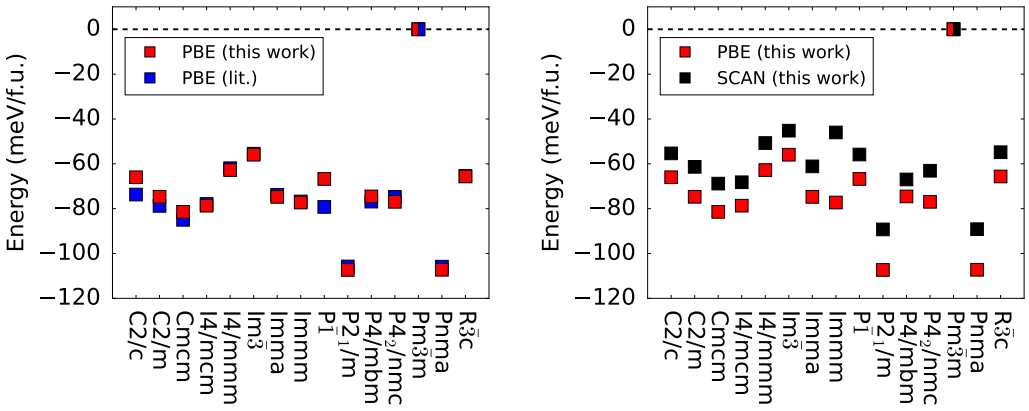

Figure 4-4: Total energies per formula unit (f.u.) of $CsPbBr_3$ for different phases, relative to the energy of the aristotype. In (a), relative energies are computed using PBE (red) and compared to literature values (blue) from Reference 79. In (b), relative energies are compared between the PBE and SCAN exchange–correlation functionals. Computed energies correspond to unit cells, fully converged using a cut-off energy of 500 eV, and k-point mesh densities equivalent to a density of 8×8×8 for the cubic aristotype, but scaled down to match the relative size of the unit cell.

4.2.2.3 Elasticity Tensor

To verify that the SCAN XC-functional is able to accurately predict the elasticity of $CsPbBr_3$, we compute the elasticity tensor of $CsPbBr_3$ in the orthorhombic phase with space group $Pnma$, based on the Hessian matrix derived from calculations of finite displacements. We compare the PBE, PBEsol and SCAN XC-functionals, using a cut-off energy of 400 eV and a $4 \times 3 \times 4$ Γ-centered k-point mesh, generated automatically according to the Monkhorst-Pack scheme. The resulting components of the elastic tensor are shown in Table 4.2.

Table 4.2: Components of the elasticity tensor of $CsPbBr_3$ in the $Pnma$ phase.

XC-functional	C_{11}	C_{22}	C_{33}	C_{44}	C_{55}	C_{66}	C_{12}	C_{13}	C_{23}
PBE (this work)	27.3	29.9	7.8	5.0	8.5	5.8	11.2	15.6	6.1
PBEsol (this work)	24.2	44.9	19.2	5.8	14.7	7.0	11.5	13.6	12.2
SCAN (this work)	33.2	42.0	27.6	6.1	16.5	7.8	12.2	20.9	12.2
optB86b-vdW [55]	33	40	21	7	14	8	12	20	13

The upper bounds of the bulk and shear moduli, corresponding to the isostrain Voigt averages, can be derived from the components C_{ij} of the elasticity tensor $\boldsymbol{C}$, while the lower bounds of the bulk and shear moduli, corresponding to the isostress Reuss averages, can be derived from the components S_{ij} of the compliance tensor $\boldsymbol{S}$, which is the inverse of the elasticity tensor 270. These values can be expressed as follows:

$$\begin{aligned} B_{\mathrm{Voigt}} &= \frac{C_{11}+C_{22}+C_{33}+2\left(C_{12}+C_{13}+C_{23}\right)}{9} \\ B_{\mathrm{Reuss}} &= \frac{1}{S_{11}+S_{22}+S_{33}+2\left(S_{12}+S_{13}+S_{23}\right)} \\ G_{\mathrm{Voigt}} &= \frac{C_{11}+C_{22}+C_{33}-\left(C_{12}+C_{13}+C_{23}\right)+3\left(C_{44}+C_{55}+C_{66}\right)}{15} \\ G_{\mathrm{Reuss}} &= \frac{15}{4\left(S_{11}+S_{22}+S_{33}\right)-4\left(S_{12}+S_{13}+S_{23}\right)+3\left(S_{44}+S_{55}+S_{66}\right)}. \end{aligned} \tag{4.1}$$

A reasonable estimate of both the bulk and shear moduli can be derived by averaging over the upper and lower bounds

$$\begin{aligned} B_{\mathrm{avg}} &= \frac{B_{\mathrm{Voigt}}+B_{\mathrm{Reuss}}}{2} \\ G_{\mathrm{avg}} &= \frac{G_{\mathrm{Voigt}}+G_{\mathrm{Reuss}}}{2}, \end{aligned} \tag{4.2}$$

from which the Poisson ratio ν can be computed as

$$\nu = \frac{3B_{\mathrm{avg}} - 2G_{\mathrm{avg}}}{6B_{\mathrm{avg}} + 2G_{\mathrm{avg}}}. \tag{4.3}$$

Finally, Young's modulus can be derived using Equation (2.5). The resulting bulk moduli, and their comparison to values in the literature are shown in Table 4.3.

Table 4.3: Elastic moduli of $CsPbBr_3$ in the $Pnma$ phase.

	E	B	G	ν
PBE	4.1	3.3	1.6	0.30
PBEsol	20.6	17.3	7.9	0.30
SCAN	23.3	21.4	8.9	0.32
optB86b-vdW [55]	20.7	19.9	7.8	0.32

While the elastic moduli derived using the PBE XC-functional are very low compared to values obtained from the literature, in the range 16.9–23.5 GPa, described in more detail in Section 2.2.1, the elastic moduli from both the PBEsol and SCAN XC-functionals compare well to the experimentally and theoretically measured and calculated elasticity components, thus giving credibility to results obtained using either of these functionals, in particular the SCAN XC-functional used predominantly in this thesis.

4.3 Connectivity of the Sublattices in the Orthorhombic Phase with Space Group $Pnma$

In general, perovskite structures of stoichiometry ABX_3 are formed of corner-sharing octahedra of X anions, with B cations at their centres and A cations in the voids between them. The perovskite structure of highest symmetry, the so-called 'aristotype', is a cubic structure with space group $Pm\bar{3}m$, and a unit cell that contains a single ABX_3 formula unit. Lower symmetry perovskite structures are considered primarily as the result of the tilting of neighbouring octahedra away from their alignment in the $Pm\bar{3}m$ structure, either in the same direction (in-phase) or opposite directions (out-of-phase) about the three axes defined by the lattice vectors. In common with other technologically relevant LHPs, such as $MAPbI_3$, $MAPbBr_3$ and $FAPbBr_3$ [271–273] (where MA stands for methylammonium, and FA for formamidinium), $CsPbBr_3$ adopts an orthorhombic *Pnma* structure at low temperatures in which the octahedra are tilted in-phase about the $[010]$ (longest) lattice vector, and out-of-phase about the other two lattice vectors ($a^-b^+a^-$ in the notation of Glazer [77]), resulting

in a unit cell that contains four ABX_3 formula units. We now look at the implications of the lower symmetry of the orthorhombic structure with space group *Pnma* on the topology of the bromide and caesium sublattices.

4.3.1 Connectivity of the Bromide Sublattice

The lower symmetry of the orthorhombic *Pnma* structure with respect to the cubic $Pm\bar{3}m$ structure can immediately be seen to have significant implications for anion vacancy migration, which are nevertheless not always considered. Most obviously, while all anion sites are symmetrically equivalent in the $Pm\bar{3}m$ structure, a schematic representation of which is shown in Figure 4-5, they are partitioned into two subsets of symmetrically equivalent sites in the *Pnma* structure. The two types of site, represented by white and black spheres in Figure 4-6, correspond to the 4c and 8d Wyckoff positions, and we refer to anion sites as being either apical or equatorial, respectively, depending on their Wyckoff position. However, this does not provide a complete picture of the effects on anion vacancy migration of the lower symmetry of the *Pnma* structure, since migration takes place via sequential hops between *pairs* of anion sites. In order to illustrate this point, we consider the pairs of sites which, when connected, describe the edges of the $PbBr_3$ octahedra.

The points at the centre of each octahedron, which are occupied by lead ions, correspond to special Wyckoff positions of the relevant space group in both the cubic $Pm\bar{3}m$ and the orthorhombic *Pnma* structures, meaning that the points are left invariant by at least one symmetry operation of the space group (in addition to the trivial identity operation); furthermore, in both phases, the points correspond to a single Wyckoff position of the space group, and as a result, we can focus on the twelve pairs of bromide sites of a single octahedron.

In the $Pm\bar{3}m$ structure, the point at the centre of an octahedron corresponds to the 1a Wyckoff position, for which the full point group symmetry of the lattice is retained; in particular, consideration of the three 4-fold rotational axes of symmetry passing through that point is sufficient to demonstrate that all twelve pairs of bromide ions are symmetrically equivalent, and indeed, in the $Pm\bar{3}m$, they are first nearest neighbours (1-NN) to each other. The 1-NN pairs of bromide ions in the $Pm\bar{3}m$ structure are connected by sticks in Figure 4-5, with the sticks being coloured the same since they are all symmetrically equivalent.

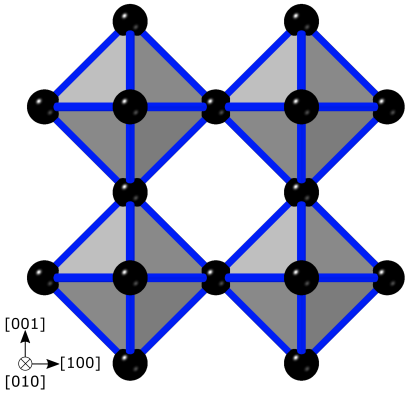

Figure 4-5: Visual representation of the sets of Br-SEPS in the aristotype of $CsPbBr_3$ at 0.0 GPa. The bromide sites are represented by black spheres. First nearest neighbor (1-NN) symmetrically equivalent pairs of sites (SEPS) are shown connected with blue sticks. The Cs and Pb atoms are not explicitly shown, but the latter are represented by the solid octahedra.

In the *Pnma* structure, the point at the centre of an octahedron corresponds to the 4a Wyckoff position, which retains inversion symmetry only (in addition to the identity). As a consequence, the twelve pairs of bromide ions are not all symmetrically equivalent; instead, each pair belongs to one of six sets of symmetrically equivalent pairs of sites (SEPS). The 1-NN pairs of bromide ions in the *Pnma* structure are connected by sticks in Figure 4-6, with the sticks being coloured according to which of the sets of SEPS the pairs belong. Despite the fact that the distances between pairs of bromide ions belonging to different sets of SEPS are not (necessarily) identical, we retain the same 1-NN terminology when referring to them due their relationship to the cubic $Pm\bar{3}m$ structure. As can be seen in Figure 4-6, four of the sets of SEPS consist of pairs of equatorial and apical anion sites, and we describe hops of a vacancy between such pairs as either apical-to-equatorial (A-to-E), or equatorial-to-apical (E-to-A), depending on the initial and final site of the hop. The remaining two sets of SEPS consist of pairs of equatorial sites, and we refer to the hops in those cases as being equatorial-to-equatorial (E-to-E).

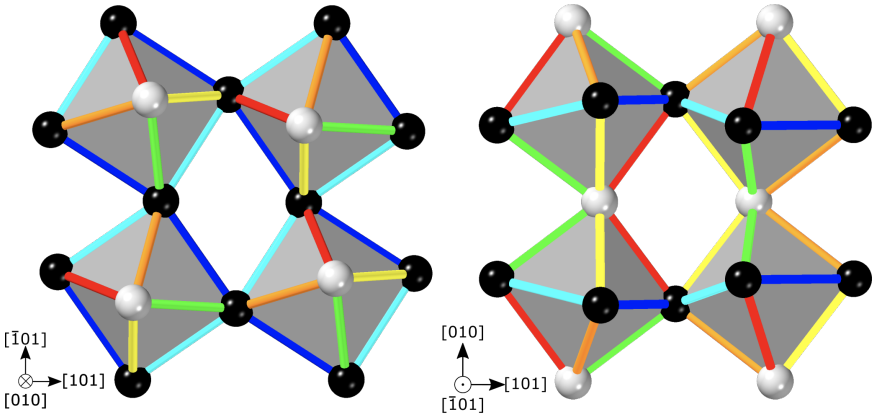

Figure 4-6: Structure of the *Pnma* phase of $CsPbBr_3$, at 0.0 GPa, shown from two different perspectives. Only the bromide anions are shown, with the apical and equatorial bromide sites represented by white and black spheres, respectively. First nearest neighbour (1-NN) symmetrically equivalent pairs of sites (SEPS) are connected with sticks of the same colour, which follow the edges of the $PbBr_3$ octahedra; see text for details.

4.3.2 Connectivity of the Caesium Sublattice

A visual representation of the connectivity of the Cs sublattice is shown in Figure 4-7 for the cubic aristotype with space group $Pm\bar{3}m$, and in Figure 4-8 for the orthorhombic phase with space group *Pnma* phase. In both phases, the Cs sites, represented by pink spheres, correspond to a single Wyckoff position (meaning they are all symmetrically equivalent with respect to the space group of the structure). As a result, we can focus on the neighbours of a single Cs site to establish the relevant pairs of sites between which hops can occur.
In the $Pm\bar{3}m$ phase, Cs occupies the the 1b Wyckoff position of the $Pm\bar{3}m$ space group. The full point group symmetry of the lattice is retained at the 1b Wyckoff position. As a result, all of the first nearest neighbour (1-NN) Cs sites, of which there are six, are symmetrically equivalent. The corresponding pairs of 1-NN Cs sites are connected by red sticks in Figure 4-7. In the *Pnma* phase, Cs occupies the 4c Wyckoff position of the *Pnma* space group, which is a special point with mirror symmetry about the (010) plane. Though the six nearest neighbours are no longer equidistant, we will refer to them as the first nearest neighbour (1-NN) atoms because of their topological similarity with respect to the cubic phase with space group $Pm\bar{3}m$. By virtue of the symmetry of the *Pnma* space group, the pairs of nearest neighbours can be grouped in three sets of symmetrically equivalent pairs of sites (SEPS). These different sets of SEPs are represented by colour-coded sticks in Figure 4-8. This partitioning can also be understood more intuitively. Relative to the aristotype, the fractional coordinates of the caesium atoms are shifted by a small amount of $\pm\Delta x$ and

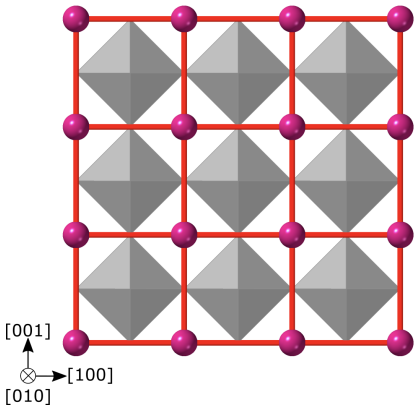

Figure 4-7: Visual representation of the sets of Cs-SEPS in the aristotype of $CsPbBr_3$ at 0.0 GPa. The caesium sites are represented by pink spheres. First nearest neighbor (1-NN) symmetrically equivalent pairs of sites (SEPS) are shown connected by red sticks. The Pb and Br atoms are not explicitly shown, but are represented by the solid octahedra.

$\pm\Delta$z in the equatorial plane, while their fractional coordinates along **b** remain fixed at $1/4$ or $3/4$, such that mirror symmetry along [010] is retained. This mirror symmetry is responsible for making two of the nearest neighbours, with displacement vectors of $[\pm 2x, \pm 1/2, \pm 2z]$ and represented by green sticks in Figure 4-8, equivalent. The four remaining nearest neighbours lie in the equatorial plane. Because of the symmetry of the glide operation $[1/2 + x,\ y\ , 1/2 - z]$ (a full list of the symmetry operations can be found in Table 6.2), the remaining neighbours can be shown to be displaced by either one of two displacement vectors, namely $[\pm 1/2, 0, \pm(1/2+2z)]$ or $[\pm 1/2, 0, \pm(1/2-2z)]$, such that the distance between two sites along [001] is either increased (corresponding to the red sticks in Figure 4-8) or decreased (corresponding to the blue sticks in Figure 4-8) by an amount $2z$. In both cases of the bromide and caesium sublattice connectivity, our own observations were confirmed by the path mapper algorithm, as implemented in pymatgen-diffusion [274], an add-on to the pymatgen package [275].

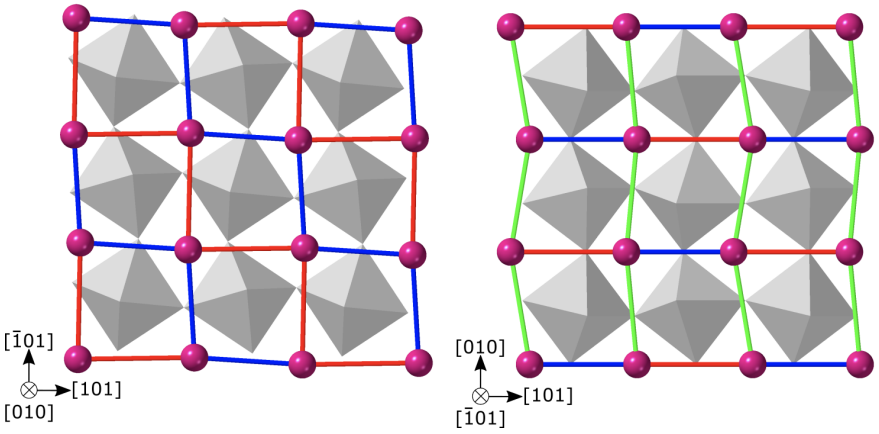

Figure 4-8: Schematic representation of the connectivity of the Cs sublattice in pristine $CsPbBr_3$ in the orthorhombic phase with space group $Pnma$. The caesium sites are represented by pink spheres. First nearest neighbor (1-NN) symmetrically equivalent pairs of sites (SEPS) are shown as sticks of the same color. The Pb and Br atoms are not explicitly shown, but are represented by the solid octahedra.

4.4 Migration Enthalpies

4.4.1 Bromide Migration

Now that we have established the connectivity of the pairs of sites in the bromide and caesium sublattices, we move on to consider hops of vacancies between them. Since ionic migration in LHPs is typically assumed to be vacancy-mediated [87, 118–120, 254, 276–278], we thus present a quantitative analysis of the migration of charged vacancies in bulk $CsPbBr_3$, starting with the bromide vacancy. The analysis is restricted to the migration of bromide vacancies in their positive charge state, since that charge state has been shown in a number of studies to be favourable for Fermi levels within the majority of the band gap [3,250,279–281]. In order to obtain the activation energies associated with hops of these positively charged bromide vacancies, we need to relax the structures associated with the initial, transition and final states corresponding to the hop between a pair of lattice sites.

In order to obtain relaxed structures for the initial and final states, calculations involving bromide vacancies were performed using supercells generated by the application of a [[2,0,2],[0,2,0],[-2,0,2]] scaling matrix to the optimised *Pnma* unit cells for each value of hydrostatic pressure, resulting in stoichiometric supercells containing 64 formula units, or 320 atoms. Following the introduction of a positively charged bromide vacancy into (i.e. the removal of a negatively charged bromide ion from) each supercell, the internal coordinates of the remaining atoms were optimised until the changes in both the total energy

and the Kohn–Sham eigenvalues between two self-consistent cycles were below 10^{-6} eV, and the magnitudes of the forces on the ionic cores were below 0.01 eV Å^{-1}. For the supercell calculations, a plane-wave cutoff energy of 300 eV was employed, and the Brillouin zone was sampled at the Γ-point only. The lattice vectors were kept fixed at the values determined previously for the pristine bulk, thus neglecting the $p\Delta V$ contribution to the change in enthalpy, as is commonly done when considering solid state systems [282, 283].

In order to obtain the transition state for all 1-NN sets of SEPS, the minimum enthalpy paths taken by a vacancy as it hops between a pair of sites belonging to each set were calculated using the CINEB method, following which the transition state structures were optimised further using the dimer method. To calculate the minimum enthalpy paths for an anion to hop between pairs of sites, climbing image nudged elastic band (CINEB) calculations were performed using the VASP Transition State Tools (VTST) package [227, 228]. Each path was evaluated using four structural images, and the optimisation was performed using a spring constant of 5 eV/Å^2, until the changes in both the total energy and the Kohn–Sham eigenvalues between two self-consistent cycles were below 10^{-6} eV, and the magnitudes of the forces on the ionic cores were below 0.05 eV Å^{-1}. Subsequently, the transition state structures were optimised further using the dimer method [230, 233] until the changes in both the total energy and the Kohn–Sham eigenvalues between two self-consistent cycles were below 10^{-6} eV, and the magnitudes of the forces on the ionic cores were below 0.02 eV Å^{-1}. For both the CINEB and dimer calculations, a plane-wave cutoff energy of 300 eV was used, while the Brillouin zone was probed solely at the Γ-point.

The paths are non-linear in general, and in particular they should not be confused with the sticks in Figure 4-6. A schematic representation of a representative mininum enthalpy path is shown in Figure 4-9b, which appears to be curved, in accordance with reports made elsewhere [87]. The resulting potential energy profiles of the minimum enthalpy paths are shown in Figure 4-9a. Relative to the *Pm*$\bar{3}$*m* structure, the reduced symmetry of the *Pnma* structure is apparent in the non-negligible spread in transition state enthalpies for hops between pairs in different sets of SEPS. Their magnitudes, in the range 0.23–0.34 eV, are in line with values reported for $CsPbBr_3$ based on experimental measurements [115, 116] and theoretical calculations of anion vacancy migration in the higher symmetry tetragonal and cubic phases [70, 120], though substantially lower than the value of 0.65 eV also reported for the cubic phase [122].

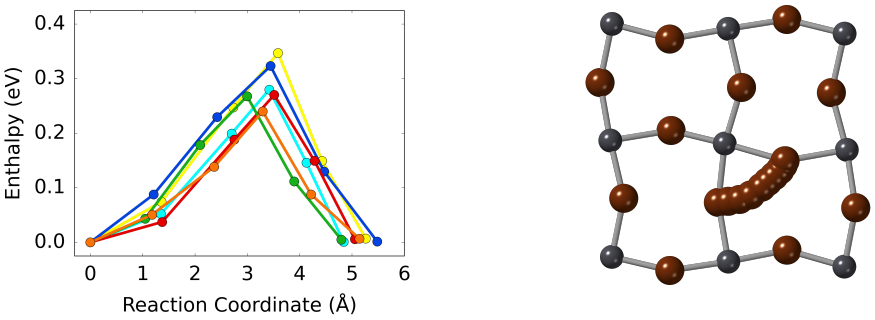

(a) (b)

Figure 4-9: (a) Schematic representation and (b) potential energy profiles of the minimum enthalpy paths of a positively charged bromide vacancy and hopping between a pair of sites belonging to each of the sets of 1-NN SEPS.

4.4.2 Caesium Migration

Similar to the migration of the anion, the migration of the A-site cation is typically considered to be vacancy-mediated [87, 284]. Here we thus compute the activation enthalpy associated with the hopping of a caesium vacancy between a representative pair of sites for each of the three sets of SEPSs. The analysis is restricted to the migration of caesium vacancies in their negative charge state, since that charge state has been shown in a number of computational studies to be favorable for Fermi levels within the majority of the band gap [3,250,281]. Again, the minimum enthalpy paths taken by a vacancy as it hops between a pair of sites belonging to each set were calculated using the CINEB method, following which the transition state structures were optimised further using the dimer method.

The potential energy profiles of the minimum enthalpy paths of a negatively charged caesium vacancy hopping between a representative pair of sites is shown as a function of the cumulative distance between images for all atoms (the reaction coodinate) for each of the three sets of SEPS at 0.0 GPa in Figure 4-10a. The colours correspond to the pairs of sites connected by sticks in Figure 4-8. We find activation enthalpies for negatively charged Cs migration in the range 0.69–0.87 eV, which is similar to values of 0.70 eV previously obtained for $CsPbBr_3$ in the tetragonal phase [120], and to values of 0.84 eV for V_{MA}^{-} migration in $MAPbI_3$ [87].

Looking forward, we note that in our study of the effects of hydrostatic pressure, which we will be discussed in the next chapter, we find the transition by first convering the CINEB calculation, after which the dimer method is used to further optimise the transition state. In our studies of the effects of biaxial and uniaxial strain, we omit the CINEB calculation and directly optimise the transition state using the dimer method, taking the fractional

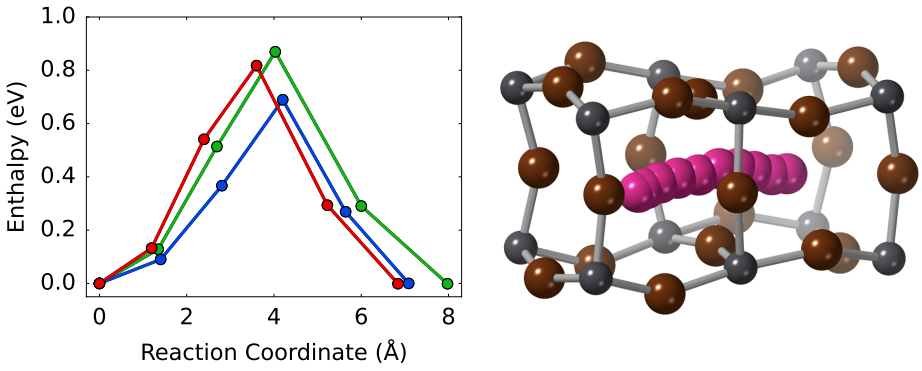

(a) (b)

Figure 4-10: Potential energy profiles (a) and schematic representation (b) of the minimum enthalpy paths of a negatively charged caesium vacancy hopping between a pair of sites belonging to each of the sets of 1-NN SEPS. Potential energy profiles shown as a function of the cumulative distance between images for all atoms (the reaction coodinate).

coordinates from the calculation in a preceding strain state as an initial guess.

4.5 Attempt Frequencies

We then compute the attempt frequencies associated with each transition, as described in more detail in Section 3.2.3. In calculating the attempt frequency ν_{ji}, which is defined by equation 3.66, we make the approximation of considering the degrees of freedom of the moving ion alone [285–287], such that:

$$\nu_{ji} \approx \frac{\prod_{n=1}^{3} (\nu^*)_{i,n}}{\prod_{n=1}^{2} (\nu^*)^{\ddagger}_{ji,n}}, \tag{4.4}$$

in which $(\nu^*)_{i,n}$ and $(\nu^*)^{\ddagger}_{ji,n}$ are the frequencies of the nth real (i.e. non-imaginary) mode of vibration of the moving ion in the initial and transition states, with all other ions held fixed.

The Hessian matrices from which the vibrational frequencies were derived were calculated using finite displacements of 0.015 Å. For bromide migration, we computed attempt frequencies in a range of 1.61–2.60 THz, while for caesium migration, the attempt frequencies were observed in a range of 0.84–0.86 THz. Interestingly, we note that the attempt frequencies for bromide migration span the same range as those features in experimentally

measured Raman spectra that have been assigned to vibrations involving the $PbBr_3$ octahedra [123, 264, 288–290].

Looking forward, we note that in our study of the effects of hydrostatic pressure, which we will be discussed in the next chapter, we compute the vibrational frequencies using Hessian matrices that were calculated using finite displacements of 0.015 Å. There is only one set of SEPS for which we make an exception, described in more detail in the next chapter, and for which we use smaller finite displacements. In our studies of the effects of biaxial and uniaxial strain, we therefore change our methodology slightly, and compute the vibrational frequencies using Hessian matrices that were calculated using finite displacements of 0.010 Å.

4.6 Setting Up the Kinetic Model

In our methodology, bromide vacancy migration is modelled using a kinetic scheme [222, 291, 292]—i.e. a discrete state, continuous time Markov chain—in which each of the states corresponds to a vacancy occupying a given site in the unit cell. The dependent variables in the kinetic scheme are the probabilities of each site being occupied by a vacancy, the time evolution of which is governed by a master equation, expressed previously in Equation 3.43: $\frac{d\vec{p}}{dt} = \mathbf{Q}\vec{p}$. $\mathbf{Q}$ is the *transition rate matrix*, each element Q_{ji} of which is the rate (probability per unit time) for a vacancy at site i to hop to site j. If sites j and $i \neq j$ are considered to be connected in the model, taking periodic boundary conditions into account, then Q_{ji} is computed according to the formula of harmonic transition state theory [223], introduced more generally in Equation 3.48:

$$Q_{ji} = \frac{\prod_{n=1}^{N} \nu_{i,n}}{\prod_{n=1}^{N-1} \nu_{ji,n}^{\ddagger}} \exp\left(-\beta \Delta H_{ji}^{\ddagger}\right) = \nu_{ji} \exp\left(-\beta \Delta H_{ji}^{\ddagger}\right), \tag{4.5}$$

in which $\nu_{i,n}$ and $\nu_{ji,n}^{\ddagger}$ are the frequencies of the nth real (i.e. non-imaginary) mode of vibration of the system in the initial and transition states, $\Delta H_{ji}^{\ddagger}$ is the activation enthalpy of the hop, and $\beta = (k_{\mathrm{B}}T)^{-1}$. In calculating the attempt frequency ν_{ji} we make the approximation of considering the degrees of freedom of the moving ion alone [285–287], as defined by Equation (4.4). If sites j and $i \neq j$ are instead considered to be disconnected, then Q_{ji} is set to zero. Finally, in order to preserve the normalisation of $\vec{p}$, the diagonal elements of $\mathbf{Q}$ must be set equal to the sum of all other elements in their corresponding column, so that $Q_{jj} = -\sum_{i \neq j} Q_{ji}$.

We wish to calculate the mobility tensor, $\boldsymbol{\mu}$, which is defined by Equation 3.93 $\vec{v}_{\mathrm{d}} = \boldsymbol{\mu}\vec{E}$, in which $\vec{v}_{\mathrm{d}}$ is the drift velocity of the bromide vacancies, which develops in response to an electric field $\vec{E}$, and therefore the influence of an electric field must be incorporated into the kinetic scheme. This is done by considering the activation enthalpy $(H_{\mathrm{a}})_{ji}$ for each hop of a vacancy from site i to site $j \neq i$ as the sum of two terms:

$$\Delta H_{ji}^{\ddagger}(\vec{E}) = \Delta H_{ji}^{\ddagger}(0) + q\left(\vec{r}_{ji}^{\ddagger} - \vec{r}_i\right) \cdot \vec{E}, \tag{4.6}$$

where the first term, $\Delta H_{ji}^{\ddagger}(0)$, is the (zero-field) activation enthalpy described previously. The second term, which takes into account the work done by, or against, the electric field in attaining the transition state, follows from the single-ion approximation such that it is equal to the difference between the position vector of the moving anion in the transition state, and the position vector of the same anion in the initial state, multiplied by its charge q. We note that this approach, which is essentially the same as that originally adopted by Mott and Gurney [240], is valid only in the low-field regime, and for stronger electric fields, non-linear effects must be taken into account [241, 242]. The mobility is a steady state quantity, so we need to solve the steady state version of Equation 3.43:

$$\frac{d\vec{p}}{dt} = \vec{0} = \mathbf{Q}\vec{p}. \tag{4.7}$$

If vacancy–vacancy interactions are neglected, corresponding to the dilute limit, then $\mathbf{Q}$ does not depend on the state of the system, and is therefore constant in time. This renders the problem sufficiently simple that Equation 4.7 can be solved directly by finding the eigenvector of the rate matrix with eigenvalue 0, which corresponds to the stationary distribution $\vec{\pi}$. In general, the number of hops of a vacancy from site i to j per unit time (the flux) is $Q_{ji}p_i$, and the steady state drift velocity, $\vec{v}_{\mathrm{d}}$, is simply the sum of the steady state fluxes multiplied by the displacement vectors associated with each hop, $\vec{r}_j - \vec{r}_i$:

$$\vec{v}_{\mathrm{d}} = \sum_i \sum_{j \neq i} Q_{ji}\pi_i(\vec{r}_j - \vec{r}_i). \tag{4.8}$$

4.6.1 Details of the Calculations

In our application of the kinetic scheme to anion vacancy migration in $CsPbBr_3$, the number of states, and their topology, are based on a [[1,0,1],[0,1,0],[-1,0,1]] supercell of the anionic sublattice of the orthorhombic *Pnma* unit cell. As a result, the number of states is 24, corresponding to the 24 bromide sites in the supercell, and the resulting transition rate matrix $\mathbf{Q}$ has 24×24 elements. In our application of the kinetic scheme to caesium

vacancy migration in $CsPbBr_3$, the number of states, and their topology, are based on a [[2,0,0],[0,2,0],[0,0,2]] supercell of the Cs sublattice of the orthorhombic *Pnma* unit cell. As a result, the number of states is 32, corresponding to the 32 caesium sites in the supercell, and the resulting transition rate matrix $\mathbf{Q}$ has 32×32 elements.

In both cases, many of the elements are set to zero because the corresponding pair of sites are considered to be disconnected, but activation enthalpies are required for those that are connected. In the absence of a field, the number of non-identical elements is equal to the number of sets of SEPS, plus an additional value for each set of SEPS for which the forward and reverse activation barriers are different. In general however, the position vector of the moving ion in the transition state (in addition to its position vector in the initial state) is required to calculate the effect of the electric field (see Equation 4.6). For most pairs of sites, the transition state is not known, since CINEB and dimer calculations were performed for just one pair of each set of SEPS. In those cases, the symmetry operations of the $Pnma$ space group were used to obtain the transition state structure from that of the pair from the same set of SEPS for which it was calculated using DFT as described above. The symmetry operations of the $Pnma$ space group were obtained using the spglib symmetry module [293], as implemented in pymatgen [275].

At a temperature of 300 K, a field was applied along the crystalline axes [100], [010] and [001] in turn, which correspond to the principal axes of $\boldsymbol{\mu}$, thereby obtaining $\vec{v}_\mathrm{d}$. We use a value for $|\vec{E}|$ of $2\times10^6\,\mathrm{V\,m^{-1}}$, which is comparable to experimental values, and which we verify to be well within the regime in which $\vec{v}_\mathrm{d}$ scales linearly with $|\vec{E}|$, and the charge of the bromide vacancy was assumed to be its formal value of $-1.0e$ [294].

4.7 Mobility Tensor Results

4.7.1 Bromide Mobility

Having described the kinetic model, we are now able to compute the macroscopic mobility tensor, $\boldsymbol{\mu}$, using the results of the activation energies and attempt frequencies obtained previously. Starting with the bromide vacancy mobility, we find that the principal axes of $\boldsymbol{\mu}$ are parallel to the orthorhombic lattice vectors, with corresponding values of the mobility of 2.2, 4.3, $3.2\times10^{-6}\,\mathrm{cm^2\,V^{-1}\,s^{-1}}$, in the [100], [010] and [001] directions respectively. Since no data on ion mobility in $CsPbBr_3$ have been reported, we compare the results of the calculations with experimentally obtained data for $MAPbI_3$, in which ion mobility has been measured using a variety of techniques. Values of the anion mobility at room temperature have been reported in the range 1.2×10^{-9}–$9.1\times10^{-7}\,\mathrm{cm^2\,V^{-1}\,s^{-1}}$ [295–297].

Our calculated values are slightly greater than the largest of those values, which is not unexpected given that the model corresponds to vacancy migration in the perfectly periodic bulk of a single crystal, in the dilute limit.
A decomposition of the computed mobility values into relative contributions from each of the six sets of 1-NN SEPS, plotted in Figure 4-11a, shows that multiple sets contribute to the mobility in each of the principal directions. The overall effect is to produce a mobility tensor which is essentially isotropic. On the other hand, taking any *one* of the computed activation enthalpies, and calculating the mobility at 300 K simply via the Arrhenius equation and Einstein relation, leads to values which vary by two orders of magnitude, emphasising the importance of taking the connectivity of bromide sublattice into account.

4.7.2 Caesium Mobility

Similar to the case of the bromide mobility, also for the caesium mobility the principal axes of $\boldsymbol{\mu}$ are found to be parallel to the orthorhombic lattice vectors, with corresponding values of the mobility of 1.9×10^{-13}, 3.4×10^{-16} and $4.8 \times 10^{-15}\,\mathrm{cm^2\,V^{-1}\,s^{-1}}$, in the [100], [010] and [001] directions, respectively. No experimental data was found for cation mobility in LHPs, and hence we compare our computed values to experimentally observed diffusion coefficients D of MA migration in $MAPbI_3$ [256, 298–302], which we assume relate to the ionic mobilities μ through the well-known Einstein–Smoluchowski equation

$$D = \mu k_B T, \tag{4.9}$$

and for which we use a temperature of 300 K. The experimental values for the mobility thus obtained span a range of $4{\times}10^{-14}$–$8{\times}10^{-6}$ $\mathrm{cm^2\,V^{-1}\,s^{-1}}$. Our results are towards the lower end of this wide range of values. We note that many of the reported values are obtained from annealed samples, and in the subsequent chapters we show that the mobility of the A-site cation is particularly sensitive to the strain resulting from such annealing steps, such that the mobility can be increased by several orders of magnitude.
Again, a decomposition of the computed mobility values into relative contributions from each of the three sets of 1-NN SEPS, plotted in Figure 4-11b, shows that multiple sets contribute to the mobility only for mobility along [001]. The mobility along the apical [010] direction is dominated by the set of SEPS depicted in green, while the mobility along [100] is dominated by the set of SEPS depicted in blue. This makes sense intuitively, looking at the schematic representation of the connectivity of the caesium sublattice, shown in Figure 4-8. The lattice is fully connected along [010] by the set of SEPS depicted in green. The equatorial plane is spanned by the sets of SEPS depicted in blue and red. Along the

[001] direction, a hopping vacancy encounters transitions corresponding to either of these sets alternatively, leading to an almost equal 50% contribution to the mobility along this direction both sets of SEPS. The deviation from 50% is solely based on the difference in hopping distances. In contrast, the [100] direction is fully connected for both sets of SEPS in parallel 'highways'. In this case, the mobility is dominated by the set of SEPS with the lowest corresponding activation enthalpy, which is the set of SEPS depicted in blue.

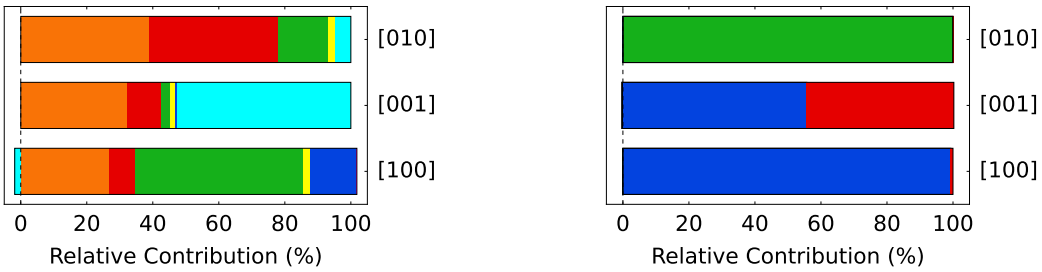

(a) Bromide mobility decomposition.

(b) Caesium mobility decomposition.

Figure 4-11: Decomposition of the mobility tensor in terms of the contribution of the individual sets of SEPS.

4.7.3 Sanity Checks

We have performed several checks along the way to verify the correct behaviour of our kinetic model. For example, we have verified the steady-state occupation probability vector, which we compute as the eigenvector of the rate matrix $\mathbf{Q}$ corresponding to an eigenvalue of zero, by comparing it to the steady-state occupation probability by explicitly solving the time-dependent master equation

$$\frac{d\vec{p}}{dt} = \mathbf{Q}\vec{p}. \tag{4.10}$$

To avoid the complication of the two symmetrically inequivalent sites in the bromide sublattice, we show the results for the occupation probability of the caesium sites for several representative states in Figure 4-12. The steady-state occupation probability derived from the eigenvector is shown as a dashed line at a value of 0.03125, which corresponds, as expected, to an equal distribution among the 32 states in our model. We find that the occupation probabilities of several representative states, shown by the coloured lines, indeed converge to the same value of 0.03125, suggesting that both approaches to obtain the steady-state occupation probability yield similar results.

To verify the correct behaviour also for the bromide states, we compute the equilibrium distribution, i.e. the steady-state occupation probability in the absence of a field, and find

that it equals the Boltzmann distribution based on the difference in total energy of the apical and equatorial sites.

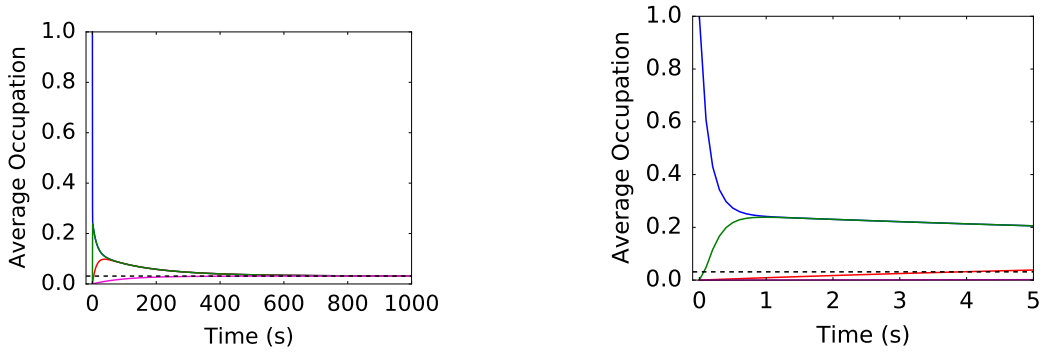

(a) (b)

Figure 4-12: Average occupation of a fully connected 2x2x2 supercell of Cs migration in the orthorhombic *Pnma* phase in the absence of an electric field. Dashed lines indicate the equilibrium occupation probability obtained via the eigenvector method, which yields an average occupation of all Cs sites.

To verify that our choice of applied potential is sufficiently low such that we compute the mobility tensor in the linear regime, we note that in general the drift velocity scales with

$$\vec{v}_d \propto \sinh\left(\frac{|z|eEd_i}{2k_BT}\right), \tag{4.11}$$

with $|z|$ the nominal charge of the moving ion, e the electron charge, E the field strength, d_i the displacement vector of the moving ion, k_B the Boltzmann constant and T the temperature [240, 241, 303]. For small enough fields, such that $|z|eEd_i \ll 2k_BT$, the term $\sinh x \approx x$, such that the drift velocity is linear with the field. We show the components of the bromide and caesium mobility tensors as a function of the applied potential in Figure 4-13, assuming a layer thickness of 500μm. In both cases, we find that the non-linearity becomes apparent at voltages around 100 V, which is much higher than the value of 1 V which we use to compute the mobility tensor, confirming that we are indeed probing the mobility in the linear regime.

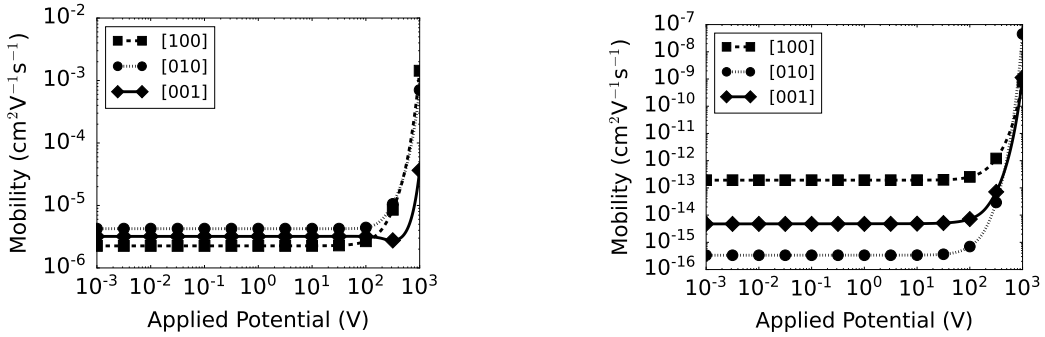

(a) Bromide Mobility

(b) Caesium Mobility

Figure 4-13: Components of the mobility tensor as a function of applied potential. For both bromide and caesium, the linear regime is probed up to an applied potential of about 100 V.

While developing the methodology, we have performed several other tests to verify correct behaviour of the kinetic scheme, to name a final few

- In the absence of a field, detailed balance is obeyed, i.e. $Q_{ji}p_i^0 = Q_{ij}p_j^0$.
- In the absence of a field, the drift velocities are zero, as are the components of the mobility tensor.
- We obtain the same drift velocity by explicitly applying a field along a generic direction, as we do from $\vec{v}_\mathrm{d} = \boldsymbol{\mu}\vec{E}$ when using the same field in combination with the mobility tensor obtained by applying fields along [100], [010], [001].
- By only including transitions into or out of a periodic supercell, and multiplying the cumulative transition rates with the supercell lattice vector, we are able to coarse grain the kinetic scheme and get identical drift velocities and mobility tensor components.

All of these tests resulted in the expected behaviour, which gives us confidence in the outcomes of the kinetic scheme. This list of tests is however not exhaustive, and more tests could be designed and performed to further verify its behaviour.

4.8 Conclusion

In this chapter, we have introduced the general methodology, which we previously summarised schematically in Figure 4-1, to compute the ionic mobility tensor using input from *ab initio* calculations. It is the main workhorse to obtain the results shown in Chapters 5 to 7. To reiterate our approach; we first relax the lattice vectors and internal coordinates of the unit cell of the orthorhombic structure under the strain constraints. We then generate a supercell with 320 atoms, and subsequently introduce vacancies in order to relax structures corresponding to the initial, final and transition states for ion vacancy transitions between symmetrically inequivalent pairs of sites. Together with the activation enthalpies thus obtained, the vibrational frequencies of the moving ion in these relaxed structures are then computed so as to derive the attempt frequencies. The results are then used as input to the rate matrix at the heart of our kinetic model. By applying fields along the three directions [100], [010] and [001] we are then able to compute the drift velocities in the steady-state, and from them derive the full mobility tensor.

By repeating these same steps for different strain states, we are then able to find trends in the mobility as a function of strain. We use the same methodology for each strain state in the remainder of this thesis. Specifically, we use the exact same parameters as described in this chapter in terms of cut-off energy and k-point mesh density. The only change we make is that for the studies on biaxial and uniaxial strain and for one set of SEPS in our study on hydrostatic pressure, the Hessian matrices from which the attempt frequencies of vacancy hopping were derived were calculated using finite displacements of 0.010 Å, in contrast to the value of 0.015 Å previously introduced. The reason for this is that we previously found that in some cases a reduction in the finite displacement resulted in a more consistent appearance of the imaginary mode at the transition state, whereas such a mode would sometimes appear absent for the higher finite displacement of 0.015 Å.

Chapter 5

Effect of Hydrostatic Pressure on Ionic Mobility

5.1 Introduction

In the following chapter, we take a first step in providing an understanding of the effects of strain on mass transport in LHPs. Arguably, the most unbiased means of inducing strain is through the application of hydrostatic pressure, which is typically exerted using a diamond anvil cell with the perovskite submerged in a pressure transmitting medium [51, 61, 152].
Though pressure is unlikely to be a viable approach to tune the properties of perovskite layers under operation, applying hydrostatic pressure does nevertheless provide an easily controllable and continuously tunable knob to alter the perovskite, and as such can yield useful insights into the general properties of perovskites under strain. Indeed, the effects of pressure on the electronic properties of LHPs have been the subject of a number of experimental studies [57, 58, 61, 304–308], and theoretical calculations have provided explanations for the observed behaviour in terms of the different modes of structural distortion, and their effects on inter-ionic bond lengths and bond angles [63–68].
However, despite a number of recent studies indicating that the ionic conductivity of LHPs is significantly affected by pressure [69, 70, 197], an atomistic understanding of the influence of strains, resulting from such stresses, on ionic migration in LHPs is largely lacking. Furthermore, for the *oxide* perovskites, it is well established that pressure modifies activation enthalpies for oxygen vacancy migration significantly [309, 310]. Given the soft nature of LHPs, such effects are likely to be at least as significant in these materials as in their oxide counterparts.

In this chapter, we present a quantitative analysis of the effects of hydrostatic (i.e. isotropic) pressure, as the simplest form of stress, on the migration of bromide and caesium vacancies in $CsPbBr_3$.

5.2 Structural Response

We now go on to examine the structural response of the pristine lattice to applied pressure. Hydrostatic pressure in the range 0.0–2.0 GPa was applied to the orthorhombic unit cell in steps of 0.4 GPa, and the lattice parameters and internal coordinates of the atoms were allowed to relax while the space group was constrained to *Pnma*. This range is consistent with the experimentally and computationally observed stability range of this phase [63, 64, 66, 123, 139] (we note that, while $CsPbBr_3$ has been reported to undergo a phase transition at 1.2 GPa, that phase transition is isostructural [63, 123]).

The evolution of the length of the lattice parameters as a function of pressure is shown in Figure 5-1. Despite the pressure being applied isotropically, the structural response is significantly anisotropic, such that the length of the $\mathbf{c}$ vector is reduced by approximately 10% at 2.0 GPa, in agreement with previous work [123]. In contrast, the lengths of $\mathbf{a}$ and $\mathbf{b}$ remain largely unaltered, increasing and decreasing by $\sim 1\%$ respectively.

Our computed values of the lengths of $\mathbf{a}$ and $\mathbf{b}$ replicate the experimentally measured values [123] almost perfectly. On the other hand, while the computed length of the $\mathbf{c}$ lattice vector follows a similar trend to what is observed experimentally, the values are consistently lower than the experimentally determined ones, with the difference increasing from 0.37 Å at 0.0 GPa to 0.58 Å at 2.0 GPa. Regarding the evolution of the unit cell volume, shown in Figure 5-1, we observe that the calculated values again follow the same general trend as the values determined experimentally, though our values are consistently lower by about 40 $Å^3$, due to the systematic difference in the length of $\mathbf{c}$.

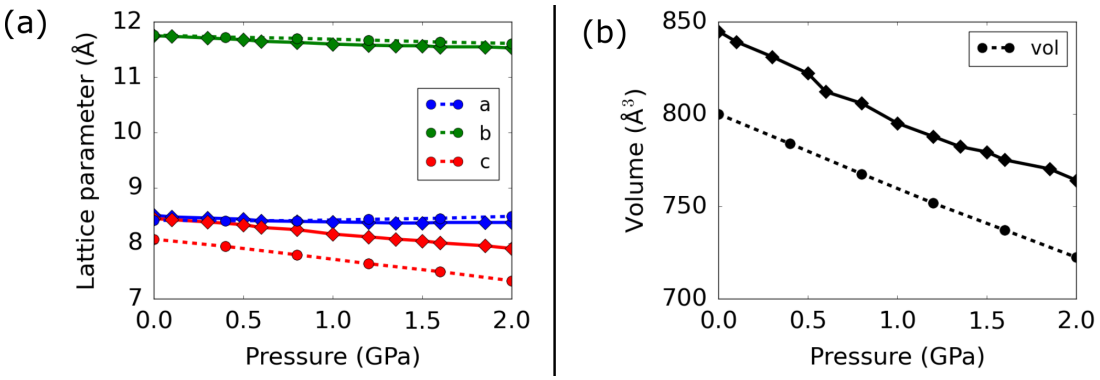

Figure 5-1: Comparison of the calculated (dashed lines) and experimental (solid lines; from Reference 123) values of (a) the lengths of the lattice vectors and (b) volume of the unit cell of $CsPbBr_3$ in the orthorhombic $Pnma$ phase under pressure.

5.2.1 Additional Set of SEPS

In addition to the change in lattice vectors, the coordinates of the ions within the unit cell are also altered significantly by the applied pressure. This effect is most obviously apparent as an increased octahedral tilting about the $[010]$ axis, leading to a structure observed and described in previous work as a 'squeezed wine-rack' [123]. This has important ramifications for the number of sets of SEPS we need to include in our study, as we argue below.

When identifying the sets of symmetrically equivalent pairs of sites (SEPS), a natural starting point is to consider pairs of sites that are connected by the octahedral edges, which we have previously described as first nearest neighbours (1-NN). To the best of our knowledge, we are not aware of any study considering vacancy hopping to sites beyond this shell of 1-NN. We note however that in principle halide pairs beyond this 1-NN set could also play a role in migration, which based on the interatomic distances can be grouped as second nearest neighbours (2-NN), third nearest neighbours (3-NN) and so on. A schematic representation of representative pairs of 1-NN, 2-NN and 3-NN sites is shown for the cubic phase with space group $Pm\bar{3}m$ in Figure 5-2. In principle, the number of sets of SEPS to consider can thus be extended indefinitely by including more and more distant pairs of sites. To limit the number of symmetrically inequivalent pairs of sites between which we need to consider hops, we now move on to analyse the intersite distance between these pairs of lattice sites. Though distance in itself is not a defining measure — the proximity and relative charge of other species in the structure are important parameters too — we assume that direct transitions between lattice sites with intersite distances beyond a certain cut-off distance are unlikely, either because the activation enthalpy is too large, or because such transitions can be decomposed in several transitions over shorter distances.

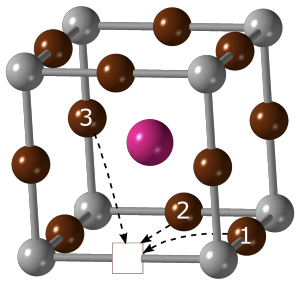

Figure 5-2: Schematic representation of the transition from a vacancy position to its first-, second- and third-nearest neighbours, represented by 1, 2 and 3, respectively.

In Figure 5-3a, the intersite distances for these SEPS in the $Pm\bar{3}m$ structure are shown, which correspond to the shells of first, second, third etc. nearest neighbours (1-NN, 2-NN, 3-NN etc.). The distances between SEPS in the orthorhombic *Pnma* structure at 0.0 GPa and 2.0 GPa are shown in Figure 5-3b and c, and we maintain the same nomenclature (1-NN, 2-NN, etc.) and colour scheme as for the $Pm\bar{3}m$ phase in order to group them, despite the fact that the distances between pairs within each group are no longer all the same and cover a range of values due to the lower symmetry of the structure. We note that the distances vary smoothly between 0.0 and 2.0 GPa, and so we do not show those corresponding to intermediate pressures.

As a result of the severe octahedral tilting, there is thus a significant reduction in the distance between particular SEPS belonging to neighbouring octahedra, which are connected by magenta sticks in Figure 5-4, such that it approaches the range of distances between the 1-NN SEPS that are connected by the edges of the octahedra. As will be shown below, hops between SEPS in this particular set contribute significantly to the anion vacancy mobility as the pressure is increased. The activation enthalpies for a number of other sets of SEPS, labeled by '10' in Figure 5-3, were also calculated, but their contributions to the mobility are negligible at all values of pressure considered. We note that the pairs of '2-NN' sites with distances of ~ 6.0 Å correspond to opposite vertices of an octahedron, and as a result direct transitions between these two sites are assumed to be blocked by the Pb at the centre of the octahedron. We thus effectively use a cut-off distance of about 6.0 Å, above which we assume hops to either have activation enthalpy that is too large, or can be decomposed in several hops over shorter distances. Looking at Figure 5-3, this creates a natural division in terms of intersite distances.

Visual representations of the 10 sets of SEPS are shown in Figures 5-5 and 5-6 for the $Pnma$ structures at 0.0 and 2.0 GPa, along with the corresponding sets of SEPS in the $Pm\bar{3}m$ structure for clarity.

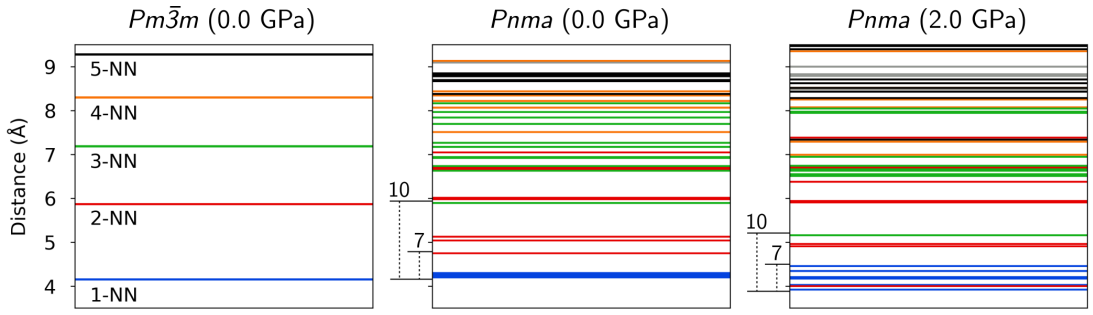

Figure 5-3: Distances between symmetrically equivalent pairs of sites (SEPS) in the bromide sublattice of cubic *Pm*$\bar{3}$*m* structure at 0.0 GPa, and the orthorhombic $Pnma$ structure at 0.0 GPa and 2.0 GPa. The distance between pairs in the first five nearest neighbour (labelled 1-NN, 2-NN, etc.) shells in the cubic structure are shown as blue, red, green, orange and black lines respectively. The colour scheme is used for pairs in the orthorhombic structure to indicate the equivalence between pairs in the two structures, with further separated shells coloured grey. The label '10' to the left of the distance axis of the two plots for the orthorhombic structure indicates the 10 sets of SEPS for which activation enthalpies were calculated, while the label '7' indicates the 7 sets that were included in the kinetic scheme. The remaining 3 sets were shown to have a negligible effect on the mobility, as discussed in more detail in Section 5.4.1.

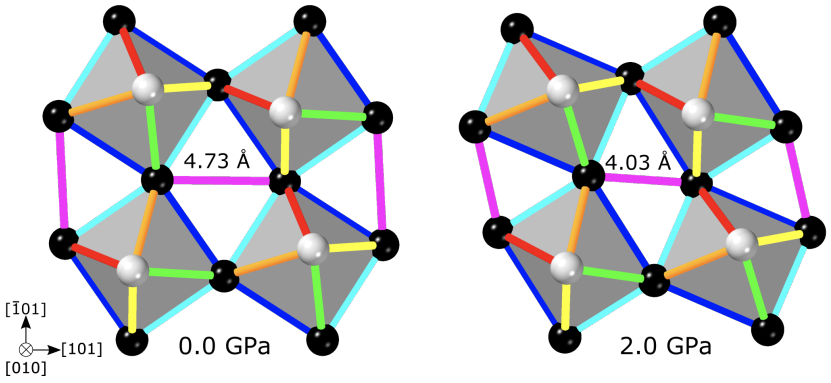

Figure 5-4: Structure of the *Pnma* phase of $CsPbBr_3$ at 0.0 GPa (left) and at 2.0 GPa (right). The distance between the pairs of bromide sites joined by magenta sticks is significantly reduced as the pressure is increased.

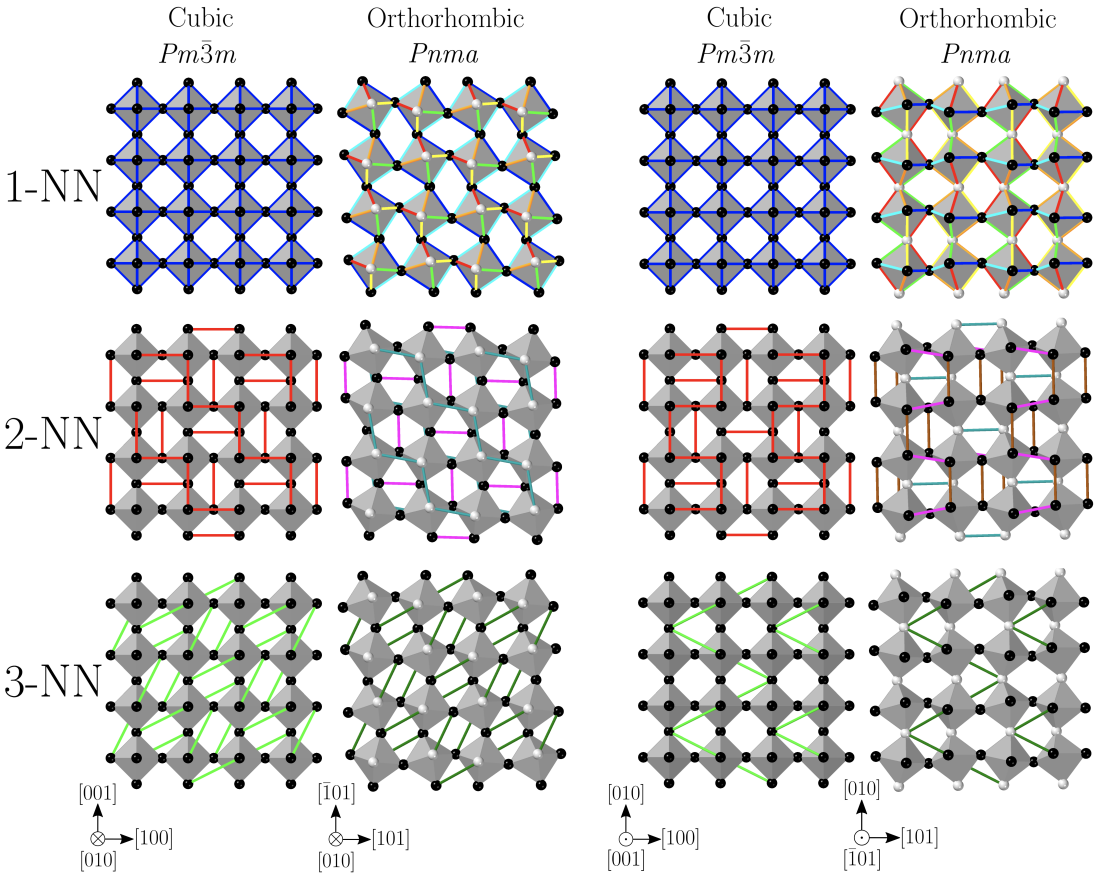

Figure 5-5: Visual representation of the sets of SEPS in the cubic $Pm\bar{3}m$ structure (columns 1 and 3) and the orthorhombic *Pnma* structure at 0.0 GPa (columns 2 and 4) of $CsPbBr_3$. The first, second and third row correspond to the 1-NN, 2-NN and 3-NN sets of SEPS, respectively, of the cubic structure. For every pair of figures (columns 1 and 2, and 3 and 4), which correspond to two perspectives of the structures (as indicated by the axes in the bottom left hand corners), the sets of SEPS are shown for the cubic $Pm\bar{3}m$ to the left, with the sticks joining the SEPS given the same colours as used in Figure 5-3a, and the corresponding sets of SEPS for the *Pnma* phase to the right. Column 2 shows the projection along the (long) [010] direction, whereas column 4 shows a projection with [010] pointing up the page, clearly showing the mirror symmetry about the bromide ions on the apical sites, which are shown as white spheres. The bromide ions at the equatorial sites are shown as black spheres.

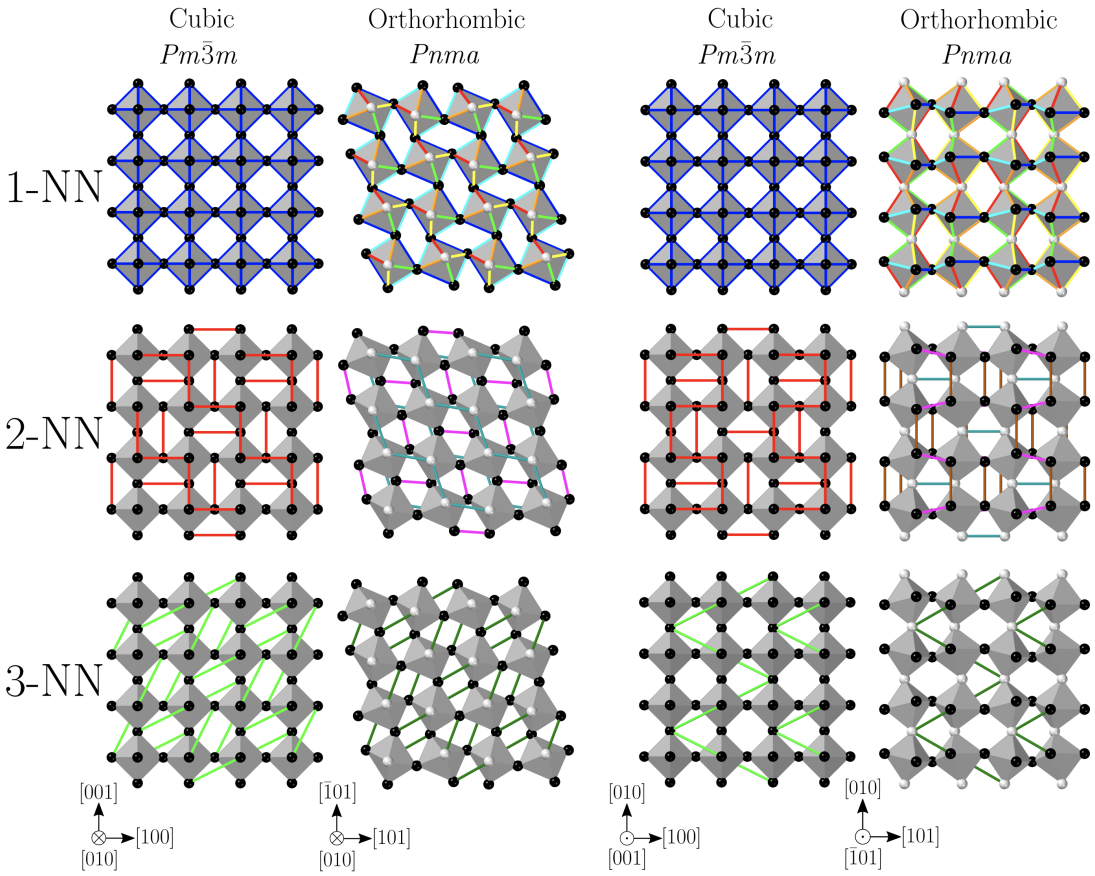

Figure 5-6: Visual representation of the sets of SEPS in the cubic $Pm\bar{3}m$ structure (columns 1 and 3) and the orthorhombic *Pnma* structure at 2.0 GPa (columns 2 and 4) of $CsPbBr_3$. The first, second and third row correspond to the 1-NN, 2-NN and 3-NN sets of SEPS, respectively, of the cubic structure. For every pair of figures (columns 1 and 2, and 3 and 4), which correspond to two perspectives of the structures (as indicated by the axes in the bottom left hand corners), the sets of SEPS are shown for the cubic $Pm\bar{3}m$ to the left, with the sticks joining the SEPS given the same colours as used in Figure 5-3a, and the corresponding sets of SEPS for the *Pnma* phase to the right. Column 2 shows the projection along the (long) [010] direction, whereas column 4 shows a projection with [010] pointing up the page, clearly showing the mirror symmetry about the bromide ions on the apical sites, which are shown as white spheres. The bromide ions at the equatorial sites are shown as black spheres.

5.3 Anion Vacancy Migration under Hydrostatic Pressure

The activation energies for transitions between the pairs of sites belonging to the 10 sets of SEPS with the shortest distance between pairs, indicated by the '10' labels in Figure 5-3b and c, in the *Pnma* structure are shown in Figure 5-7. The enthalpy profiles of the optimised paths from which they are derived are shown in Figure 5-8. We note that because of the two symmetrically inequivalent (viz. apical and equatorial) halide sites, the profiles for the apical-to-equatorial (A-to-E) paths differ from those for the equatorial-to-apical (E-to-A) paths by the difference in formation enthalpy of a vacancy at the two sites. The profiles for the A-to-E transitions are shown relative to the formation enthalpy of the vacancy at the apical site, at a normalised reaction coordinate value of 0. For the apical-to-apical (A-to-A) and equatorial-to-equatorial (E-to-E) profiles, the enthalpies are shown relative to the formation enthalpy of the vacancy at the apical and equatorial sites, respectively.

While most activation enthalpies increase with pressure, those corresponding to transitions in two E–E sets of SEPS, namely one in which the initial and final sites are members of the same octahedron (connected by cyan sticks in Figures 5-5 and 5-6), and one in which the the initial and final belong to neighbouring octahedra (connected by magenta sticks in Figures 5-5 and 5-6), decrease such that they are significantly lower at 2.0 GPa than any other, having values of 0.16–0.17 eV. We observe that the activation enthalpies for hops associated with the 2-NN and 3-NN sets of SEPS are generally higher than those for hops for the 1-NN sets of SEPS, with the exception of the 2-NN_E-to-E_1 set of SEPS, indicated by a magenta stick in Figures 5-5 and 5-6. Therefore, only the six 1-NN sets of SEPS and the one 2-NN_E-to-E_1 set of SEPS are included in the kinetic scheme. We show the convergence of our results with respect to the number of included sets of SEPS in Section 5.4.1.

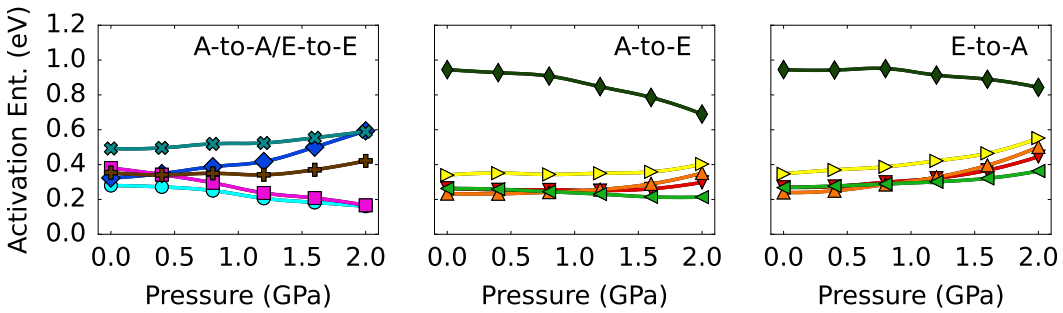

Figure 5-7: Activation enthalpies of vacancy migration under pressure for hopping between the apical-to-apical/equatorial-to-equatorial (A-to-A/E-to-E), apical-to-equatorial (A-to-E) and equatorial-to-apical (E-to-A) SEPS that are included in the kinetic scheme.

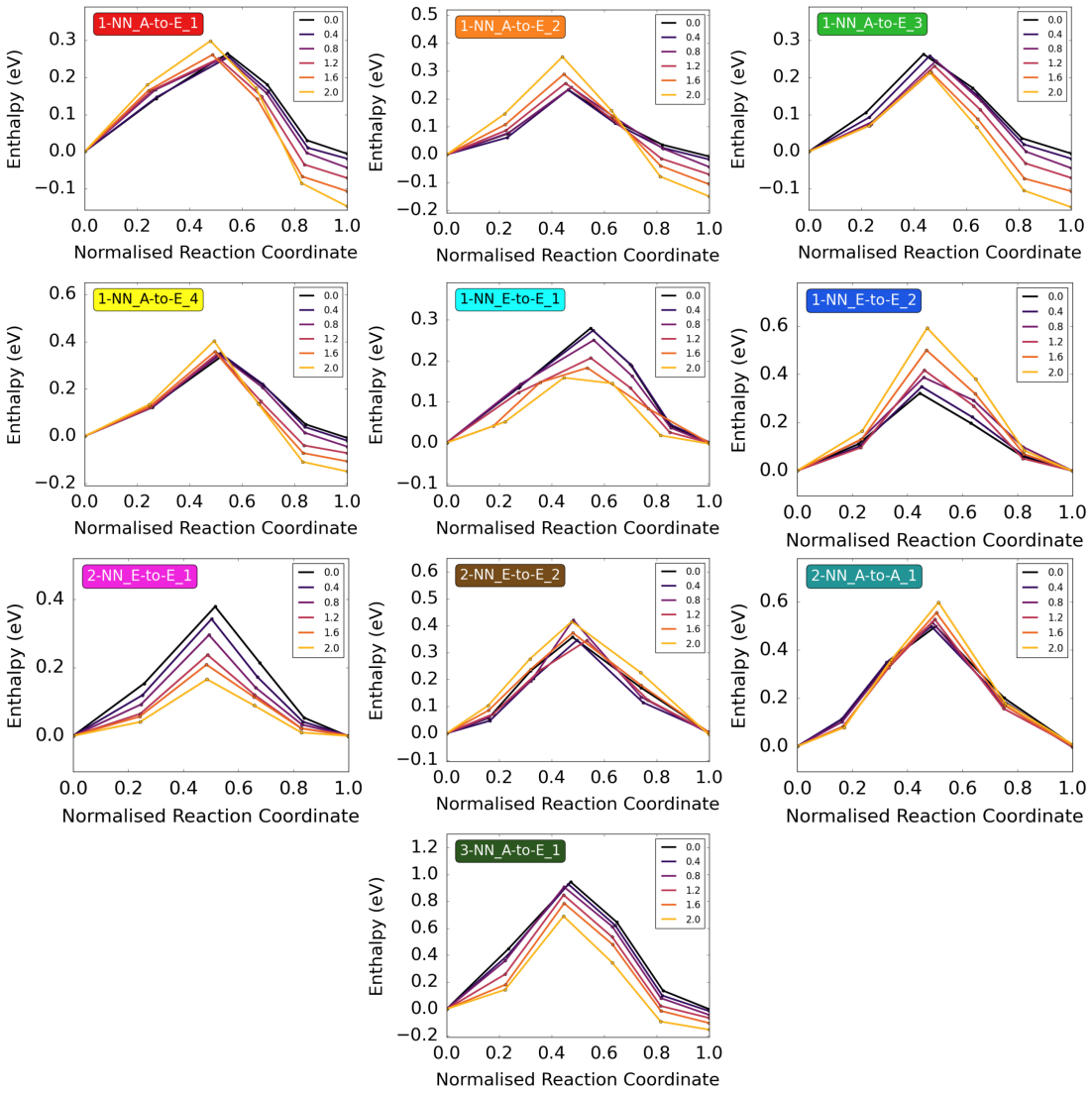

Figure 5-8: Minimum enthalpy paths for a positively charged bromide vacancy to move between members of the 10 sets of SEPS at pressures up to 2.0 GPa. The colours of the title boxes correspond to the colours of the sticks in Figures 5-5 and 5-6.

5.3.1 Convergence of the Activation Enthalpies

To check the convergence of the activation enthalpies, we compare the computed activation energies from different XC-functionals, different supercell sizes and different calculation methods. First, we compare the activation energies as computed using either the PBEsol (black/dashed lines) or SCAN (colour/full lines) XC-functionals, the results of which are shown in Figure 5-9. We find that the differences are relatively small, meaning that the results we obtain are not the result of exotic behaviour of the SCAN XC-functional, but rather a genuine representation of the response to hydrostatic pressure.

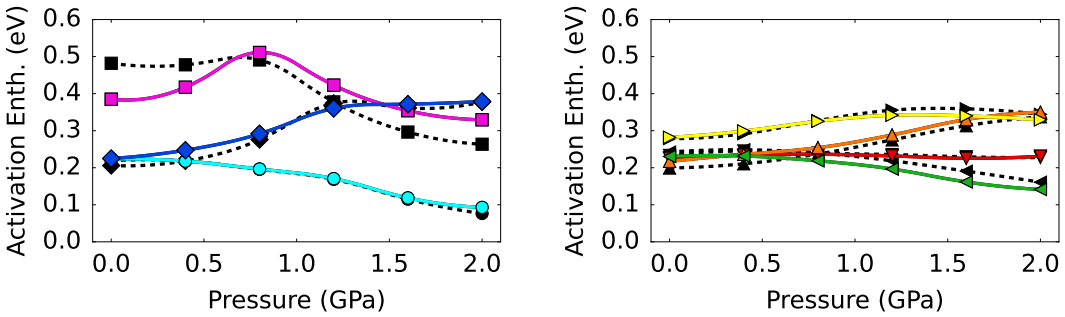

(a) E-to-E

(b) A-to-E

Figure 5-9: Comparison of the activation enthalpies of the different sets of SEPS using either the PBEsol (black/dashed) and the SCAN (colour/full) XC-functionals. Activation enthalpies obtained from NEB calculations, using a fairly small supercell containing only 40 atoms.

We also compare the results arising from a change in supercell size. In particular, we compare the activation enthalpies obtained for supercells with 40 (black/dashed lines) and 320 (coloured/full lines) atoms. The 40-atom cell is generated using a [[1,0,1],[0,1,0],[-1,0,1]] supercell of the orthorhombic unit cell with space group $Pnma$. The 320-atom cell is a factor of two larger in all three directions, corresponding to a [[2,0,2],[0,2,0],[-2,0,2]] supercell. The activation energies obtained using either of these two cells are shown in Figure 5-10. We observe that the differences between the two cells are quite large. It should be kept in mind that the use of supercells implies a periodic array of defects, resulting in artificial interactions between the defects [203]. As a result, we consider the activation enthalpies obtained using the larger cell, for which these interactions are reduced, to be more accurate.

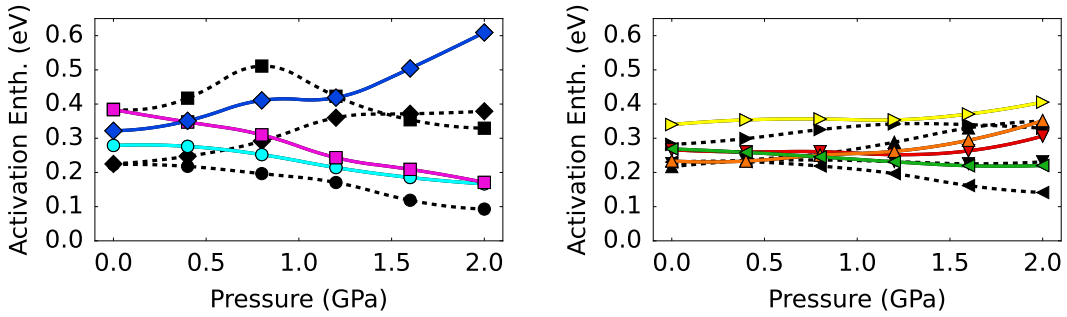

(a) E-to-E (b) A-to-E

Figure 5-10: Comparison of the activation enthalpies of the different sets of SEPS using a supercell with 40 atoms (black/dashed) and one with 320 atoms (colour/full). Activation enthalpies obtained from NEB calculations, using the SCAN XC-functional.

Finally, we compare the activation enthalpies obtained using the CI-NEB (black/dashed lines) and dimer (colour/full lines) methods, the results of which are shown in Figure 5-11. We observe only very small differences between the two methods, with the results from the dimer method appearing slightly smoother. As such, either approach is expected to give reliable results and in the subsequent studies on biaxial and uniaxial strain, the transition states are optimised using only the dimer method.

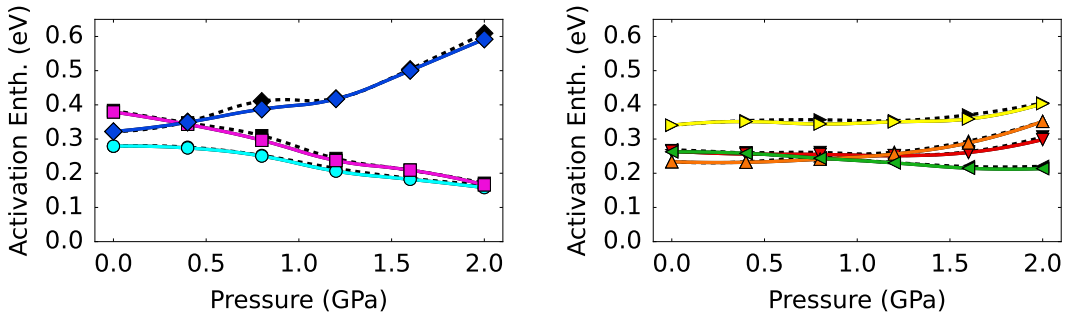

(a) E-to-E (b) A-to-E

Figure 5-11: Comparison of the activation enthalpies of the different sets of SEPS using the CI-NEB approach (black/dashed) or the dimer approach (colour/full). Activation enthalpies obtained using the SCAN XC-functional, for supercells with 320 atoms.

5.3.2 Attempt Frequencies for Bromide Vacancy Hops

The attempt frequencies for bromide vacancy hops between pairs of sites included in the kinetic scheme are derived from the vibrational frequencies of the initial and transition state structures, as expressed in Equation (4.4). The vibrational frequencies are computed using Hessian matrices that were calculated using finite displacements of 0.015 Å. There is only one set of SEPS for which we make an exception, specifically the 2-NN_E-to-E_2 set of SEPS indicated by a brown stick in Figures 5-5 and 5-6, and for which we use smaller finite displacements since no imaginary mode was observed for the transition state when using finite displacements of 0.015 Å at some of the pressures. Specifically, finite displacements of 0.005 Å were used for pressures of 0.4 and 0.8 GPa, finite displacements of 0.010 Å were used for pressures of 0.0 and 2.0 GPa, and finite displacements of 0.015 Å were used for pressures of 1.2 and 1.6 GPa. Since these prefactors only have a small influence on the mobility, compared to the exponential dependence on the activation enthalpy, this inconsistency is unlikely to lead to significant errors. Nonetheless, a more thorough analysis of the convergence of the prefactors is an important avenue left for future studies. In subsequent studies of the effects of biaxial and uniaxial strain, we compute the vibrational frequencies using Hessian matrices that are calculated using finite displacements of 0.010 Å.
The values corresponding to each of the 10 sets of SEPS included in the kinetic scheme are shown in Figure 5-12. As can be seen, the values do not vary smoothly with pressure, which we attribute to numerical noise. Therefore, the values for each set of SEPS are averaged over the pressure range, and these average values, indicated by the solid lines, are used as the attempt frequency values in the kinetic scheme for all values of pressure.

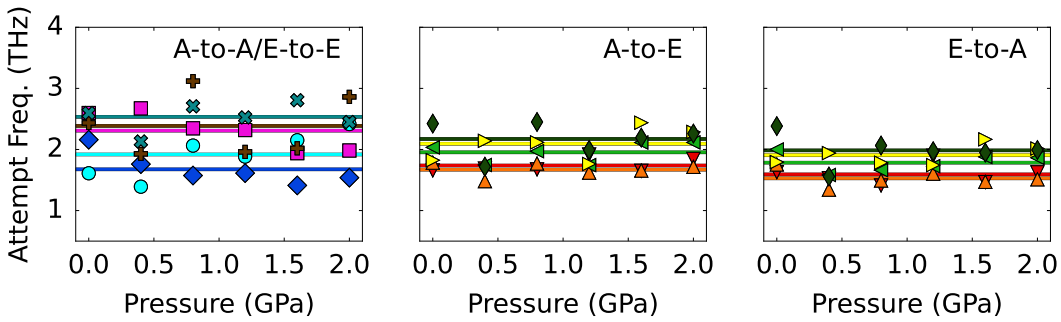

Figure 5-12: Attempt frequencies of vacancy migration under pressure for hopping between the apical-to-apical/equatorial-to-equatorial (A-to-A/E-to-E), apical-to-equatorial (A-to-E) and equatorial-to-apical (E-to-A) SEPS that are included in the kinetic scheme.

5.3.3 Mobility

We then use the kinetic scheme to compute the mobility tensor as a function of pressure, using the transition states structures, activation enthalpies and attempt frequencies for vacancy hopping calculated for each value of pressure in the range 0.0–2.0 GPa. While the eigenvectors of the mobility tensor remain parallel to the crystalline lattice vectors, the relative magnitudes of their eigenvalues change dramatically with increasing pressure as shown in Figure 5-13a. The pressure dependence is such that at 2.0 GPa, the mobility in the (010) plane is approximately three orders of magnitude greater than the mobility in the direction normal to it (i.e. parallel to $[010]$), leading to an effective 3D-to-2D transition of the mobility. A decomposition of the diagonal components of the mobility tensor in terms of the contributions of the different sets of SEPS shows that migration at 2.0 GPa is predominantly due to hops between SEPS connected by the cyan and magenta sticks in Figure 5-13b, for which the activation enthalpies are significantly decreased at elevated pressures.

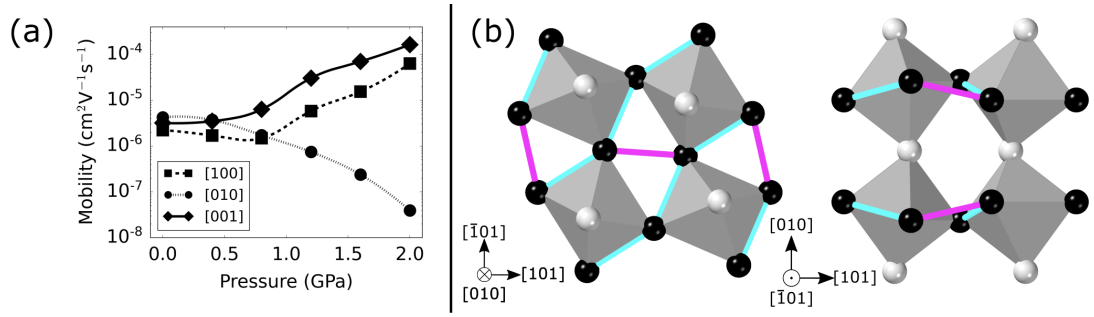

Figure 5-13: (a): Dependence on pressure of the diagonal components of the mobility tensor calculated using the kinetic model incorporating seven sets of SEPS. (b): Structure of the *Pnma* phase of $CsPbBr_3$, at 2.0 GPa, shown from two different perspectives. The two sets of SEPS which make the overwhelmingly major contribution to the mobility at 2.0 GPa are connected by coloured sticks. The colour scheme is the same as that of Figures 5-5 and 5-6.

5.4 Additional Analysis

5.4.1 Convergence of the Mobility Tensor with Respect to the Number of Paths

We now show the convergence with respect to the number of paths. Because of the higher activation enthalpies, the inclusion of these additional sets of SEPS in our kinetic model

is not expected to change the mobility tensor. To verify this, we compare the computed values for the mobility tensor using either 6, 7 or 10 sets of SEPS. To reiterate, the six sets correspond to the 1-NN sets of SEPS, while the seventh set corresponds to the set of 2-NN SEPS connected by magenta sticks in Figures 5-5 and 5-6. Finally, the group of 10 sets also includes the additional two sets of 2-NN SEPS and the set of 3-NN SEPS we have included in our previous analyses of the activation enthalpies and prefactors. The computed mobility tensor components are shown in Figure 5-14. We observe that the addition of the seventh set of SEPS is criticial; in its absence we observe that the mobility in the [100] direction is orders of magnitude lower at high pressures, resulting in an effective 3D-to-1D transition, instead of the 3D-to-2D transition we observe when including seven sets of SEPS. In contrast, we observe that the components of the mobility tensor remain largely unaltered when including all 10 sets of SEPS, such that the results are indeed well-converged upon the inclusion of the 7 sets of SEPS.

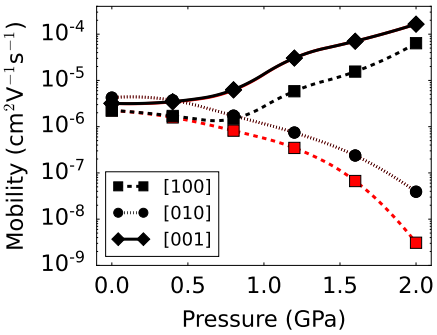

(a) Comparison between 6 (red) and 7 (black) sets of SEPS.

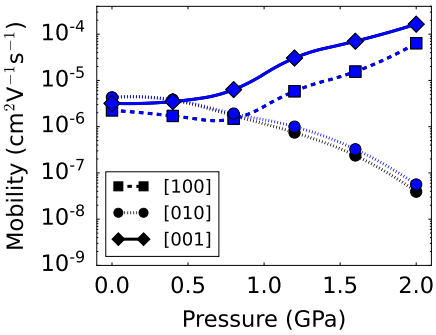

(b) Comparison between 7 (black) and 10 (blue) sets of SEPS.

Figure 5-14: Comparison of the components of the mobility tensor under hydrostatic pressure, when including either 6 (red), 7 (black) or 10 (blue) sets of SEPS.

Interestingly, we can check our results by reverse engineering an effective activation energy, which can be derived from the mobility μ using the following expression

$$\mu = \frac{\nu a^2 e^{-E_a/k_B T}}{k_B T}, \tag{5.1}$$

which gives an estimate of μ based on the attempt frequency ν, activation enthalpy E_a and hopping distance a, assuming that such a hop is representative for an isotropic mobility in all three directions [222]. Using an attempt frequency of 2 THz and a hopping distance of 4.2 Å, we derive the effective activation energies as a function of hydrostatic pressure, the results of which are shown in Figure 5-15. We find that the effective activation energies are close to the lowest activation energy in any given direction, giving further credibility to our approach.

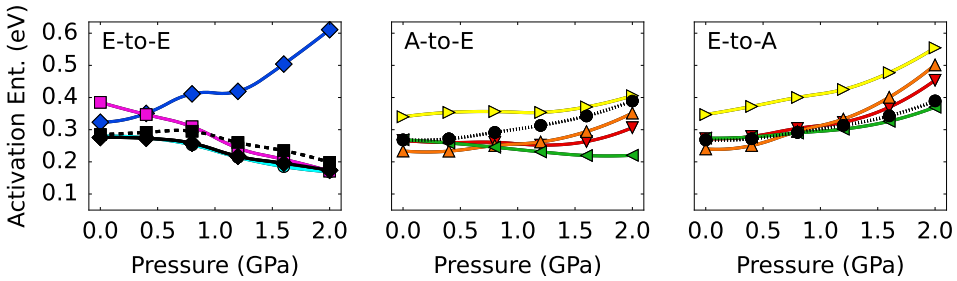

Figure 5-15: We compute the 'effective' activation energies in all three directions from the Arrhenius expression of the mobility, and find that interestingly, these align very well with the lowest energy barriers in all three directions.

5.4.2 Effective Dipole Approaches

In general, we wish to compute the work (W) done when charged ions move under the influence of an electric field $\vec{E}$: $W = \vec{\mu}_{\text{eff}} \cdot \vec{E}$. In the development of our methodology, we have included this so-called effective dipole $\vec{\mu}_{\text{eff}}$ as the difference between the position vector of the moving anion in the transition state, and the position vector of the same anion in the initial state, multiplied by its charge q, as described in Equation (4.6). We have however tested other methods to include W, which we discuss below.

In their seminal work, Mott and Gurney laid the foundation for a description of the effect of an electric field on the activation energy for ionic motion in a crystal lattice [240]. For an ion moving perpendicular to the field, the activation energies are unaltered. In the direction of the field however, they express the change in activation energy as $\pm\frac{1}{2}eFa$, in which e is the elementary charge, F is the strength of the electric field and a is the distance between adjacent lattice sites, such that the effective dipole can be described as $\vec{\mu}_{\text{eff}} = \frac{qd}{2}$. In this approach, it is thus assumed that at the transition state the moving ion is exactly halfway in between the two lattice sites between which it hops. A schematic description of this process is shown schematically in Figure 5-16. This approach is denoted as method 1 in the remainder of this work.

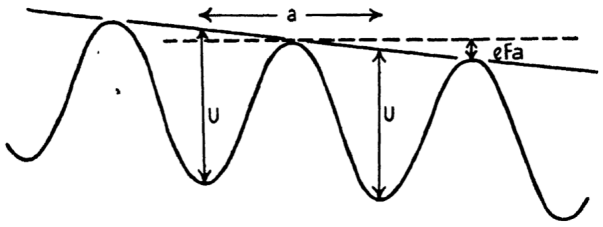

Figure 5-16: The change in the height of the potential energy barrier for the motion of ions between lattice sites, as originaly postulated by Mott and Gurney [240].

A natural extension of the model removes the assumption that at the transition state the moving ion is exactly halfway in between the lattice sites, but rather derives the position of the moving ion from atomistic simulations. The effective dipole can in such cases be expressed as

$$\vec{\mu}_{\text{eff}} = q\left(\vec{r}_{\text{s}} - \vec{r}_{\text{i}}\right),$$

in which q is the charge of the moving ion, and $\vec{r}_{\text{s,i}}$ denote the position of the moving ion at the transition and initial state, respectively. Effectively, the term $\frac{d}{2}$ has thus been replaced with $(\vec{r}_{\text{s}} - \vec{r}_{\text{i}})$. In this approach, which we denote as method 2, the moving charge is considered equal to the formal charge of the ion and thus takes on integer values [294]. Going from the initial state to the transition state however, the moving ion will generally

displace other atoms in its vicinity. Therefore, instead of considering just the moving ion, the displacement of all other atoms between the initial and transition state can also be computed and included, such that the effective dipole can be described as

$$\vec{\mu}_{\mathrm{eff}} = \sum_{n} q_{\mathrm{n}} \left(\vec{r}_{\mathrm{n,s}} - \vec{r}_{\mathrm{n,i}} \right),$$

again taking the formal charges q_{n} for each of the atoms in the simulation cell. We denote this as method 3 in the remainder of this sectiion.

Finally, we can consider not only the movement of ions as point charges, but rather take into account effects from changes in the corresponding electron density and compute the change in the polarisation between the initial and transition state. Though this approach is fairly straightforward for finite systems such as molecules, it has only been formalised for periodic systems some 30 years ago [311–313], the reason being that the absolute value of the polarisation is not well-defined and depends on the choice of unit cell. An excellent entry-level explanation of this formalism, named the Modern Theory of Polarisation, is given in Reference 314. In summary, the polarisation of a periodic system is a lattice, rather than a single value, such that equally valid values of the polarisation of a certain system differ by integer values of the so-called polarisation quanta $P_{\mathrm{Q,n}}$, which can be derived from

$$P_{\mathrm{Q,n}} = \frac{1}{\Omega} e R_{\mathrm{n}},$$

in which e is the elementary charge, Ω is the volume of the unit cell, and R_{n} is the nth lattice vector of the unit cell. Though the absolute value of the polarisation in a periodic system is thus ill-defined, polarisation *differences* are well-defined and independent of the choice of unit cell, as long as the same choice of unit cell and basis is maintained throughout the analysis. More strictly, the change in polarization along an arbitrary path does not depend on the path taken but can be derived from only a knowledge of the system at the initial, transition and final state. Computationally, the expression for the polarisation is equivalent to that of the Berry Phase, which is readily calculated in most *ab initio* DFT software packages, including VASP. Hence, the difference in polarisation going from the initial to the transition state can be expressed as

$$\vec{\mu}_{\mathrm{eff}} = \vec{\mu}_{\mathrm{s}} - \vec{\mu}_{\mathrm{i}},$$

in which $\vec{\mu}_{\mathrm{s,i}}$ describes the polarisation in the transition and initial states. To ensure that the polarisation values in both cases exist on the same polarisation branch - that is, they do not differ by integer values of the polarisation quanta - the polarisation can be computed for several intermediate structures as well, in which case the difference in polarisation between

subsequent structures should be much smaller than any of the polarisation quanta and if done correctly, the polarisation should change smoothly along an arbitrary path.
An example calculation of the polarisation along the minimum enthalpy path as computed using method 4 is shown in Figure 5-17, and shows that the polarisation changes along the path are smooth, which indicates that the values are on the same polarisation branch; the changes along the path are much smaller than the polarisation quanta, which are 16 eÅ.

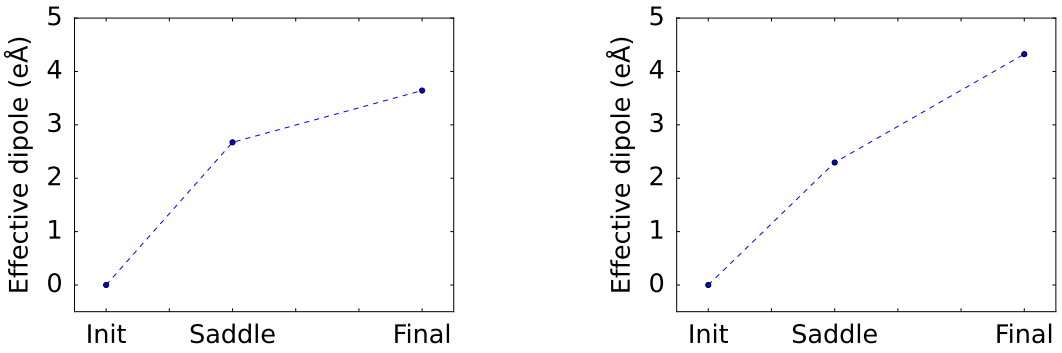

(a) 0.0 GPa (b) 2.0 GPa

Figure 5-17: Change in the effective dipole as computed from the change in the Berry phase along the minimum enthalpy path associated with the 1-NN_E-to-E_2 set of SEPS.

In the discussion of all four of these methods we have implicitly assumed sufficiently low fields, such that the effective dipole can be assumed to be constant as a function of the electric field. For high electric fields however, other methods should be considered [241,303].
In summary, we discussed the following methods:

Method 1: The original Mott and Guerney approach: $\vec{\mu}_{\mathrm{eff}} = \frac{qd}{2}$

Method 2: From atomistic calculations, in the moving-ion approximation: $\vec{\mu}_{\mathrm{eff}} = q\left(\vec{r}_{\mathrm{s}} - \vec{r}_{\mathrm{i}}\right)$

Method 3: From atomistic calculations, including all ions: $\vec{\mu}_{\mathrm{eff}} = \sum_n q_{\mathrm{n}}\left(\vec{r}_{\mathrm{n,s}} - \vec{r}_{\mathrm{n,i}}\right)$

Method 4: Within the modern theory of polarisation, from the change in the Berry phase: $\vec{\mu}_{\mathrm{eff}} = \vec{\mu}_{\mathrm{s}} - \vec{\mu}_{\mathrm{i}}$

The effective dipoles, computed using methods 1, 2, 3 and 4, for the 10 different sets of SEPS are shown in Figure 5-18. The results from method 1 do not give us any information on the anisotropy of the ionic displacement during a hop, and are thus less informative than either of those obtained from the other three methods. Clearly, the effective dipoles obtained from method 4 are much less smooth than those computed using methods 2 and 3. In some cases, such as shown in Figure 5-18f, the polarisation difference even swaps

sign as a function of the hydrostatic pressure. Effectively, this corresponds to a reverse in the direction of ion migration, which does not seem physical. Though the reason for this is not entirely clear, the apparent noise could result from noise in the electronic contribution. Hence, we have decided not to include these results in our kinetic model.

The differences between the results from methods 2 and 3 are relatively small, which means that the effect of the electric field on the migration can be captured sufficiently well using just a description of the moving ion. This enables a direct calculation of the attempt frequency, which is only computationally reasonable in the moving-ion approximation. In conclusion, method 2 is thus most computationally efficient, yet reliable.

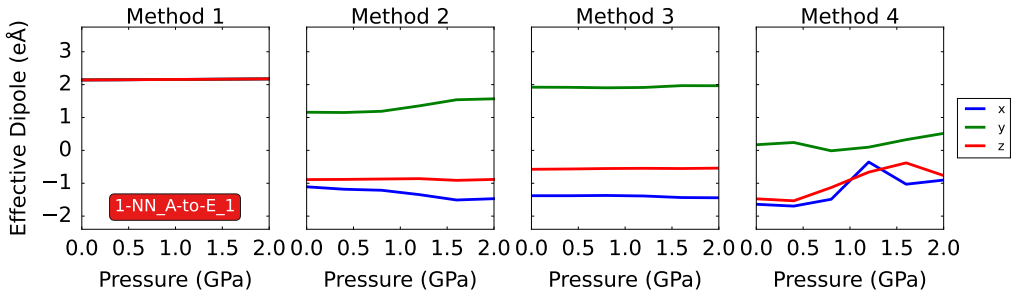

(a) 1-NN_A-to-E_1

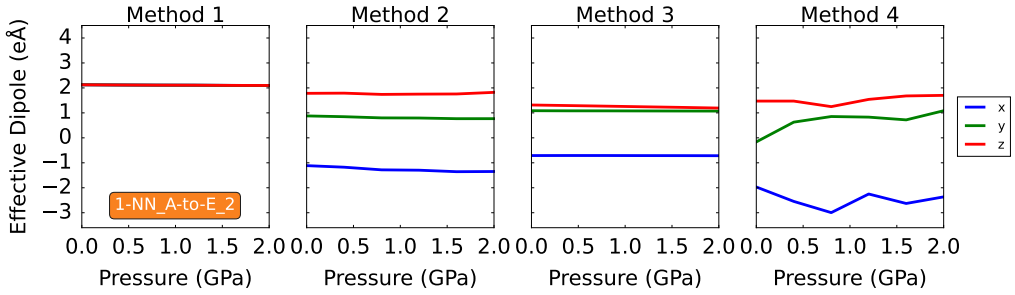

(b) 1-NN_A-to-E_2

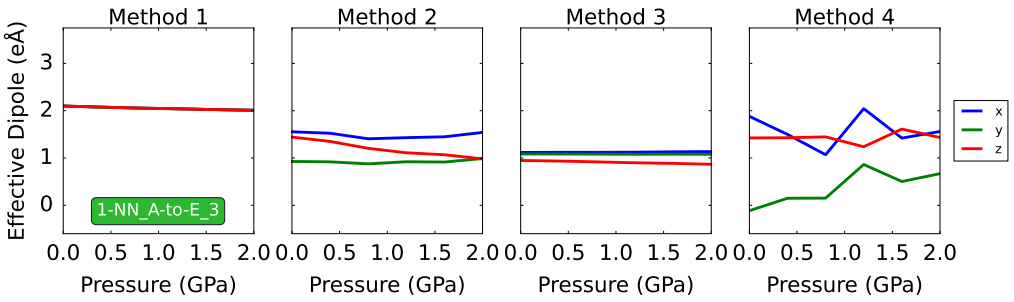

(c) 1-NN_A-to-E_3

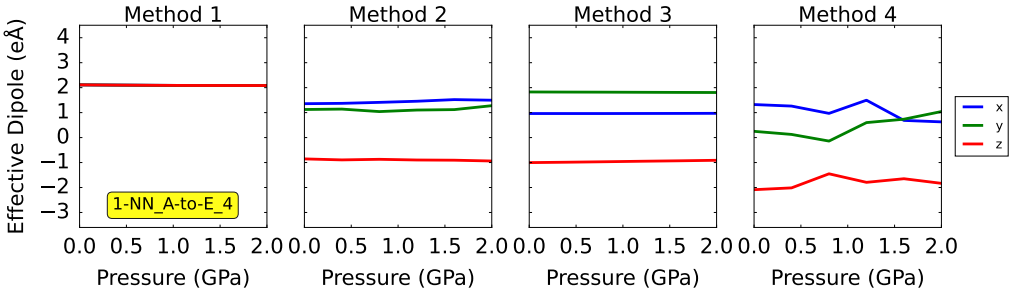

(d) 1-NN_A-to-E_4

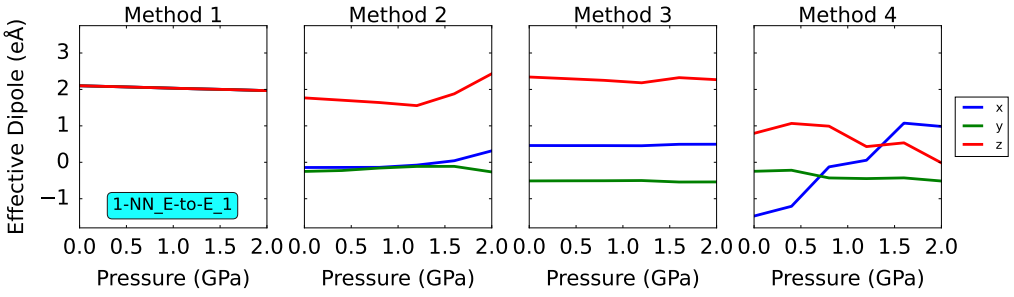

(e) 1-NN_E-to-E_1

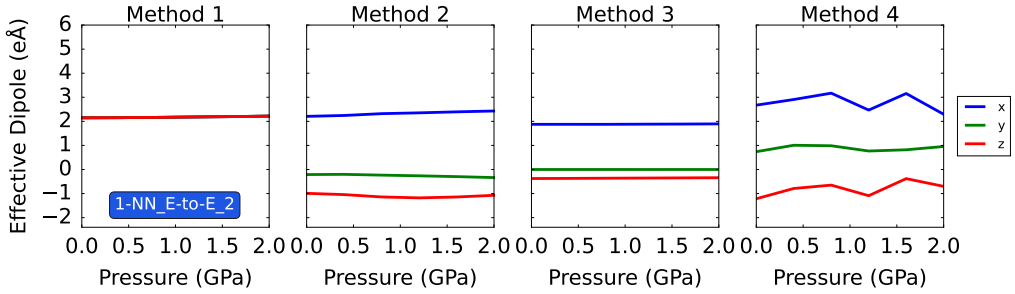

(f) 1-NN_E-to-E_2

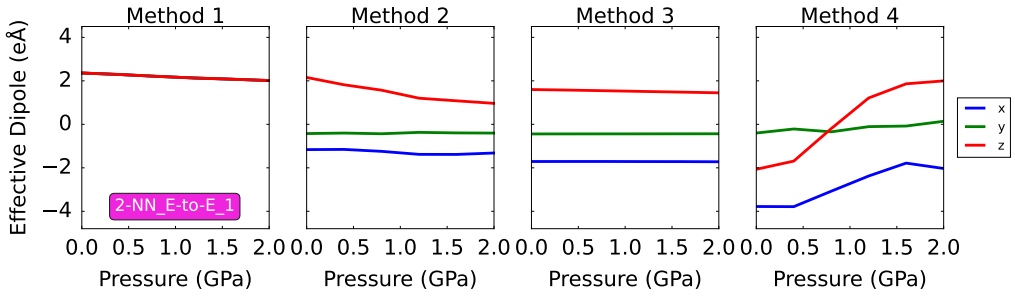

(g) 2-NN_E-to-E_1

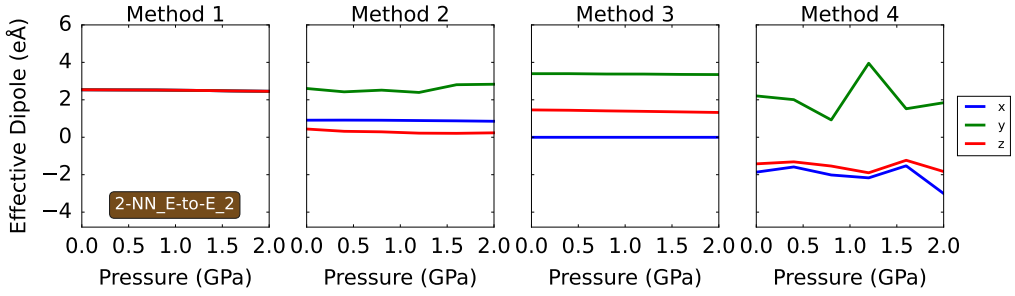

(h) 2-NN_E-to-E_2

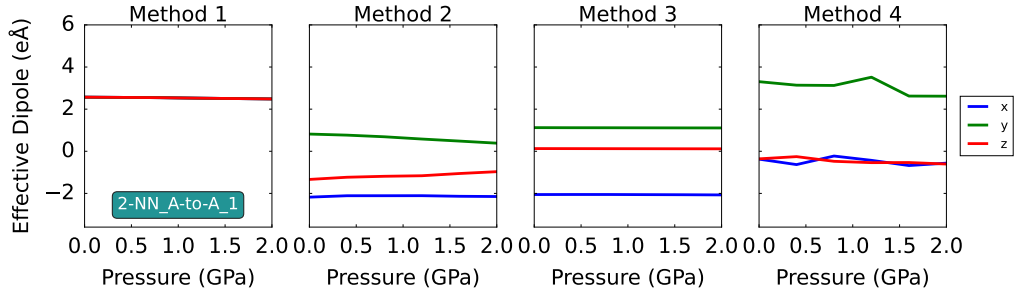

(i) 2-NN_A-to-A_1

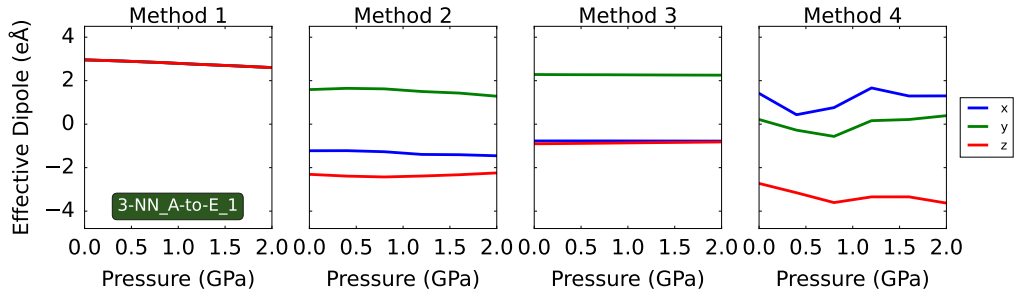

(j) 3-NN_A-to-E_1

Figure 5-18: Density functional theory calculations of the change in the effective dipole associated with the transition of the vacancy structure from the local minimum to the transition state for the different sets of SEPS as a function of hydrostatic pressure. In the left panel the effective dipole is shown as calculated in the moving ion approximation, in the middle panel the computed effective dipole is shown as calculated from the displacement of all ions between the initial and transition state, in the right panel the effective dipole is shown as calculated from the change in the Berry phase, corresponding to methods 2, 3 and 4, respectively.

5.5 Caesium Vacancy Migration under Hydrostatic Pressure

5.5.1 Activation Enthalpies

The activation enthalpies for hopping of a negatively charged caesium vacancy between a representative pair of sites is shown as a function of pressure for each of the three sets of SEPS in Figure 5-19a. The colours correspond to the pairs of sites connected by sticks in Figure 4-8. We find that the activation enthalpies associated with all three sets of SEPS increase with increasing hydrostatic pressure, such that at 2.0 GPa, the values are in a range of 0.85–1.59 eV. A similar increase of activation enthalpies as a function of hydrostatic pressure has previously been observed for Mg migration in $MgSiO_3$ [309, 310, 315]. The increase in activation enthalpy as a function of pressure can be intuitively understood in terms of the reduction of the aperture size through which the Cs passes during a hop, a more thorough discussion of which is given in Section 8.2.

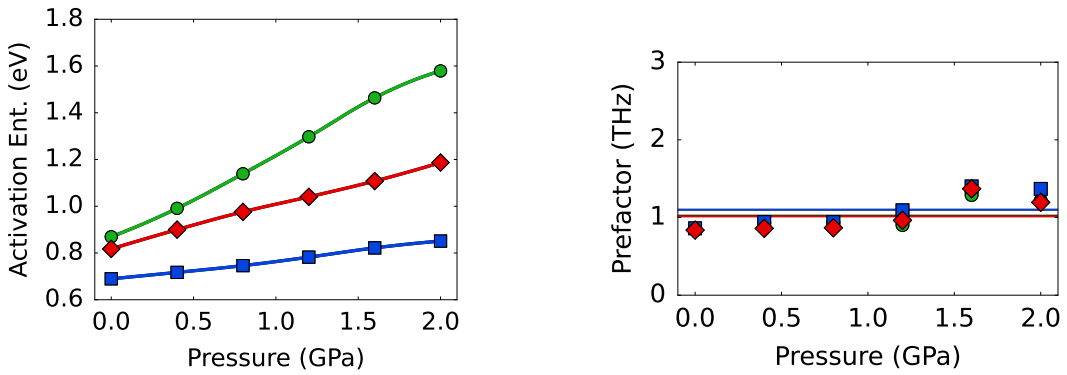

(a) (b)

Figure 5-19: (a) Activation enthalpies for negatively charged caesium vacancy migration under pressure for each of the three sets of SEPS. (b) Prefactors for negatively charged caesium vacancy migration under pressure between a representative pair of sites for each of the three sets of SEPS. The colours correspond to the pairs of sites connected by sticks in Figure 4-8.

5.5.2 Attempt Frequencies

The computed attempt frequencies are shown as a function of pressure in Figure 5-19b. We note that compared to the values we obtained for bromide vacancy migration, the values for

caesium vacancy vary more smoothly with pressure, but in keeping with the same methodology, we average the attempt frequencies associated with each set of SEPS over the range of pressures, and use these averaged values as the attempt frequency in our kinetic scheme for all pressures. The attempt frequencies thus obtained are approximately equal to 1 THz, and shown as horizontal lines in Figure 5-19b. These values are thus slightly lower than but similar to the ones we computed for bromide vacancy migration, which were spread around 2 THz. Interestingly, peaks which were attributed to vibrations involving the $PbBr_3$ octahedra and Cs atoms were observed in the vibrational spectrum of $CsPbBr_3$ in the THz range [123, 264, 288–290], though the Raman frequencies associated with the Cs motion were higher than those associated with vibrations of the $PbBr_3$ octahedra. Nonethelesss, the experimentally observed peaks in the vibrational frequencies referred to above remain in the THz range for hydrostatic pressures up to 2.0 GPa [123], justifying our approach of taking the average value over the pressure range of 0.0–2.0 GPa.

5.5.3 Mobilities

We use the activation enthalpies and attempt frequencies as input to our kinetic scheme, described in detail in Chapter 4. While the eigenvectors of the mobility tensor remain parallel to the crystalline lattice vectors, the relative magnitudes of their eigenvalues again change dramatically with increasing pressure. We find that all components of the mobility tensor decrease with increasing pressure, such that at 2.0 GPa, they have values of 3.8×10^{-16}, 4.0×10^{-28} and $2.4 \times 10^{-21}\,cm^2\,V^{-1}\,s^{-1}$, in the [100], [010] and [001] directions respectively. Similar to the case of bromide migration, the mobility tensor for caesium vacancy migration is thus strongly anisotropic, yet much more pronouced with principal values at 2.0 GPa varying by over 10 orders of magnitude. We show the relative contributions of the three sets of SEPS to the prinicipal components of the mobility tensor in Figure 5-21. We observe that the relative contributions to the mobility remain approximately constant over the full range of pressures. In the [010] direction, the mobility tensor is dominated by the contributions from the pairs of sites depicted in green in Figure 4-8. For these pairs of sites, the displacement vector $\vec{r}$ is indeed approximately aligned with the [010] direction. The pairs of sites from the other two sets of SEPS, depicted in red and blue in Figure 4-8, instead span the equatorial (010) plane, with negligble contributions in the [010] direction. This is reflected in the relative contributions to the mobility in the [100] and [001] directions. In the [100] direction, long-range migration can occur through pairs of sites belonging to a single set of SEPS. As a result, ions predominantly hop between pairs of sites from the set with the lowest associated activation enthalpy, which are the pairs of sites connected by blue sticks

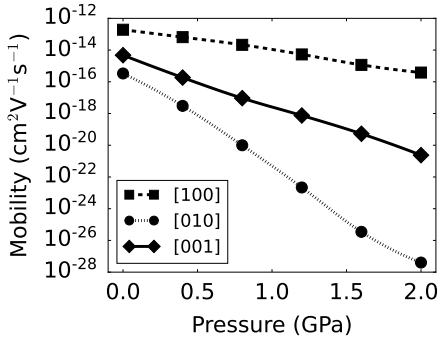

(a)

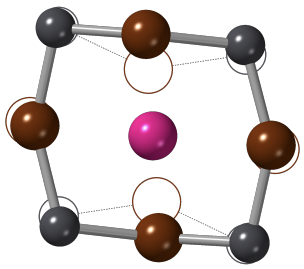

(b)

Figure 5-20: (a) Dependence on pressure of the diagonal components of the caesium vacancy mobility tensor. (b) Visual representation of the bromide aperture in the initial state (unfilled spheres and dotted lines) and at the transition state (solid spheres and lines), showing significant displacements. This suggests that the increased pressure leads to increased steric hindrance from the nearby atoms to attain the transition state, which leads to increased activation energies and lowers the mobilities. For a more thorough discussion of this analysis, the reader is refered to Section 8.2.

in Figure 4-8. In contrast, migration along the [001] direction cannot occur through pairs of sites belonging to a single set of SEPS. The mobility in the [001] direction is thus limited by the highest activation enthalpy of the activation enthalpies associated with the two sets of SEPS, and both sets of SEPS have approximately equal contributions to the mobility with the differences between the two corresponding to the differences in the displacement vectors $\vec{r}$ associated with the hops between the pairs of sites in these sets.

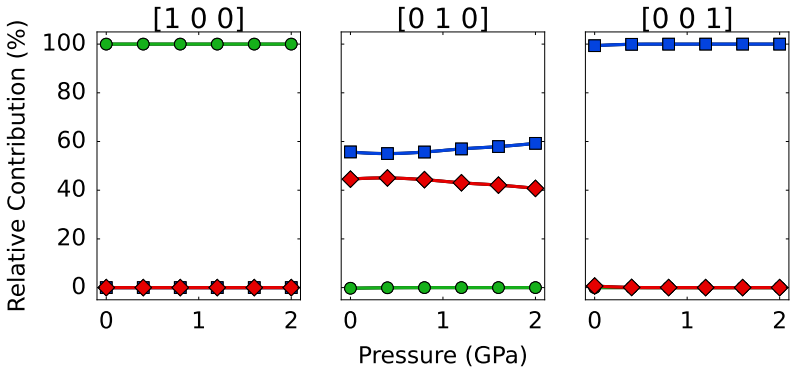

Figure 5-21: Dependence on pressure of the relative contributions to the caesium vacancy mobility in each of the principal directions of hops between members of each of the three sets of SEPS.

5.6 Conclusion

In conclusion, we have studied the effects of pressure on anion and A-site cation vacancy migration in $CsPbBr_3$. At low pressures, anion vacancy migration involves hops between multiple first-nearest neighbour (1-NN) pairs of sites, which are partitioned into six sets of symmetrically equivalent pairs of sites (SEPS), and the mobility tensor is approximately isotropic. As pressure is increased, the activation enthalpies associated with most sets of 1-NN SEPS increase, with only one decreasing significantly. Additionally, the activation enthalpy for hops between SEPS in neighbouring octahedra is reduced significantly at higher pressures. The two effects combined lead to enhanced mobilities in the (010), and a reduced mobility normal to it, such that the difference is approximately three orders of magnitude, corresponding to an effective transition from 3D mobility in the absence of pressure, to 2D mobility at 2.0 GPa. Interestingly, we thus find that though we apply an isotropic stress, the effects on the ionic mobility are strongly anisotropic. This observation demonstrates the necessity of a proper consideration of the symmetry and connectivity of the lattice structure in modelling and understanding anion migration in LHPs.

The activation enthalpies of caesium vacancy migration are even more strongly affected by hydrostatic pressure, and all increase with increasing pressure. The activation enthalpy associated with one set of SEPS, depicted in green, are particularly strongy affected and increases by almost 0.8 eV over the 0.0–2.0 GPa range of pressures. As a result, the components of the caesium vacancy mobility tensor strongly decrease with increasing pressure, reaching values as low as $4.0 \times 10^{-28}\,\mathrm{cm^2\,V^{-1}\,s^{-1}}$.

More broadly, our results demonstrate the potential of hydrostatic pressure to act as means

of controlling both the magnitude and directionality of ionic migration in $CsPbBr_3$, and possibly other LHPs. In the next chapters we will investigate whether such observations can be extended to other forms of stress.

Chapter 6

Effect of Biaxial Strain on Ionic Mobility

6.1 Introduction

We now move our focus to the effects of biaxial strain, which, in terms of technological importance, is a particularly relevant type of strain to study, with a number of studies reporting a strong correlation between biaxial strain and stability [71–73, 162]. Generally, the stability of the perovskite layer has been shown to destabilise with tensile biaxial strain, while its stability is enhanced with compressive biaxial strain.
In these studies, the changes in the relative stability have been attributed to changes in the levels of ionic migration, as exemplified by the following two quotes;

- 'The accelerated ion migration in the strained perovskite films can explain the faster degradation of $MAPbI_3$ into PbI_2, because MA^+ and I^- ions can migrate more easily from the $MAPbI_3$ films, producing PbI_2.' [71]
- 'We propose that the improved stability on a polymeric substrate and with lower annealing temperature could be attributed to increased steric barriers to the mobility of the volatile organic cation, preventing its egress and the subsequent formation of PbI_2.' [162]

However, attempts at providing an atomistic understanding towards these hypotheses have been very limited 73, 199. While these studies suggest that tensile biaxial strain can indeed lower the migration barrier for anion vacancy migration, as shown in Figure 6-1, a much more thorough investigation of the effects of biaxial strain on the anisotropic migration of both halide and A-site cation migration is necessary, in particular because similar studies have yielded valuable insights in the oxide perovskites [316–322].

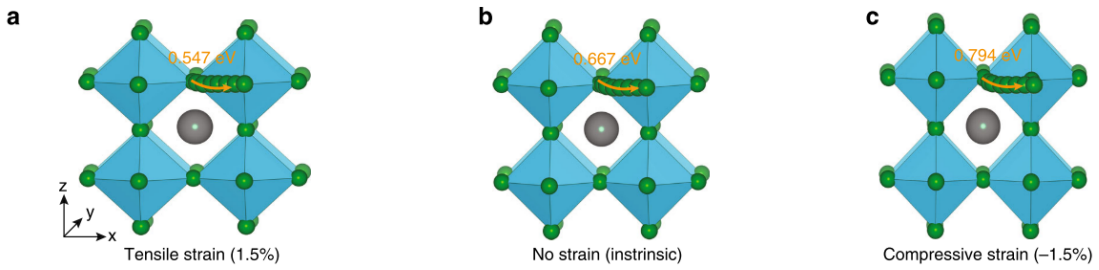

Figure 6-1: Calculated activation energies for halide anion vacancy migration in perovskites under tensile biaxial strain (a), no strain (b) and compressive biaxial strain (c). Reproduced from Reference 73.

In this chapter, we therefore present a quantitative analysis of the effects of biaxial strain on the migration of bromide and caesium vacancies in $CsPbBr_3$. To be able to restrict our study to a reasonable range of strain values, we reiterate that biaxial strain typically results from a mismatch of thermal expansion coefficients, as described in more detail in Section 2.2.2.2. We refer back to equation Equation (2.8), which is used to estimate the stress $\sigma_{\Delta T}$ due to a mismatch in thermal expansion coefficients ($\alpha_{\mathrm{s,p}}$) as a function of the annealing temperature ΔT

$$\sigma_{\Delta T} = \frac{E_{\mathrm{p}}}{1-\nu_{\mathrm{p}}} \left(\alpha_{\mathrm{s}} - \alpha_{\mathrm{p}}\right) \Delta T. \tag{6.1}$$

Representative values for E_p, ν_p, α_{s} and α_{p} are shown in Table 6.1.

Table 6.1: Representative values for E_p, ν_p, α_{s} and α_{p}, used to model the biaxial stress as a function of annealing temperature.

Parameter	Value	Reference
E_p	10–20 GPa	[55, 162]
ν_p	0.3	[162]
α_{s}	$1 \times 10^{-5}\,\mathrm{K}^{-1}$	[162]
α_{p}	$12 \times 10^{-5}\,\mathrm{K}^{-1}$	[153]

We can now estimate the biaxial stress as a function of the annealing temperature. Annealing temperatures for $CsPbBr_3$ have been reported over a wide range of temperatures. In general, the inorganic halide perovskites can withstand higher annealing temperatures than their hybrid counterparts because of the volatility of the organic components [73], such that an annealing temperature of 240°C is reported for $CsPbBr_3$, which is significantly higher than those of the hybrid perovskites, which are reported around 100°C. Interestingly, in a study testing the viability of using a carbon stack as the hole transporting material, champion

devices were obtained after heat processing at 400°C [323]. In another study, both the crystallinity and PCE were found to be significantly improved at an annealing temperature of 500°C, both compared to control experiments without any annealing, and annealing at 400°C [324]. In yet another study, the crystallinity and performance of the $CsPbBr_3$ layer were shown to decrease for annealing temperatures above 350°C due to the formation of pinholes. Annealing at such high temperatures can even be improved by invoking a pressurised environment, which prevents any of the constituents from evaporating [325].

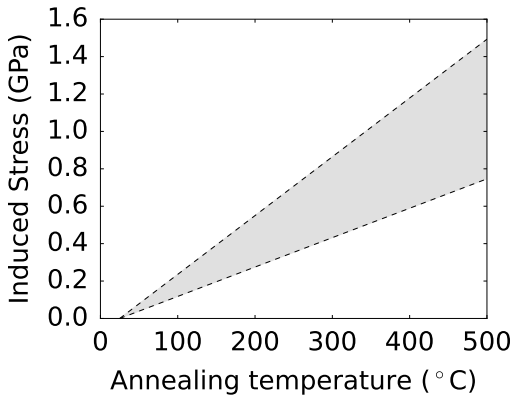

Figure 6-2: Induced stress as a function of annealing temperature for $CsPbBr_3$.

Taking 500°C as an upper bound for the annealing temperature, we find biaxial stresses upwards of 1 GPa, as shown in Figure 6-2. With bulk and Young's moduli of $CsPbBr_3$ of the order of 20 GPa, such stresses of the order of 1 GPa thus lead to strains of the order of +5%. We note that these strains are substantially larger than those that have been reported in the literature over a range of -2.4–1% [62, 73]. Compared to experiment however, we have the computational freedom to push the limits of the this range slightly, to get an insight into the effects of slightly more severe conditions. Hence, we limit our analysis to a range of -3% to +5% biaxial strain.

6.2 Structural Response to Strain

We look at the structural response of $CsPbBr_3$ in response to biaxial strains applied to either **a** and **b**, **a** and **c**, and **b** and **c**, corresponding to strain in either of the three planes (001), (010) and (100), respectively. We use this nomenclature interchangably. Strain is applied uniformly in these planes, e.g. for a tensile biaxial strain of +2% in the (010) plane, the lattice vectors $\boldsymbol{a}$ and $\boldsymbol{c}$ are increased by 2% each. Meanwhile, the remaining lattice vector, $\boldsymbol{b}$ in this case, is allowed to relax, as are the internal coordinates of the atoms.
We show the lattice parameters as a function of biaxial strain in Figure 6-3, along with the evolution of the lattice volume. We find for each of the three strain states, that the length of the lattice direction perpendicular to the strain plane reduces/increases to compensate for the increase/decrease in the other two lattice parameters. This effect is weakest for strain in the (010) plane; at a biaxial strain of 5%, the length of $\boldsymbol{b}$ is decreased by only 3% compared to the pristine structure, resulting in an overall volume increase of about 7%. In comparison, the out-of-plane lattice directions reduce by about 7% for biaxial strains of +5% strains in the (100) and (001) planes, resulting in a volume increase of only 3%. These results are in line with the components of the elasticity tensor, with C_{22} being significantly higher than both C_{11} and C_{33}, meaning the structure is least deformable along the [010] direction.

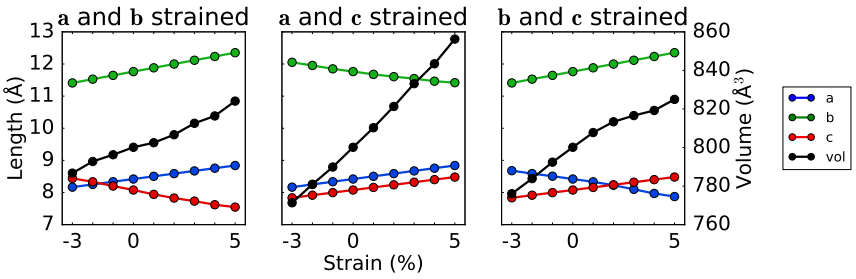

Figure 6-3: Structural response under biaxial strain for $CsPbBr_3$ in the orthorhombic phase with space group $Pnma$. The length of the lattice vectors **a** (blue), **b** (green) and **c** (red) is shown on the left axis, the lattice volume (black) is shown on the right axis.

Furthermore, we find that in the cases of strain in the (100)- and (001)-planes, the relative ordering of the $\boldsymbol{a}$ and $\boldsymbol{c}$ changes around a value of +2% biaxial strain in the case of strain in the (100)-plane, and -2% in the case of the strain in the (001)-plane. To investigate the effect of this inversion on the stability of the structure with space group $Pnma$, we compare it to an equivalent structure with space group $Pcmn$. This $Pcmn$ space group corresponds to a $\bar{c}ba$ permutation of the abc orientation of the $Pnma$ space group. Schematic representations of these structures are shown in Figure 6-4. In addition the symmetry operations for both of these space groups are shown in Table 6.2.

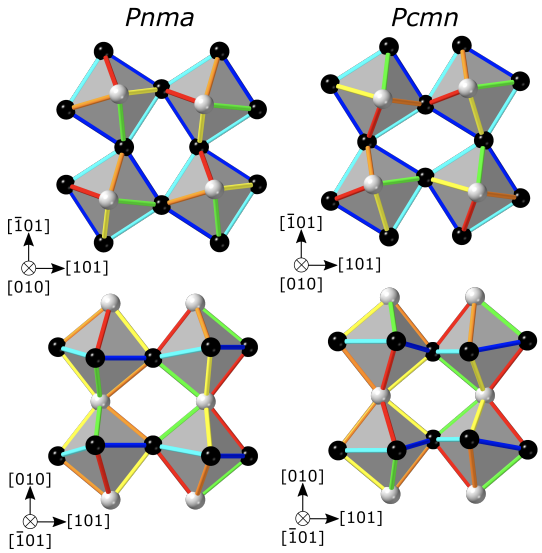

Figure 6-4: Schematic representation of $CsPbBr_3$ in the orthorhombic phase with the space groups $Pnma$ and $Pcmn$.

Table 6.2: Symmetry operations of the *Pnma* (left) and *Pcmn* (right) space groups.

Number	*Pnma*		
1	x	y	z
2	$\bar{x}$	$\bar{y}$	$\bar{z}$
3	$1/2 - x$	$-y$	$1/2 + z$
4	$1/2 + x$	y	$1/2 - z$
5	$1/2 + x$	$1/2 - y$	$1/2 - z$
6	$1/2 - x$	$1/2 + y$	$1/2 + z$
7	$\bar{x}$	$y + 1/2$	$\bar{z}$
8	x	$1/2 - y$	z

Number	*Pcmn*		
1	x	y	z
2	$\bar{x}$	$\bar{y}$	$\bar{z}$
3	$1/2 + x$	$-y$	$1/2 - z$
4	$1/2 - x$	y	$1/2 + z$
5	$1/2 - x$	$1/2 - y$	$1/2 + z$
6	$1/2 + x$	$1/2 + y$	$1/2 - z$
7	$\bar{x}$	$y + 1/2$	$\bar{z}$
8	x	$1/2 - y$	z

We then compute the relative energies of both of these structures as a function of tensile biaxial strain. The lengths of the lattice vectors corresponding to the strain plane are restricted to the same values for both structures, while allowing the length of the lattice vector out of the plane, as well as the internal coordinates, to fully relax. The relative energies of both structures are shown in Figure 6-5. Indeed, we find that for strains in the (100) plane of 2% and above and for strains in the (001) of 2% and below, the structure with space group $Pcmn$ is stabilised relative to the structure with space group $Pnma$. In all other cases, the structure with space group $Pnma$ remains more stable.

To verify how likely it is for the structure with space group $Pnma$ to transition to a structure with space group $Pcmn$, we perform a solid-state nudged elastic band calculations [229], in which both the internal coordinates as well as the lattice parameters are relaxed for all the

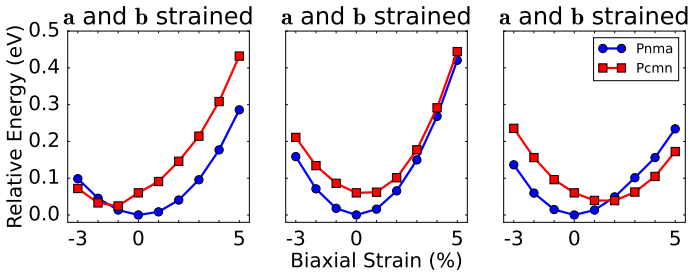

Figure 6-5: Relative energies of $CsPbBr_3$ in the orthorhombic phase with space groups $Pnma$ and $Pcmn$.

intermediate images. The resulting minimum enthalpy paths for transitions from a structure with space group $Pnma$ to a structure with space group $Pcmn$ are shown in Figure 6-6. We find that the barrier for such a transition is only about 10 meV per formula unit, which is sufficiently low compared to an approximate kinetic energy of the order of about 25 meV per atom at room temperature, that such transitions should occur spontaneously.

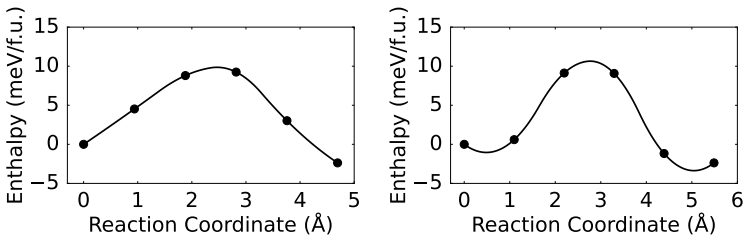

(a) -2% (001) (b) +2% (100)

Figure 6-6: Minimum enthalpy path for transitions between the $Pnma$ and $Pcmn$ orientations of the unit cell, where (a); the lattice directions in the (001) plane are restricted to be 2% shorter, and (b); the lattice directions in the (100) plane are restricted to be +2% longer than in the pristine unit cell with space group $Pnma$.

As it is likely for the structure to adopt the $Pcmn$ space group when this is energetically favourable, we will compute activation enthalpies and attempt frequencies for transitions between pairs of sites in structures with the $Pnma$ and $Pcmn$ space groups, whichever one is energetically favourable at any given level of strain. We show the new lattice parameters for this set of structures in Figure 6-7, in which we disconnect the trend between biaxial strains of -2% and -1% in the (001) plane and +1 and +2% in the (100) plane, to indicate the change in space group from $Pnma$ to $Pcmn$. As can be seen from Figure 6-7, the change in space group is accompanied by a change in volume towards the equilibrium volume. For example, the volume at +5% biaxial strain in the (100) plane is only 2% higher than in the pristine structure, while it was 3% for the structure with space group $Pnma$.

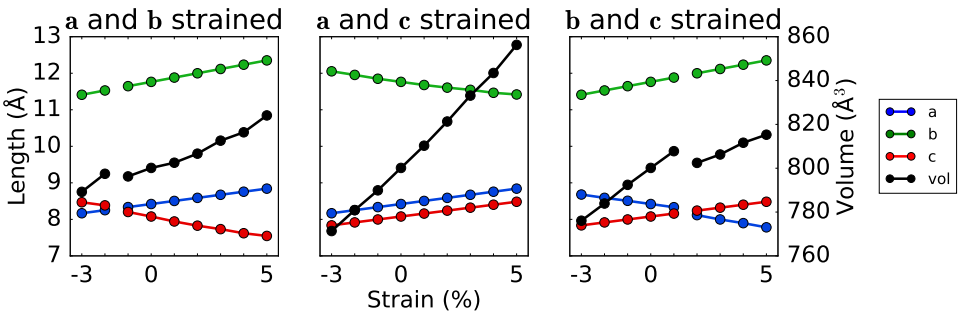

Figure 6-7: Structural response under biaxial strain for $CsPbBr_3$ in the orthorhombic phase with space group $Pnma$ or $Pcmn$, whichever one has the lowest energy. The length of the lattice vectors **a** (blue), **b** (green) and **c** (red) is shown on the left axis, the lattice volume (black) is shown on the right axis.

6.3 Bromide Migration under Biaxial Strain

The evolution under biaxial strain of the activation enthalpies for bromide vacancy hops corresponding to the six sets of 1-NN SEPS is shown in Figure 6-8. We reiterate that due to the asymmetry of the apical and equatorial sites, the activation energies are shown both for vacancy transitions from an apical to an equatorial (A-to-E) site, as well as the reverse (E-to-A), and that the higher of the two values acts as an effective bottleneck.

In general, we find that biaxial strain can strongly influence the activation enthalpy of bromide vacancy migration, as evidenced by the range of values we observe, in the range 0.10–0.42 eV. Despite the general assumption that activation enthalpies increase with compressive strain, and decrease with tensile strain, we observe no such trends for the activation enthalpies, not just in general, but also not for individual sets of SEPS. Instead, we observe that the change in activation enthalpy depends not only on the magnitude of the strain, but also on its direction. For example, the activation enthalpy for equatorial-to-equatorial transition corresponding to the cyan path, and indicated by cyan circles in Figure 6-8, decreases to about 0.12 eV for 5% tensile strain in the (001) plane, while it increases to about 0.35 eV for 5% tensile strain in the (100) plane. To understand the effect of biaxial strain on the ionic migration we thus wish to compute the ionic mobility tensor.

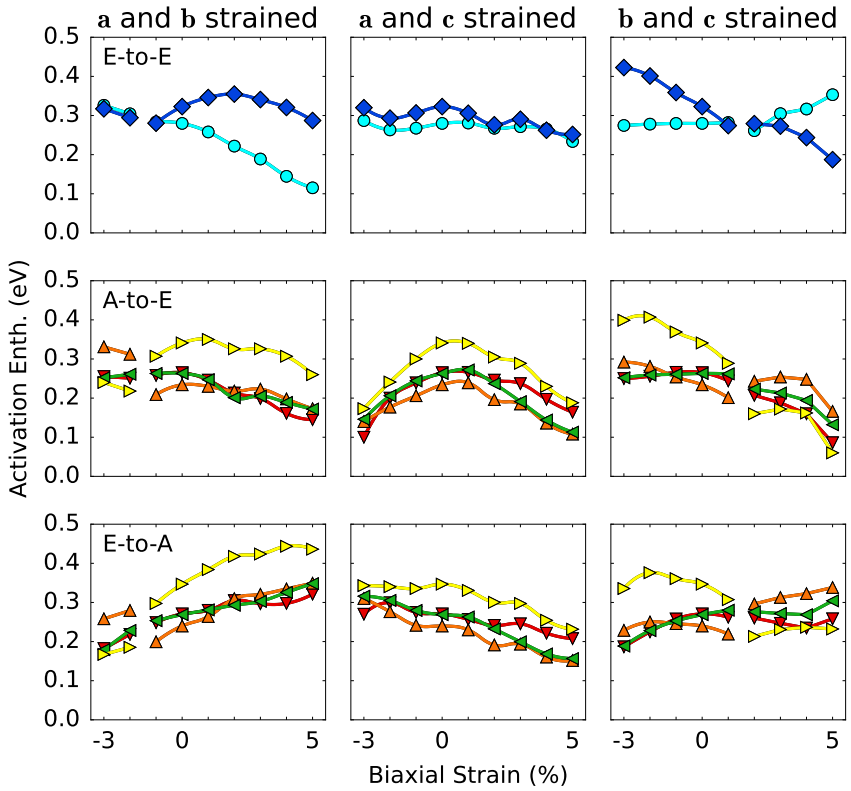

Figure 6-8: Activation enthalpy for V_{Br}^{+} migration in biaxially strained $CsPbBr_3$.

In order to do so, we first compute the attempt frequencies associated with transitions corresponding to the six sets of 1-NN SEPS. The Hessian matrices from which the attempt frequencies of vacancy hopping were derived were calculated using finite displacements of 0.010 Å, in contrast to the value of 0.015 Å which we introduced in the development of the general methodology. We previously found that in some cases, a reduction in this finite displacement resulted in a more consistent appearance of the imaginary mode at the transition state, whereas such a mode would sometimes appear absent for the higher finite displacement of 0.015 Å.

The resulting attempt frequencies for transitions of the bromide vacancy between pairs of sites are shown in Figure 6-9. Similar to what we observed in our study on hydrostatic pressure, we find that the spread in values is substantial, and that since the values do not vary smoothly with strain, we attribute this spread to numerical noise. Previously we calculated the average value for each set of SEPS over the range of pressures. However, as a result of the changes between the structures with space groups $Pnma$ and $Pcmn$, the sets of SEPS do not retain their topological equivalence over the full range of values probed in the study. Instead of taking the individual values for each set of SEPS, we instead derive three representative attempt frequencies, namely those for equatorial-to-equatorial, apical-to-equatorial and equatorial-to-apical transitions, which take on values of average values of 1.25, 1.11 and 1.23 THz, respectively.

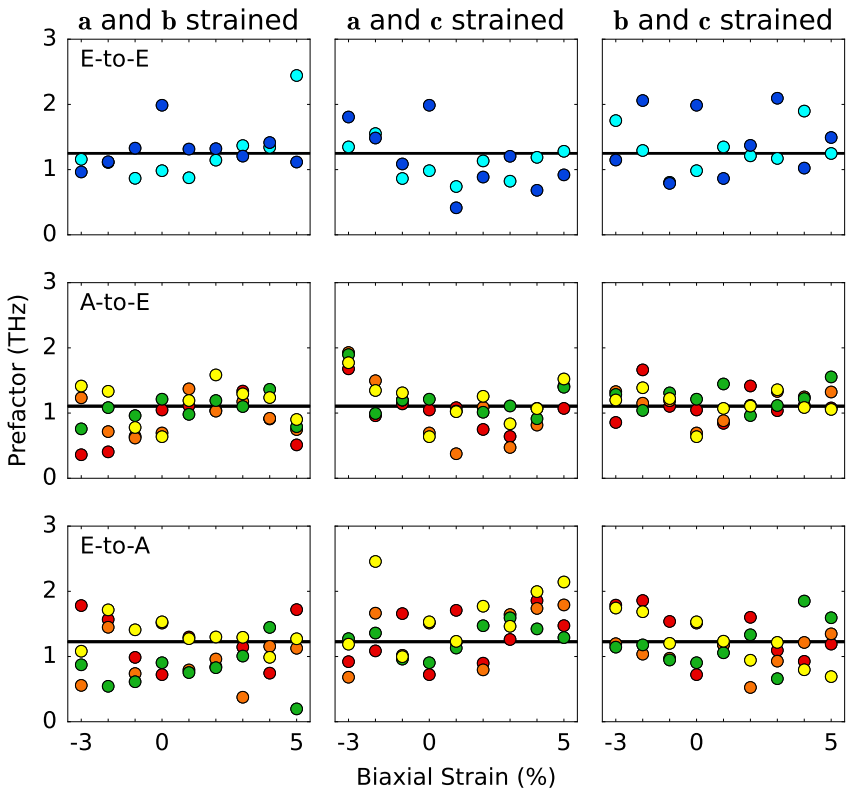

Figure 6-9: Prefactors for V_{Br}^{+} migration in biaxially strained $CsPbBr_3$. The black lines indicate the average values of 1.23, 1.11 and 1.19 THz, used to set up the rate matrix.

Finally, taking the activation enthalpies and prefactors as input, we compute the mobility tensor, which we find diagonalises along the [100], [010] and [001] directions. The components of this diagonalised mobility tensor are shown in Figure 6-10. In it, the directions corresponding to the strained plane are depicted in black for each panel, with the out-of-plane direction depicted in red.

For all three strain planes, we find that the ionic mobility in the direction out of the plane increases with tensile strain. In the most severe case of 5% tensile strain in the (001) plane, it increases by almost three orders up to a value of almost $1\times10^{-3}\,\mathrm{cm^2\,V^{-1}\,s^{-1}}$. For strain in this (001) plane, the ionic mobility in the plane decreases with tensile strain, effectively resulting in a 1D mobility. In the case of strain in the (010) plane, the mobilty remains effectively 3D and increases with tensile strain, while it decreases with compressive strain, covering a range of 10^{-6}–$10^{-4}\,\mathrm{cm^2\,V^{-1}\,s^{-1}}$. The mobility also remains fairly isotropic and also fairly constant for strains in the (100) plane. The components remain mostly below $10^{-5}\,\mathrm{cm^2\,V^{-1}\,s^{-1}}$, with the exception at a value of 5% tensile strain, in which case the mobility out of the plane approaches a value of $10^{-4}\,\mathrm{cm^2\,V^{-1}\,s^{-1}}$.

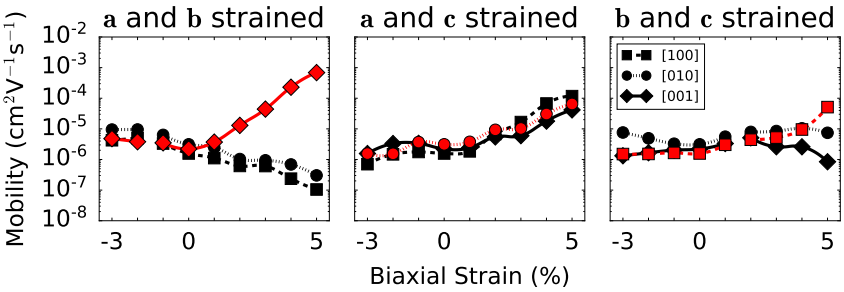

Figure 6-10: Br vacancy mobility under biaxial strain.

6.4 Caesium Migration Under Biaxial Strain

The evolution under biaxial strain of the activation enthalpies for caesium vacancy transitions corresponding to the three sets of SEPS is shown in Figure 6-11. In general, we find that biaxial strain can strongly influence the activation enthalpy of caesium vacancy migration. One transition, which is predominantly along [010] and the activation enthalpies of which are depicted by green circles in Figure 6-11, is particularly influenced by biaxial strain in the equatorial (010) plane. While the activation enthalpy increases to about 1.34 eV at 3% compressive strain, it decreases to a value of 0.33 eV for 5% tensile strain, thus covering a range of more than one eV. The activation enthalpies corresponding to transitions for the other two sets of SEPS cover a much smaller range of values around 0.53–0.97 eV. To understand the effect of biaxial strain on the macroscopic mobility we now wish to compute the ionic mobility tensor.

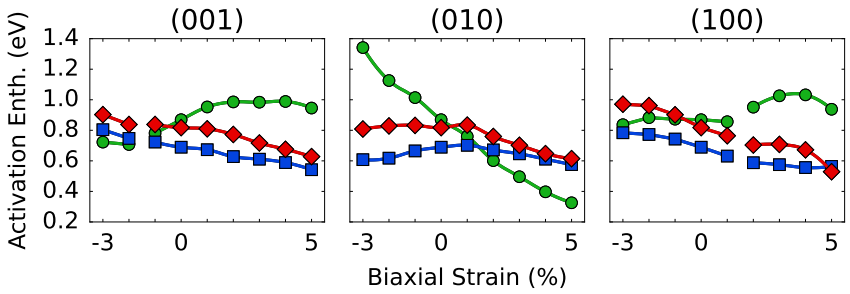

Figure 6-11: Activation enthalpy for V_{Cs}^{-} migration under biaxial strain.

In order to do so, we first compute the attempt frequencies associated with transitions corresponding to the three sets of 1-NN SEPS. The Hessian matrices from which the attempt frequencies of vacancy hopping were derived were calculated using finite displacements of 0.010 Å. The resulting attempt frequencies for transitions of the bromide vacancy between pairs of sites is shown in Figure 6-12. Similar to what we observed in our study on hydrostatic pressure, we find that the spread in values is substantial, and that since the values do not vary smoothly with strain, we attribute this spread to numerical noise. Previously we calculated the average value for each set of SEPS over the range of pressures. However, as a result of the changes between the structures with space groups $Pnma$ and $Pcmn$, the sets of SEPS do not retain their topological equivalence over the full range of values probed in the study. Instead of taking the individual values for each set of SEPS, we instead derive a single representative attempt frequency, which takes on an average value of 0.69 THz.

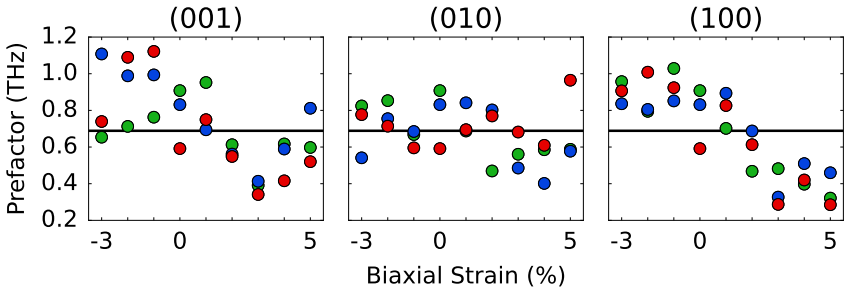

Figure 6-12: Attempt frequencies for V_{Cs}^{-} migration under biaxial strain.

Finally, we compute the mobility tensor, which we find diagonalises along the [100], [010] and [001] directions. The components of this diagonalised mobility tensor are shown in Figure 6-10. In it, the directions corresponding to the strained plane are depicted in black for each panel, with the out-of-plane direction depicted in red. In addition, the range of bromide mobility values computed in the absence of strain, being 2.2–4.3$\times 10^{-6}$ cm^2 V^{-1} s^{-1}, is shown as a grey bar.

We observe that for all three strain planes, the mobility out of the plane increases with tensile strain and decreases with compressive strain. This effect is strongest for strain in the (010) plane, with the out of plane mobility varying by over 10 orders of magnitude over the full range. At 5% tensile strain, the mobility takes on a value of 2.8$\times 10^{-7}$ cm^2 V^{-1} s^{-1}, which is only an order of magnitude below the values we computed for the bromide mobilty in the absence of strain.

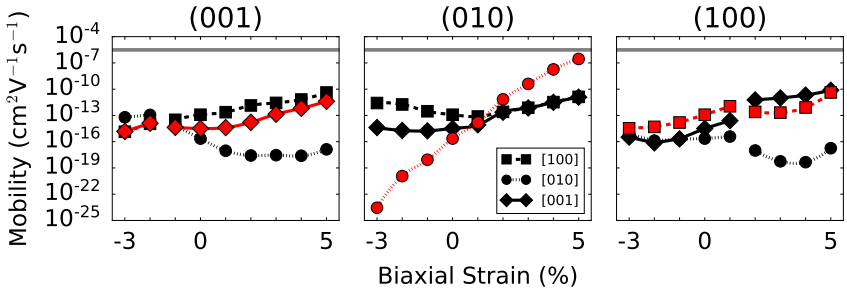

Figure 6-13: Cs vacancy mobility under biaxial strain.

6.5 Conclusion

In summary, we have shown the changes in both the bromide and caesium vacancy mobility as a function of biaxial strain in the range of -3–5%. Such strains have been strongly linked to the stability of the perovskite structure, with tensile biaxial strain being linked to increased degradation while compressive strain has been linked to increased stability.

Our results indicate that the mobilities perpendicular to the plane that is strained, both in the case of the bromide and caesium vacancy mobility, do increase with biaxial strain and decrease with compressive strain. In perovskite-based layered devices, this out-of-plane direction is generally parallel to the aplied field, such that enhanced levels of ionic mobility could indeed be responsible for the reduced stability under tensile strain. In contrast, the mobilities in the strained plane however show different trends, some increasing and some decreasing, depending on the type of strain that is applied. However, these mobilities are not generally parallel to the electric field, such that enhanced mobilities in the strained plane are less influential on the structural stability of the perovskite layer.

Though it is hard to distill a single trend describing the behaviour of the mobility as a function of biaxial strain, the results varying with the type of strain applied, we can nonetheless get an idea of the effects of such strain by looking at the range of values that are induced. In the case of the bromide mobility, the overall components of the mobility tensor cover a range of about three orders of magnitude, roughly between 1×10^{-7}–$1\times10^{-3}\,\mathrm{cm^2\,V^{-1}\,s^{-1}}$. Though this amounts to no insignificant variation, we also show that the caesium vacancy mobility varies over an even wider range, of the order of about seventeen orders of magnitude, roughly between 2.8×10^{-24}–$2.8\times10^{-7}\,\mathrm{cm^2\,V^{-1}\,s^{-1}}$. Remarkably, at a tensile strain of about 5% in the $\boldsymbol{a}$ and $\boldsymbol{c}$ directions, the out-of-plane mobility approaches values observed for the bromide mobility, of the order of $1\times10^{-6}\,\mathrm{cm^2\,V^{-1}\,s^{-1}}$. This puts into question which of the mobile species are the most important in terms of material degradation. Our results suggest that because of the strong response of the caesium vacancy mobility, such instabilities could perhaps be more a result of migration of the A-site cation, rather than the X-site anion.

Chapter 7

Effect of Uniaxial Strain on Ionic Mobility

7.1 Introduction

Finally, we wish to finalise our study of the general effects of strain on the ionic migration in $CsPbBr_3$ by focussing on the effects of uniaxial strain. As discussed previously, such strains are mainly relevant in the context of flexible solar cells, which are typically bent not only during operation but also during production [164–169].

Such conditions are mimicked experimentally by rolling the flexible solar cell of thickness z over a cylinder of radius R, such that the strain can be estimated using $z/2R$. Such radii are typically of the order of a few millimeter [172,326], the highest being about 10 mm [171,327], and the lowest being as low as 0.5 mm [170]. In the latter case, various film thicknesses were used to test the stability of the flexible devices. Specifically, thicknesses of 2.5, 30 and 100 μm were tested, corresponding to uniaxial strains of the order of 0.25, 3 and 10%, respectively. The devices under 10% were shown to be very unstable, with the device under 3% also showing significant degradation. In contrast, the thinnest device, the unprecedented flexibility of which was facilitated by an ultra-thin polymer substrate of $\approx 2.5\,\mu$m, showed remarkable stability.

In a different study, the effects of bending on the photoluminescence lifetimes were measured for flexible films of $MAPbI_3$ [328]. The PL lifetimes were shown to decrease with compressive strain and increase with tensile strain over a range of -3.7–3.3% strain, which are comparable to values up to 3.06% observed in Reference 163.

Despite another report in which a perovskite film is stretched to accomodate a strain of 50% [329], we limit our study to a more conservative range of -5–5% uniaxial strain. Given that experimentally reported activation energies in $MAPbI_3$ in the dark, as shown in Figure 7-

1, have been reported to vary over a range of 0.53–0.29 eV for strains of 0.2–0.62% lattice strain [71], the range that we suggest should yield sufficient insight in the underlying trends regarding the ionic migration under uniaxial strain.

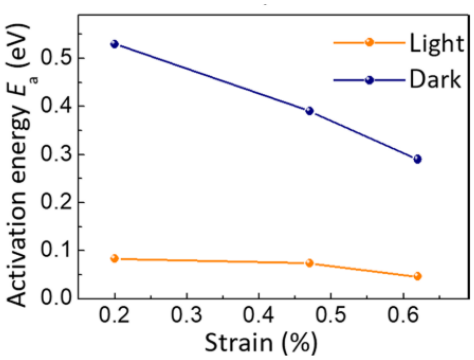

Figure 7-1: Activation energy for ion migration in $MAPbI_3$ in the light and the dark as a function of uniaxial strain. From Reference 71. Reprinted with permission from AAAS.

7.2 Structural Response to Strain

We then look at the structural response of $CsPbBr_3$, in response to both compressive and tensile uniaxial strains up to 5%, applied along either of three lattice vectors [100], [010] and [001]. For each of these directions, strain is applied uniformly along this direction, while the remaining lattice vectors along the other two directions are allowed to relax, as are the internal coordinates of the atoms.

We show the lattice parameters as a function of uniaxial strain in Figure 7-2, both in terms of absolute values and values relative to the pristine structure. We find for each of the three strain states, that the lengths of both of the other two lattice directions change in an opposite way compared to the strained direction, so as to compensate for the change in volume. This effect is weakest for strain in the [010] direction, where the volume is decreased by 2% for a compressive uniaxial strain of 5%, while it is increased by 2% for a tensile uniaxial strain of 5%. It is interesting to observe that the response of $\boldsymbol{a}$ and $\boldsymbol{c}$ is very different in the case of compressive or tensile strain in the [010] direction. Compressive strain along the [010] direction is solely compensated by a change in the length of $\boldsymbol{c}$, while $\boldsymbol{a}$ remains constant. Under weak tensile strain, up to 3%, both $\boldsymbol{a}$ and $\boldsymbol{c}$ decrease, after which $\boldsymbol{c}$ remains more or less constant and the change in [010] is compensated only by a change in $\boldsymbol{a}$.

For uniaxial strain along the [001] direction, both $\boldsymbol{a}$ and $\boldsymbol{b}$ change quasi-linearly to mitigate

the volume change due to the change along [001]. The change in $\boldsymbol{a}$ is larger than that of $\boldsymbol{b}$, which is in line with the fact that C_{22} is higher than C_{11}. Along with these changes, the volume is reduced by about 2% for 5% compressive strain along the [001] direction, while it is increased by about 1% for a 5% tensile strain.

The changes in volume are lowest for strain along the [100] direction, with less than a 1% reduction under compressive strain, and a 0.5% increase under tensile strain. In these cases, the change in $\boldsymbol{a}$ is almost solely compensated by a change in $\boldsymbol{c}$, while $\boldsymbol{b}$ remains more or less constant. This is again in line with the fact C_{22} is higher than C_{33}.

Surprisingly, we find that the evolution of the volume seemingly makes several jumps, in particular for the case of strain in the [100] and [010] directions. Since we use very strict convergence criteria in optimising the unit cells, these are unlikely to be a result of poor convergence. Nevertheless, they do seem to be indicative of small fluctuations of the lengths of the lattice parameters in the directions orthogonal to the strained direction. The observation that these fluctuations are absent when the length of $\boldsymbol{c}$ is kept fixed could indicate that these fluctuations are largest for the $\boldsymbol{c}$, which is in agreement with the fact that it is the softest direction, with C_{33} being lower than both C_{11} and C_{22}.

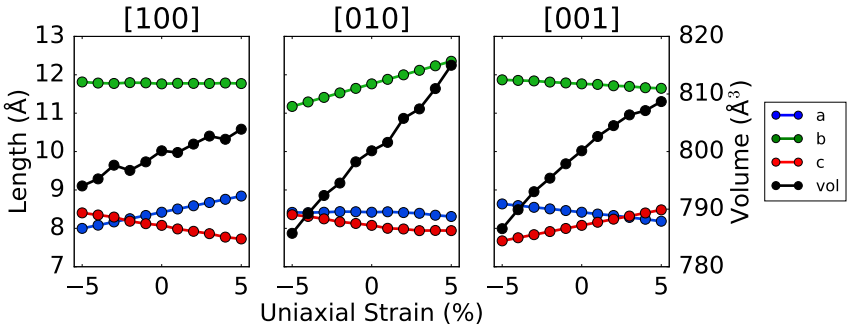

Figure 7-2: Structural response under uniaxial strain.

Furthermore, we find that in the case of strains in the [100] and [001]-directions, the relative ordering of the $\boldsymbol{a}$ and $\boldsymbol{c}$ changes, in the case of strain in the [100]-direction around a value of 2% compressive strain and in the case of [001]-direction around a value of 2% tensile strain. To investigate the effect of this inversion on the stability of the structure with space group $Pnma$, we compare it to an equivalent structure with space group $Pcmn$. This $Pcmn$ space group corresponds to a $\bar{c}ba$ permutation of the abc orientation of the $Pnma$ space group, discussed previously also in our study onthe role of biaxial strain.

We compute the relative energies of both of these structures as a function of uniaxial strain. We restrict the lengths of the lattice vector corresponding to the strained direction to the same value for both structures, while allowing the length of the other two lattice vectors,

as well as the internal coordinates, to fully relax. The relative energies of both structures are shown in Figure 7-3. For strains along [010], we find that the structures with space group $Pcmn$ relax to structures structurally identical to their counterparts with space group $Pnma$, but with a permutation of the lattice vectors and the correspondng fractional coordinates. Interestingly, we find for compressive strains along the [100] direction of 2% and below, and for tensile strains along the [001] direction of 3% and above, that the structure with space group $Pcmn$ is stabilised relative to the structure with space group $Pnma$. In all other cases, the structure with space group $Pnma$ remains more stable.

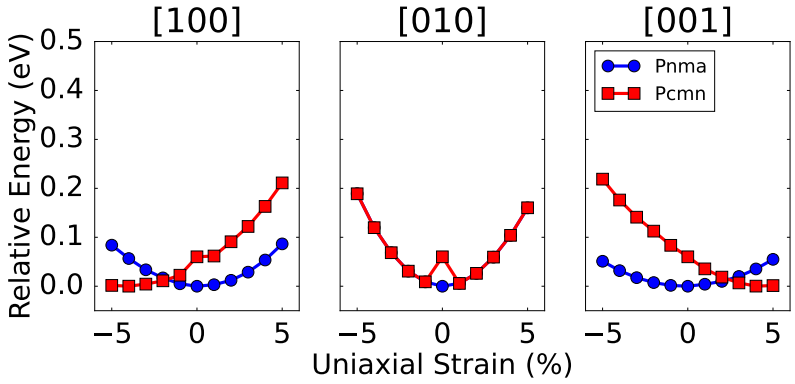

Figure 7-3: Relative total energies of the structures with space group $Pnma$ and $Pcmn$ under uniaxial strain.

To verify how likely it is for the structure with space group $Pnma$ to convert a structure with space group $Pcmn$, we perform a solid-state nudged elastic band calculations [229], in which both the internal coordinates as well as the lattice parameters are relaxed for all the intermediate images. For two levels of strains, namely 2% compressive strain along [100] and 2% tensile strain along [001], the resulting minimum enthalpy paths for a transition from a structure with space group $Pnma$ to a structure with space group $Pcmn$ are shown in Figure 7-4. We find that in both cases the enthalpy barrier for these transitions is only about 20 meV per formula unit, which is sufficiently low compared to a kinetic energy of the order of approximately 25 meV per atom at room temperature, that such transitions can occur spontaneously.

As it is thus likely for the structure to adopt the $Pcmn$ space group when this is energetically favourable, we continue our analysis using a combination of structures with the $Pnma$ and $Pcmn$ space groups, whichever one is energetically favourable at any given level of strain. We show the new lattice parameters for this set of structures in Figure 7-5, in which we disconnect the trend between strains of -1 and -2% along [100] and +2 and +3% along [001], to indicate the change in space group from $Pnma$ to $Pcmn$. As can be seen from

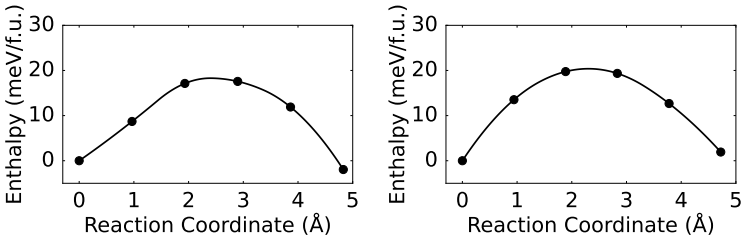

Figure 7-4: Minimum enthalpy path for transitions between the $Pnma$ and $Pcmn$ orientations of the unit cell, for 2% compressive strain along [100] (a) and 2% tensile strain along [001] (b), relative to their values in the pristine unit cell with space group $Pnma$.

Figure 7-5, the switch to the $Pcmn$ space group is accompanied by a rather sharp discontinuity in the trends of the two lattice vectors that are relaxed in both cases. In the case of strain along the [100] direction, the length of $\boldsymbol{b}$ drops below its pristine value, though it showed a slight expansion in the structure with space group $Pnma$. The length of $\boldsymbol{c}$ shows a sharp increase of about 2%-points, which results in an increase in the total lattice volume with respect to its pristine value, while it was reduced in the structure with space group $Pnma$. We observe similar, but opposite, behaviours for strain in the [001] direction, where $\boldsymbol{b}$ shows an elongation and $\boldsymbol{a}$ a large contraction, resulting in an overall contraction of the lattice volume relative to its pristine value.

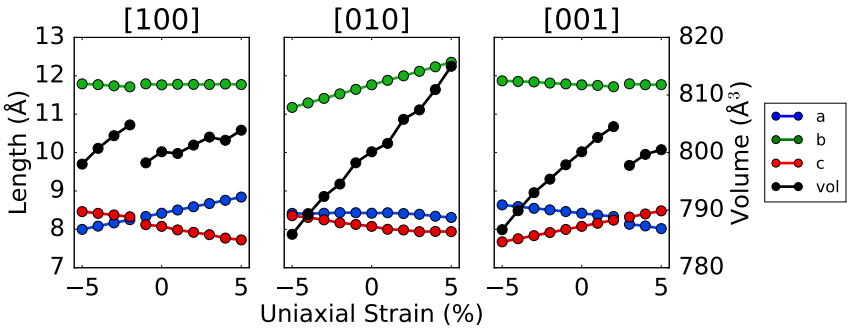

Figure 7-5: Structural response under uniaxial strain including permutation.

7.3 Bromide Migration under Uniaxial Strain

The evolution under uniaxial strain of the activation enthalpies for transitions corresponding to the six sets of 1-NN SEPS is shown in Figure 7-6. We reiterate that due to the asymmetry of the apical and equatorial sites, the activation energies are shown both for vacancy transitions from an apical to an equatorial site (A-to-E), as well as the reverse (E-to-A), and that the higher of the two values acts as an effective bottleneck.

In general, we find that uniaxial strain has a strong influence on the activation enthalpy of bromide vacancy migration, as evidenced by the range of values we observe, in the range 0.16–0.47 eV. Despite the general assumption that activation enthalpies increase with compressive strain, and decrease with tensile strain, we observe no such trends for the activation enthalpies, not just in general, but also not for individual sets of SEPS. Instead, we observe that the change in activation enthalpy depends not only on the magnitude of the strain, but also on its direction. For example, the activation enthalpy for equatorial-to-equatorial transition corresponding to the cyan path, and indicated by cyan circles in Figure 7-6, decreases to about 0.21 eV for 5% tensile strain in the [100] direction, while it increases to about 0.35 eV for 5% tensile strain in the [001] direction. To understand the effect of uniaxial strain on the ionic migration we thus wish to compute the ionic mobility tensor.

In order to do so, we first compute the attempt frequencies associated with transitions corresponding to the six sets of 1-NN SEPS. The Hessian matrices from which the attempt frequencies of vacancy hopping were derived were calculated using finite displacements of 0.010 Å. The resulting attempt frequencies for transitions of the bromide vacancy between pairs of sites are shown in Figure 7-7. In analogy with our study on biaxial strain, we derive three representative attempt frequencies, namely those for equatorial-to-equatorial, apical-to-equatorial and equatorial-to-apical transitions, which take on average values of 1.20, 1.08 and 1.17 THz respectively. These values are very similar to the ones computed in the study of the effects of biaxial strain, which were computed at 1.25, 1.11 and 1.23 THz. In both studies, the value of the A-to-E transition is slightly lower, which could be indicative of overall lower vibrational frequencies for the moving ion at an equatorial site compared to an apical site.

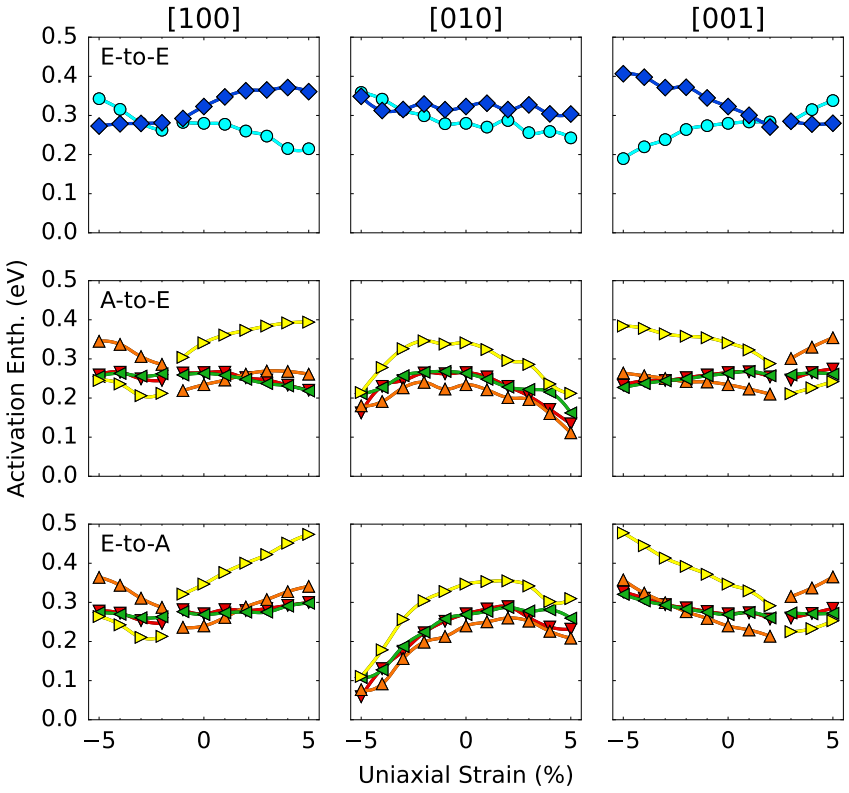

Figure 7-6: Activation enthalpy for V_{Br}^{+} migration in uniaxially strained $CsPbBr_3$ for equatorial to equatorial, apical to equatorial and equatorial to apical positions.

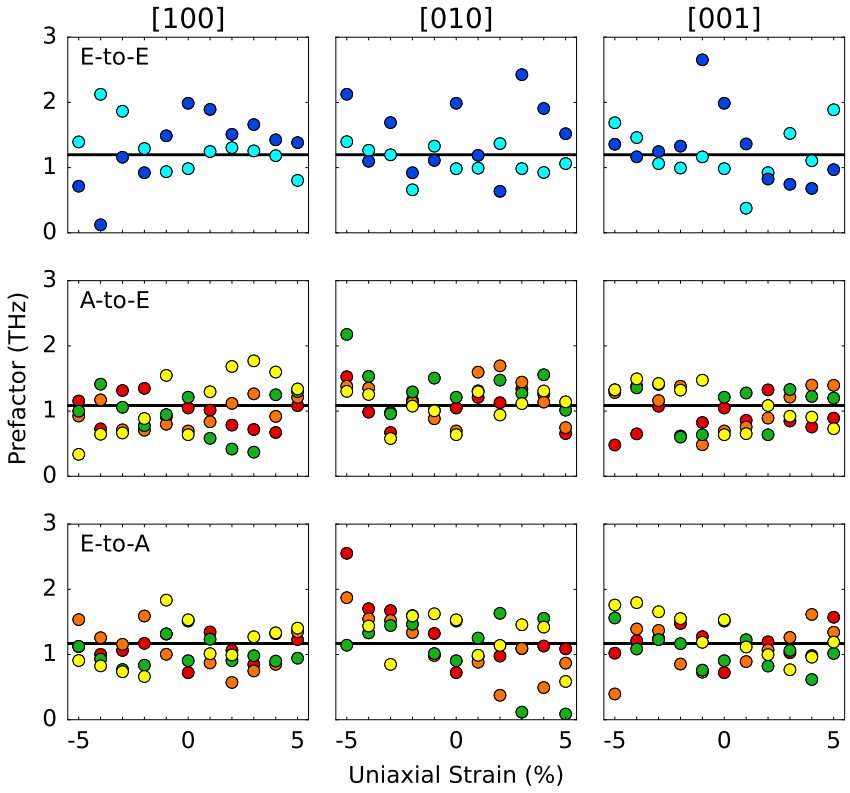

Figure 7-7: Prefactors for V_{Br}^{+} migration in uniaxially strained $CsPbBr_3$. The black lines indicate the average values of 1.20, 1.08 and 1.17 THz, used to set up the rate matrix.

Finally, we compute the mobility tensor, which we find diagonalises along the [100], [010] and [001] directions. The components of this diagonalised mobility tensor are shown in Figure 7-8. In it, the directions corresponding to the strained direction are depicted in red for each panel, with the other two direction depicted in black.

Contrary to the common assumption that tensile strain increases and compressive strain decreases the ionic mobility, we observe no such trend for our data. The mobility rises most strongly for compressive strain in the [010] and [001] directions, reaching values upwards of $1\times10^{-4}\,\mathrm{cm^2\,V^{-1}\,s^{-1}}$. Interestingly, the mobility also increases for tensile strain in the [010] direction, such that strain in this plane should be particularly avoided. In most cases, the mobility also remains fairly isotropic, apart from the effective 3D-to-1D transitions that we observe for tensile strain in the [100] direction and compressive strain in the [001] direction. In the latter case, the trend is similar to what was observed in the case of tensile biaxial strain in the (001) plane. This is not surprising given that both strain states are comparable, with the tensile biaxial strain in the (001) plane being compensated by compressive strain in the [001] direction.

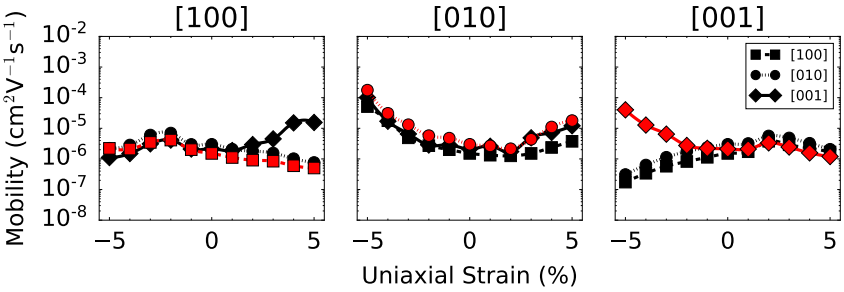

Figure 7-8: Br vacancy mobility under uniaxial strain.

7.4 Caesium Migration under Uniaxial Strain

The evolution under uniaxial strain of the activation enthalpies for caesium vacancy transitions corresponding to the three sets of SEPS is shown in Figure 7-9. Despite the general assumption that activation enthalpies increase with compressive strain, and decrease with tensile strain, we observe no such trends for the activation enthalpies, not just in general, but also not for individual sets of SEPS. In general, we do find however that uniaxial strain can strongly influence the activation enthalpy of caesium vacancy migration. One transition, which is predominantly along [010] and the activation enthalpies of which are depicted by green circles in Figure 7-9, is particularly influenced by uniaxial strain in the apical [010] direction. While the activation enthalpy increases to about 1.12 eV at 5% tensile strain, it decreases to a value of 0.52 eV for 5% compressive strain. Interestingly, this trend is opposite to that observed for biaxial in the (010) plane, but not inconsistent given that tensile biaxial strain in this plain is compensated by compressive uniaxial strain in the [010] direction, and vice versa for compressive biaxial strain and tensile uniaxial strain. The activation enthalpies corresponding to transitions for the other two sets of SEPS cover a smaller range of values around 0.52–0.89 eV. To understand the effect of biaxial strain on the macroscopic mobility we now wish to compute the ionic mobility tensor.

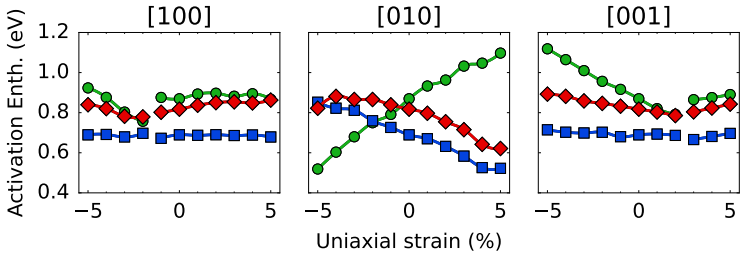

Figure 7-9: Activation enthalpy for V_{Cs}^{-} migration under uniaxial strain.

In order to do so, we first compute the attempt frequencies associated with transitions corresponding to the three sets of 1-NN SEPS. The Hessian matrices from which the attempt frequencies of vacancy hopping were derived were calculated using finite displacements of 0.010 Å. The resulting attempt frequencies for transitions of the bromide vacancy between pairs of sites is shown in Figure 7-10. In analogy with our study on biaxial strain, we derive a single representative attempt frequency which takes on an average value of 0.73 THz.

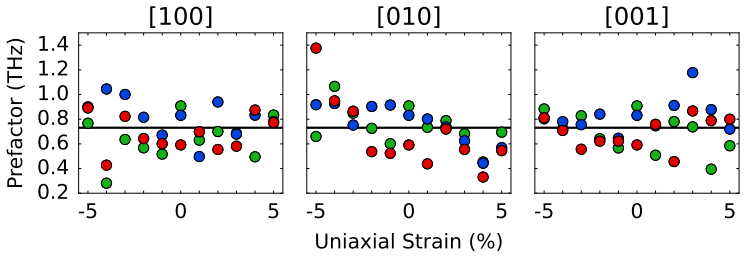

Figure 7-10: Attempt frequencies for V_{Cs}^{-} migration under uniaxial strain.

Finally, we compute the mobility tensor, which we find diagonalises along the [100], [010] and [001] directions. The components of this diagonalised mobility tensor are shown in Figure 7-11. In it, the directions corresponding to the strained direction are depicted in red for each panel, with the other two direction depicted in black.

Contrary to the common assumption that tensile strain increases and compressive strain decreases the ionic mobility, we observe no such trend for our data. Instead, we find that the mobility rises most strongly for strains in the [010] direction. For compressive strain, the mobility along the strained direction reaches a value of $1.6\times10^{-10}\,\mathrm{cm^2\,V^{-1}\,s^{-1}}$, while the mobility in the plane perpendicular also reaches just below $1\times10^{-10}\,\mathrm{cm^2\,V^{-1}\,s^{-1}}$ for tensile strain of 5%. The lowest mobilities are found along [010], having values of $4.0\times10^{-20}\,\mathrm{cm^2\,V^{-1}\,s^{-1}}$ for 5% tensile uniaxial strain along [010], and $1.6\times10^{-20}\,\mathrm{cm^2\,V^{-1}\,s^{-1}}$ for 5% compressive uniaxial strain along [001]. Overall, the range of values for the caesium mobility thus span a range of 10 orders of magnitude over a range of -5 to +5% uniaxial strain.

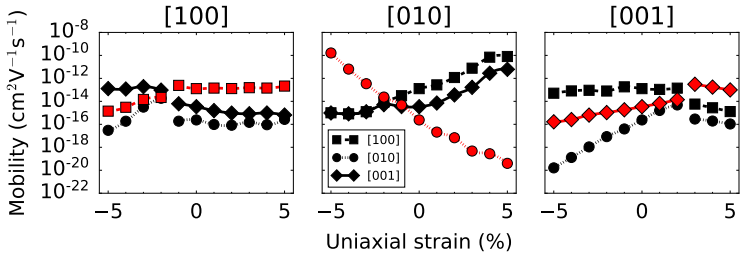

Figure 7-11: Cs vacancy mobility under uniaxial strain.

7.5 Conclusion

In summary, we have shown the changes in both the bromide and caesium vacancy mobility as a function of uniaxial strain in the range of -5 to +5%. Such strains have been linked to the stability of the perovskite structure, with tensile uniaxial strain being linked to increased degradation while compressive strain has been linked to increased stability.
We find that the response of the mobility to uniaxial strain is more complex. In some directions, it may indeed increase with tensile strain in a given direction, but for others it can be shown to decrease. The same contrasting observations hold for compressive strain. These results are strongly linked with the structural response to uniaxial strain. While we may strain the perovskite along a certain lattice vector, the two lattice vectors perpendicular to it will relax in the opposite direction to compensate for the induce strain. If such compensation occurs along a direction to which the change in migration enthalpy is particularly sensitive, this may lead to opposite behaviour as expected purely based on the induced strain. To make this point more clearly, we refer to the pair of Cs sites depicted in green. The activation enthalpy associated with transitions between this pair of sites is shown to decrease with compressive strain and increase with tensile strain in the [010] direction, in contrast to the general understanding. The reason for this behaviour is the compensation of the $\boldsymbol{a}$ and $\boldsymbol{c}$ lattice vectors in response to straining $\boldsymbol{b}$, thus mimicking the case of biaxial strain of the $\boldsymbol{a}$ and $\boldsymbol{c}$ lattice vectors. The results we observe here are thus consistent with our previous study on the effects of biaxial strain.
Despite the apparent complexity of describing trends in the components of the mobility tensor, we may still discuss the range of values that can be induced under uniaxial strain. In the case of the bromide mobility, the overall components of the mobility tensor cover a range of about three orders of magnitude, roughly between 1×10^{-7}–$1\times10^{-4}\,\mathrm{cm^2\,V^{-1}\,s^{-1}}$. Though this amounts to no insignificant variation, we also show that the caesium vacancy mobility varies over an even wider range, of the order of about ten orders of magnitude, roughly between 1×10^{-20}–$1\times10^{-10}\,\mathrm{cm^2\,V^{-1}\,s^{-1}}$. Overall, we find these ranges to be smaller than in the case of biaxial strain, but the ranges of values that can be observed under uniaxial strain could nevertheless have significant implications to the operation of perovskite layers under uniaxial strain, for example in flexible devices.

Chapter 8

Migration Barrier Analysis

In the previous chapters, we have observed that the activation enthalpies for both bromide and caesium vacancy transitions can be significantly affected by structural deformation. The question remains why the corresponding activation enthalpy increases for some types of strain while it decreases for others. In the final chapter of this thesis we will therefore look back at all the activation enthalpies we explicitly computed, and look at potential structural descriptors that can be used to predict the change in activation enthalpy in response to strain.

8.1 Bromide Migration

First, we will elaborate on several common descriptors that have been used to predict the change of anion vacancy migration barriers in perovskites, most generally in response to changes in the perovskite composition [330, 331]. Firstly, we look at the intersite distance to estimate whether transitions between sites that are closer together are generally more facile than transition between sites further apart. Next, we look at two descriptors that have been developed and used to predict changes for the oxygen vacancy migration barrier between 1-NN pairs of sites in the analogous class of oxide perovskites, namely the critical radius and the metal-anion bond order.

8.1.1 Intersite Distance Approach

A first logical attempt at deriving a description is linked to the question whether transitions to more distant sites have a higher corresponding activation enthalpy compared to transi-

tions to more nearby sites. As such, we consider the cartesian distance between the two sites between which a transition can occur. More specifically, this distance is extracted from the pristine crystal under strain but in the absence of structural relaxation upon the inclusion of a vacancy. These distances are shown in Figures 8-1 to 8-3, for the structures under hydrostatic pressure and biaxial and uniaxial strain.

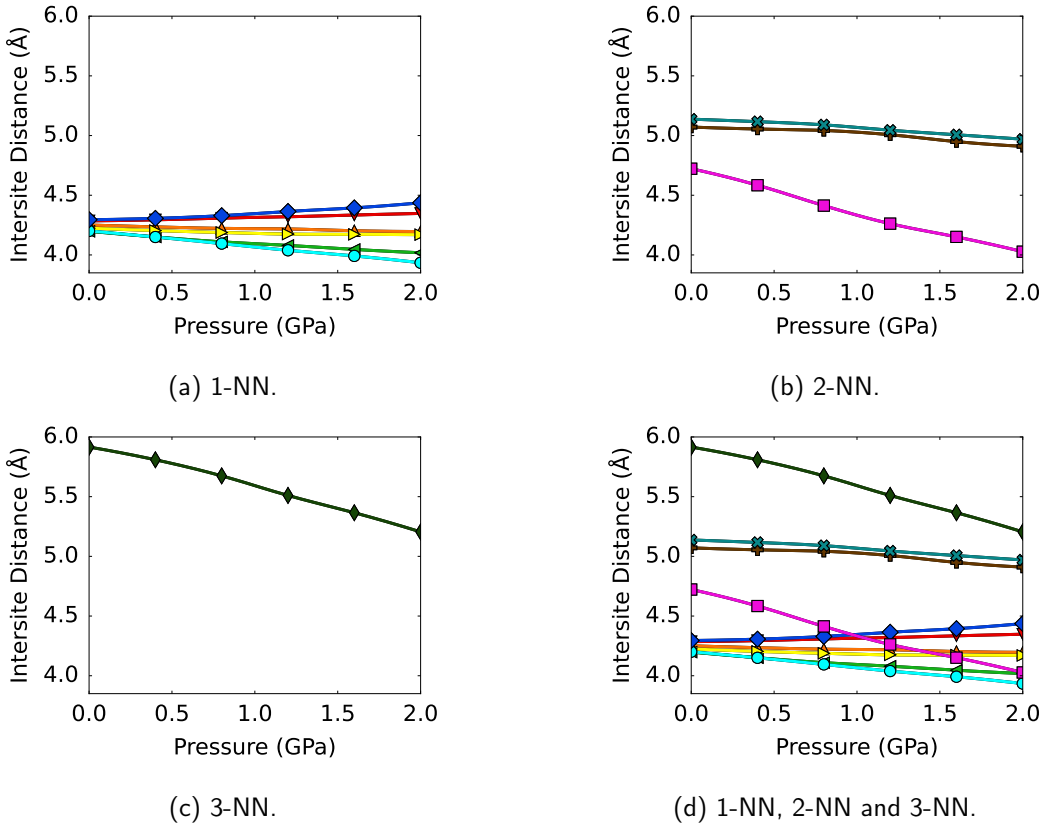

(a) 1-NN.

(b) 2-NN.

(c) 3-NN.

(d) 1-NN, 2-NN and 3-NN.

Figure 8-1: Intersite distances for anion vacancy transitions between pairs of sites belonging to the 10 sets of SEPS, labeled by '10' in Figure 5-3, as a function of hydrostatic pressure. The colour scheme is equivalent to that adopted in Figures 5-5 and 5-6. The lines provide a guide to the eye.

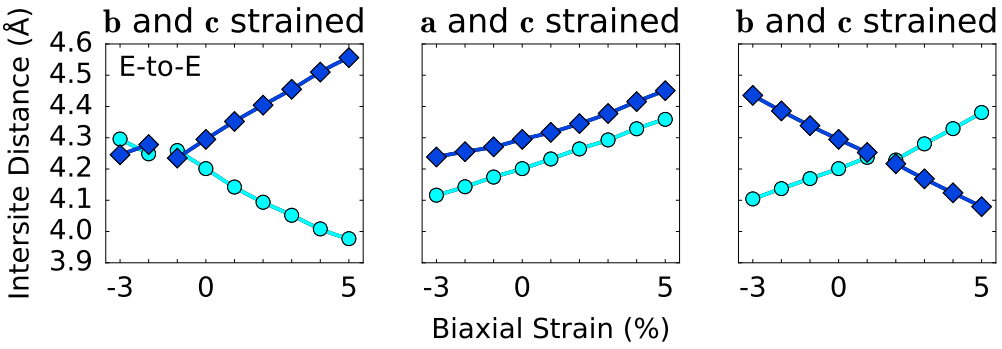

(a) 1-NN E-to-E.

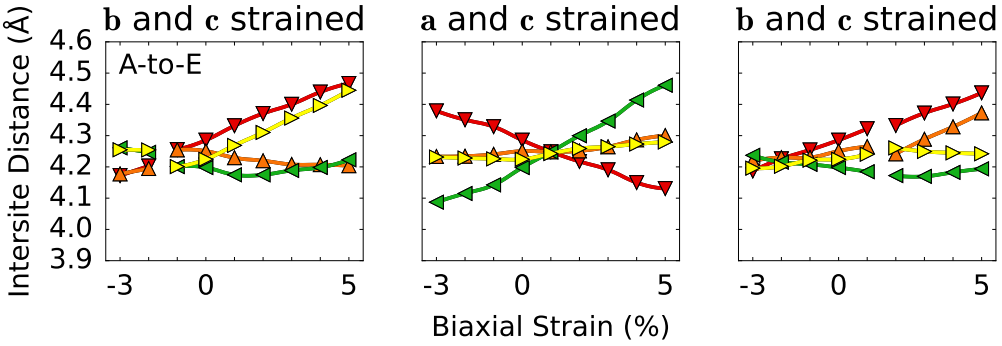

(b) 1-NN A-to-E.

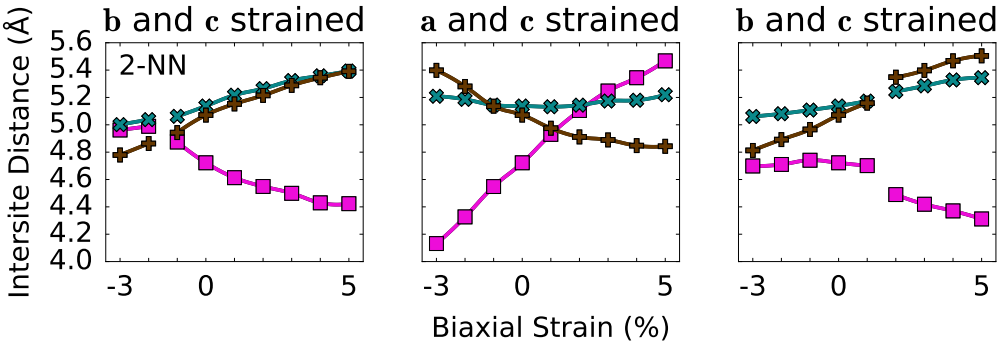

(c) 2-NN A-to-A/E-to-E.

Figure 8-2: Intersite distances for anion vacancy transitions between 1-NN and 2-NN pairs of sites, as a function of biaxial strain. Activation enthalpies are only computed for the sets of 1-NN SEPS. The colour scheme is equivalent to that adopted in Figures 5-5 and 5-6. The lines provide a guide to the eye.

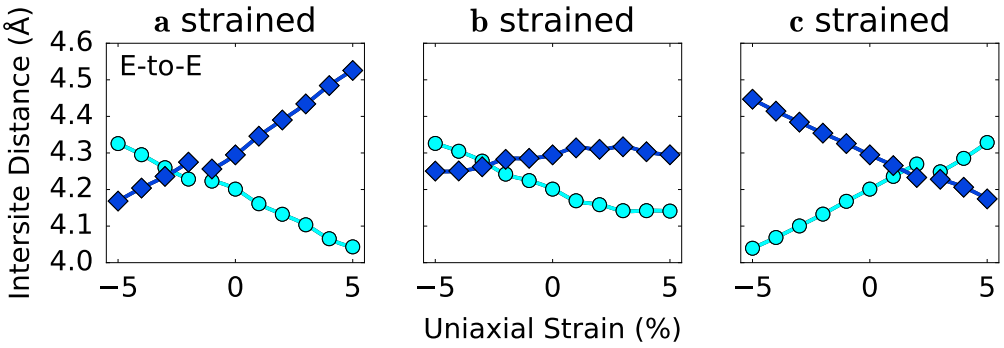

(a) 1-NN E-to-E.

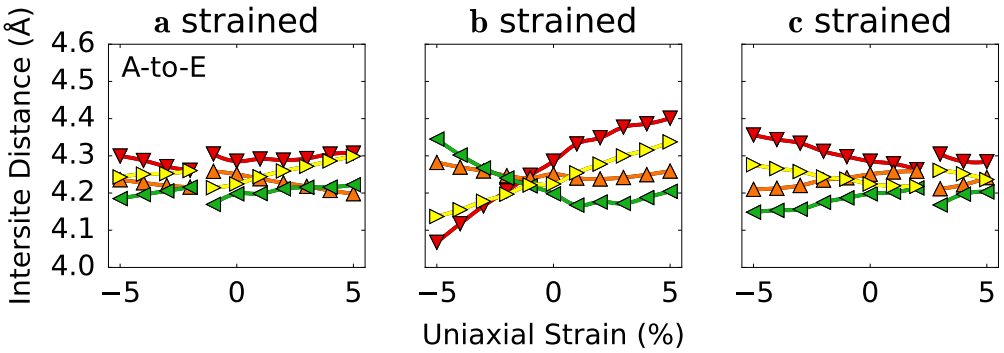

(b) 1-NN A-to-E.

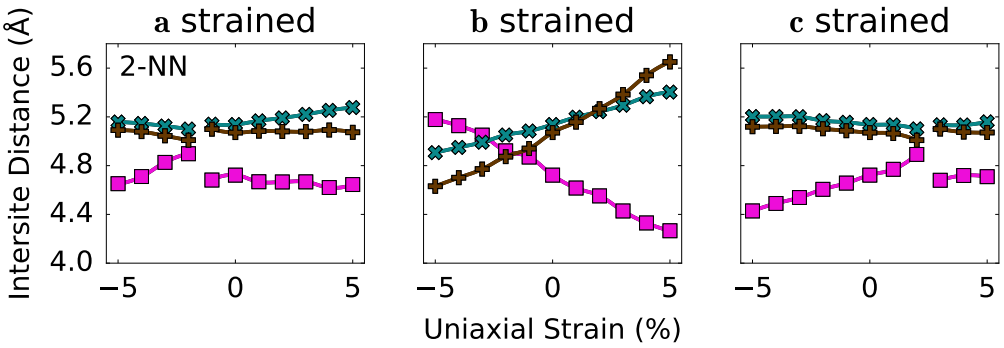

(c) 2-NN A-to-A/E-to-E.

Figure 8-3: Intersite distances for anion vacancy transitions between 1-NN and 2-NN pairs of sites, as a function of uniaxial strain. Activation enthalpies are only computed for the sets of 1-NN SEPS. The colour scheme is equivalent to that adopted in Figures 5-5 and 5-6. The lines provide a guide to the eye.

The correlation with the corresponding activation enthalpies are shown in Figure 8-4 for the results from our study on the effects of hydrostatic pressure, in which the correlations for the 1-NN, 2-NN and 3-NN are included. The combined results for hydrostatic pressure and biaxial and uniaxial strain are shown in Figure 8-5, and are limited to the sets of 1-NN SEPS.

The activation enthalpies computed in our study on the effects of hydrostatic pressure show very mixed results when correlated with the intersite distances. While the correlation is excellent for certain transitions, the cyan and green 1-NN, the magenta 2-NN and the dark green 3-NN transitions in particular, there appears to be no apparent correlation for others. Such large differences are somewhat surprising, given that despite the lower symmetry of the $Pnma$ space group compared to the aristotype, the topology is not very strongly affected. Interestingly, the correlation is best for the set of 3-NN SEPS and worst for the set of 1-NN SEPS. This need not be surprising, given that the 1-NN, 2-NN and 3-NN transitions are quite different. Schematic representations of representative cases of these transitions are shown in Figure 8-6. While in the case of 1-NN transitions, the moving ion remains close to the Pb-atom to which it is bound, this is not the case for transitions to more distant neighbours, the minimum enthalpy path of which is slightly more linear.

In our studies on the effects of biaxial and uniaxial strain, we have limited our analysis to the computation of transitions between sets of 1-NN SEPS. Again, we observe a reasonable correlation between the activation enthalpy and the intersite distance corresponding to the cyan set of SEPS, as well as for the blue set of SEPS, both of which correspond to equatorial-to-equatorial transitions. For the remaining sets of SEPS, we observe no strong correlation. Overall, we conclude that the intersite distance is a rather poor descriptor for predicting the changes in activation enthalpies, in particular for transitions between pairs of 1-NN sites, as exemplified by the low coefficient of correlation of 0.059 over the full dataset.

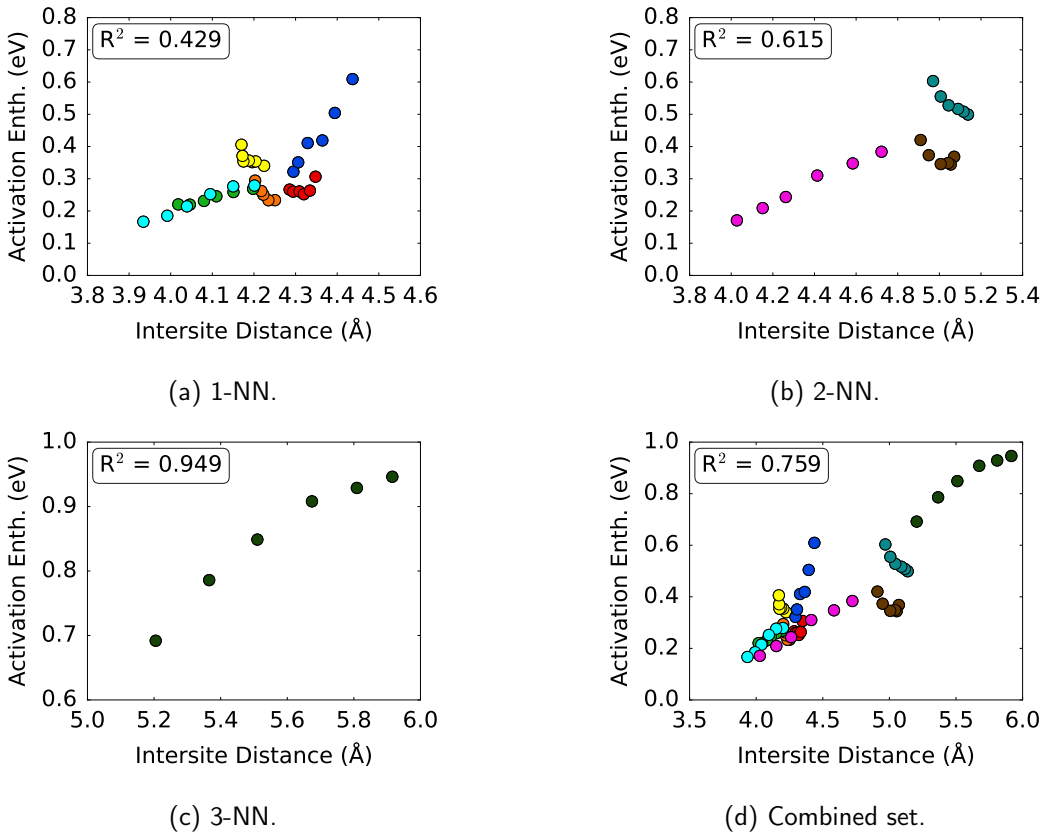

(a) 1-NN.

(b) 2-NN.

(c) 3-NN.

(d) Combined set.

Figure 8-4: Correlations between the activation enthalpy and the intersite distance for transitions between 1-NN, 2-NN and 3-NN sites in the $Pnma$ structure under hydrostatic pressure. The colour scheme is equivalent to that adopted in Figures 5-5 and 5-6.

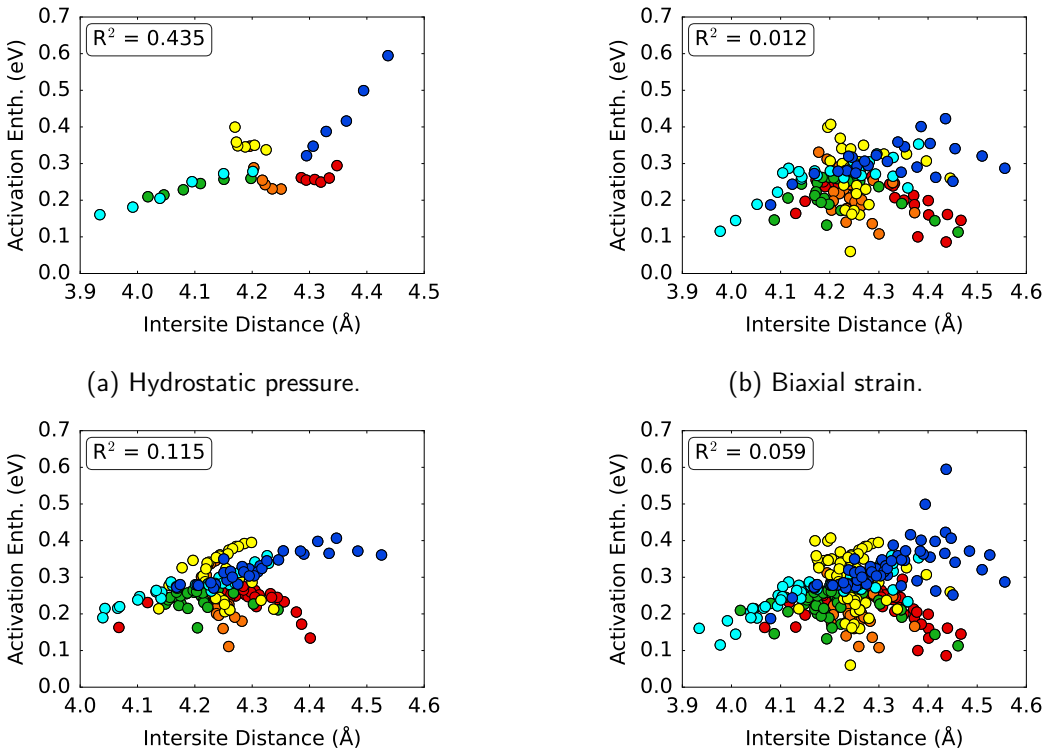

(a) Hydrostatic pressure.

(b) Biaxial strain.

(c) Uniaxial strain.

(d) Combined dataset.

Figure 8-5: Correlations between the activation enthalpy and the intersite distance for transitions between 1-NN sites in the $Pnma$ structure under hydrostatic pressure, biaxial strain and uniaxial strain. The colour scheme is equivalent to that adopted in Figures 5-5 and 5-6.

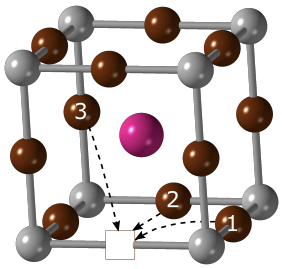

(a) Aristotype.

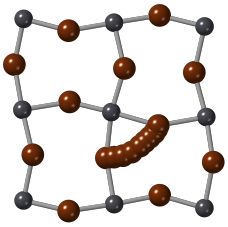

(b) 1-NN.

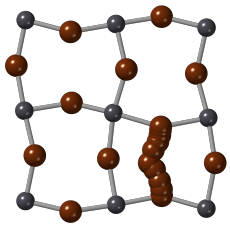

(c) 2-NN.

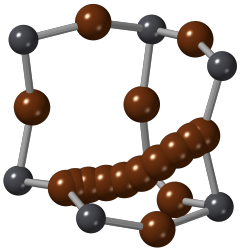

(d) 3-NN.

Figure 8-6: Schematic representations of representative cases of 1-NN, 2-NN and 3-NN transitions. The origin of their nomenclature and classificiation is depicted in (a), while minimum enthalpy trajectories are visualised for transitions between representative pairs of 1-NN (b), 2-NN (c) and 3-NN (d) sites in the orthorhombic strucure with space group $Pnma$.

8.1.2 Critical Radius Analysis

To go beyond the simple picture of the intersite distance, we look more closely at the atomic configuration at the transition state, in particular which atoms in the direct vicinity of the moving ion need to be displaced in order to facilitate the passage of the moving ion. Such questions have been investigated previously mainly for oxide migration in the oxide perovskites [332–334]. This has led to the development of a so-called critical radius model, in which the critical radius is used as a descriptor for trends in the activation energy, again mainly to compare different perovskite compositions.
A schematic representation of this critical radius is shown in Figure 8-7. It shows the atomic configuration at the transition state in the vicinity of the moving ion, which needs to pass through an opening between two A-site and one B-site cation(s).

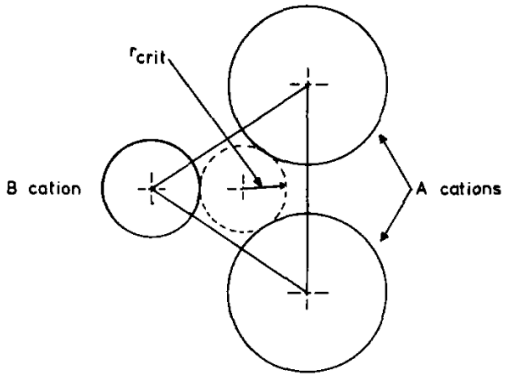

Figure 8-7: Critical radius model of the saddle point configuration for anion vacancy migration in perovskite structures. Reprinted from Reference 332, with permission from Elsevier.

The critical radius r_{c} can be derived from geometric considerations, and for the cubic aristotype it can be expressed as

$$r_{\mathrm{c}} = a_0 \left(\frac{3}{4} a_0 - \sqrt{2} r_{\mathrm{B}} \right) - \frac{(r_{\mathrm{A}} - r_{\mathrm{B}})\,(r_{\mathrm{A}} + r_{\mathrm{B}})}{2\,(r_{\mathrm{A}} - r_{\mathrm{B}}) + \sqrt{2} a_0}, \tag{8.1}$$

with a_0 the lattice constant, and with r_{A} and r_{B} the ionic radii of the A-site and B-site cations, respectively. Here, we adopt a slightly different expression, based on Reference 335, which can be formulated in terms of the Pb-Cs and Cs-Cs interatomic distances as

$$r_{\mathrm{c}} = \frac{\alpha + \beta^2 - r_{\mathrm{A}}^2 - 2\beta r_{\mathrm{A}} + r_{\mathrm{B}}^2}{2r_{\mathrm{A}} + 2\beta - 2r_{\mathrm{B}}}, \tag{8.2}$$

in which $\alpha = d_{\mathrm{AA}}^2/4$ and $\beta = \sqrt{d_{\mathrm{AB}} d_{\mathrm{AB}^*} - \alpha}$, where d_{AA} denotes the Cs-Cs distance and d_{AB} and d_{AB^*} denote the distances between the Pb-atom and either of the Cs-atoms.

These distances are computed from the structure under strain before the introduction of a vacancy.

The correlation between the activation barriers and the critical radius in the pristine structure is shown in Figure 8-8. As we can see from the very low coefficients of correlation, the critical radius does not seem to be a particularly useful descriptor to predict trends in activation enthalpy for symmetrically distinct transitions within the pristine material, nor trends in response to strain, despite its usefulness in predicting trends between different compositions in the class of oxide perovskites.

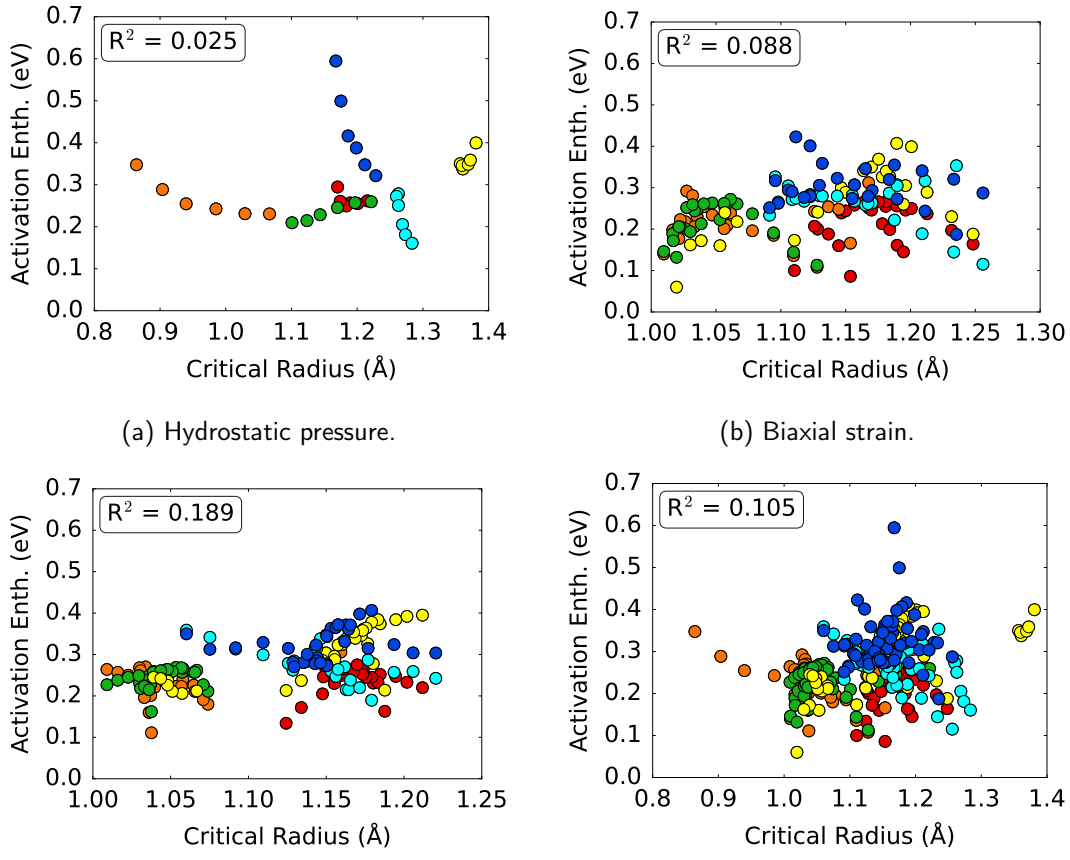

(a) Hydrostatic pressure.

(b) Biaxial strain.

(c) Uniaxial strain.

(d) Combined dataset.

Figure 8-8: Correlation between the activation enthalpy for anion vacancy migration and the critical radius, derived from the pristine structure under strain, before the introduction of a vacancy, using Equation (8.2). The colour scheme is equivalent to that adopted in Figures 5-5 and 5-6.

8.1.3 Metal-Anion Bond Order

In the case of oxygen vacancy migration, analyses have also been aimed at the average metal-oxygen bond energy [331, 333, 336, 337]. To the best of our knowledge, this analysis has not previously been extended to describe activation enthalpy differences within a single material, and hence we will aim to provide such an attempt here.
First, we analyse the Pb-Br distance during a representative transition, the results of which are shown in Figure 8-9. We observe that the Pb-Br distance shortens significantly during the transition, and reaches a minimum value at the transition state. While it is a commonly observed phenomenon that anion vacancy transitions between 1-NN sites follow a curved trajectory [87], these results indicate that along the minimum enthalpy path this curvature is not necessarily uniform.

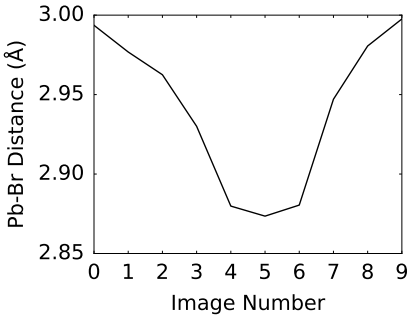

Figure 8-9: Pb-Br distance along the minimum enthalpy path for one of the 1-NN sets of E-to-E SEPS, corresponding to a transition between the pair of sites depicted in cyan (1-NN_E-to-E_1) in the absence of strain. It is well-known that the instead of being linear, the path for anion migration along an octahedral edge is typically curved. Here we show that at the transition state, corresponding to image 5, the Pb-Br distance goes through a minimum distance, which indicates that along the minimum enthalpy path the curvature is not necessarily uniform.

To show that this also holds more generally, we show the Pb-Br distance at the transition state as a function of the Pb-Br distance in the pristine structure in Figure 8-10. In this figure, the grey line along the diagonal is enveloped by a shaded area, corresponding to a 1% error margin on either side. Moreover, the dashed black lines at 3.15 Å indicate the expected Pb-Br distance based on the sum of their crystal ionic radii [338]. As we can see, the interatomic distances remain below this value, both in the pristine structure, as well as in the transition state structures, suggesting a relatively strong interaction between Pb and Br atoms. Moreover, we observe that in virtually all cases, the Pb-Br distance is lower at the transtion state than it is in the pristine structure.
Interestingly, while the range of values adopted in the pristine structure is relatively sim-

ilar, the range of values adopted at the transition state is quite different for the E-to-E transitions, shown in Figure 8-10a, compared to those for the A-to-E transitions, shown in Figure 8-10b. While the interatomic distances stay within a narrow range of 2.8–2.9 Å in the case of the A-to-E transitions, the range is about 2.75–3.00 Å in the case of the E-to-E transitions. In the cubic phase, we would have observed no such different between symmetrically inequivalent pairs of sites, which is another remarkable result of the reduced symmetry of the orthorhombic phase with space group $Pnma$.

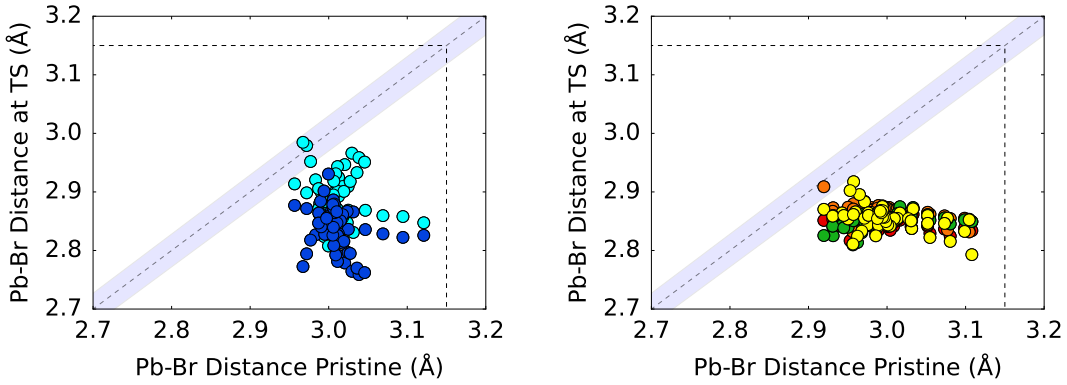

(a) E-to-E.

(b) A-to-E.

Figure 8-10: Correlation between Pb-Br distance in the initial pristine structure, and that at the transition state. The grey line along the diagonal is enveloped by a shaded area, corresponding to a 1% error margin on either side. Moreover, the dashed black lines at 3.15 Å indicate the expected Pb-Br distance based on the sum of their crystal ionic radii. The colour scheme is equivalent to that adopted in Figures 5-5 and 5-6.

The correlations between the Pb-Br interatomic distance in the pristine structure and the corresponding activation energies are shown in Figure 8-11. In general, the correlation is very poor, suggesting that the Pb-Br distance in the initial state is not a good descriptor of the activation energy. Interestingly, despite the seemingly more sensitive response for the E-to-E transitions, the correlation is actually poorer than that of the A-to-E transitions.

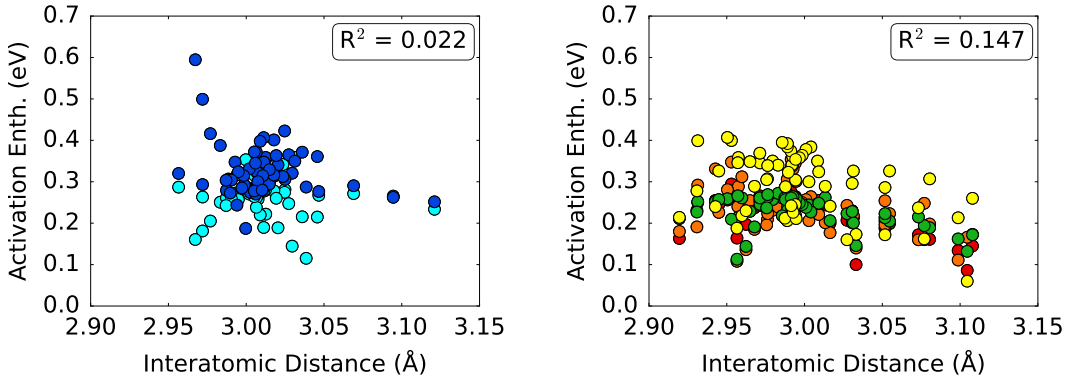

(a) E-to-E.

(b) A-to-E.

Figure 8-11: Correlation between Pb-Br distance in the initial pristine structure and the corresponding activation enthalpy. The colour scheme is equivalent to that adopted in Figures 5-5 and 5-6.

8.1.4 Predictions from Elasticity Theory

Finally, we consider the dependence of the activation enthalpy, as predicted by linear response theory, described in more detail in Section 3.7. In particular, we use the elastic dipole tensor to compute activation enthalpy changes, as described previously in Equation (3.110) and which we state here again for clarity.

$$\begin{aligned} H_a &= H_a^0 - (\boldsymbol{P}_{ij}^{\ddagger} - \boldsymbol{P}_{ij})\boldsymbol{\epsilon}_{ij}, \\ &= H_a^0 - \Delta\boldsymbol{P}_{ij}\boldsymbol{\epsilon}_{ij}. \end{aligned} \tag{8.3}$$

In general, stress-dependent calculations require a high cut-off energy to reach convergence. Below, we will test the convergence of the elastic dipole tensor components.

8.1.4.1 Convergence Test

We test the convergence of the components of the elastic dipole tensor for the initial state $\boldsymbol{P}_{ij}$, transition state $\boldsymbol{P}_{ij}^{\ddagger}$ and their difference $\Delta\boldsymbol{P}_{ij} = \boldsymbol{P}_{ij}^{\ddagger} - \boldsymbol{P}_{ij}$, and show the results in Figure 8-12. While we observe that both $\boldsymbol{P}_{ij}$ and $\boldsymbol{P}_{ij}^{\ddagger}$ only reach convergence at a cutoff energy of about 450 eV, the difference is well-converged already at 300 eV. Hence, we can use the results from our calculations at 300 eV to compute the elastic dipole tensor components and predict the change in migration enthalpy in response to general strain.

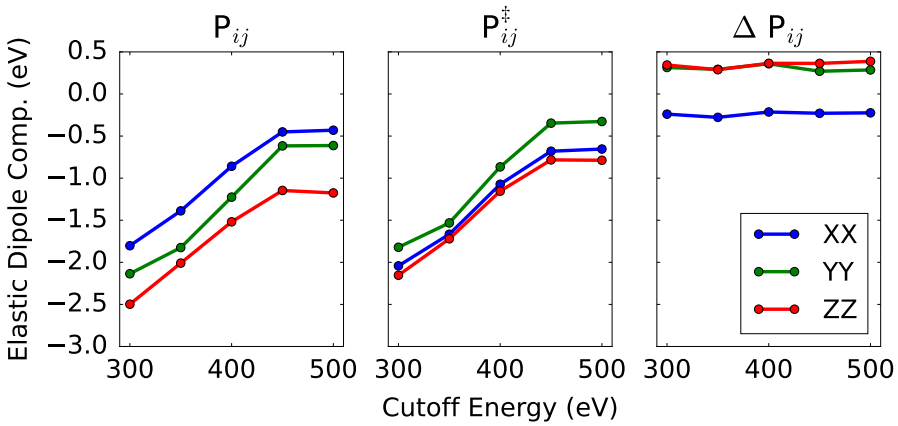

Figure 8-12: Convergence of the components of the elastic dipole tensor for the initial state $\boldsymbol{P}_{ij}$, transition state $\boldsymbol{P}^{\ddagger}_{ij}$ and their difference $\Delta\boldsymbol{P}_{ij} = \boldsymbol{P}^{\ddagger}_{ij} - \boldsymbol{P}_{ij}$, corresponding to a transition between the pair of sites depicted in cyan (1-NN_E-to-E_1) in the absence of strain.

8.1.4.2 Results for Bromide Migration

Using the linear response theory, the changes in the activation enthalpies can thus be derived from an effective dipole tensor, which we derive from the initial and transition states in the absence of strain, in combination with the structural deformation resulting from the stress we apply. The predictions and computed values for the evolution of the activation enthalpies are shown for the E-to-E transitions in Figures 8-13 to 8-15, and for the A-to-E transitions in Figures 8-16 to 8-18. In these, the predictions are shown as solid lines, with alternating black and coloured sections, the colours corresponding to those presented in Figures 5-5 and 5-6. We emphasize that though these lines do not appear to be linear, the predictions are linear and the variations in the slope are due to the non-linear evolution of the lattice vectors. The explicitly computed values are shown by coloured markers, again following the colour scheme of Figures 5-5 and 5-6.

Overall, we find that though the trends predicted by the linear response theory are generally qualitatively correct for small deformations, the predictions become noticably poorer the higher the level of strain. It is therefore a suitable tool to identify which transitions are likely sensitive in a general direction, or to find the general type of strain to which a transition is most sensitive. Despite its qualities in predicting qualitative trends, we conclude that to obtain quantitatively correct values for the activation enthalpies, explicit calculations are nevertheless necessary, in line with previous studies on the linear response theory [320].

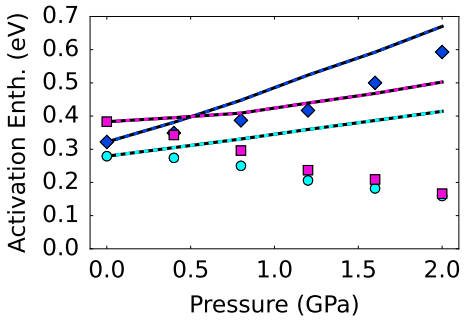

Figure 8-13: Linear predictions (solid lines) compared to computed values (marked points) of the evolution of the activation enthalpy of E-to-E transitions in response to hydrostatic pressure. The colour scheme is equivalent to that adopted in Figures 5-5 and 5-6.

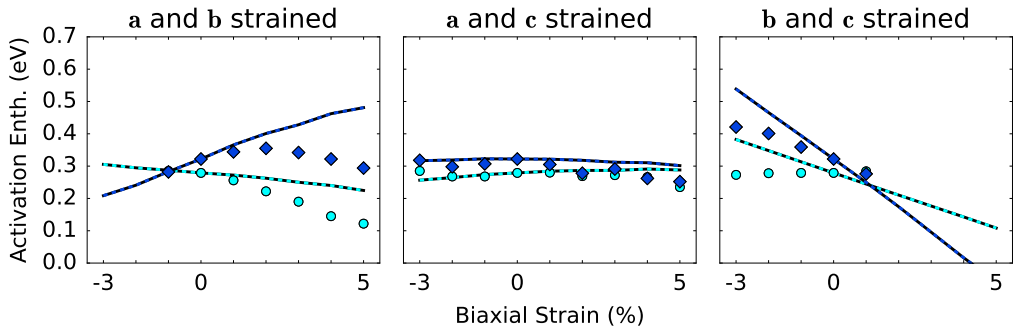

Figure 8-14: Linear predictions (solid lines) compared to computed values (marked points) of the evolution of the activation enthalpy of E-to-E transitions in response to biaxial strain. The colour scheme is equivalent to that adopted in Figures 5-5 and 5-6.

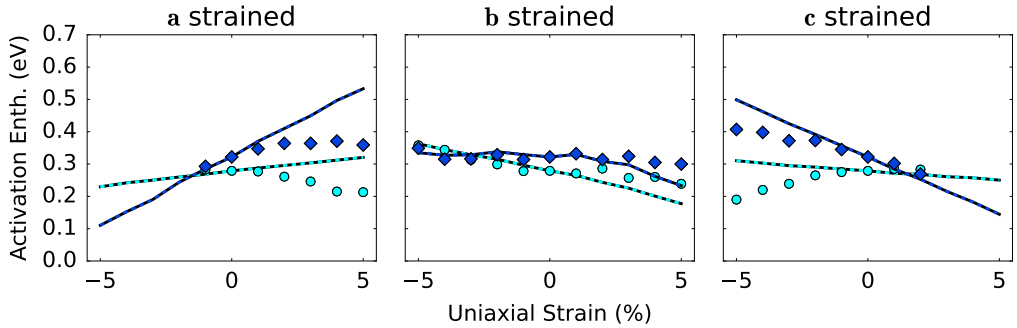

Figure 8-15: Linear predictions (solid lines) compared to computed values (marked points) of the evolution of the activation enthalpy of E-to-E transitions in response to uniaxial strain. The colour scheme is equivalent to that adopted in Figures 5-5 and 5-6.

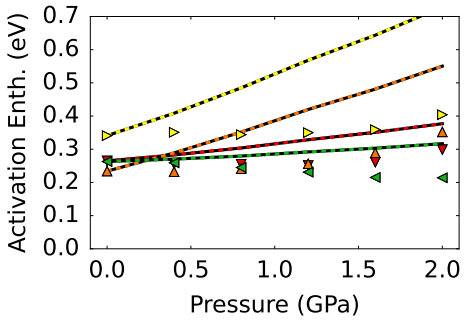

Figure 8-16: Linear predictions (solid lines) compared to computed values (marked points) of the evolution of the activation enthalpy of A-to-E transitions in response to hydrostatic pressure. The colour scheme is equivalent to that adopted in Figures 5-5 and 5-6.

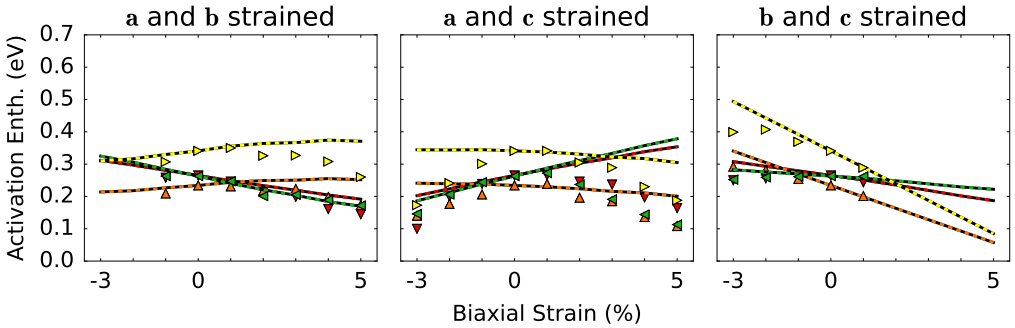

Figure 8-17: Linear predictions (solid lines) compared to computed values (marked points) of the evolution of the activation enthalpy of A-to-E transitions in response to biaxial strain. The colour scheme is equivalent to that adopted in Figures 5-5 and 5-6.

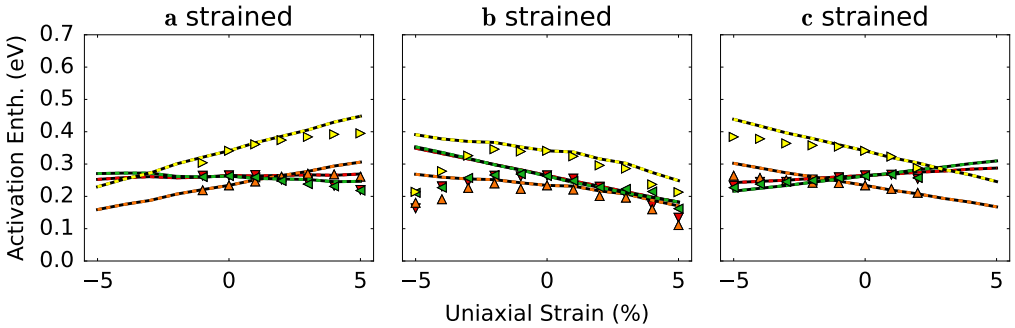

Figure 8-18: Linear predictions (solid lines) compared to computed values (marked points) of the evolution of the activation enthalpy of A-to-E transitions in response to biaxial strain. The colour scheme is equivalent to that adopted in Figures 5-5 and 5-6.

8.1.5 Other Methods

Other approaches have been to look material properties such as the Goldschmidt tolerance factor and the lattice free volume, which is the volume of the lattice minus the volume taken up by the ions [331, 333, 336, 337, 339]. Though these approaches have been useful in predicting trends between different compositions, they are not useful to describe the anisotropy in any given material, since these descriptors do not include any information on the anistropy of the system.

8.2 Caesium Migration

We will now analyse various descriptors for A-site cation migration. We first analyse the predictive power of the intersite distance, after which we consider an anion aperture model from the literature, and our own extension thereof.

8.2.1 Intersite Distance Approach

Similar to the case of bromide, we first consider the intersite distance between the pair of sites for a given hop as a potential descriptor. A schematic representation of this intersite distance is shown in Figure 8-19, in which the Cs sites occupying two neighbouring PbBr 'cages', being first-nearest neighbours of each other, are connected by a simple stick.

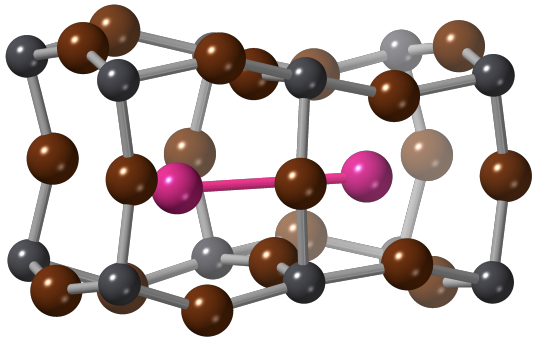

Figure 8-19: Schematic representation of the intersite distance between a pair of 1-NN Cs sites. Caesium, lead and bromide atoms are shown in pink, grey and brown colours, respectively.

Again our hypothesis is that the further these sites are apart, the harder it might be for an

ion to hop between them, with a higher corresponding activation enthalpy. The intersite distances between the pairs of sites belonging to the different sets of SEPS are shown for the different types of strain in Figures 8-20a, 8-21a and 8-22a, and can be seen to change noticably with strain.

We then look at the activation enthalpies for a transition between two Cs sites, as a function of the intersite distance, as shown in Figures 8-20b, 8-21b and 8-22b. There appears to be no clear correlation between the activation enthalpy and the intersite distance; in some cases the activation enthalpy increases with increasing intersite distance while in others the activation enthalpy shows the opposite tendency. The lack of correlation is also apparent from the low values for the coefficient of determination R^2. Hence, the intersite distance does not seem to be a useful descriptor for the change in activation enthalpy as a function of strain.

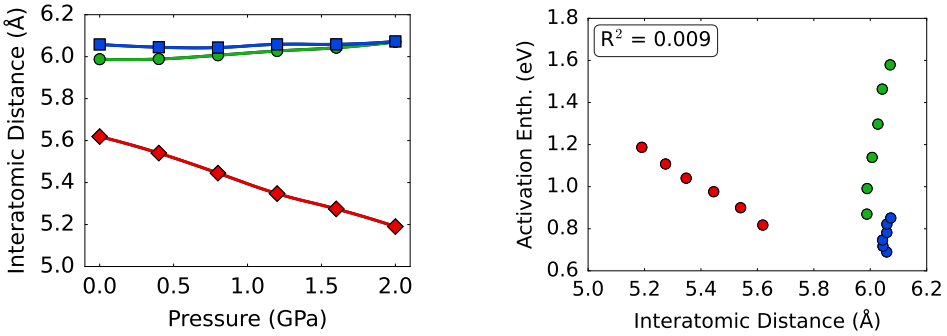

(a) Evolution of the intersite distance as a function of hydrostatic pressure.

(b) Correlation between the intersite distance and the activation enthalpy.

Figure 8-20: Evolution of the intersite distance between pairs of 1-NN Cs sites in the strained structure, before the inclusion of a vacancy, as a function of hydrostatic pressure (a), along with its correlation with the corresponding activation energy for a transition between these pairs of sites (b). The colour scheme is equivalent to that adopted in Figure 4-8. The lines provide a guide to the eye.

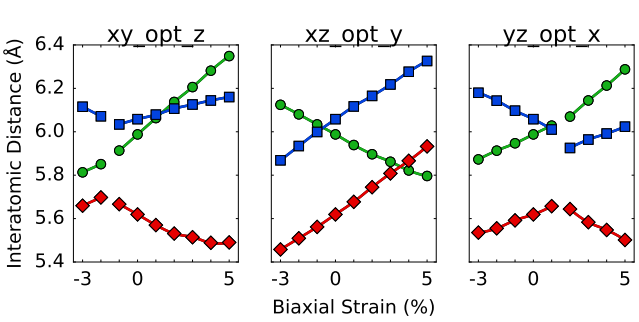

(a) Evolution of the intersite distance under biaxial strain.

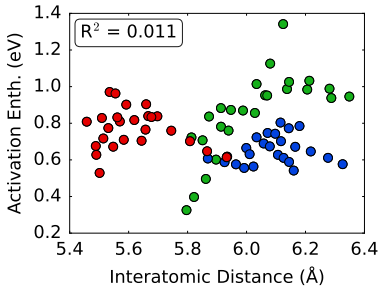

(b) Correlation between the intersite distance and the activation enthalpy.

Figure 8-21: Evolution of the intersite distance between pairs of 1-NN Cs sites in the strained structure, before the inclusion of a vacancy, as a function of biaxial strain (a), along with its correlation with the corresponding activation energy for a transition between these pairs of sites (b). The colour scheme is equivalent to that adopted in Figure 4-8. The lines provide a guide to the eye.

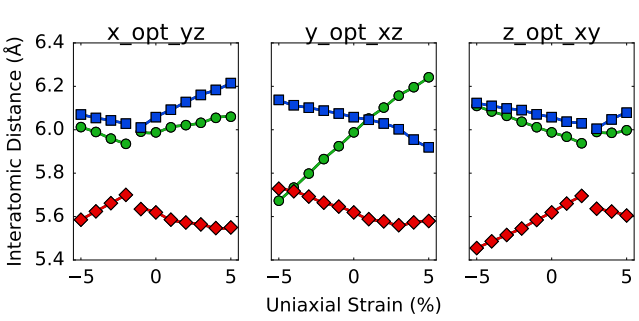

(a) Evolution of the intersite distance under uniaxial strain.

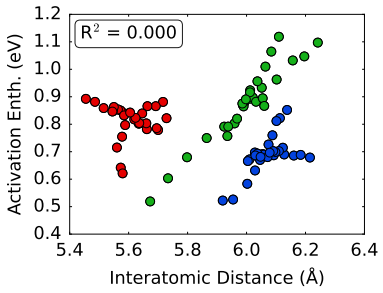

(b) Correlation between the intersite distance and the activation enthalpy.

Figure 8-22: Evolution of the intersite distance between pairs of 1-NN Cs sites in the strained structure, before the inclusion of a vacancy, as a function of uniaxial strain (a), along with its correlation with the corresponding activation energy for a transition between these pairs of sites (b). The colour scheme is equivalent to that adopted in Figure 4-8. The lines provide a guide to the eye.

8.2.2 Halide Aperture Approach

To go beyond the simplistic picture of the intersite distance, we introduce an atomistic model that has been developed for A-site cation migration in oxide perovskites [340–342]. This model is based on the observation that the A-site cation has to pass through an effective aperture, spanned by four X-site anions, and which must be sufficiently large to facilitate the passage of the A-site cation. A schematic representation of the minimum enthalpy path is shown in Figure 8-23a, and schematic representations of the aperture are shown in Figures 8-23b and 8-23c, corresponding to the structure under strain, before the introduction of a vacancy, and a representative transition state. The four X-site halides spanning the aperature are denoted by the letters S and L, standing for short and long, respectively; in the initial state, shown in Figure 8-23b, the interatomic distance between the S-denoted halide atoms is much smaller than the interatomic distance between the L-denoted atoms. At the transition state, the octahedra in the vicinity of the moving ion are strongly distorted, such that the interatomic distance between the S-denoted atoms is greatly increased, while the interatomic distance between the L-denoted atoms is much less affected. We note that in such cases, a distinction between long and short pairs of sites is less straightforward, but because of the topological correspondence of the atoms between the initial and transition state, we adopt the same nomenclature also for the transition state.

A structural overlay of the atomic displacements for a representative transition in the unstrained system, the transition along the [010] direction, depicted in green in Figure 4-8 to be precise, is shown in Figure 8-24. The atomic positions in the initial state are shown by dotted lines and spheres, while the atomic positions in the transition state are shown using solid bonds and spheres. As can be seen, the structural relaxation is mostly confined to the near vicinity of the moving ion. Noticable displacements can be observed for both bromide and lead atoms, though the displacement is by far largest for the S-denoted bromide atoms. To gain further insight in the structural differences that can best explain the changes in activation enthalpy under certain types of strain, we show the structural displacements corresponding to the transitions for which we find the highest and lowest activation enthalpies for caesium migration in our full dataset, as shown in Figure 8-25. The highest activation energy in our dataset, having a value of 1.58 eV, corresponds to a transition under a hydrostatic pressure of 2.0 GPa. The lowest activation energy, having a value of only 0.33 eV, corresponds to a transition under 5% biaxial strain in the [100] and [001] directions. Both of these transitions correspond to the same set of SEPS, namely the transition roughly along [010], depicted by green sticks in Figure 4-8, which we previously found to be the most sensitive to strain.

In both cases the structural relaxation appears to be strongest for the pair of S-denoted

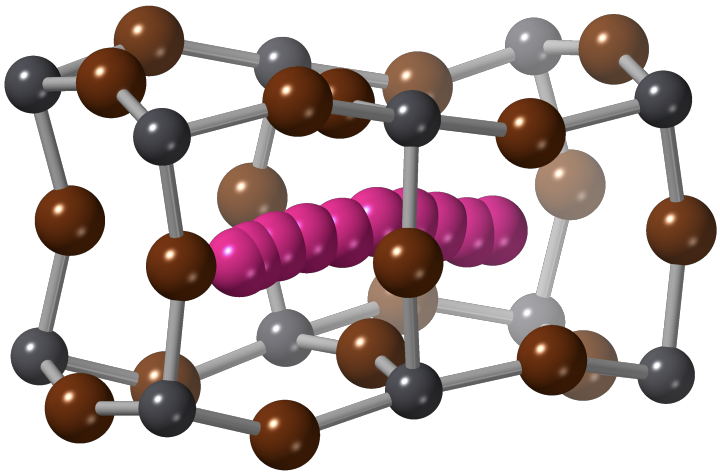

(a) Schematic representation of the minimum enthalpy path for transitions between a pair of 1-NN Cs sites, with pink spheres indicating the position of the moving ion during a transition. For clarity, the lead-halide framework is kept fixed at the configuration of the initial state.

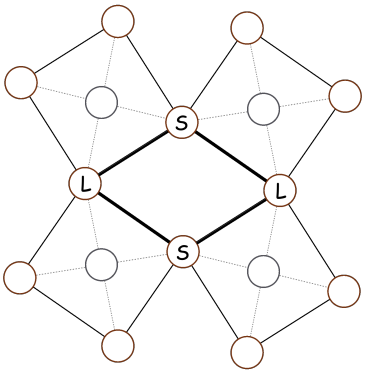

(b) Schematic representation of the halide aperture in the structure under strain.

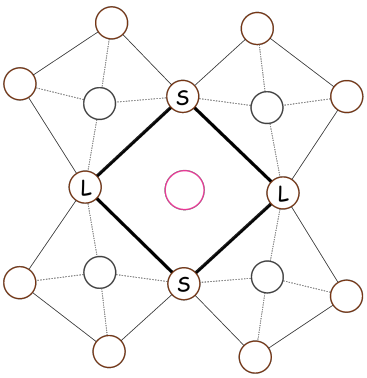

(c) Schematic representation of the halide aperture at the transition state.

Figure 8-23: Schematic representations of the minimum enthalpy path (a) and the halide aperture in the structure under strain (b) and at the transition state (c) for transitions between pairs of Cs 1-NN lattice sites. The schematic representation in (b) corresponds to the bulk structure under strain, but before the inclusion of a vacancy. Caesium, lead and bromide atoms are shown in pink, grey and brown colours, respectively.

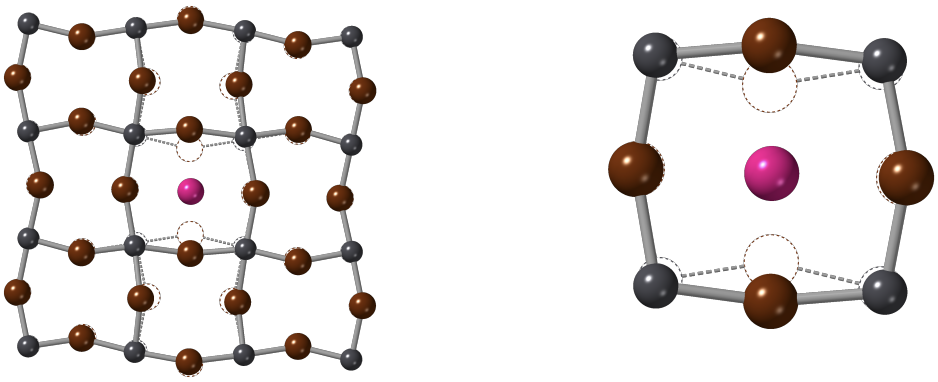

(a) (b)

Figure 8-24: View down [010] showing a migrating Cs ion at the saddle point and the consequent local relaxation of the surrounding ions in the absence of strain 0.0 GPa. The unfilled spheres depict the atomic postions in the pristine structure, with the dashed line representing the migration aperture before relaxation. Caesium, lead and bromide atoms are shown in pink, grey and brown colours, respectively.

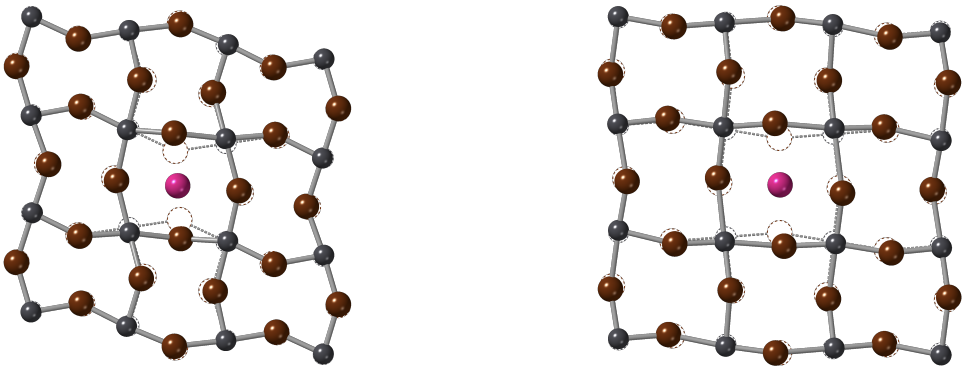

(a) (b)

Figure 8-25: View down [010] showing a migrating Cs ion at the saddle point and the consequent local relaxation of the surrounding ions at +5% biaxial strain in the [100] and [001] directions (a) and 2.0 GPa (b), with corresponding activation enthalpies of 0.33 and 1.58 eV. The dashed line represents the migration aperture before relaxation. Caesium, lead and bromide atoms are shown in pink, grey and brown colours, respectively.

atoms. Interestingly, the overall structural relaxation seems much more confined to the near vicinity of the moving ion in Figure 8-25a, while the structural relaxation clearly extends beyond the first shell of four bromide and four lead atoms in Figure 8-25b. This observation can be reconciled with the fact that under severe compressive strain, resulting from the hydrostatic pressure, the overall volume is strongly reduced, which gives the atoms less room to relax. In contrast, the volume is greatly increased with tensile strain, such that atoms can relax more freely to accommodate the moving ion.

8.2.2.1 d_{SS} as a Descriptor

In a previous study on A-site cation diffusion in $LaMnO_3$, the initial interatomic distance between the S-denoted atoms was found to be strongly correlated to the activation enthalpy [340]. Here we test the same correlation, looking at the interatomic distance between the pair of S-denoted sites in the strained system, not taking into account any structural relaxation related to the introduction of a vacancy. We denote this distance d_{SS}, and show how it changes with strain in Figures 8-26a, 8-27a and 8-28a.
This interatomic distance d_{SS} can either increase or decrease, depending on the level and type of strain, and can be linked to the the relative level of tilting of the octahedra in response to strain. Its correlation with the associated activation enthalpy for caesium vacancy transitions is shown in Figures 8-26b, 8-27b and 8-28b. Indeed, we find that the correlation between the activation enthalpy and d_{SS} is stronger than the correlation with the intersite distance, as indicated by the higher coefficients of determination, in the range of 0.714–0.763. The value for d_{SS}, and particularly how it changes with strain, can thus be a useful descriptor to predict the trends for the activation enthalpy under strain.

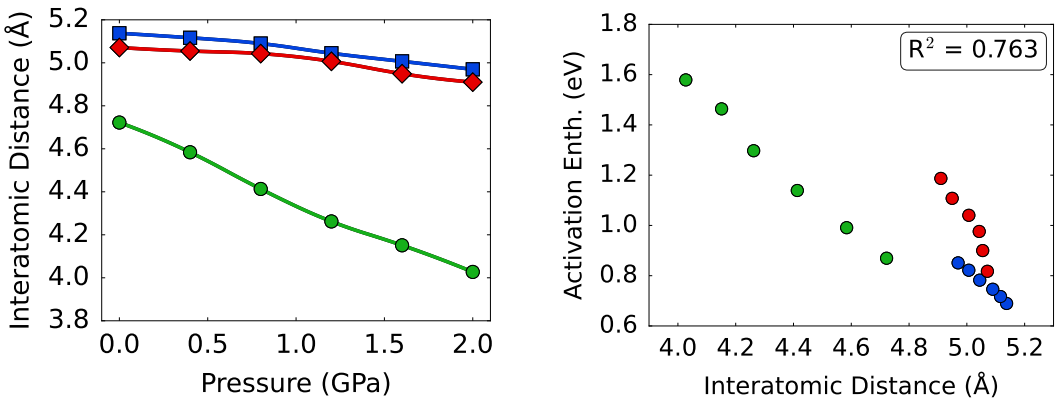

(a) (b)

Figure 8-26: Evolution of d_{SS} as a function of hydrostatic pressure (a), along with its correlation with the corresponding activation energy (b). The value of d_{SS} is obtained from the structure under strain, not taking into account structural relaxations due to the introduction of a vacancy. The colour scheme is equivalent to that adopted in Figure 4-8. The lines provide a guide to the eye.

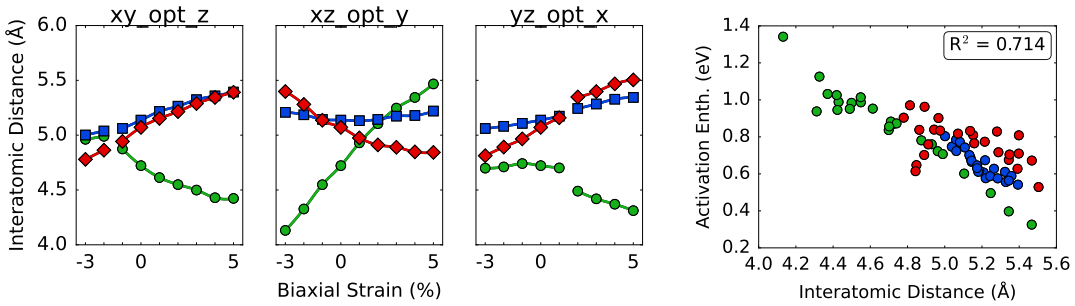

(a) (b)

Figure 8-27: Evolution of d_{SS}, defined as the interatomic distance between the two S-denoted sites of the aperture in the strained system, as a function of biaxial strain (a), along with its correlation with the corresponding activation energy (b). The value of d_{SS} is obtained from the structure under strain, not taking into account structural relaxations due to the introduction of a vacancy. The colour scheme is equivalent to that adopted in Figure 4-8. The lines provide a guide to the eye. The colour scheme is equivalent to that adopted in Figure 4-8. The lines provide a guide to the eye.

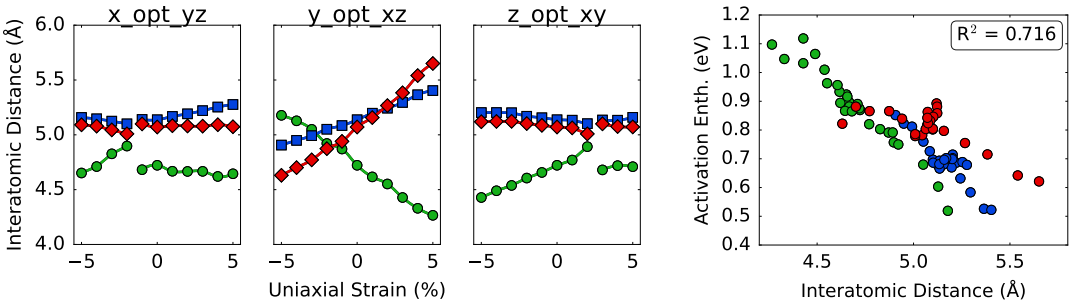

(a) (b)

Figure 8-28: Evolution of d_{SS} as a function of uniaxial strain (a), along with its correlation with the corresponding activation energy (b). The value of d_{SS} is obtained from the structure under strain, not taking into account structural relaxations due to the introduction of a vacancy. The colour scheme is equivalent to that adopted in Figure 4-8. The lines provide a guide to the eye.

8.2.2.2 Aperture Area as a Descriptor

Based on the previous analysis, we can thus conclude that the interatomic distance d_{SS} is a useful descriptor to predict changes in the activation enthalpy as a function of strain. It is, to the best of our knowledge, the prevailing descriptor for A-site cation migration in perovskites. However, not only the distance between the S-denoted anion sites needs to be sufficiently large to accommodate the moving ions, but so should the distance between the L-denoted anions. To test whether the d_{SS} descriptor can be improved upon, we thus wish to include some description of d_{LL}, which we do by computing the effective area of the aperture. Under the assumption that the aperture can be considered as a diamond, the effective area can be approximated as half of the product of the diagonals, i.e. the effective aperture Δ_{SSLL} can be calculated from

$$\Delta_{\mathrm{SSLL}} = \frac{1}{2} d_{\mathrm{SS}} d_{\mathrm{LL}}, \tag{8.4}$$

in which d_{SS} and d_{LL} are the distances between the S-denoted and L-denoted bromide atoms. Though the S- and L-denoted bromide are not always coplanar, deviations from coplanarity are sufficiently small that this measure of the effective aperture is sufficiently accurate to test it as a possible descriptor for the changes we observe in the activation enthalpy as a function of strain. The effective apertures are shown as a function of strain in Figures 8-29a, 8-30a and 8-34a, along with the correlation between these apertures and the activation enthalpies, the results of which are shown in Figures 8-29b, 8-30b and 8-31b. The correlation we find is very good, exemplified by the high coefficients of determination

in the range 0.837–0.989. The effective area seems to be particularly good at predicting changes in the activation enthalpy under hydrostatic pressure, for which the value of R^2 is as high as 0.989. For comparison, both the correlation of the activation enthalpy with d_{SS} and Δ_{SSLL} are shown side-by-side in Figure 8-32. From these figures, it is clear that the full aperture area is a signficant improvement as a descriptor, when compared to simply the interatomic distance d_{SS}, with an increased R^2 from 0.691 to 0.867.

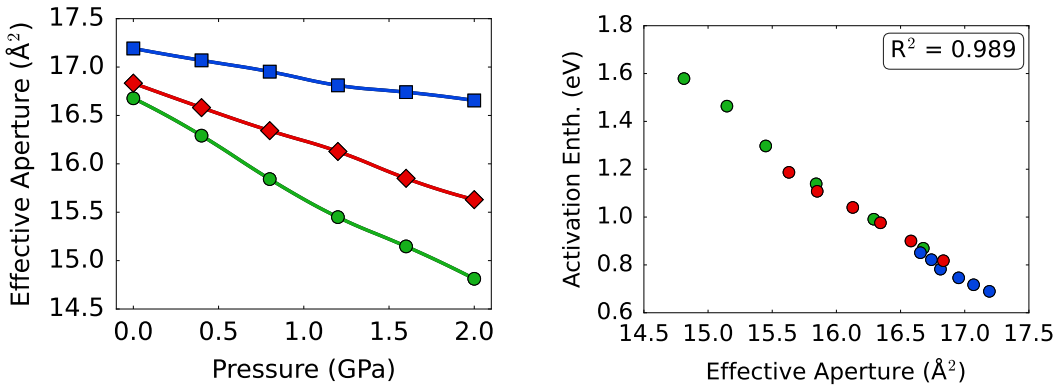

(a) (b)

Figure 8-29: Evolution of Δ_{SSLL} as a function of hydrostatic pressure (a), along with its correlation with the corresponding activation energy (b). The values of d_{SS} and d_{LL} used to compute Δ_{SSLL} are obtained from the structure under strain, not taking into account structural relaxations due to the introduction of a vacancy. The colour scheme is equivalent to that adopted in Figure 4-8. The lines provide a guide to the eye.

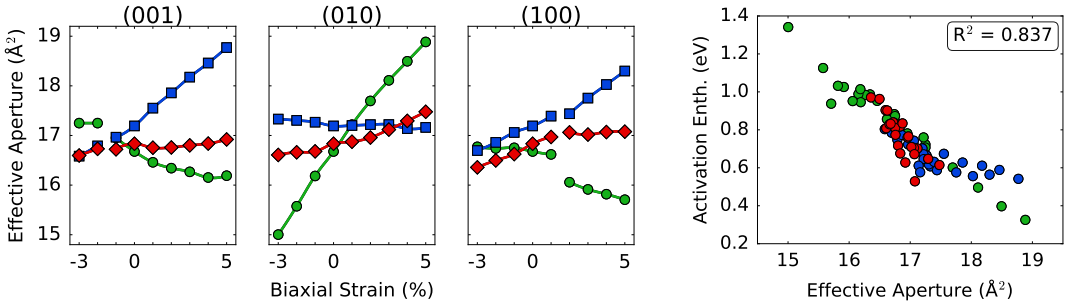

(a) (b)

Figure 8-30: Evolution of Δ_{SSLL} as a function of biaxial strain (a), along with its correlation with the corresponding activation energy (b). The values of d_{SS} and d_{LL} used to compute Δ_{SSLL} are obtained from the structure under strain, not taking into account structural relaxations due to the introduction of a vacancy. The colour scheme is equivalent to that adopted in Figure 4-8. The lines provide a guide to the eye.

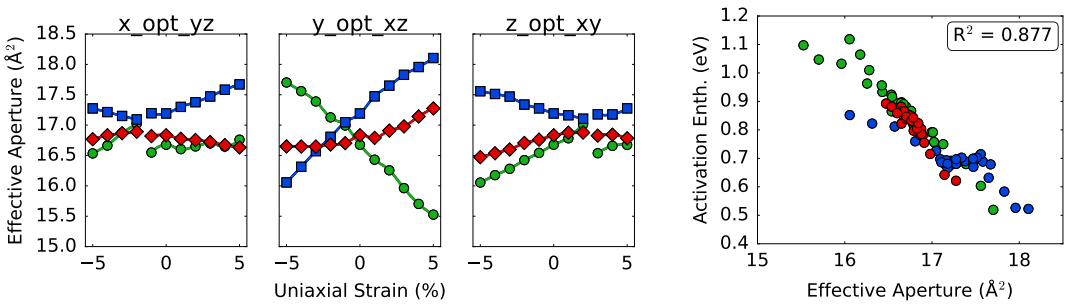

(a) (b)

Figure 8-31: Evolution of Δ_{SSLL} as a function of uniaxial strain (a), along with its correlation with the corresponding activation energy (b). The values of d_{SS} and d_{LL} used to compute Δ_{SSLL} are obtained from the structure under strain, not taking into account structural relaxations due to the introduction of a vacancy. The colour scheme is equivalent to that adopted in Figure 4-8. The lines provide a guide to the eye.

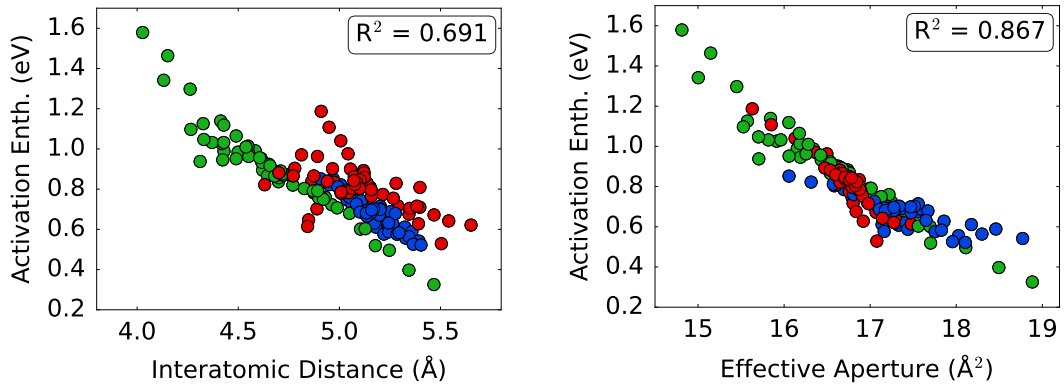

(a) (b)

Figure 8-32: Comparison of the correlation between the activation enthalpy for A-site cation vacancy migration and the shortest anion-anion distance (a) and the effective aperture area (b), which we find gives a significantly improved correlation for A-site cation migration in $CsPbBr_3$. The data are a compilation of the results from the studies on hydrostatic pressure, biaxial strain and uniaxial strain. The colour scheme is equivalent to that adopted in Figure 4-8.

We also show the change in effective aperture area upon the introduction of a vacancy, and at the transition state, both as a function of the initial effective aperture area in the pristine structure under strain in Figure 8-33. From Figure 8-33a, we observe that the effective aperture area generally increases slightly upon the introduction of a vacancy, though the changes are not very large as can be observed from the proximity to the line $x = y$. As a result, the aperture area in the vacancy structure will likely also be a good predictor for the migration enthalpy of caesium vacancy migration, but since it involves an extra step to obtain, we consider it a less useful descriptor.

As we could already observe from Figures 8-23 to 8-25, the structural relaxation is much more pronounced in the transition state, where the aperture is 'opened up' to facilitate the passage of the moving caesium atom. We show the effective surface area at the transition state as a function of the aperture area in the pristine structure under strain in Figure 8-33b. As expected, the aperture area shows a significant increase to values of about 23–25 $Å^2$, with the vast majority just above 24 $Å^2$. Though one could expect that the effective aperture area at the transition state does not strongly depend on strain and is more or less constant, it is interesting to observe that this expectation is not quite met as the range of values is still rather large.

Finally, we show the values for d_{SS} and d_{LL} in the initial and transition states in Figure 8-34, both as a function of their respective values in the structure under strain, not taking into account structural relaxations due to the introduction of a vacancy. Because of the large

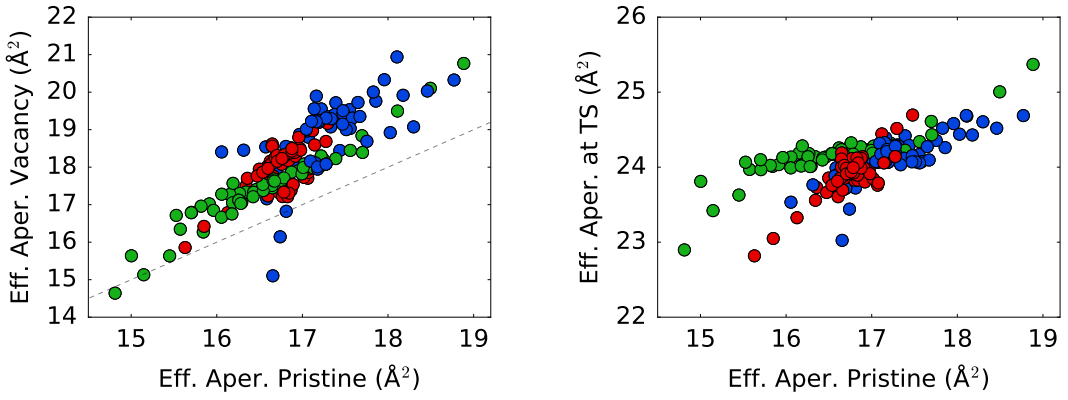

(a) (b)

Figure 8-33: Change in the effective aperture area Δ_{SSLL} upon structural relaxation due to the inclusion of a vacancy (a) and in adopting the transition state (TS) (b), both relative to the effective aperture area in the structure under strain, not taking into account structural relaxations due to the introduction of a vacancy. The colour scheme is equivalent to that adopted in Figure 4-8. The dotted line indicates $y = x$.

difference in their values in the pristine structure under strain, we can easily separate them visually, and group them in boxes denoted with d_{SS} and d_{LL}. Similar to the case of the effective aperture area, we observe that d_{SS} and d_{LL} show only a slight increase linked to the structural relaxation upon the introduction of a vacancy. At the transition state, the value of d_{SS} is increased significantly, from a range of roughly 4–5.6 Å to a range of roughly 6.5–7.0 Å. The change in d_{LL} is much smaller, going from a range of roughly 6–7.4 Å to a range of 6.8–7.2 Å. In general, these distances are thus increased to allow the passage of the moving caesium ion, though it is interesting to note that d_{LL} decreases in a few cases. Moreover, the range of values at the transition state is much smaller than in either the structure under strain in the absence of a vacancy or the initial vacancy state. This begs the question whether some threshold distance needs to be reached in order to accommodate the moving Cs ion.

To answer this question, we look at the distances at the transition state between the moving caesium ion and the bromide ions spanning the aperture. There are four such Cs-Br distances at the transition state, two corresponding to the S-denoted and two corresponding to the L-denoted bromide atoms. The distance between the caesium ion and one of the S-denoted bromide atom is plotted versus the distance between the caesium ion and the other S-denoted bromide atom, and likewise for the L-denoted bromide atoms. In doing so, we can verify how close the caesium ion gets to the bromide atoms, but also to what extent the caesium atom is halfway between the pairs of S- and L-denoted bromide atoms. The

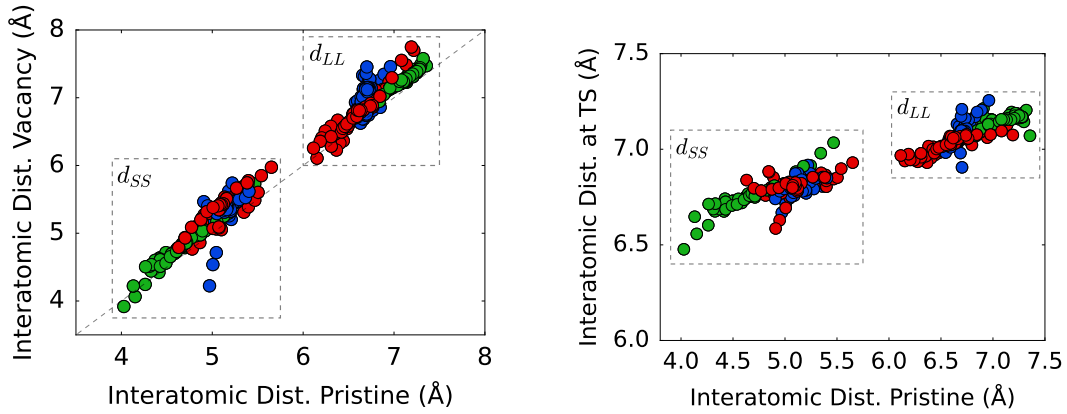

(a) (b)

Figure 8-34: Change in the interatomic distances between the S- and L-denoted halides upon structural relaxation due to the inclusion of a vacancy (a) and in adopting the transition state (TS) (b), both relative to the interatomic distances in the structure under strain, not taking into account structural relaxations due to the introduction of a vacancy. The colour scheme is equivalent to that adopted in Figure 4-8. The data points can be grouped in terms of d_{SS} and d_{LL} distances.

resulting plots are shown in Figure 8-35.

We can make several interesting observations from these plots. Firstly, the data points fall almost perfectly on the line $x = y$, which is shown as a grey dashed line, along with a 1% error margin to this linear slope indicated by the light blue area about this line. Almost all of the data points lie within this 1% error margin, indicating that at the saddle point the moving caesium ion is approximately equidistant to either of the S-denoted and either of the L-denoted bromide atoms. Secondly, we observe that the interatomic distances cover a reasonably large range of values, roughly between 3.2 and 3.7 Å. We note that the crystal ionic radii of bromide and caesium are about 1.82 and 1.67 Å [338], respectively, summing to a value of 3.49 Å. This threshold is shown in Figure 8-35 as a dashed box, and we observe that many of the interatomic distances are well below what we would expect based on the sum of their crystal ionic radii. We note that more recently, ionic radii were computed from first-principles, based on the sphere around an ion which contains 95% of the electron density, with resulting ionic radii of 1.76, 1.19 and 2.22 Å for Cs^{+}, Pb^{2+} and Br^{-}, respectively. This results in a sum of the Cs and Br ionic radii of about 3.98 Å, which is subsantially larger than the Cs-Br distances we observe at the transitions state for all sets of SEPS and all different strain states.

In the previous discussions of the descriptors we have adopted considerations from the viewpoint of a pure hard-sphere model, for which we, perhaps remarkably, obtained very useful

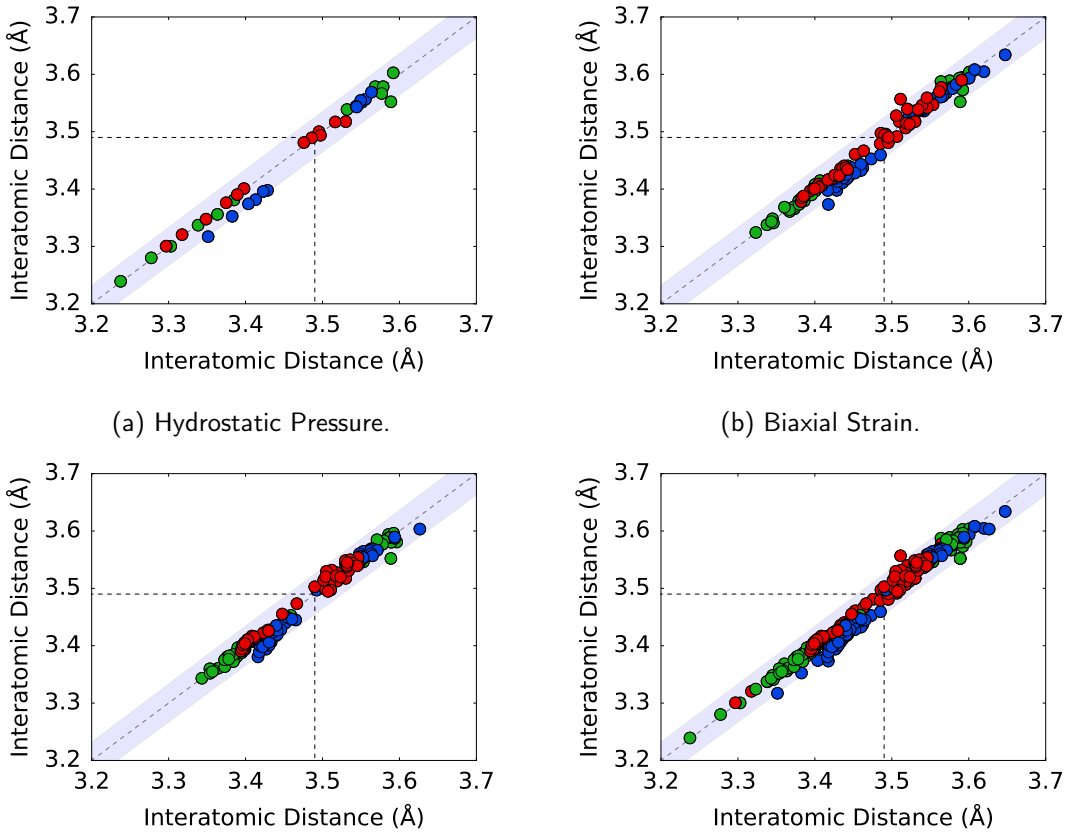

(a) Hydrostatic Pressure.

(b) Biaxial Strain.

(c) Uniaxial Strain.

(d) Combined Dataset.

Figure 8-35: Correlation between the distances at the transition state of Cs to either of the S-denoted and either of the L-denoted bromide atoms. The dashed grey line indicates a perfect correlation, while the shaded region indicates the range of a 1% deviation. The dashed black lines indicate the sum of the crystal ionic radii, being equal to 3.49 Å. A significant number of Cs-Br distances fall below these thresholds, indicating that a hard-sphere model may not be accurate. The colour scheme is equivalent to that adopted in Figure 4-8.

and valuable descriptors. These considerations are a natural continuation from the wealth of knowledge that has been obtained on perovskites in general, a lot of which is based on studies using interatomic potentials. However, in our current study we adopt quantum chemical approaches, and find that even if we just take the crystal ionic radii into account, there is significant overlap between the atoms at the transition state. This begs the natural question whether such a hard-sphere model is really valid in these types of calculations, or whether there are better ways in which we can define the proximity and level of contact of atoms from a quantum chemical point of view.
As said, the descriptors described above correspond to the pristine structures, in the sense that strain can be applied but no vacancies have been introduced. Of course, similar descriptors can also be investigated for structures in which vacancies have been introduced, or even at the transition state. Though the possible search space for useful descriptors is hard to exhaust, we have investigated several others, such as the Cs-Br distance at the transition state, the displacement of both the lead and the bromide atoms at the transition state (similar to the analysis of cation migration in $LaGaO_3$ [341]), and the effective aperture corresponding to both the initial and the transition state (rather than the pristine material), but found that none seemed to give a better correlation with the activation enthalpy. Moreover, the predictive power of a descriptor also lies in the relative ease with which it can be computed, which favours the implementation of descriptors that can be derived solely from the pristine material, which is the easiest to compute.

8.2.3 Linear Response Predictions

Finally, the changes in the activation enthalpies can also be derived from the effective dipole tensor, which we derive from the initial and transition states in the absence of strain, in combination with the structural deformation resulting from the stress we apply. The predictions and computed values for the evolution of the activation enthalpies are shown in Figures 8-36 to 8-38. In these, the predictions are shown as solid lines, with alternating black and coloured sections, the colours corresponding to those presented in Figure 4-8. We emphasize that though these lines do not appear to be linear, the predictions are linear and the variations in the slope are due to the non-linear evolution of the lattice vectors. The explicitly computed values are shown by coloured markers, again following the colour scheme of Figure 4-8.

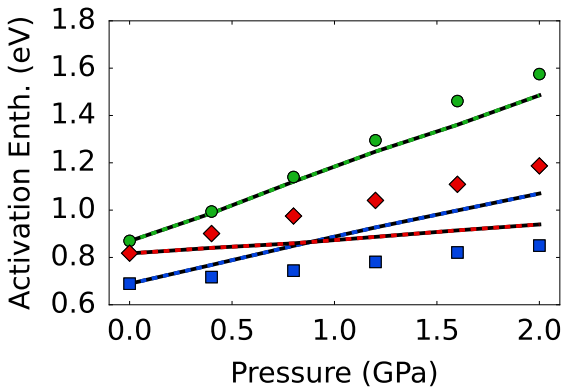

Figure 8-36: Linear predictions (solid lines) compared to computed values (marked points) of the evolution of the activation enthalpy of E-to-E transitions in response to hydrostatic pressure. The colour scheme is equivalent to that adopted in Figure 4-8.

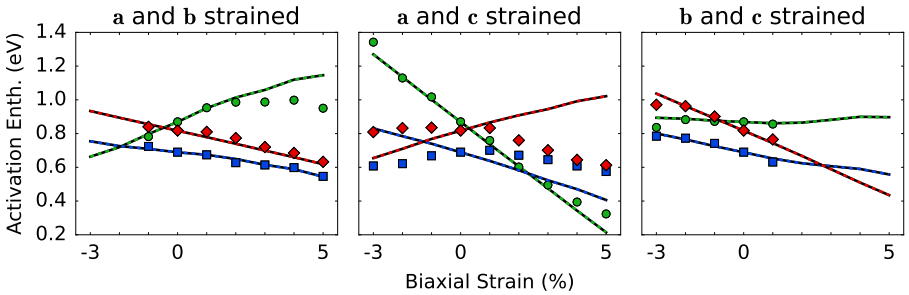

Figure 8-37: Linear predictions (solid lines) compared to computed values (marked points) of the evolution of the activation enthalpy of E-to-E transitions in response to biaxial strain. The colour scheme is equivalent to that adopted in Figure 4-8.

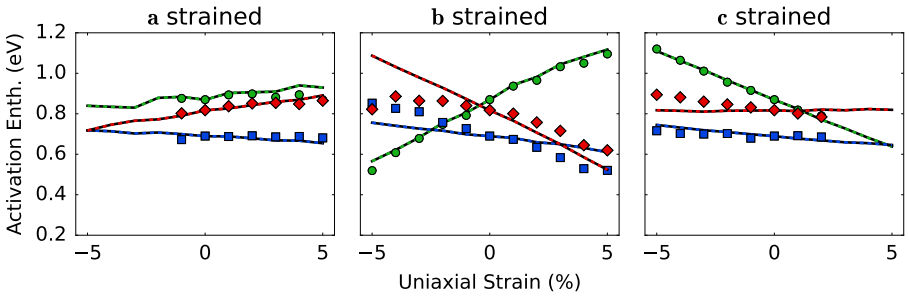

Figure 8-38: Linear predictions (solid lines) compared to computed values (marked points) of the evolution of the activation enthalpy of E-to-E transitions in response to uniaxial strain. The colour scheme is equivalent to that adopted in Figure 4-8.

Overall we find that in many cases, the predictions based on the effective dipole tensor are remarkably close to the actually computed values. This is particularly true for the set of SEPS denoted by the green spheres. The superior predictive power for caesium migration compared to bromide migration is another reflection of differences in their migration mechanism, which is not surprising given that the bromide is likely more covalently bound to the Pb-atom, while the caesium is more ionic.
However, despite this remarkable predictive power of the linear response theory for caesium migration, we still find a sufficient number of activation enthalpies that are poorly predicted. Again, we conclude that to obtain quantitatively correct values for the activation enthalpies, explicit calculations are nevertheless necessary, in line with previous studies on the linear response theory [320].

Chapter 9

Insights

In this thesis, we have developed a thorough methodology to study the general effects of stress and strain on the ionic mobility in $CsPbBr_3$. We show that both the directionality and the magnitude of the ionic mobility can be strongly affected by strain. For example, we observed a surprising 3D-to-2D transition of the bromide vacancy mobility tensor under hydrostatic pressure, and an increase of the caesium vacancy mobility tensor by many orders of magnitude under tensile biaxial strain, which may be linked to the relative instability of the perovskite layer in typical solar cell devices.

We reiterate that LHPs are generally considered to be about a factor of 10 softer than their oxide perovskite counterparts, such that such that even moderate levels of stress can induce significant levels of strain. Many reports have suggested a direct link between strain in the perovskite layer and the stability, which remains the bottleneck to the commercialisation of LHP-based devices. Since the degradation of the perovskite layer is assumed to be facilitated by mass transport in the perovskite layer, a careful analysis of the effects of strain on the mass transport in LHPs is necessary, in particular since several experimental studies have suggested a strong influence of stress and strain on the level of ionic migration in LHPs.

Taking $CsPbBr_3$ as a model system for the larger class of LHPs, we provide an atomistic understanding of the effects of hydrostatic pressure, biaxial strain and uniaxial strain on anion and A-site cation vacancy migration. We use results from DFT calculations, in particular the climbing image nudged elastic band and dimer methods and vibrational frequency analysis, as input for kinetic modelling. In doing so, we can relate atomistic observations to macroscopic properties, specifically the anion and A-site cation vacancy mobility tensors.

We emphasize the importance of treating the structural anisotropy of the orthorhombic phase with space group $Pnma$, which is the phase adopted by $CsPbBr_3$ over a large range of operating temperatures, but is also relevant for other LHP compositions. We find that it

has important implications for the structural response to strain. In the case of hydrostatic pressure, the pressure is mainly absorbed through increased levels of octahedral tilting and a reduction of the length of the lattice vector $\boldsymbol{c}$, along which direction the structure is softest. It is also relevant in terms of the different levels of compensation of the lattice vectors that are not strained in the studies on biaxial and uniaxial strain.

An even more important consequence of the reduced symmetry of the orthorhombic structure with respect to the aristotype, is that the pairs of 1-NN sites split up into six distinct sets of symmetrically equivalent pairs of sites (SEPS) in the case of the bromide sublattice, and three sets of SEPS in the case of the caesium sublattice. Interestingly, we find that in the case of the bromide mobility, the inclusion of an additional set of SEPS, corresponding to transitions between neighbouring octahedra, is crucial in describing the correct behaviour in response to hydrostatic pressure. In its absence, we observe an effective 3D-to-1D transition, while by including it this changes to an effective 3D-to-2D transition of the bromide mobility, such that the mobility in the apical [010] direction is three orders of magnitude smaller than those in the equatorial (010) plane. Though the trends depend strongly on the direction and magnitude of the applied biaxial and uniaxial strain, we find that the mobility can cover a wide range of values in response to strain, from a value of $4\times10^{-8}\,\mathrm{cm^2\,V^{-1}\,s^{-1}}$ up to a value close to $10^{-3}\,\mathrm{cm^2\,V^{-1}\,s^{-1}}$.

The response of the caesium vacancy mobility to strain is even stronger, with values ranging over more than 20 orders of magnitude, down from $4\times10^{-28}\,\mathrm{cm^2\,V^{-1}\,s^{-1}}$ under 2.0 GPa up to almost $3\times10^{-7}\,\mathrm{cm^2\,V^{-1}\,s^{-1}}$ under 5% tensile biaxial strain along **a** and **c**. The latter of these values approaches the range of mobilities typically observed for the halide species, which is generally considered to be the most mobile. These results however suggest that under strain the migration of caesium vacancies becomes substantially enhanced, such that they could significantly affect device properties. In particular, the device stability has been shown to decrease with tensile biaxial strain and increase with compressive biaxial strain. Since the caesium mobility is enhanced under tensile strain by a much larger amount than the bromide mobility, this could indicate that the A-site cation migration should be addressed in particular in order to improve perovskite stability.

Finally, we have analysed several descriptors for both bromide and caesium vacancy migration in order to investigate why the activation enthalpies associated with the transitions increase with some types of strain while decreasing for others. For bromide migration, we tested descriptors previously used to describe trends in migration enthalpies upon changing compositions of oxide perovskites, but found them to be unable to describe trends for $CsPbBr_3$ under strain. We also tested various descriptors for caesium migration, and found them to be much better at describing trends in the migration enthalpies. The effective area of the halide aperture through which a moving caesium ion moves during a transition

was found to be a particularly good descriptor. The reason for the differences between the predictability in bromide and caesium is likely linked to their relative levels of ionicity; while caesium is considered to be strongly ionic, the bromide is assumed to be more covalently bound in the PbBr framework. As a result, purely steric considerations, such as the effective aperture area, are likely more accurate for caesium than they are for bromide migration. Most likely, there are several competing interactions that describe the activation enthalpy of the bromide migration, some of which are steric, but some of which depend more strongly on the covalent bond with the lead atom, and as a result it has proven much more difficult to find simple yet accurate descriptors to describe the change in the activation enthalpy of anion migration in response to strain.

Since $CsPbBr_3$ has been used as a model system for the larger class of LHPs, a natural question to ask is whether similar behaviour can be expected for other LHPs. Though this question can only be answered by explicitly performing similar studies, we can make some predictions based on our current knowledge and insights. For one, the elastic moduli of $CsPbBr_3$ are comparable to those of different LHP compositions, as was described in more detail in Section 2.2.1, such that similar structural responses to stress and strain can be expected also. Based on the atomistic insights we have developed in this model, we may therefore expect similar trends in the activation energies too, in particular in the case of A-site cation migration, though the overall correlation between the effective aperture area and the activation enthalpy might be poorer if hydrogen bonding of the organic molecules has a strong effect.

To develop better rules of thumb to predict trends in the activation enthalpies for ionic migration, we would need to extend our migration barrier analysis to go beyond a hard-sphere model. The current atomistic models, such as the critical radius model for anion migration and our description of the effective surface area for A-site cation migration, are based on a minimum volume of space that is necessary such that the moving ion does not touch any of the atoms in its vicinity at the transition state. However, we observed for both bromide as well as caesium migration, that the moving ion is often closer to the atoms in its vicinity than would be allowed purely based on the ionic radii. There have been a lot of recent advancements on determining the ionic size and shape from first principles, for instance through Hirshfeld surface analysis [343]. Another very interesting approach that has seen a lot of recent improvements, is that based on the classical turning surface of the Kohn–Sham potential [344, 345], which can be used to quantitatively describe the ionic volume and shape, and the level of covalent and ionic interactions in crystals and molecules [346, 347]. Such a development would thus allow us to get a better description of the interactions of the moving ion at the transition state with atoms in its direct vicinity and to extract which interactions are most important in describing the changes in the activation enthalpy.

When doing similar studies on other LHPs, the phase stability under strain needs to be carefully tested, as has been done to some degree for $MAPbI_3$ [348, 349], especially since the energy differences between the different tilting patterns and their corresponding phases are relatively small even in the absence of strain. In our study on the effects of hydrostatic pressure, we were able to directly compare the structural response to experimental data, giving us confidence that the orthorhombic structure with space group $Pnma$, the anisotropy of which is critical to our study, remains stable in the range of 0.0–2.0 GPa. No such experimental evidence was available in the case of biaxial or uniaxial strain. In these studies, we based our range of study on experimentally observed or exerted strains. Since in some cases such strains lead to enhanced degradation, this is no guarantee that the orthorhombic structure with space group $Pnma$ remains stable. In our studies, we have found no evidence of any other structure becoming more stable, though we observe that we need to take into account a different representation of the orthorhombic phase. We have found evidence of only one such permutation to become lower in energy than the original structure, namely that with space group $Pcmn$, for which the axes are permuted with respect to the structure with space group $Pcmn$. However, 4 such other permutations of the same structure exist, and to get a more comprehensive overview of the phase stability under strain, all of these, in addition to those of the other tilting patterns, should be analysed. Though this search space was prohibitively large to study for the current purposes, this limiation should be kept in mind.

Another point to keep in mind regarding the computation of any property of LHPs using DFT calculations, is that for the vast majority of perovskite compositions the ground state is the orthorhombic phase with space group $Pnma$, though many of these compositions might adopt a higher symmetry phase at room temperature. Though it is reasonable to want to model such higher symmetry phases using DFT, such calculations must be performed with a lot of care. Though such higher symmetries can easily be constrained in the pristine system, the symmetry is broken upon the introduction of a defect, such as a vacancy. Typically, the structure is then relaxed using structural relaxation to find vacancy formation energies and/or defect migration enthalpies when considering the transition states. Such relaxations however also include a (favourable) energy component that describes the additional energy gain for the overall structure to go from the higher symmetry configuration to its lower symmetry groundstate. Such effects are hard to disentangle afterwards, and sometimes formation energies or migration enthalpies are published including these energy terms, which make the reported values appear unrealistically low. An example of a study in which this is observed, yet correctly discussed, is that of the negative formation energy of a grain boundary in $FAPbI_3$ [350].

Another interesting line of questioning to pursue is the role of anharmonicity. In employing

Vineyard's rate theory, we have assumed that the potential energy surface for the moving ion is harmonic in the initial and transition states. However, there has been quite some evidence suggesting the level of anharmonicity in LHPs can be quite high [85, 351–355]. Anharmonic corrections to Vineyard's rate equation exist [235, 356], but since those would only modify the prefactors by a multiplicative factor, the trends we have observed would remain unaltered and we have therefore not implemented these modifications though it would be an interesting development to the model to make. Interestingly, we find slightly smaller values, roughly a factor of two thirds, for the prefactor when generating Hessian matrices using finite displacements of 0.010 Å compared to a finite displacement of 0.015 Å.

In the current methodology, we have also assumed that the macroscopic mobility can be computed in the dilute limit, i.e. that the concentration of vacancies is sufficiently low that there is no interaction between mobile vacancies. In doing so, we thus neglect electrostatic interactions between charged defects, but also blocking effects with sites potentially being (partially) occupied. It would nevertheless be interesting to study how good this approximation is given the fact that defect concentrations in LHPs can be quite high, especially in the case of a build-up of vacancies near interfaces in so called Debye layers.

Going beyond the dilute limit, another interesting question to pursue is whether nearby vacancies can affect the local strain field. Such interactions have been studied in other systems in the context of the linear elasticity theory [243, 244], and such studies could be extended to the class of LHPs. For example, the presence of a nearby vacancy might locally induce a lattice contraction, which might affect the activation enthalpy for subsequent hops. Another interesting question is that of the interaction between the A-site and X-site vacancies in terms of the ionic migration. In particular because several studies on the oxide perovskites have found that the migration enthalpy of the A-site cation is significantly reduced in the vicinity of an anion vacancy [357–359].

Finally, though we have developed a methodology to describe ionic migration in the bulk, it would be interesting to study how the presence of interfaces and extended defects affect the ionic migration. Perovskite films, being solution-processed at low temperatures, are generally riddled with grain boundaries, which have been shown to facilitate ionic migration [360–363]. Whether such enhanced ionic migration is the result of the necessarily induced local strains in the vicinity of the grain boundaries, or whether they are the result of a different transport mechanism remain to be explored.

Chapter 10

Acknowledgements

It is fair to say that the last few years have been remarkable in more ways than one. Naive as I was, I remember starting my PhD fully convinced that my work was going to be revolutionary and that I would ensure clean and abundant energy for all. One of the more profound lessons I have however learned is that scientific development need not come in leaps, but that even the smallest of steps is a sign of progress nonetheless. Had it not been for the guidance, motivation and general support of others, I would never have been able to learn and appreciate this, and develop myself, both professionally and personally, as much as I have.

First of all, I want to thank you, Matthew, for all of the the guidance you have given me. I can only thank you for the hours and hours that have gone into our daily discussions, as it has really shaped the researcher I am today. It has been through your critical eye and continuous support that the work in this thesis has materialised. It is as much a reflection of my development as a researcher, as of your development as a mentor.

I also want to thank you, Alison, for the opportunity you have given me to work in your group and to be a part of the MAESTRO network. You have always been supportive, not only by giving me the chance to foster my own research interests, but also by allowing me the freedom to work remotely when this suited my personal situation better. I do not wish to faff around, but also many thanks for the many idioms and turns of phrase you have taught me.

I also wish to thank all other members of the ABW group, current or of times past, for their help, guidance and general support. Freddie, Ian, James, Joe, Smithy, Tom and Will, many thanks for all the things you've taught me, from compiling software to the rules of cricket. Antonio, Dimitrios, Matt and Jamie, the best of luck and joy in all of your PhDs. Finally, many thanks to Lewis - I'm glad we have been able to spend a large part of this journey

together and keep each other sharp. Congratulations with your successful viva, and best of luck in your future career.
Nothing but thanks also to the many colleagues in Bath I've had the pleasure of discussing mine and their work with; Petra, Kamal, Tom and Steve.
Nothing but thanks also to many others who have guided and supported me during my placements in Konstanz and Uppsala. Gabriel, I look back fondly on our many discussions on the proper implementation of drift-diffusion equations. Many thanks also to Barbara and Giso for having me, and making me feel very welcome in your group at the University of Konstanz.
I also feel grateful to have met so many lovely people during my visit to Konstanz. Samu and Caro, living with you exceeded all of my expectations. I am very grateful for your kindness and willingness to introduce to your groups of friends and even families, and for teaching me that the German language is actually far prettier than we are sometimes led to believe. I can only describe my time spent at the Friedrichstraße as wunderhübsch, though my memory of the song Dance Monkey is forever tainted. Many thanks also to Carmen, for hosting me and for inviting me for the Oktoberfest celebrations in Munich. Though I was quite proud to have picked up some German during my stay, the dialect you spoke with your friends still amazes me to this day. In keeping with the festive theme, I finally wish to thank Jana, Maywa, Jeroen and Caro for some of the most memorable nights of my life at the Oktoberfest in Konstanz, dancing along to Die Fischerin vom Bodensee. Jeroen's lovely homemade cake, including some typical Dutch ingredients, and the several Maße that we had surely had a part to play in making these nights out so much fun, but it wouldn't have been half as enjoyable had it not been for your company.
I also have nothing but gratitude to all the members of the Teoroo group at Uppsala University. Many thanks to you, Kersti, for having me and making me feel very much a part of the group, though my stay was only brief. Jolla, many thanks for helping me get familiar with the fitting of interatomic potentials, and the CCS method in particular. I really cherish our many nice discussions in the office, and hope others have taken on my duty of bringing you your daily dose of vitamins. Many thanks also to Peter for your help in developing the DFTB parameters, you also still owe me a game of table-hockey. Also many thanks to you, Amber, for your interest in my work and appreciating its applicability to your own project.
I'm also incredibly grateful for meeting so many wonderful people in Uppsala, I'm happy to say there are simply too many to name. Of the lucky few that have made it to the shortlist, Ignacio surely has to be number one. Your enthusiasm and energy are truly remarkable, and I hope you can be an inspiration to others as you have been to me. Souzan, I can only imagine how much it hurt to hear that you did not make it to Nacho's top 10, so as consolation I have bumped you up my list, though I don't know if it is of much comfort to

you. Nevertheless, I am eternally grateful for your warmness and hospitality and hope we can remain book buddies for years to come. I also want to thank you, Melania, for very similar qualities. You are kind and caring and I look back fondly on our active discussions on a wide range of topics, from politics to pheromones. To both of you, Souzan and Melania, I can only hope that you enjoyed our daily lunch breaks together as much as I did, though I will never be sure whether it was my presence or that of the pancakes and ice cream that made you both so happy. Also a massive thanks to all of the other Teoroo members for being so warm and inviting to me during my stay; Ageo, Andreas, Ben, Daniel, Erik, Klara, Linnéa, Lisanne, Lorenzo and Yunqi.

Also the warmest wishes to all of my wonderful Flogsta-flatmates. Adham, habibi, thank you for being such an incredible human being, and for introducing me to some of the wonders of Egyptian music, culture and cuisine. You are one of the kindest and humblest people I have ever met, so I am glad you decided to swap the dusty desert in Gizeh for the metres of Swedish snow. I know I owe you a presentation of my work, but hopefully this acknowledgement is a good substitute for now. Maybe even more thanks by the way for introducing me to your good friend Mo Salah; it is now my favourite claim to fame. Sabrina, many thanks for, well, just always being around. Despite the faulty stoves and the small cupboards, your presence made the kitchen a fun place to be. Though I am still a bit suspicious of your love for hot water, I also have very strong suspicions you are an incredibly generous, kind and hard-working person, and that we haven't heard the last of you. PS; I'm getting you a working alarm clock for your birthday, please don't forget mine. Sören, though we did not spend the longest time in the corridor together, it was long enough for me to find in you a kindred spirit. You know I'm honest, because though the truth hurts, a lie's worse. Not to forget all of the other ones with whom I have made such happy memories, not in the very least bonding over a Flogsta scream, including a Bohemian Rhapsody rendition; Alenka, Anna, Harshith, Rahul, Sharon, Torsten and Vera.

My deepest appreciation also to my fellow ESRs in the MAESTRO network, who have all worked so hard on our common goal of MAking pErovskiteS TRuly explOitable and whom I have come to cherish, each in their own way; Agustin, Christina, Emily, Emmy, Lefteris, Luigi, Nadja, Philippe, Prathibha, Rahul, Reddy, René, Sijo, Vaidvile and Vivek. I am incredibly proud to have been able to witness all of your developments, both professionally and personally. I remember some of you being a bit shy when we first on the sunny Swiss slopes of Sion, but such shyness was hard to find when we last met, dancing along to patati, a patata mangi tu on the Tuscan shores. Christina and Rahul, it was an absolute pleasure to host both of you in Bath and I am really proud of what you have both accomplished during your stays. Emily, I really enjoyed having you over and running the Bath Half Marathon together, I am proud of both of our achievements and the money we raised for charity.

Agustin, thanks for showing me what true greatness is like in the boardgame of Ricochet. Philippe, maybe you should take note of that, as I am still not quite over you making me lose in our game of Mascarade. Though I might have been a bit of a sore loser, I feel like your decision to move to the other side of the planet to avoid me is also somewhat dramatic, but no worries mate. Otherwise I am very happy to have met you, and want to thank you for showing Rahul, Christina and me the wonders of Oxford student life, from deluxe dinners to a classy game of croquet in Trinity College. Danke, gracias, ευχαριστώ, diolch and grazie to Nadja, Agustin, Lefteris, Rahul and Luigi for hosting us during our visits to Sion, Castellón, Athens, Swansea and Rome. Also a very big thanks to all of the others who have been part of the MAESTRO consortium, to all of the group leaders, all of the ones who have taken the time to guide, educate and entertain us during our training events and to those who have worked so hard in the background to keep everything running smoothly; Anni, Beatrice, Stuart and Yankı.

A massive thanks to all of those who have, each in their own way, made Bath feel like home over the last few years. To Ben, Dylan, Malte and Matt, with whom I have spent many a pint in the pub watching memorable games of football, and with whom it was impossible not to end up in the Common Room dancing away the late hours, even though I had promised myself to be sensible and just go out for one drink. I am very proud of all of your accomplishments over the last few years, and I am sure we will, in the years to come, find many more excuses to not be sensible and dance the night away. To Alex and Harry, who have adopted me as their surrogate father. I am incredibly proud of what you have both already achieved and are continuing to achieve. Though being locked up together was not always easy, it was most certainly never dull, and I cherish having had both of your bubbly characters around to brighten up my days, especially the many interesting insights into the games of cricket, and the well-substantiated opinions on Jersey and Guernsey. To Charlotte, with whom I was lucky enough to share the custody of our surrogate children, until she eloped with her lockdown lover. I have long since forgiven you though, since you are such a remarkably beautiful character and I am very grateful to be able to call you a friend. I deliberated over including your secret Santa song in the appendix of this thesis. Luckily for you I ran out of pages and hence it has not made it to the current iteration, but if I am not included in the acknowledgements of your own thesis, I might wish to reconsider. To Matt, with whom it was an absolute joy to live together in our posh Pulteney palace despite a second year of being mostly locked down. I cannot thank you enough for introducing me to many gems of British culture; watching Hot Fuzz, Peep Show, Line of Duty and many football memes have truly enriched my life. I am also sad to say that to this day, I have not been able to equal your chili sin carne. Many thanks to all of my wonderful teammates in our seven-a-side Physics delegation; Aimee, Alberto, Ben, David, Dylan, Freddie, Ian, Jim, Lewis, Matt, Pete

and Zoe. Playing football with you on the Friday afternoon was usually the highlight of my week. Winning the league with you is still one of the more noteworthy accomplishments on my C.V., though perhaps I should try to improve my goalscoring skills, should we wish to contend for another season. Many thanks also to some wonderful opponents against, and on occasion with whom, it was an absolute pleasure to play; Cameron, Jacob, Petros, Saul, Will and many others. My thanks to everyone else with whom I shared many happy moments; Abi, Ainhoa, Anastasia, Antonio, Bianca, Caroline, Danila, Eliot, Freya, Holly, Lukáš, Marco, Nuria and Rita. Last, but most definitely not least, many thanks to Raj. I want to thank you not only for nourishing me in the more literal sense of the word, but also for nourishing me mentally. You are one of the most inspiring people I have ever met, and I hope many other people in Bath can find as much comfort in your positive mindset as I so often have. You, and Chaiwalla, will always hold a special place in my heart.

I am also eternally grateful for the many friends I am lucky to have back at home in the Netherlands. Despite the physical distance between us, I have always felt close to you in spirit. Ik ga me in het vervolg aan het Nederlands wagen, maar de twee voorgaande zinnen hadden daarin nog afgezaagder geklonken dan ze in het Engels al doen. Ik heb er ontzettend van genoten dat zoveel van jullie op bezoek zijn gekomen, en dat ik jullie heb kunnen laten zien hoe de prachtige stad en het leven erin eruit zien. Pim, met jou erbij is het altijd een feest, en dat was bij jouw bezoek zeker niet anders. Even een potje Bath rugby meepakken was heel gaaf, maar er gaat bij ons toch niks boven een avondje PSV. Daar hebben we er inmiddels een aantal van gehad, en ik hoop dat er nog vele mogen volgen. Arvid, Irene, Mira en Rozemarijn, ik vond het ook echt heel erg leuk om jullie over de vloer te hebben, en dat zullen ze in de kroeg hopelijk ook gedacht hebben toen we daar urenlang hetzelfde spel zaten te spelen. Dat was natuurlijk wel een stuk vermakelijker dan in de stromende regen Bathwick Hill af te lopen, ook al konden we ons na afloop verheugen op heerlijke wraps en zelfgemaakte bosbessencake. Ook Cas, Luuk, Marco, Ruud, Stijn en Tom moesten aan de wraps van Chaiwalla geloven. Dat kostte in eerste instantie iets meer overredingskracht, maar ik was blij verrast toen jullie zeiden dat jullie niet hadden gedacht dat vegan eten zó ontzettend lekker kon zijn. Lennert en Lizzy, jullie moesten er later nog een keer voor terugkomen, maar dat was in combinatie met de mooie wandelingen in en om de stad zeker de moeite waard. Ook heel erg bedankt dat ik altijd bij jullie terechtkon, voor al die keren dat ik een vroege trein moest halen, maar ook zeker ook voor ons tripje naar Wembley. Anne, ook bedankt voor jouw bezoekje, en je onvoorwaardelijke steun aan de Cambridge-franchise van Chaiwalla. Het spijt me dat het me niet gelukt is die eens met je te komen testen. Arvid, aan jouw bezoek heb ik een beter rendement overgehouden, met tripjes naar Basel, Brighton en Zürich tot gevolg. Brida, ook jou wil ik graag bedanken voor je gastvrijheid in Brighton en Basel! Het bezoek aan Basel was memorabel om meer dan een reden, niet in

het allerminst omdat daar ook de Brus brothers aanwezig waren, en dat is altijd genieten. Jeroen, toen we elkaar daar met plechtige handdruk beloofden dat we samen de marathon zouden gaan rennen, had ik niet verwacht dat dat nog een aantal jaren zou duren, al was het uitstel voor ons allebei waarschijnlijk geen nadeel. Ik ben blij dat we Matt ook hebben kunnen overtuigen, en dat we in Parijs ondanks alle fysieke ongemakken toch alledrie een hele mooie tijd hebben weten neer te zetten. Ik dacht eventjes dat ik je verslagen had, totdat je me erop wees dat je met jouw langere tijd ook langer aan het sporten was geweest. Misschien moeten we volgende keer de regels even vantevoren afspreken. Ook ontzettend bedankt voor alle gezelligheid en schaaklessen aan de Mexicaanse kust, waar we volgens mij genoeg taco's hebben gegeten voor de rest van ons leven. Als we Mexico noemen, kunnen we Peru ook zeker niet overslaan; Simone, ik heb er ontzettend van genoten om samen Peru te ontdekken, het zal vrij zeker letterlijk maar waarschijnlijk ook figuurlijk een van de hoogtepunten van mijn leven blijven.

Doordat we voor een lange tijd met zijn allen aan huis gekluisterd zijn geweest, hebben we ook online veel kunnen afspreken waardoor ik velen van jullie toch allemaal net wat minder heb hoeven te missen. Simone, ik heb van onze gezellige online koffiepauzes erg genoten. Bij jou vond ik altijd een luisterend oor, als ik leuke verhalen te vertellen had, maar ook zeker als ik gewoon even wilde klagen. Ik heb dit al vaker gezegd, maar ik ben echt onder de indruk van hoeveel jij de laatste jaren als persoon gegroeid bent, en dat komt je nu van pas in je eigen PhD. Je hebt daarin nog even te gaan, maar ik wil je bij deze nog een keer ontzettend veel succes wensen en ik hoop er ook altijd voor je te kunnen zijn als je een luisterend oor zoekt. Ook met Arvid, Freek, Imke, Irene, Mira en Rudo heb ik op afstand heel veel lief en leed mogen delen. Ik heb van jullie verhalen genoten, de mijne met jullie mogen delen, en daarnaast heel veel goede raad mogen ontvangen waarvoor ik jullie ontzettend dankbaar ben. Ik wens jullie allemaal veel liefde en geluk toe. Ilonka, Imke, Irene en Rozemarijn, jullie hebben van jullie hart nooit een moordkuil gemaakt en hebben vanaf dag één al flink gelobbyd om mij naar Utrecht te lokken, en met succes, want deze regels worden nota bene in Utrecht op papier gezet. Ik hou jullie voorlopig nog even in spanning over hoelang ik hier ook daadwerkelijk blijf, maar als we de komende tijd nog net zo vaak naar de pingpongclub gaan, samen eten, voetbal kijken, rondjes wandelen en andere leuke dingen doen, dan maken jullie de keuze voor deze kneus niet erg moeilijk. Ook Arnoud, Enna, Fabian, Floor, Gijs, Irene G., Jasper, Joey, Jordi, Lieke, Pauline, Roos, Shannon, Shauny, Sjors en Vincent wil ik ontzettend graag bedanken voor alle vriendschap en herinneringen die ik al met jullie heb mogen beleven, en waarvan ik hoop dat dat voor ons nog in veelvoud in het verschiet ligt.

Tot slot wil ik mijn familie heel erg graag bedanken voor alle steun die ze mij al jarenlang onvoorwaardelijk geven. Ome Jos, bedankt voor alle keren dat je ons pap en mam hebt vergezeld op hun avonturen. Ik heb daar in ieder geval ontzettend van genoten, en ik weet

zeker dat dat ook voor hen geldt. Ook wil ik jou en tante Bets allebei bedanken voor jullie oprechte interesse in mijn onderzoek. Hoewel de uitleg soms te wensen overliet, heb ik jullie vragen altijd enorm gewaardeerd. Mayke, ik ben ontzettend trots dat ik jouw grote broer mag zijn. Behalve misschien toen je niet doorhad dat de deuren van de metro in London zo snel dichtgingen en dat toen je je hoofd stootte, Nicole zo hard moest lachen dat ze helemaal vergat zich ergens aan vast te houden, waardoor het ijsje die ze een seconde eerder nog in haar hand had inmiddels deels op de vloer en deels op de jas van een hulpeloze vrouw was beland. Toen twijfelde ik dus even, maar al zeg ik het niet vaak genoeg, ik ben wel ontzettend trots op je, en op alles wat je in al die jaren al bereikt hebt. Je hebt een hart van goud en hebt altijd voor me klaargestaan, en ik hoop dat ik er ook altijd voor jou kan zijn als je me nodig hebt. Behalve dan als jij en Jeroen me nodig hebben om in jullie nieuwe huis te komen klussen, het is voor iedereen beter als ik me daar met mijn twee linkerhanden niet teveel mee bemoei. Ik ben heel blij dat jullie zo'n leuk plekje dichtbij huis hebben gevonden, en wens jullie daar en op misschien nog volgende plekken heel veel geluk toe. Tenslotte wil ik graag met jullie eindigen, pap en mam, omdat jullie me van jongs af aan al gemotiveerd en gesteund hebben in alles wat ik heb gedaan. Toen jullie me aan het begin van mijn studie een kompas meegaven, opdat ik niet zou verdwalen in Nijmegen, hadden jullie waarschijnlijk niet kunnen bedenken dat jullie me aan aantal jaren later zouden opzoeken in warmere oorden met kangoeroes en koala's, maar die reis zijn jullie toch mooi samen aangegaan. Dat smaakte klaarblijkelijk naar meer, want jullie zijn me daarna ook nog op komen zoeken in Duitsland, Engeland en Zweden. Ik ben heel erg blij dat jullie jezelf nu ook wat meer gunnen en dat jullie van het leven durven te genieten, want ik weet ook dat jullie je al die jaren volledig hebben weggecijfert en altijd keihard hebben gewerkt, zodat het ons Mayke en mij aan niets ontbrak. Jullie hebben daar nooit iets voor terugverlangd, behalve de wens dat ik mijn best zou doen, dan waren jullie al lang tevreden. Meer kun je toch niet doen, ik heb het jullie zo vaak horen zeggen. Daar heb ik me dan ook jarenlang aan gespiegeld, en ik kan met trots zeggen dat ik voor deze scriptie, en al dat eraan vooraf is gegaan, echt mijn best heb gedaan. Ik heb altijd hard gewerkt zodat ik trots kon zijn op mezelf, maar misschien nog wel meer zodat jullie ook trots op me konden zijn. Ik ben daarom heel erg blij dat ik deze prestatie met jullie mag delen, omdat die naast mijn eigen inbreng ook voor een groot deel te danken is aan jullie onvoorwaardelijke liefde.

Bibliography

[1] Mary Soon Lee. Elemental Haiku. *Science*, 357:461-463, 2017.

[2] David A. Egger, Achintya Bera, David Cahen, Gary Hodes, Thomas Kirchartz, Leeor Kronik, Robert Lovrincic, Andrew M. Rappe, David R. Reichman, and Omer Yaffe. What Remains Unexplained about the Properties of Halide Perovskites? *Adv. Mater.*, 30:1800691, 2018.

[3] Jun Kang and Lin Wang Wang. High Defect Tolerance in Lead Halide Perovskite $CsPbBr_3$. *J. Phys. Chem. Lett.*, 8:489–493, 2017.

[4] Xie Zhang, Mark E. Turiansky, and Chris G. Van de Walle. Correctly Assessing Defect Tolerance in Halide Perovskites. *J. Phys. Chem. C*, 124:6022–6027, 2020.

[5] Guan Woo Kim and Annamaria Petrozza. Defect Tolerance and Intolerance in Metal-Halide Perovskites. *Adv. Energy Mater.*, 10:2001959, 2020.

[6] Constantinos C. Stoumpos and Mercouri G. Kanatzidis. Halide Perovskites: Poor Man's High-Performance Semiconductors. *Adv. Mater.*, 28:5778–5793, 2016.

[7] Haiwen Yuan, Yuanyuan Zhao, Jialong Duan, Yudi Wang, Xiya Yang, and Qunwei Tang. All-Inorganic $CsPbBr_3$ Perovskite Solar Cell with 10.26% Efficiency by Spectra Engineering. *J. Mater. Chem. A*, 6:24324–24329, 2018.

[8] Weijie Chen, Jingwen Zhang, Guiying Xu, Rongming Xue, Yaowen Li, Yinhua Zhou, Jianhui Hou, and Yongfang Li. A Semitransparent Inorganic Perovskite Film for Overcoming Ultraviolet Light Instability of Organic Solar Cells and Achieving 14.03% Efficiency. *Adv. Mater.*, 30:1800855, 2018.

[9] Qingwei Zhou, Jialong Duan, Jian Du, Qiyao Guo, Qiaoyu Zhang, Xiya Yang, Yanyan Duan, and Qunwei Tang. Tailored Lattice "Tape" to Confine Tensile Interface for

11.08%-Efficiency All-Inorganic $CsPbBr_3$ Perovskite Solar Cell with an Ultrahigh Voltage of 1.702 V. *Adv. Sci.*, 8:2101418, 2021.

[10] Abhishek Swarnkar, Ramya Chulliyil, Vikash Kumar Ravi, Mir Irfanullah, Arindam Chowdhury, and Angshuman Nag. Colloidal $CsPbBr_3$ Perovskite Nanocrystals: Luminescence beyond Traditional Quantum Dots. *Angew. Chem.*, 127:15644–15648, 2015.

[11] Kebin Lin, Jun Xing, Li Na Quan, F. Pelayo García de Arquer, Xiwen Gong, Jianxun Lu, Liqiang Xie, Weijie Zhao, Di Zhang, Chuanzhong Yan, Wenqiang Li, Xinyi Liu, Yan Lu, Jeffrey Kirman, Edward H. Sargent, Qihua Xiong, and Zhanhua Wei. Perovskite Light-Emitting Diodes with External Quantum Efficiency Exceeding 20 per Cent. *Nature*, 562:245–248, 2018.

[12] Dexin Yang and Dexuan Huo. Cation Doping and Strain Engineering of $CsPbBr_3$-Based Perovskite Light Emitting Diodes. *J. Mater. Chem. C*, 8:6640–6653, 2020.

[13] Tianjun Hu, Dongyu Li, Qingsong Shan, Yuhui Dong, Hengyang Xiang, Wallace C.H. Choy, and Haibo Zeng. Defect Behaviors in Perovskite Light-Emitting Diodes. *ACS Mater. Lett.*, 3:1702–1728, 2021.

[14] Dmitry N. Dirin, Ihor Cherniukh, Sergii Yakunin, Yevhen Shynkarenko, and Maksym V. Kovalenko. Solution-Grown $CsPbBr_3$ Perovskite Single Crystals for Photon Detection. *Chem. Mater.*, 28:8470–8474, 2016.

[15] Qiang Xu, Xiang Wang, Hang Zhang, Wenyi Shao, Jing Nie, Yong Guo, Juan Wang, and Xiaoping Ouyang. $CsPbBr_3$ Single Crystal X-ray Detector with Schottky Barrier for X-ray Imaging Application. *ACS Appl. Electron. Mater.*, 2:879–884, 2020.

[16] Yihui He, Matthew Petryk, Zhifu Liu, Daniel G. Chica, Ido Hadar, Charles Leak, Weijun Ke, Ioannis Spanopoulos, Wenwen Lin, Duck Young Chung, Bruce W. Wessels, Zhong He, and Mercouri G. Kanatzidis. $CsPbBr_3$ Perovskite Detectors with 1.4% Energy Resolution for High-Energy γ-rays. *Nat. Photonics*, 15:36–42, 2021.

[17] Yang Fan Xu, Mu Zi Yang, Bai Xue Chen, Xu Dong Wang, Hong Yan Chen, Dai Bin Kuang, and Cheng Yong Su. A $CsPbBr_3$ Perovskite Quantum Dot/Graphene Oxide Composite for Photocatalytic CO_2 Reduction. *J. Am. Chem. Soc.*, 139:5660–5663, 2017.

[18] Santosh Kumar, Miriam Regue, Mark A. Isaacs, Emma Freeman, and Salvador Eslava. All-Inorganic $CsPbBr_3$ Nanocrystals: Gram-Scale Mechanochemical Synthesis and Se-

lective Photocatalytic CO_2 Reduction to Methane. *ACS Appl. Energy Mater.*, 3:4509–4522, 2020.

[19] Sina G. Lewis, Dibyajyoti Ghosh, Kevin L. Jensen, Daniel Finkenstadt, Andrew Shabaev, Samuel G. Lambrakos, Fangze Liu, Wanyi Nie, Jean Christophe Blancon, Liujiang Zhou, Jared J. Crochet, Nathan Moody, Aditya D. Mohite, Sergei Tretiak, and Amanda J. Neukirch. Cesium-Coated Halide Perovskites as a Photocathode Material: Modeling Insights. *J. Phys. Chem. Lett.*, 12:6269–6276, 2021.

[20] Isabella Poli, Ulrich Hintermair, Miriam Regue, Santosh Kumar, Emma V. Sackville, Jenny Baker, Trystan M. Watson, Salvador Eslava, and Petra J. Cameron. Graphite-Protected $CsPbBr_3$ Perovskite Photoanodes Functionalised with Water Oxidation Catalyst for Oxygen Evolution in Water. *Nat. Commun.*, 10:2097, 2019.

[21] Hao Yuan, Yuxiang Min, and Lai Xu. Prediction of Dual-Doped Integrated $CsPbBr_3$-$CsPbCl_3$ Perovskite Heterostructure for Practical Photocatalytic Water Splitting with a New Descriptor. *J. Phys. Chem. Lett.*, 12:822–828, 2021.

[22] Fabian Paulus, Colin Tyznik, Oana D. Jurchescu, and Yana Vaynzof. Switched-On: Progress, Challenges, and Opportunities in Metal Halide Perovskite Transistors. *Adv. Funct. Mater.*, 31:2101029, 2021.

[23] Beomjin Jeong, Lothar Veith, Thijs J.A.M. Smolders, Matthew J. Wolf, and Kamal Asadi. Room-Temperature Halide Perovskite Field-Effect Transistors by Ion Transport Mitigation. *Adv. Mater.*, 33:2100486, 2021.

[24] Beomjin Jeong, Paschalis Gkoupidenis, and Kamal Asadi. Solution-Processed Perovskite Field-Effect Transistor Artificial Synapses. *Adv. Mater.*, 33:2104034, 2021.

[25] Tufan Paul, Soumen Maiti, Biplab Kr Chatterjee, Partha Bairi, Bikram Kumar Das, Subhasish Thakur, and Kalyan Kumar Chattopadhyay. Electrochemical Performance of 3D Network $CsPbBr_3$Perovskite Anodes for Li-Ion Batteries: Experimental Venture with Theoretical Expedition. *J. Phys. Chem. C*, 125:16892–16902, 2021.

[26] Yin Zhou, Qianfeng Gu, Yiju Li, Lu Tao, Hao Tan, Kun Yin, Jinhui Zhou, and Shaojun Guo. Cesium Lead Bromide Perovskite-Based Lithium-Oxygen Batteries. *Nano Lett.*, 21:4861–4867, 2021.

[27] Moritz H. Futscher and Jovana V. Milić. Mixed Conductivity of Hybrid Halide Perovskites: Emerging Opportunities and Challenges. *Front. Energy Res.*, 9:629074, 2021.

[28] Cheng Li, Steffen Tscheuschner, Fabian Paulus, Paul E. Hopkinson, Johannes Kießling, Anna Köhler, Yana Vaynzof, and Sven Huettner. Iodine Migration and its Effect on Hysteresis in Perovskite Solar Cells. *Adv. Mater.*, 28:2446–2454, 2016.

[29] Teng Zhang, Haining Chen, Yang Bai, Shuang Xiao, Lei Zhu, Chen Hu, Qingzhong Xue, and Shihe Yang. Understanding the Relationship between Ion Migration and the Anomalous Hysteresis in High-Efficiency Perovskite Solar Cells: A Fresh Perspective from Halide Substitution. *Nano Energy*, 26:620–630, 2016.

[30] James M. Cave, Nicola E. Courtier, Isabelle A. Blakborn, Timothy W. Jones, Dibyajyoti Ghosh, Kenrick F. Anderson, Liangyou Lin, Andrew A. Dijkhoff, Gregory J. Wilson, Krishna Feron, M. Saiful Islam, Jamie M. Foster, Giles Richardson, and Alison B. Walker. Deducing Transport Properties of Mobile Vacancies from Perovskite Solar Cell Characteristics. *J. Appl. Phys.*, 128:184501, 2020.

[31] Taame Abraha Berhe, Wei Nien Su, Ching Hsiang Chen, Chun Jern Pan, Ju Hsiang Cheng, Hung Ming Chen, Meng Che Tsai, Liang Yih Chen, Amare Aregahegn Dubale, and Bing Joe Hwang. Organometal Halide Perovskite Solar Cells: Degradation and Stability. *Energy Environ. Sci.*, 9:323–356, 2016.

[32] Vikas Nandal and Pradeep R. Nair. Predictive Modeling of Ion Migration Induced Degradation in Perovskite Solar Cells. *ACS Nano*, 11:11505–11512, 2017.

[33] Ziru Huang, Andrew H. Proppe, Hairen Tan, Makhsud I. Saidaminov, Furui Tan, Anyi Mei, Chih Shan Tan, Mingyang Wei, Yi Hou, Hongwei Han, Shana O. Kelley, and Edward H. Sargent. Suppressed Ion Migration in Reduced-Dimensional Perovskites Improves Operating Stability. *ACS Energy Lett.*, 4:1521–1527, 2019.

[34] Jin Wook Lee, Seul Gi Kim, June Mo Yang, Yang Yang, and Nam Gyu Park. Verification and Mitigation of Ion Migration in Perovskite Solar Cells. *APL Mater.*, 7:041111, 2019.

[35] Lucie McGovern, Moritz H. Futscher, Loreta A. Muscarella, and Bruno Ehrler. Understanding the Stability of $MAPbBr_3$ versus $MAPbI_3$: Suppression of Methylammonium Migration and Reduction of Halide Migration. *J. Phys. Chem. Lett.*, 11:7127–7132, 2020.

[36] Nam-Gyu Park, Michael Grätzel, Tsutomu Miyasaka, Kai Zhu, and Keith Emery. Towards Stable and Commercially Available Perovskite Solar Cells. *Nat. Energy*, 1:16152, 2016.

[37] Yaoguang Rong, Yue Hu, Anyi Mei, Hairen Tan, Makhsud I. Saidaminov, Sang Il Seok, Michael D. McGehee, Edward H. Sargent, and Hongwei Han. Challenges for Commercializing Perovskite Solar Cells. *Science*, 361:1214, 2018.

[38] Lei Meng, Jingbi You, and Yang Yang. Addressing the Stability Issue of Perovskite Solar Cells for Commercial Applications. *Nat. Commun.*, 9:5265, 2018.

[39] Nengxu Li, Xiuxiu Niu, Qi Chen, and Huanping Zhou. Towards Commercialization: The Operational Stability of Perovskite Solar Cells. *Chem. Soc. Rev.*, 49:8235–8286, 2020.

[40] Zexiong Qiu, Anyi Mei, Yue Hu, Yaoguang Rong, and Hongwei Han. Aiming at the Industrialization of Perovskite Solar Cells: Coping with Stability Challenge. *Appl. Phys. Lett.*, 119:250503, 2021.

[41] Tyler J Smart, Hiroyuki Takenaka, Tuan Anh Pham, Liang Z Tan, Jin Z Zhang, Tadashi Ogitsu, and Yuan Ping. Enhancing Defect Tolerance with Ligands at the Surface of Lead Halide Perovskites. *J. Phys. Chem. Lett.*, 12:6299–6304, 2021.

[42] Mojtaba Abdi-Jalebi, Zahra Andaji-Garmaroudi, Stefania Cacovich, Camille Stavrakas, Bertrand Philippe, Johannes M. Richter, Mejd Alsari, Edward P. Booker, Eline M. Hutter, Andrew J. Pearson, Samuele Lilliu, Tom J. Savenije, Håkan Rensmo, Giorgio Divitini, Caterina Ducati, Richard H. Friend, and Samuel D. Stranks. Maximizing and Stabilizing Luminescence from Halide Perovskites with Potassium Passivation. *Nature*, 555:497–501, 2018.

[43] Dae Yong Son, Seul Gi Kim, Ja Young Seo, Seon Hee Lee, Hyunjung Shin, Donghwa Lee, and Nam Gyu Park. Universal Approach toward Hysteresis-Free Perovskite Solar Cell via Defect Engineering. *J. Am. Chem. Soc.*, 140:1358–1364, 2018.

[44] Jiangzhao Chen, Donghwa Lee, and Nam Gyu Park. Stabilizing the Ag Electrode and Reducing J-V Hysteresis through Suppression of Iodide Migration in Perovskite Solar Cells. *ACS Appl. Mater. Interfaces*, 9:36338–36349, 2017.

[45] Yun Lin, Yang Bai, Yanjun Fang, Qi Wang, Yehao Deng, and Jinsong Huang. Suppressed Ion Migration in Low-Dimensional Perovskites. *ACS Energy Lett.*, 2(7):1571–1572, 2017.

[46] Jin Wook Lee, Zhenghong Dai, Tae Hee Han, Chungseok Choi, Sheng Yung Chang, Sung Joon Lee, Nicholas De Marco, Hongxiang Zhao, Pengyu Sun, Yu Huang, and Yang Yang. 2D Perovskite Stabilized Phase-Pure Formamidinium Perovskite Solar Cells. *Nat. Commun.*, 9:3021, 2018.

[47] Dominic W. Ferdani, Samuel R. Pering, Dibyajyoti Ghosh, Peter Kubiak, Alison B. Walker, Simon E. Lewis, Andrew L. Johnson, Peter J. Baker, M. Saiful Islam, and Petra J. Cameron. Partial Cation Substitution Reduces Iodide Ion Transport in Lead Iodide Perovskite Solar Cells. *Energy Environ. Sci.*, 12:2264–2272, 2019.

[48] Shaun Tan, Ilhan Yavuz, Nicholas De Marco, Tianyi Huang, Sung Joon Lee, Christopher S. Choi, Minhuan Wang, Selbi Nuryyeva, Rui Wang, Yepin Zhao, Hao Cheng Wang, Tae Hee Han, Bruce Dunn, Yu Huang, Jin Wook Lee, and Yang Yang. Steric Impediment of Ion Migration Contributes to Improved Operational Stability of Perovskite Solar Cells. *Adv. Mater.*, 32:1906995, 2020.

[49] Cheng Zhu, Xiuxiu Niu, Yuhao Fu, Nengxu Li, Chen Hu, Yihua Chen, Xin He, Guangren Na, Pengfei Liu, Huachao Zai, Yang Ge, Yue Lu, Xiaoxing Ke, Yang Bai, Shihe Yang, Pengwan Chen, Yujing Li, Manling Sui, Lijun Zhang, Huanping Zhou, and Qi Chen. Strain Engineering in Perovskite Solar Cells and its Impacts on Carrier Dynamics. *Nat. Commun.*, 10:815, 2019.

[50] Hui Seon Kim and Nam Gyu Park. Importance of Tailoring Lattice Strain in Halide Perovskite Crystals. *NPG Asia Mater.*, 12:78, 2020.

[51] Erin G. Moloney, Vishal Yeddu, and Makhsud I. Saidaminov. Strain Engineering in Halide Perovskites. *ACS Mater. Lett.*, 2:1495–1508, 2020.

[52] Aron Walsh. Atomistic Models of Metal Halide Perovskites. *Matter*, 4:3867–3873, 2021.

[53] Shijing Sun, Yanan Fang, Gregor Kieslich, Tim J. White, and Anthony K. Cheetham. Mechanical Properties of Organic-Inorganic Halide Perovskites, $CH_3NH_3PbX_3$ (X = I, Br and Cl), by Nanoindentation. *J. Mater. Chem. A*, 3:18450–18455, 2015.

[54] Antoine Létoublon, Serge Paofai, Benoît Rufflé, Philippe Bourges, Bernard Hehlen, Thierry Michel, Claude Ecolivet, Olivier Durand, Stéphane Cordier, Claudine Katan, and Jacky Even. Elastic Constants, Optical Phonons, and Molecular Relaxations in the High Temperature Plastic Phase of the $CH_3NH_3PbBr_3$ Hybrid Perovskite. *J. Phys. Chem. Lett.*, 7:3776–3784, 2016.

[55] Jung Hoon Lee, Zeyu Deng, Nicholas C. Bristowe, Paul D. Bristowe, and Anthony K. Cheetham. The Competition between Mechanical Stability and Charge Carrier Mobility in MA-Based Hybrid Perovskites: Insight from DFT. *J. Mater. Chem. C*, 6:12252–12259, 2018.

[56] A. C. Ferreira, A. Létoublon, S. Paofai, S. Raymond, C. Ecolivet, B. Rufflé, S. Cordier, C. Katan, M. I. Saidaminov, A. A. Zhumekenov, O. M. Bakr, J. Even, and P. Bourges. Elastic Softness of Hybrid Lead Halide Perovskites. *Phys. Rev. Lett.*, 121:085502, 2018.

[57] Adam Jaffe, Yu Lin, and Hemamala I. Karunadasa. Halide Perovskites under Pressure: Accessing New Properties through Lattice Compression. *ACS Energy Lett.*, 2:1549–1555, 2017.

[58] Xujie Lü, Wenge Yang, Quanxi Jia, and Hongwu Xu. Pressure-Induced Dramatic Changes in Organic-Inorganic Halide Perovskites. *Chem. Sci.*, 8:6764–6776, 2017.

[59] Timothy W. Jones, Anna Osherov, Mejd Alsari, Melany Sponseller, Benjamin C. Duck, Young Kwang Jung, Charles Settens, Farnaz Niroui, Roberto Brenes, Camelia V. Stan, Yao Li, Mojtaba Abdi-Jalebi, Nobumichi Tamura, J. Emyr MacDonald, Manfred Burghammer, Richard H. Friend, Vladimir Bulović, Aron Walsh, Gregory J. Wilson, Samuele Lilliu, and Samuel D. Stranks. Lattice Strain Causes Non-Radiative Losses in Halide Perovskites. *Energy Environ. Sci.*, 12:596–606, 2019.

[60] Xueying Li, Yanqi Luo, Martin V. Holt, Zhonghou Cai, and David P. Fenning. Residual Nanoscale Strain in Cesium Lead Bromide Perovskite Reduces Stability and Shifts Local Luminescence. *Chem. Mater.*, 31:2778–2785, 2019.

[61] Mei Li, Tianbiao Liu, Yonggang Wang, Wenge Yang, and Xujie Lü. Pressure Responses of Halide Perovskites with Various Compositions, Dimensionalities, and Morphologies. *Matter Radiat. Extrem.*, 5:018201, 2020.

[62] Yimu Chen, Yusheng Lei, Yuheng Li, Yugang Yu, Jinze Cai, Ming Hui Chiu, Rahul Rao, Yue Gu, Chunfeng Wang, Woojin Choi, Hongjie Hu, Chonghe Wang, Yang Li, Jiawei Song, Jingxin Zhang, Baiyan Qi, Muyang Lin, Zhuorui Zhang, Ahmad E. Islam, Benji Maruyama, Shadi Dayeh, Lain Jong Li, Kesong Yang, Yu Hwa Lo, and Sheng Xu. Strain Engineering and Epitaxial Stabilization of Halide Perovskites. *Nature*, 577:209–215, 2020.

[63] Guanjun Xiao, Ye Cao, Guangyu Qi, Lingrui Wang, Chuang Liu, Zhiwei Ma, Xinyi Yang, Yongming Sui, Weitao Zheng, and Bo Zou. Pressure Effects on Structure and Optical Properties in Cesium Lead Bromide Perovskite Nanocrystals. *J. Am. Chem. Soc.*, 139:10087–10094, 2017.

[64] Yang Huang, Lingrui Wang, Zhuang Ma, and Fei Wang. Pressure-Induced Band Structure Evolution of Halide Perovskites: A First-Principles Atomic and Electronic

Structure Study. *J. Phys. Chem. C*, 123:739–745, 2019.

[65] Fei Wang, Mengping Tan, Chong Li, Chunyao Niu, and Xin Zhao. Unusual Pressure-Induced Electronic Structure Evolution in Organometal Halide Perovskite Predicted from First-Principles. *Org. Electron.*, 67:89–94, 2019.

[66] Yutong Wang and Run Long. Unravelling the Effects of Pressure-Induced Suppressed Electron-Hole Recombination in $CsPbBr_3$ Perovskite: Time-Domain ab Initio Analysis. *J. Phys. Chem. Lett.*, 10:4354–4361, 2019.

[67] Dibyajyoti Ghosh, Alex Aziz, James A. Dawson, Alison B. Walker, and M. Saiful Islam. Putting the Squeeze on Lead Iodide Perovskites: Pressure-Induced Effects to Tune Their Structural and Optoelectronic Behavior. *Chem. Mater.*, 31:4063–4071, 2019.

[68] Wei Li, Zhi Chen, Jianfeng Tang, and Oleg V. Prezhdo. Anti-Correlation between Band Gap and Carrier Lifetime in Lead Halide Perovskites under Compression Rationalized by Ab Initio Quantum Dynamics. *Chem. Mater.*, 32:4707–4715, 2020.

[69] Tianji Ou, Cailong Liu, Huacai Yan, Yonghao Han, Qinglin Wang, Xizhe Liu, Yanzhang Ma, and Chunxiao Gao. Effects of Pressure on the Ionic Transport and Photoelectrical Properties of $CsPbBr_3$. *Appl. Phys. Lett.*, 114:062105, 2019.

[70] Loreta A. Muscarella, Eline M. Hutter, Francesca Wittmann, Young Won Woo, Young-Kwang Jung, Lucie McGovern, Jan Versluis, Aron Walsh, Huib J. Bakker, and Bruno Ehrler. Lattice Compression Increases the Activation Barrier for Phase Segregation in Mixed-Halide Perovskites. *ACS Energy Lett.*, 5:3152–3158, 2020.

[71] Jingjing Zhao, Yehao Deng, Haotong Wei, Xiaopeng Zheng, Zhenhua Yu, Yuchuan Shao, Jeffrey E. Shield, and Jinsong Huang. Strained Hybrid Perovskite Thin Films and Their Impact on the Intrinsic Stability of Perovskite Solar Cells. *Sci. Adv.*, 3:eaao5616, 2017.

[72] Qingwei Zhou, Jialong Duan, Xiya Yang, Yanyan Duan, and Qunwei Tang. Interfacial Strain Release from the $WS_2/CsPbBr_3$ van der Waals Heterostructure for 1.7 V Voltage All-Inorganic Perovskite Solar Cells. *Angew. Chem.*, 132:22181–22185, 2020.

[73] Ding Jiang Xue, Yi Hou, Shun Chang Liu, Mingyang Wei, Bin Chen, Ziru Huang, Zongbao Li, Bin Sun, Andrew H. Proppe, Yitong Dong, Makhsud I. Saidaminov, Shana O. Kelley, Jin Song Hu, and Edward H. Sargent. Regulating Strain in Perovskite Thin Films Through Charge-Transport Layers. *Nat. Commun.*, 11:1514, 2020.

[74] Fengzhu Li, Xiang Deng, Feng Qi, Zhen Li, Danjun Liu, Dong Shen, Minchao Qin, Shengfan Wu, Francis Lin, Sei Hum Jang, Jie Zhang, Xinhui Lu, Dangyuan Lei, Chun Sing Lee, Zonglong Zhu, and Alex K.Y. Jen. Regulating Surface Termination for Efficient Inverted Perovskite Solar Cells with Greater Than 23% Efficiency. *J. Am. Chem. Soc.*, 142:20134–20142, 2020.

[75] Jiangzhao Chen, Dongmei He, and Nam Gyu Park. Methodologies for >30% Efficient Perovskite Solar Cells via Enhancement of Voltage and Fill Factor. *Sol. RRL*, 6:2100767, 2022.

[76] V.M. Goldschmidt. Die Gesetze der Krystallochemie. *Naturwissenschaften*, 14:477–485, 1926.

[77] A. M. Glazer. The Classification of Tilted Octahedra in Perovskites. *Acta Crystallogr. Sect. B*, 28:3384–3392, 1972.

[78] A. M. Glazer. Simple Ways of Determining Perovskite Structures. *Acta Crystallogr. Sect. A*, 31:756–762, 1975.

[79] Jonathon S. Bechtel and Anton Van Der Ven. Octahedral Tilting Instabilities in Inorganic Halide Perovskites. *Phys. Rev. Mater.*, 2:025401, 2018.

[80] Christopher J. Howard and Harold T. Stokes. Group-Theoretical Analysis of Octahedral Tilting in Perovskites. *Acta Crystallogr. Sect. B Struct. Sci.*, 54:782–789, 1998.

[81] R. E. Marsh. Non-Conventional Unit Cells. *Acta Crystallogr. Sect. A*, 45:FC9, 1989.

[82] Tom Baikie, Yanan Fang, Jeannette M. Kadro, Martin Schreyer, Fengxia Wei, Subodh G. Mhaisalkar, Michael Graetzel, and Tim J. White. Synthesis and Crystal Chemistry of the Hybrid Perovskite $(CH_3NH_3)PbI_3$ for Solid-State Sensitised Solar Cell Applications. *J. Mater. Chem. A*, 1:5628–5641, 2013.

[83] Constantinos C. Stoumpos, Christos D. Malliakas, John A. Peters, Zhifu Liu, Maria Sebastian, Jino Im, Thomas C. Chasapis, Arief C. Wibowo, Duck Young Chung, Arthur J. Freeman, Bruce W. Wessels, and Mercouri G. Kanatzidis. Crystal Growth of the Perovskite Semiconductor $CsPbBr_3$: A New Material for High-Energy Radiation Detection. *Cryst. Growth Des.*, 13:2722–2727, 2013.

[84] Jonathon S. Bechtel and Anton Van der Ven. First-Principles Thermodynamics Study of Phase Stability in Inorganic Halide Perovskite Solid Solutions. *Phys. Rev. Mater.*, 2:045401, 2018.

[85] Jonathon S. Bechtel, John C. Thomas, and Anton Van Der Ven. Finite-Temperature Simulation of Anharmonicity and Octahedral Tilting Transitions in Halide Perovskites. *Phys. Rev. Mater.*, 3:113605, 2019.

[86] Wanchun Xiang, Shengzhong Liu, and Wolfgang Tress. A Review on the Stability of Inorganic Metal Halide Perovskites: Challenges and Opportunities for Stable Solar Cells. *Energy Environ. Sci.*, 14:2090–2113, 2021.

[87] Christopher Eames, Jarvist M. Frost, Piers R.F. Barnes, Brian C. O'Regan, Aron Walsh, and M. Saiful Islam. Ionic Transport in Hybrid Lead Iodide Perovskite Solar Cells. *Nat. Commun.*, 6:7497, 2015.

[88] Adam Pockett, Giles E Eperon, Nobuya Sakai, Henry J Snaith, Laurence M Peter, and Petra J Cameron. Microseconds, Milliseconds and Seconds: Deconvoluting the Dynamic Behaviour of Planar Perovskite Solar Cells. *Phys. Chem. Chem. Phys.*, 19:5959–5970, 2017.

[89] Wolfgang Tress. Metal Halide Perovskites as Mixed Electronic-Ionic Conductors: Challenges and Opportunities - From Hysteresis to Memristivity. *J. Phys. Chem. Lett.*, 8:3106–3114, 2017.

[90] Teng Zhang, Chen Hu, and Shihe Yang. Ion Migration: A "Double-Edged Sword" for Halide-Perovskite-Based Electronic Devices. *Small Methods*, 4:1900552, 2020.

[91] Wenke Zhou, Juan Gu, Zhiqian Yang, Mingyang Wang, and Qing Zhao. Basis and Effects of Ion Migration on Photovoltaic Performance of Perovskite Solar Cells. *J. Phys. D. Appl. Phys.*, 54:063001, 2020.

[92] Huachao Zai, Yue Ma, Qi Chen, and Huanping Zhou. Ion Migration in Halide Perovskite Solar Cells: Mechanism, Characterization, Impact and Suppression. *J. Energy Chem.*, 63:528–549, 2021.

[93] Yao Zhao, Wenke Zhou, Zhengyuan Han, Dapeng Yu, and Qing Zhao. Effects of Ion Migration and Improvement Strategies for the Operational Stability of Perovskite Solar Cells. *Phys. Chem. Chem. Phys.*, 23:94–106, 2021.

[94] Henry J. Snaith, Antonio Abate, James M. Ball, Giles E. Eperon, Tomas Leijtens, Nakita K. Noel, Samuel D. Stranks, Jacob Tse-Wei Wang, Konrad Wojciechowski, and Wei Zhang. Anomalous Hysteresis in Perovskite Solar Cells. *J. Phys. Chem. Lett.*, 5:1511–1515, 2014.

[95] J. Beilsten-Edmands, G. E. Eperon, R. D. Johnson, H. J. Snaith, and P. G. Radaelli. Non-ferroelectric nature of the conductance hysteresis in $CH_3NH_3PbI_3$ perovskite-based photovoltaic devices. *Appl. Phys. Lett.*, 106:173502, 2015.

[96] Giles Richardson, Simon E.J. O'Kane, Ralf G. Niemann, Timo A. Peltola, Jamie M. Foster, Petra J. Cameron, and Alison B. Walker. Can Slow-Moving Ions Explain Hysteresis in the Current-Voltage Curves of Perovskite Solar Cells? *Energy Environ. Sci.*, 9:1476–1485, 2016.

[97] Elizabeth von Hauff and Dino Klotz. Impedance Spectroscopy for Perovskite Solar Cells: Characterisation, Analysis, and Diagnosis. *J. Mater. Chem. C*, 10:742–761, 2022.

[98] Prashant V. Kamat and Masaru Kuno. Halide Ion Migration in Perovskite Nanocrystals and Nanostructures. *Acc. Chem. Res.*, 54:520–531, 2021.

[99] Georgian Nedelcu, Loredana Protesescu, Sergii Yakunin, Maryna I. Bodnarchuk, Matthias J. Grotevent, and Maksym V. Kovalenko. Fast Anion-Exchange in Highly Luminescent Nanocrystals of Cesium Lead Halide Perovskites ($CsPbX_3$, X = Cl, Br, I). *Nano Lett.*, 15:5635–5640, 2015.

[100] Norman Pellet, Joël Teuscher, Joachim Maier, and Michael Grätzel. Transforming Hybrid Organic Inorganic Perovskites by Rapid Halide Exchange. *Chem. Mater.*, 27:2181–2188, 2015.

[101] Vikash Kumar Ravi, Rebecca A. Scheidt, Angshuman Nag, Masaru Kuno, and Prashant V. Kamat. To Exchange or Not to Exchange. Suppressing Anion Exchange in Cesium Lead Halide Perovskites with $PbSO_4$-Oleate Capping. *ACS Energy Lett.*, 3:1049–1055, 2018.

[102] Giles E. Eperon, Clara E. Beck, and Henry J. Snaith. Cation Exchange for Thin Film Lead Iodide Perovskite Interconversion. *Mater. Horizons*, 3:63–71, 2016.

[103] Yue Min Xie, Binbin Yu, Chunqing Ma, Xiuwen Xu, Yuanhang Cheng, Shuai Yuan, Zhao Kui Wang, Hrisheekesh Thachoth Chandran, Chun Sing Lee, Liang Sheng Liao, and Sai Wing Tsang. Direct Observation of Cation-Exchange in Liquid-to-Solid Phase Transformation in $FA_{1-x}MA_xPbI_3$ Based Perovskite Solar Cells. *J. Mater. Chem. A*, 6:9081–9088, 2018.

[104] Alessandro Greco, Alexander Hinderhofer, M. Ibrahim Dar, Neha Arora, Jan Hagenlocher, Andrey Chumakov, Michael Grätzel, and Frank Schreiber. Kinetics of Ion-

Exchange Reactions in Hybrid Organic-Inorganic Perovskite Thin Films Studied by In Situ Real-Time X-ray Scattering. *J. Phys. Chem. Lett.*, 9:6750–6754, 2018.

[105] Junke Jiang, Chidozie K. Onwudinanti, Ross A. Hatton, Peter A. Bobbert, and Shuxia Tao. Stabilizing Lead-Free All-Inorganic Tin Halide Perovskites by Ion Exchange. *J. Phys. Chem. C*, 122:17660–17667, 2018.

[106] Brent A. Koscher, Noah D. Bronstein, Jacob H. Olshansky, Yehonadav Bekenstein, and A. Paul Alivisatos. Surface- vs Diffusion-Limited Mechanisms of Anion Exchange in $CsPbBr_3$ Nanocrystal Cubes Revealed through Kinetic Studies. *J. Am. Chem. Soc.*, 138:12065–12068, 2016.

[107] Anamul Haque, Trupthi Devaiah Chonamada, Arka Bikash Dey, and Pralay K. Santra. Insights into the Interparticle Mixing of $CsPbBr_3$ and $CsPbI_3$ Nanocubes: Halide Ion Migration and Kinetics. *Nanoscale*, 12:20840–20848, 2020.

[108] Tor Elmelund, Brian Seger, Masaru Kuno, and Prashant V. Kamat. How Interplay between Photo and Thermal Activation Dictates Halide Ion Segregation in Mixed Halide Perovskites. *ACS Energy Lett.*, 5:56–63, 2019.

[109] Dongxu Pan, Yongping Fu, Jie Chen, Kyle J. Czech, John C. Wright, and Song Jin. Visualization and Studies of Ion-Diffusion Kinetics in Cesium Lead Bromide Perovskite Nanowires. *Nano Lett.*, 18:1807–1813, 2018.

[110] Abhijit Hazarika, Qian Zhao, E. Ashley Gaulding, Jeffrey A. Christians, Benjia Dou, Ashley R. Marshall, Taylor Moot, Joseph J. Berry, Justin C. Johnson, and Joseph M. Luther. Perovskite Quantum Dot Photovoltaic Materials beyond the Reach of Thin Films: Full-Range Tuning of A-Site Cation Composition. *ACS Nano*, 12:10327–10337, 2018.

[111] Jacob B. Hoffman, A. Lennart Schleper, and Prashant V. Kamat. Transformation of Sintered $CsPbBr_3$ Nanocrystals to Cubic $CsPbI_3$ and Gradient $CsPbBr_xI_{3-x}$ through Halide Exchange. *J. Am. Chem. Soc.*, 138:8603–8611, 2016.

[112] Tor Elmelund, Rebecca A. Scheidt, Brian Seger, and Prashant V. Kamat. Bidirectional Halide Ion Exchange in Paired Lead Halide Perovskite Films with Thermal Activation. *ACS Energy Lett.*, 4:1961–1969, 2019.

[113] Rebecca A. Scheidt and Prashant V. Kamat. Temperature-Driven Anion Migration in Gradient Halide Perovskites. *J. Chem. Phys.*, 151:134703, 2019.

[114] Ye Zhang, Dylan Lu, Mengyu Gao, Minliang Lai, Jia Lin, Teng Lei, Zhenni Lin, Li Na Quan, and Peidong Yang. Quantitative Imaging of Anion Exchange Kinetics in Halide Perovskites. *Proc. Natl. Acad. Sci. U. S. A.*, 116:12648–12653, 2019.

[115] Junichiro Mizusaki, Kimiyasu Arai, and Kazuo Fueki. Ionic Conduction of the Perovskite-Type Halides. *Solid State Ionics*, 11:203–211, 1983.

[116] R. Lakshmi Narayan, M. V.S. Sarma, and S. V. Suryanarayana. Ionic Conductivity of $CsPbCl_3$ and $CsPbBr_3$. *J. Mater. Sci. Lett.*, 6:93–94, 1987.

[117] Koji Yamada, Satomi Hino, Satoshi Hirose, Yohei Yamane, Ivan Turkevych, Toshiyuki Urano, Hiroshi Tomiyasu, Hideo Yamagishi, and Shinji Aramaki. Static and Dynamic Structures of Perovskite Halides ABX_3 (B = Pb, Sn) and Their Characteristic Semiconducting Properties by a Hückel Analytical Calculation. *Bull. Chem. Soc. Jpn.*, 91:1196–1204, 2018.

[118] Cheng Chen, Qiuyun Fu, Pengju Guo, Hualin Chen, Mei Wang, Wei Luo, and Zhiping Zheng. Ionic Transport Characteristics of Large-Size $CsPbBr_3$ Single Crystals. *Mater. Res. Express*, 6:115808, 2019.

[119] Bin Bin Zhang, Fangbao Wang, Hongjian Zhang, Bao Xiao, Qihao Sun, Jun Guo, Ahmed Ben Hafsia, Aihui Shao, Yadong Xu, and Jian Zhou. Defect Proliferation in $CsPbBr_3$ Crystal Induced by Ion Migration. *Appl. Phys. Lett.*, 116:063505, 2020.

[120] Simone Meloni, Thomas Moehl, Wolfgang Tress, Marius Franckevičius, Michael Saliba, Yong Hui Lee, Peng Gao, Mohammad Khaja Nazeeruddin, Shaik Mohammed Zakeeruddin, Ursula Rothlisberger, and Michael Graetzel. Ionic Polarization-Induced Current–Voltage Hysteresis in $CH_3NH_3PbX_3$ Perovskite Solar Cells. *Nat. Commun.*, 7:10334, 2016.

[121] Minliang Lai, Amael Obliger, Dylan Lu, Christopher S. Kley, Connor G. Bischak, Qiao Kong, Teng Lei, Letian Dou, Naomi S. Ginsberg, David T. Limmer, and Peidong Yang. Intrinsic Anion Diffusivity in Lead Halide Perovskites is Facilitated by a Soft Lattice. *Proc. Natl. Acad. Sci. U. S. A.*, 115:11929–11934, 2018.

[122] R. I. Biega and L. Leppert. Halogen Vacancy Migration at Surfaces of $CsPbBr_3$ Perovskites: Insights from Density Functional Theory. *JPhys Energy*, 3:034017, 2021.

[123] Long Zhang, Qingxin Zeng, and Kai Wang. Pressure-Induced Structural and Optical Properties of Inorganic Halide Perovskite $CsPbBr_3$. *J. Phys. Chem. Lett.*, 8:3752–3758, 2017.

[124] Manas Likhit Holekevi Chandrappa, Zhuoying Zhu, David P. Fenning, and Shyue Ping Ong. Correlated Octahedral Rotation and Organic Cation Reorientation Assist Halide Ion Migration in Lead Halide Perovskites. *Chem. Mater.*, 33:4672–4678, 2021.

[125] Jarvist M. Frost, Keith T. Butler, and Aron Walsh. Molecular Ferroelectric Contributions to Anomalous Hysteresis in Hybrid Perovskite Solar Cells. *APL Mater.*, 2:081506, 2014.

[126] Yinan Jiao, Shenghui Yi, Hanwen Wang, Bing Li, Weizhong Hao, Lulu Pan, Yan Shi, Xiangyu Li, Pengfei Liu, He Zhang, Cunfa Gao, Jinjin Zhao, and Jian Lu. Strain Engineering of Metal Halide Perovskites on Coupling Anisotropic Behaviors. *Adv. Funct. Mater.*, 31:2006243, 2021.

[127] Lei Gu, Deli Li, Lingfeng Chao, He Dong, Wei Hui, Tingting Niu, Chenxin Ran, Yingdong Xia, Lin Song, Yonghua Chen, and Wei Huang. Strain Engineering of Metal–Halide Perovskites toward Efficient Photovoltaics: Advances and Perspectives. *Sol. RRL*, 5:2000672, 2021.

[128] D. Parfitt, A. Kordatos, P. P. Filippatos, and A. Chroneos. Diffusion in Energy Materials: Governing Dynamics from Atomistic Modelling. *Appl. Phys. Rev.*, 4:031305, 2017.

[129] Zhendong Guo, Jing Wang, and Wan-Jian Yin. Atomistic Origin of Lattice Softness and its Impact on Structural and Carrier Dynamics in Three Dimensional Perovskites. *Energy Environ. Sci.*, 15:660–671, 2022.

[130] Robert Hooke. *Lectiones Cutlerianæ, or a Collection of Lectures: Physical, Mechanical, Geographical & Astronomical*. London, 1 edition, 1679.

[131] Robert Hooke. *Lectures de Potentia Restitutiva, or of Spring*. London, 1 edition, 1678.

[132] Y H Chang and C H Park. First-Principles Study of the Structural and the Electronic Properties of the $CsPbX_3$ and $CH_3NH_3PbX_3$. *J. Korean Phys. Soc.*, 44:889–893, 2004.

[133] G. Murtaza and Iftikhar Ahmad. First principle study of the structural and optoelectronic properties of cubic perovskites $CsPbM_3$ (M=Cl, Br, I). *Phys. B Condens. Matter*, 406:3222–3229, 2011.

[134] Md Roknuzzaman, Kostya Ken Ostrikov, Hongxia Wang, Aijun Du, and Tuquabo Tesfamichael. Towards Lead-Free Perovskite Photovoltaics and Optoelectronics by ab-initio Simulations. *Sci. Rep.*, 7:14025, 2017.

[135] Eric W. Welch, Young Kwang Jung, Aron Walsh, Luisa Scolfaro, and Alex Zakhidov. A Density Functional Theory Study on the Interface Stability between $CsPbBr_3$ and CuI. *AIP Adv.*, 10:085023, 2020.

[136] Khandaker Monower Hossain, Md Zahid Hasan, and Md Lokman Ali. Narrowing Bandgap and Enhanced Mechanical and Optoelectronic Properties of Perovskite Halides: Effects of Metal Doping. *AIP Adv.*, 11:015052, 2021.

[137] Abdessamad Najim, Bouchaib Hartiti, Hanan Absike, Hervé Joël Tchognia Nkuissi, Hicham Labrim, Salah Fadili, Philippe Thevenin, and Mehmet Ertugrul. Theoretical Investigation of Structural, Electronic, and Optical Properties of Halide Cubic Perovskite $CsPbBr_{3-x}I_x$. *Mater. Sci. Semicond. Process.*, 141:106442, 2022.

[138] Yevgeny Rakita, Sidney R. Cohen, Nir Klein Kedem, Gary Hodes, and David Cahen. Mechanical Properties of $APbX_3$ (A = Cs or CH_3NH_3; X = I or Br) Perovskite Single Crystals. *MRS Commun.*, 5:623–629, 2015.

[139] Yasutaka Nagaoka, Katie Hills-Kimball, Rui Tan, Ruipeng Li, Zhongwu Wang, and Ou Chen. Nanocube Superlattices of Cesium Lead Bromide Perovskites and Pressure-Induced Phase Transformations at Atomic and Mesoscale Levels. *Adv. Mater.*, 29:1606666, 2017.

[140] George J. Fischer, Zichao Wang, and Shun ichiro Karato. Elasticity of $CaTiO_3$, $SrTiO_3$ and $BaTiO_3$ Perovskites up to 3.0 GPa: the Effect of Crystallographic Structure. *Phys. Chem. Miner.*, 20:97–103, 1993.

[141] A. Yeganeh-Haeri, D. J. Weidner, and E. Ito. Elasticity of $MgSiO_3$ in the Perovskite Structure. *Science*, 243:787–789, 1989.

[142] Yang Zhou, Lu You, Shiwei Wang, Zhiliang Ku, Hongjin Fan, Daniel Schmidt, Andrivo Rusydi, Lei Chang, Le Wang, Peng Ren, Liufang Chen, Guoliang Yuan, Lang Chen, and Junling Wang. Giant Photostriction in Organic-Inorganic Lead Halide Perovskites. *Nat. Commun.*, 7:11193, 2016.

[143] Tzu Chiao Wei, Hsin Ping Wang, Ting You Li, Chun Ho Lin, Ying Hui Hsieh, Ying Hao Chu, and Jr Hau He. Photostriction of $CH_3NH_3PbBr_3$ Perovskite Crystals. *Adv. Mater.*, 29:1701789, 2017.

[144] Yongtao Liu, Bobby G. Sumpter, Jong K. Keum, Bin Hu, Mahshid Ahmadi, and Olga S. Ovchinnikova. Strain in Metal Halide Perovskites: The Critical Role of A-Site Cation. *ACS Appl. Energy Mater.*, 4:2068–2072, 2021.

[145] Bo Chen, Tao Li, Qingfeng Dong, Edoardo Mosconi, Jingfeng Song, Zhaolai Chen, Yehao Deng, Ye Liu, Stephen Ducharme, Alexei Gruverman, Filippo De Angelis, and Jinsong Huang. Large Electrostrictive Response in Lead Halide Perovskites. *Nat. Mater.*, 17:1020–1026, 2018.

[146] Haian Qiu and Jeffrey M. Mativetsky. Nanoscale Light- and Voltage-Induced Lattice Strain in Perovskite Thin Films. *Nanoscale*, 13:746–752, 2021.

[147] Junjie Fang, Zicheng Ding, Xiaoming Chang, Jing Lu, Tinghuan Yang, Jialun Wen, Yuanyuan Fan, Yalan Zhang, Tao Luo, Yonghua Chen, Shengzhong (Frank) Liu, and Kui Zhao. Microstructure and Lattice Strain Control towards High-Performance Ambient Green-Printed Perovskite Solar Cells. *J. Mater. Chem. A*, 9:13297–13305, 2021.

[148] Waqaas Rehman, David P. McMeekin, Jay B. Patel, Rebecca L. Milot, Michael B. Johnston, Henry J. Snaith, and Laura M. Herz. Photovoltaic Mixed-Cation Lead Mixed-Halide Perovskites: Links between Crystallinity, Photo-Stability and Electronic Properties. *Energy Environ. Sci.*, 10:361–369, 2017.

[149] Qian Li, Liming Zhang, Zhongwei Chen, and Zewei Quan. Metal Halide Perovskites under Compression. *J. Mater. Chem. A*, 7:16089–16108, 2019.

[150] Gang Liu, Lingping Kong, W. Yang, and Ho-kwang Mao. Pressure Engineering of Photovoltaic Perovskites. *Mater. Today*, 27:91–106, 2019.

[151] Zhaosheng Hu, Zhenhua Lin, Jie Su, Jincheng Zhang, Jingjing Chang, and Yue Hao. A Review on Energy Band-Gap Engineering for Perovskite Photovoltaics. *Sol. RRL*, 3:1900304, 2019.

[152] Sheng Liu, Shishuai Sun, Chee Kwan Gan, Andrés Granados Del Águila, Yanan Fang, Jun Xing, T. Thu Ha Do, Timothy J. White, Hongguo Li, Wei Huang, and Qihua Xiong. Manipulating Efficient Light Emission in Two-Dimensional Perovskite Crystals by Pressure-Induced Anisotropic Deformation. *Sci. Adv.*, 5:eaav9445, 2019.

[153] Constantinos C. Stoumpos, Christos D. Malliakas, John A. Peters, Zhifu Liu, Maria Sebastian, Jino Im, Thomas C. Chasapis, Arief C. Wibowo, Duck Young Chung, Arthur J. Freeman, Bruce W. Wessels, and Mercouri G. Kanatzidis. Crystal Growth

of the Perovskite Semiconductor $CsPbBr_3$: A New Material for High-Energy Radiation Detection. *Cryst. Growth Des.*, 13:2722–2727, 2013.

[154] Makhsud I. Saidaminov, Md Azimul Haque, Jawaher Almutlaq, Smritakshi Sarmah, Xiao He Miao, Raihana Begum, Ayan A. Zhumekenov, Ibrahim Dursun, Namchul Cho, Banavoth Murali, Omar F. Mohammed, Tom Wu, and Osman M. Bakr. Inorganic Lead Halide Perovskite Single Crystals: Phase-Selective Low-Temperature Growth, Carrier Transport Properties, and Self-Powered Photodetection. *Adv. Opt. Mater.*, 5:1600704, 2017.

[155] Xiaoliang Miao, Ting Qiu, Shufang Zhang, He Ma, Yanqiang Hu, Fan Bai, and Zhuangchun Wu. Air-stable $CsPb_{1-x}Bi_xBr_3$ ($0 \leq x \ll 1$) Perovskite Crystals: Optoelectronic and Photostriction Properties. *J. Mater. Chem. C*, 5:4931–4939, 2017.

[156] Jizhong Song, Qingzhi Cui, Jianhai Li, Jiayue Xu, Yue Wang, Leimeng Xu, Jie Xue, Yuhui Dong, Tian Tian, Handong Sun, and Haibo Zeng. Ultralarge All-Inorganic Perovskite Bulk Single Crystal for High-Performance Visible–Infrared Dual-Modal Photodetectors. *Adv. Opt. Mater.*, 5:1700157, 2017.

[157] Hongjian Zhang, Xin Liu, Jiangpeng Dong, Hui Yu, Ce Zhou, Binbin Zhang, Yadong Xu, and Wanqi Jie. Centimeter-Sized Inorganic Lead Halide Perovskite $CsPbBr_3$ Crystals Grown by an Improved Solution Method. *Cryst. Growth Des.*, 17:6426–6431, 2017.

[158] Peng Zhang, Guodong Zhang, Lin Liu, Dianxing Ju, Longzhen Zhang, Kui Cheng, and Xutang Tao. Anisotropic Optoelectronic Properties of Melt-Grown Bulk $CsPbBr_3$ Single Crystal. *J. Phys. Chem. Lett.*, 9:5040–5046, 2018.

[159] Yihui He, Liviu Matei, Hee Joon Jung, Kyle M. McCall, Michelle Chen, Constantinos C. Stoumpos, Zhifu Liu, John A. Peters, Duck Young Chung, Bruce W. Wessels, Michael R. Wasielewski, Vinayak P. Dravid, Arnold Burger, and Mercouri G. Kanatzidis. High Spectral Resolution of Gamma-Rays at Room Temperature by Perovskite $CsPbBr_3$ Single Crystals. *Nat. Commun.*, 9:1609, 2018.

[160] Peng Zhang, Qihao Sun, Yadong Xu, Xiang Li, Lin Liu, Guodong Zhang, and Xutang Tao. Enhancing Carrier Transport Properties of Melt-grown $CsPbBr_3$ Single Crystals by Eliminating Inclusions. *Cryst. Growth Des.*, 20:2424–2431, 2020.

[161] X. C. Liu, J. H. Han, H. F. Zhao, H. C. Yan, Y. Shi, M. X. Jin, C. L. Liu, and D. J. Ding. Pressure Dependence of Excited-State Charge-Carrier Dynamics in Organolead Tribromide Berovskites. *Appl. Phys. Lett.*, 112:191903, 2018.

[162] Nicholas Rolston, Kevin A. Bush, Adam D. Printz, Aryeh Gold-Parker, Yichuan Ding, Michael F. Toney, Michael D. McGehee, and Reinhold H. Dauskardt. Engineering Stress in Perovskite Solar Cells to Improve Stability. *Adv. Energy Mater.*, 8:1802139, 2018.

[163] Rhys M. Kennard, Clayton J. Dahlman, Ryan A. Decrescent, Jon A. Schuller, Kunal Mukherjee, Ram Seshadri, and Michael L. Chabinyc. Ferroelastic Hysteresis in Thin Films of Methylammonium Lead Iodide. *Chem. Mater.*, 33:298–309, 2021.

[164] Snehangshu Mishra, Subrata Ghosh, and Trilok Singh. Progress in Materials Development for Flexible Perovskite Solar Cells and Future Prospects. *ChemSusChem*, 14:512–538, 2021.

[165] Yingzhen Hu, Tingting Niu, Yanghua Liu, Yipeng Zhou, Yingdong Xia, Chenxin Ran, Zhongbin Wu, Lin Song, Peter Müller-Buschbaum, Yonghua Chen, and Wei Huang. Flexible Perovskite Solar Cells with High Power-Per-Weight: Progress, Application, and Perspectives. *ACS Energy Lett.*, 6:2917–2943, 2021.

[166] Guanqi Tang and Feng Yan. Recent Progress of Flexible Perovskite Solar Cells. *Nano Today*, 39:101155, 2021.

[167] Xiao Liang, Chuangye Ge, Qianru Fang, Wanyuan Deng, Sukumar Dey, Haoran Lin, Yong Zhang, Xintao Zhang, Quanyao Zhu, and Hanlin Hu. Flexible Perovskite Solar Cells: Progress and Prospects. *Front. Mater.*, 8:634353, 2021.

[168] Rudai Zhao, Zhenkun Gu, Pengwei Li, Yiqiang Zhang, and Yanlin Song. Flexible and Wearable Optoelectronic Devices Based on Perovskites. *Adv. Mater. Technol.*, 7:2101124, 2022.

[169] Rahul Patidar, Daniel Burkitt, Katherine Hooper, David Richards, and Trystan Watson. Slot-Die Coating of Perovskite Solar Cells: An Overview. *Mater. Today Commun.*, 22:100808, 2020.

[170] Gunhee Lee, Min Cheol Kim, Yong Whan Choi, Namyoung Ahn, Jihun Jang, Jungjin Yoon, Sang Moon Kim, Jong Gu Lee, Daeshik Kang, Hyun Suk Jung, and Mansoo Choi. Ultra-Flexible Perovskite Solar Cells with Crumpling Durability: Toward a Wearable Power Source. *Energy Environ. Sci.*, 12:3182–3191, 2019.

[171] Xiangchuan Meng, Zheren Cai, Yanyan Zhang, Xiaotian Hu, Zhi Xing, Zengqi Huang, Zhandong Huang, Yongjie Cui, Ting Hu, Meng Su, Xunfan Liao, Lin Zhang, Fuyi Wang, Yanlin Song, and Yiwang Chen. Bio-Inspired Vertebral Design for Scalable and Flexible Perovskite Solar Cells. *Nat. Commun.*, 11:3016, 2020.

[172] Qingshun Dong, Min Chen, Yuhang Liu, Felix T. Eickemeyer, Weidong Zhao, Zhenghong Dai, Yanfeng Yin, Chen Jiang, Jiangshan Feng, Shengye Jin, Shengzhong (Frank) Liu, Shaik M. Zakeeruddin, Michael Grätzel, Nitin P. Padture, and Yantao Shi. Flexible Perovskite Solar Cells with Simultaneously Improved Efficiency, Operational Stability, and Mechanical Reliability. *Joule*, 5:1587–1601, 2021.

[173] Jingru Zhang, Gary Hodes, Zhiwen Jin, and Shengzhong Liu. All-Inorganic $CsPbX_3$ Perovksite Solar Cells: Progress and Prospects. *Angew. Chem. , Int. Ed.*, 58:2–25, 2019.

[174] Caleb C. Boyd, Rongrong Cheacharoen, Tomas Leijtens, and Michael D. McGehee. Understanding Degradation Mechanisms and Improving Stability of Perovskite Photovoltaics. *Chem. Rev.*, 119:3418–3451, 2019.

[175] M. Bilal Faheem, Bilawal Khan, Chao Feng, M. Umar Farooq, Fazal Raziq, Yequan Xiao, and Yanbo Li. All-Inorganic Perovskite Solar Cells: Energetics, Key Challenges, and Strategies toward Commercialization. *ACS Energy Lett.*, 5:290–320, 2020.

[176] Shurong Wang, Aili Wang, and Feng Hao. Toward Stable Lead Halide Perovskite Solar Cells: A Knob on the A/X sites Components. *iScience*, 25:103599, 2022.

[177] Jianbing Huang, Shunquan Tan, Peter D. Lund, and Huanping Zhou. Impact of H2O on Organic-Inorganic Hybrid Perovskite Solar Cells. *Energy Environ. Sci.*, 10:2284–2311, 2017.

[178] Jeffrey A. Christians, Pierre A. Miranda Herrera, and Prashant V. Kamat. Transformation of the Excited State and Photovoltaic Efficiency of $CH_3NH_3PbI_3$ Perovskite upon Controlled Exposure to Humidified Air. *J. Am. Chem. Soc.*, 137:1530–1538, 2015.

[179] Jarvist M. Frost, Keith T. Butler, Federico Brivio, Christopher H. Hendon, Mark Van Schilfgaarde, and Aron Walsh. Atomistic Origins of High-Performance in Hybrid Halide Perovskite Solar Cells. *Nano Lett.*, 14:2584–2590, 2014.

[180] Nicholas Aristidou, Irene Sanchez-Molina, Thana Chotchuangchutchaval, Michael Brown, Luis Martinez, Thomas Rath, and Saif A. Haque. The Role of Oxygen in the Degradation of Methylammonium Lead Trihalide Perovskite Photoactive Layers. *Angew. Chem.*, 127:8326–8330, 2015.

[181] Daniel Bryant, Nicholas Aristidou, Sebastian Pont, Irene Sanchez-Molina, Thana Chotchunangatchaval, Scot Wheeler, James R. Durrant, and Saif A. Haque. Light

and Oxygen Induced Degradation Limits the Operational Stability of Methylammonium Lead Triiodide Perovskite Solar Cells. *Energy Environ. Sci.*, 9:1655–1660, 2016.

[182] Nicholas Aristidou, Christopher Eames, Irene Sanchez-Molina, Xiangnan Bu, Jan Kosco, M. Saiful Islam, and Saif A. Haque. Fast Oxygen Diffusion and Iodide Defects Mediate Oxygen-Induced Degradation of Perovskite Solar Cells. *Nat. Commun.*, 8:15218, 2017.

[183] Yan Jiang, Longbin Qiu, Emilio J. Juarez-Perez, Luis K. Ono, Zhanhao Hu, Zonghao Liu, Zhifang Wu, Lingqiang Meng, Qijing Wang, and Yabing Qi. Reduction of Lead Leakage from Damaged Lead Halide Perovskite Solar Modules using Self-Healing Polymer-Based Encapsulation. *Nat. Energy*, 4:585–593, 2019.

[184] Yifan Lv, Hui Zhang, Ruqing Liu, Yanan Sun, and Wei Huang. Composite Encapsulation Enabled Superior Comprehensive Stability of Perovskite Solar Cells. *ACS Appl. Mater. Interfaces*, 12:27277–27285, 2020.

[185] Clara A. Aranda, Laura Caliò, and Manuel Salado. Toward Commercialization of Stable Devices: An Overview on Encapsulation of Hybrid Organic-Inorganic Perovskite Solar Cells. *Crystals*, 11:519, 2021.

[186] Jiale Li, Rui Xia, Wenjing Qi, Xin Zhou, Jian Cheng, Yifeng Chen, Guofu Hou, Yi Ding, Yuelong Li, Ying Zhao, and Xiaodan Zhang. Encapsulation of Perovskite Solar Cells for Enhanced Stability: Structures, Materials and Characterization. *J. Power Sources*, 485:229313, 2021.

[187] Sai Ma, Guizhou Yuan, Ying Zhang, Ning Yang, Yujing Li, and Qi Chen. Development of Encapsulation Strategies Towards the Commercialization of Perovskite Solar Cells. *Energy Environ. Sci.*, 15:13–55, 2022.

[188] Azat F. Akbulatov, Sergey Yu Luchkin, Lyubov A. Frolova, Nadezhda N. Dremova, Kirill L. Gerasimov, Ivan S. Zhidkov, Denis V. Anokhin, Ernst Z. Kurmaev, Keith J. Stevenson, and Pavel A. Troshin. Probing the Intrinsic Thermal and Photochemical Stability of Hybrid and Inorganic Lead Halide Perovskites. *J. Phys. Chem. Lett.*, 8:1211–1218, 2017.

[189] Meiqian Tai, Cho Fai Jonathan Lau, Hong Lin, and Zhiping Wang. Advances in Phase Stability of Cesium Lead Halide Perovskites. *Sol. RRL*, 4:2000495, 2020.

[190] Julian A. Steele, Handong Jin, Iurii Dovgaliuk, Robert F. Berger, Tom Braeckevelt, Haifeng Yuan, Cristina Martin, Eduardo Solano, Kurt Lejaeghere, Sven M. J. Rogge,

Charlotte Notebaert, Wouter Vandezande, Kris P. F. Janssen, Bart Goderis, Elke Debroye, Ya-Kun Wang, Yitong Dong, Dongxin Ma, Makhsud Saidaminov, Hairen Tan, Zhenghong Lu, Vadim Dyadkin, Dmitry Chernyshov, Veronique Van Speybroeck, Edward H. Sargent, Johan Hofkens, and Maarten B. J. Roeffaers. Thermal Unequilibrium of Strained Black $CsPbI_3$ Thin Films. *Science*, 365:679–684, 2019.

[191] Sunihl Ma, Seong Hun Kim, Beomjin Jeong, Hyeok Chan Kwon, Seong Cheol Yun, Gyumin Jang, Hyunha Yang, Cheolmin Park, Donghwa Lee, and Jooho Moon. Strain-Mediated Phase Stabilization: A New Strategy for Ultrastable α-$CsPbI_3$ Perovskite by Nanoconfined Growth. *Small*, 15:1900219, 2019.

[192] Da Bin Kim, Jung Won Lee, and Yong Soo Cho. Anisotropic In Situ Strain-Engineered Halide Perovskites for High Mechanical Flexibility. *Adv. Funct. Mater.*, 31:2007131, 2020.

[193] Yifan Liu, Zhengli Wu, Yuxi Dou, Junwen Zhang, Tongle Bu, Kaicheng Zhang, De Fang, Zhiliang Ku, Fuzhi Huang, Yi-Bing Cheng, and Jie Zhong. Formamidinium-based Perovskite Solar Cells with Enhanced Moisture Stability and Performance via Confined Pressure Annealing. *J. Phys. Chem. C*, 124:12249-12258, 2020.

[194] Linn Leppert, Sebastian E. Reyes-Lillo, and Jeffrey B. Neaton. Electric Field- and Strain-Induced Rashba Effect in Hybrid Halide Perovskites. *J. Phys. Chem. Lett.*, 7:3683–3689, 2016.

[195] Christopher Grote and Robert F. Berger. Strain Tuning of Tin-Halide and Lead-Halide Perovskites: A First-Principles Atomic and Electronic Structure Study. *J. Phys. Chem. C*, 119:22832–22837, 2015.

[196] Guang Song, Benling Gao, Guannan Li, and Jun Zhang. First-Principles Study on the Electric Structure and Ferroelectricity in Epitaxial $CsSnI_3$ Films. *RSC Adv.*, 7:41077–41083, 2017.

[197] Tianji Ou, Xinjun Ma, Huacai Yan, Wenshu Shen, Hao Liu, Yonghao Han, Xizhe Liu, Cailong Liu, Yanzhang Ma, and Chunxiao Gao. Pressure Effects on the Inductive Loop, Mixed Conduction, and Photoresponsivity in Formamidinium Lead Bromide Perovskite. *Appl. Phys. Lett.*, 113:262105, 2018.

[198] Yicheng Zhao, Peng Miao, Jack Elia, Huiying Hu, Xiaoxia Wang, Thomas Heumueller, Yi Hou, Gebhard J. Matt, Andres Osvet, Yu Ting Chen, Mariona Tarragó, Dominique de Ligny, Thomas Przybilla, Peter Denninger, Johannes Will, Jiyun Zhang, Xiaofeng Tang, Ning Li, Chenglin He, Anlian Pan, Alfred J. Meixner, Erdmann Spiecker, Dai

Zhang, and Christoph J. Brabec. Strain-Activated Light-Induced Halide Segregation in Mixed-Halide Perovskite Solids. *Nat. Commun.*, 11:6328, 2020.

[199] Lei Guo, Gao Xu, Gang Tang, Daining Fang, and Jiawang Hong. Structural Stability and Optoelectronic Properties of Tetragonal $MAPbI_3$ under Strain. *Nanotechnology*, 31:225204, 2020.

[200] Zhun Yao, Zhuo Xu, Wangen Zhao, Jingru Zhang, Hui Bian, Yuankun Fang, Yan Yang, and Shengzhong Liu. Enhanced Efficiency of Inorganic $CsPbI_{3-x}Br_x$ Perovskite Solar Cell via Self-Regulation of Antisite Defects. *Adv. Energy Mater.*, 11:2100403, 2021.

[201] Konrad Domanski, Juan Pablo Correa-Baena, Nicolas Mine, Mohammad Khaja Nazeeruddin, Antonio Abate, Michael Saliba, Wolfgang Tress, Anders Hagfeldt, and Michael Grätzel. Not All That Glitters Is Gold: Metal-Migration-Induced Degradation in Perovskite Solar Cells. *ACS Nano*, 10:6306–6314, 2016.

[202] Yongbo Yuan, Qi Wang, Yuchuan Shao, Haidong Lu, Tao Li, Alexei Gruverman, and Jinsong Huang. Electric-Field-Driven Reversible Conversion between Methylammonium Lead Triiodide Perovskites and Lead Iodide at Elevated Temperatures. *Adv. Energy Mater.*, 6:1501803, 2016.

[203] Christoph Freysoldt, Blazej Grabowski, Tilmann Hickel, Jörg Neugebauer, Georg Kresse, Anderson Janotti, and Chris G. Van De Walle. First-Principles Calculations for Point Defects in Solids. *Rev. Mod. Phys.*, 86:253–305, 2014.

[204] Pierre Hohenberg and Walter Kohn. Inhomogeneous Electron Gas. *Phys. Rev.*, 136:864–871, 1964.

[205] Jorge Kohanoff and Nikitas I. Gidopoulos. *Density Functional Theory: Basics, New Trends and Applications*. John Wiley & Sons, Chichester, 2003.

[206] M. Born and R. Oppenheimer. Zur Quantentheorie der Molekeln. *Ann. Phys.*, 389:457–484, 1927.

[207] D. R. Hartree. The Wave Mechanics of an Atom with a Non-Coulomb Central Field Part I Theory and Methods. *Math. Proc. Cambridge Philos. Soc.*, 24:89–110, 1928.

[208] V. Fock. Näherungsmethode zur Lösung des Quantenmechanischen Mehrkörperproblems. *Zeitschrift für Phys.*, 61:126–148, 1930.

[209] J. C. Slater. Note on Hartree's Method. *Phys. Rev.*, 35:210–211, 1930.

[210] L. H. Thomas. The Calculation of Atomic Fields. *Math. Proc. Cambridge Philos. Soc.*, 23:542–548, 1927.

[211] Enrico Fermi. Un Metodo Statistico per la Determinazione di Alcune Prioprietà dell'Atomo. *Accad. Naz. dei Lincei*, 6:602–607, 1927.

[212] Walter Kohn and Lu Jeu Sham. Self-Consistent Equations Including Exchange and Correlation Effects. *Phys. Rev.*, 140:1133–1138, 1965.

[213] John P. Perdew and Karla Schmidt. Jacob's Ladder of Density Functional Approximations for the Exchange-Correlation Energy. *AIP Conf. Proc.*, 577:1–20, 2001.

[214] John P. Perdew, Kieron Burke, and Matthias Ernzerhof. Generalized Gradient Approximation Made Simple. *Phys. Rev. Lett.*, 77:3865–3868, 1996.

[215] John P. Perdew, Adrienn Ruzsinszky, Gábor I. Csonka, Oleg A. Vydrov, Gustavo E. Scuseria, Lucian A. Constantin, Xiaolan Zhou, and Kieron Burke. Restoring the Density-Gradient Expansion for Exchange in Solids and Surfaces. *Phys. Rev. Lett.*, 100:136406, 2008.

[216] Jianwei Sun, Adrienn Ruzsinszky, and John p. Perdew. Strongly Constrained and Appropriately Normed Semilocal Density Functional. *Phys. Rev. Lett.*, 115:036402, 2015.

[217] Jianwei Sun, Richard C. Remsing, Yubo Zhang, Zhaoru Sun, Adrienn Ruzsinszky, Haowei Peng, Zenghui Yang, Arpita Paul, Umesh Waghmare, Xifan Wu, Michael L. Klein, and John P. Perdew. Accurate First-Principles Structures and Energies of Diversely Bonded Systems from an Efficient Density Functional. *Nat. Chem.*, 8:831–836, 2016.

[218] Albert P. Bartók and Jonathan R. Yates. Regularized SCAN Functional. *J. Chem. Phys.*, 150:161101, 2019.

[219] Stefan Grimme, Andreas Hansen, Sebastian Ehlert, and Jan Michael Mewes. R2SCAN-3c: A "Swiss Army Knife" Composite Electronic-Structure Method. *J. Chem. Phys.*, 154:064103, 2021.

[220] Sebastian Ehlert, Uwe Huniar, Jinliang Ning, James W. Furness, Jianwei Sun, Aaron D. Kaplan, John P. Perdew, and Jan Gerit Brandenburg. R2SCAN-D4: Dispersion Corrected Meta-Generalized Gradient Approximation for General Chemical Applications. *J. Chem. Phys.*, 154:061101, 2021.

[221] Hendrik J. Monkhorst and James D. Pack. Special Points for Brillouin-Zone Integrations. *Phys. Rev. B*, 13:5188–5192, 1976.

[222] A.R. Allnatt and A.B. Lidiard. *Atomic Transport in Solids*. Cambridge University Press, Cambridge, 1st edition, 1993.

[223] George H. Vineyard. Frequency Factors and Isotope Effects in Solid State Rate Processes. *J. Phys. Chem. Solids*, 3:121–127, 1957.

[224] Henry Eyring. The Activated Complex in Chemical Reactions. *J. Chem. Phys.*, 3:63–71, 1935.

[225] M. G. Evans and M. Polanyi. Some Applications of the Transition State Method to the Calculation of Reaction Velocities, Especially in Solution. *Trans. Faraday Soc.*, 31:875–894, 1935.

[226] Keith J. Laidler and M. Christine King. The Development of Transition-State Theory. *J. Phys. Chem.*, 87:2657–2664, 1983.

[227] Graeme Henkelman, Blas P. Uberuaga, and Hannes Jónsson. Climbing Image Nudged Elastic Band Method for Finding Saddle Points and Minimum Energy Paths. *J. Chem. Phys.*, 113:9901–9904, 2000.

[228] Daniel Sheppard, Rye Terrell, and Graeme Henkelman. Optimization Methods for Finding Minimum Energy Paths. *J. Chem. Phys.*, 128:134106, 2008.

[229] Daniel Sheppard, Penghao Xiao, William Chemelewski, Duane D. Johnson, and Graeme Henkelman. A Generalized Solid-State Nudged Elastic Band Method. *J. Chem. Phys.*, 136:074103, 2012.

[230] Graeme Henkelman and Hannes Jónsson. A Dimer Method for Finding Saddle Points on High Dimensional Potential Surfaces Using Only First Derivatives. *J. Chem. Phys.*, 111:7010–7022, 1999.

[231] Andreas Heyden, Alexis T. Bell, and Frerich J. Keil. Efficient Methods for Finding Transition States in Chemical Reactions: Comparison of Improved Dimer Method and Partitioned Rational Function Optimization Method. *J. Chem. Phys.*, 123:224101, 2005.

[232] Johannes Kästner and Paul Sherwood. Superlinearly Converging Dimer Method for Transition State Search. *J. Chem. Phys.*, 128:014106, 2008.

[233] Penghao Xiao, Daniel Sheppard, Jutta Rogal, and Graeme Henkelman. Solid-State Dimer Method for Calculating Solid-Solid Phase Transitions. *J. Chem. Phys.*, 140:174104, 2014.

[234] Atsushi Togo and Isao Tanaka. First Principles Phonon Calculations in Materials Science. *Scr. Mater.*, 108:1–5, 2015.

[235] M. W. Ammann. *Diffusion in Minerals of the Earth's Lower Mantle: Constraining Rheology from First Principles from First Principles*. PhD thesis, 2011.

[236] G. Kresse, J. Furthmüller, and J. Hafner. Ab Initio Force Constant Approach to Phonon Dispersion Relations of Diamond and Graphite. *EPL*, 32:729–734, 1995.

[237] K. Parlinski, Z. Q. Li, and Y. Kawazoe. First-Principles Determination of the Soft Mode in Cubic ZrO_2. *Phys. Rev. Lett.*, 78:4063–4066, 1997.

[238] P. Giannozzi, S. de Gironcoli, P Pavone, and S Baroni. Ab Initio Calculation of Phonon Dispersions in Semiconductors. *Phys. Rev. B*, 43:7231–7242, 1991.

[239] Xavier Gonze and Changyol Lee. Dynamical Matrices, Born Effective Charges, Dielectric Permittivity Tensors, and Interatomic Force Constants from Density-Functional Perturbation Theory. *Phys. Rev. B - Condens. Matter Mater. Phys.*, 55:10355–10368, 1997.

[240] N. F. Mott and R. W. Gurney. *Electronic Processes in Ionic Crystals*. The Clarendon Press, Oxford, 2nd edition, 1950.

[241] A. R. Genreith-Schriever and R. A. De Souza. Field-Enhanced Ion Transport in Solids: Reexamination with Molecular Dynamics Simulations. *Phys. Rev. B*, 94:224304, 2016.

[242] Al-Moatasem El-Sayed, Matthew B. Watkins, Tibor Grasser, and Alexander L. Shluger. Effect of Electric Field on Migration of Defects in Oxides: Vacancies and Interstitials in Bulk MgO. *Phys. Rev. B*, 98:064102, 2018.

[243] R.W. Balluffi. *Introduction to Elasticity Theory for Crystal Defects*. Cambridge University Press, New York, 1st edition, 2012.

[244] Emmanuel Clouet, Céline Varvenne, and Thomas Jourdan. Elastic Modeling of Point-Defects and Their Interaction. *Comput. Mater. Sci.*, 147:49–63, 2018.

[245] Ashkan Moradabadi, Payam Kaghazchi, Jochen Rohrer, and Karsten Albe. Influence of Elastic Strain on the Thermodynamics and Kinetics of Lithium Vacancy in Bulk $LiCoO_2$. *Phys. Rev. Mater.*, 2(1):1–9, 2018.

[246] P. Maugis, S. Chentouf, and D. Connétable. Stress-Controlled Carbon Diffusion Channeling in bct-Iron: A Mean-Field Theory. *J. Alloys Compd.*, 769:1121–1131, 2018.

[247] Damien Connétable and Philippe Maugis. Effect of Stress on Vacancy Formation and Diffusion in fcc Systems: Comparison between DFT Calculations and Elasticity Theory. *Acta Mater.*, 200:869–882, nov 2020.

[248] Nam Gyu Park. Perovskite Solar Cells: An Emerging Photovoltaic Technology. *Mater. Today*, 18:65–72, 2015.

[249] Robert F. Service. Perovskite LEDs Begin to Shine. *Science*, 364(6444):918, 2019.

[250] M. Sebastian, J. A. Peters, C. C. Stoumpos, J. Im, S. S. Kostina, Z. Liu, M. G. Kanatzidis, A. J. Freeman, and B. W. Wessels. Excitonic Emissions and Above-Band-Gap Luminescence in the Single-Crystal Perovskite Semiconductors $CsPbBr_3$ and $CsPbCl_3$. *Phys. Rev. B - Condens. Matter Mater. Phys.*, 92:235210, 2015.

[251] Guangda Niu, Xudong Guo, and Liduo Wang. Review of Recent Progress in Chemical Stability of Perovskite Solar Cells. *J. Mater. Chem. A*, 3:8970–8980, 2015.

[252] Sofia Masi, Andrés F. Gualdrón-Reyes, and Iván Mora-Seró. Stabilization of Black Perovskite Phase in $FAPbI_3$ and $CsPbI_3$. *ACS Energy Lett.*, 5:1974–1985, 2020.

[253] Johan Klarbring. Low-Energy Paths for Octahedral Tilting in Inorganic Halide Perovskites. *Phys. Rev. B*, 99:104105, 2019.

[254] Jon M. Azpiroz, Edoardo Mosconi, Juan Bisquert, and Filippo De Angelis. Defect Migration in Methylammonium Lead Iodide and its Role in Perovskite Solar Cell Operation. *Energy Environ. Sci.*, 8:2118–2127, 2015.

[255] Aron Walsh and Samuel D. Stranks. Taking Control of Ion Transport in Halide Perovskite Solar Cells. *ACS Energy Lett.*, 3:1983–1990, 2018.

[256] Alessandro Senocrate, Igor Moudrakovski, Tolga Acartürk, Rotraut Merkle, Gee Yeong Kim, Ulrich Starke, Michael Grätzel, and Joachim Maier. Slow $CH_3NH_3^+$ Diffusion in $CH_3NH_3PbI_3$ under Light Measured by Solid-State NMR and Tracer Diffusion. *J. Phys. Chem. C*, 122:21803–21806, 2018.

[257] Konrad Domanski, Bart Roose, Taisuke Matsui, Michael Saliba, Silver Hamill Turren-Cruz, Juan Pablo Correa-Baena, Cristina Roldan Carmona, Giles Richardson, Jamie M. Foster, Filippo De Angelis, James M. Ball, Annamaria Petrozza, Nicolas Mine, Mohammad K. Nazeeruddin, Wolfgang Tress, Michael Grätzel, Ullrich Steiner, Anders Hagfeldt, and Antonio Abate. Migration of Cations Induces Reversible Performance

Losses over Day/Night Cycling in Perovskite Solar Cells. *Energy Environ. Sci.*, 10:604–613, 2017.

[258] Fanhao Jia, Georg Kresse, Cesare Franchini, Peitao Liu, Jian Wang, Alessandro Stroppa, and Wei Ren. Cubic and Tetragonal Perovskites from the Random Phase Approximation. *Phys. Rev. Mater.*, 3:103801, 2019.

[259] Menno Bokdam, Jonathan Lahnsteiner, Benjamin Ramberger, Tobias Schäfer, and Georg Kresse. Assessing Density Functionals Using Many Body Theory for Hybrid Perovskites. *Phys. Rev. Lett.*, 119:145501, 2017.

[260] C. Shahi. *Assessment of the Meta-GGA SCAN and Self-Interaction Corrected SCAN Density Functional*. PhD thesis, Temple University, 2019.

[261] Haibo Xue, Geert Brocks, and Shuxia Tao. Comparison of Different Functionals for Density Functional Theory Calculations of Defects in Metal Halide Perovskites. *arXiv*, page 2104.01087v1, 2021.

[262] Eric B. Isaacs and Chris Wolverton. Performance of the Strongly Constrained and Appropriately Normed Density Functional for Solid-State Materials. *Phys. Rev. Mater.*, 2:063801, 2018.

[263] M. Rodová, J. Brožek, K. Knížek, and K. Nitsch. Phase Transitions in Ternary Caesium Lead Bromide. *J. Therm. Anal. Calorim.*, 71:667–673, 2003.

[264] Jie Xue, Dandan Yang, Bo Cai, Xiaobao Xu, Jian Wang, He Ma, Xuechao Yu, Guoliang Yuan, Yousheng Zou, Jizhong Song, and Haibo Zeng. Photon-Induced Reversible Phase Transition in $CsPbBr_3$ Perovskite. *Adv. Funct. Mater.*, 29:1807922, 2019.

[265] Raouia Ben Sadok, Dalila Hammoutène, and Neculai Plugaru. New Phase Transitions Driven by Soft Phonon Modes for $CsPbBr_3$: Density Functional Theory Study. *Phys. Status Solidi Basic Res.*, 258:2000289, 2021.

[266] Hamid M. Ghaithan, Zeyad A. Alahmed, Saif M.H. Qaid, Mahmoud Hezam, and Abdullah S. Aldwayyan. Density Functional Study of Cubic, Tetragonal, and Orthorhombic $CsPbBr_3$ Perovskite. *ACS Omega*, 5:7468–7480, 2020.

[267] Kateřina Tomanová, Václav Čuba, Mikhail G. Brik, Eva Mihóková, Rosana Martinez Turtos, Paul Lecoq, Etiennette Auffray, and Martin Nikl. On the Structure, Synthesis, and Characterization of Ultrafast Blue-Emitting $CsPbBr_3$ Nanoplatelets. *APL Mater.*, 7:011104, 2019.

[268] Peter Blaha, Karlheinz Schwarz, Fabien Tran, Robert Laskowski, Georg K.H. Madsen, and Laurence D. Marks. WIEN2k: An APW+lo Program for Calculating the Properties of Solids. *J. Chem. Phys.*, 152:074101, 2020.

[269] X. Gonze, B. Amadon, P. M. Anglade, J. M. Beuken, F. Bottin, P. Boulanger, F. Bruneval, D. Caliste, R. Caracas, M. Côté, T. Deutsch, L. Genovese, Ph Ghosez, M. Giantomassi, S. Goedecker, D. R. Hamann, P. Hermet, F. Jollet, G. Jomard, S. Leroux, M. Mancini, S. Mazevet, M. J.T. Oliveira, G. Onida, Y. Pouillon, T. Rangel, G. M. Rignanese, D. Sangalli, R. Shaltaf, M. Torrent, M. J. Verstraete, G. Zerah, and J. W. Zwanziger. ABINIT: First-Principles Approach to Material and Nanosystem Properties. *Comput. Phys. Commun.*, 180:2582–2615, 2009.

[270] Maarten De Jong, Wei Chen, Thomas Angsten, Anubhav Jain, Randy Notestine, Anthony Gamst, Marcel Sluiter, Chaitanya Krishna Ande, Sybrand Van Der Zwaag, Jose J. Plata, Cormac Toher, Stefano Curtarolo, Gerbrand Ceder, Kristin A. Persson, and Mark Asta. Charting the Complete Elastic Properties of Inorganic Crystalline Compounds. *Sci. Data*, 2:150009, 2015.

[271] Jung Hoon Lee, Nicholas C. Bristowe, June Ho Lee, Sung Hoon Lee, Paul D. Bristowe, Anthony K. Cheetham, and Hyun Myung Jang. Resolving the Physical Origin of Octahedral Tilting in Halide Perovskites. *Chem. Mater.*, 28:4259–4266, 2016.

[272] Andrea Bernasconi and Lorenzo Malavasi. Direct Evidence of Permanent Octahedra Distortion in $MAPbBr_3$ Hybrid Perovskite. *ACS Energy Lett.*, 2:863–868, 2017.

[273] Emily C. Schueller, Geneva Laurita, Douglas H. Fabini, Constantinos C. Stoumpos, Mercouri G. Kanatzidis, and Ram Seshadri. Crystal Structure Evolution and Notable Thermal Expansion in Hybrid Perovskites Formamidinium Tin Iodide and Formamidinium Lead Bromide. *Inorg. Chem.*, 57:695–701, 2018.

[274] `https://github.com/materialsvirtuallab/pymatgen-analysis-diffusion`.

[275] Shyue Ping Ong, William Davidson Richards, Anubhav Jain, Geoffroy Hautier, Michael Kocher, Shreyas Cholia, Dan Gunter, Vincent L. Chevrier, Kristin A. Persson, and Gerbrand Ceder. Python Materials Genomics (pymatgen): A Robust, Open-Source Python Library for Materials Analysis. *Comput. Mater. Sci.*, 68:314–319, feb 2013.

[276] Jun Haruyama, Keitaro Sodeyama, Liyuan Han, and Yoshitaka Tateyama. First-Principles Study of Ion Diffusion in Perovskite Solar Cell Sensitizers. *J. Am. Chem. Soc.*, 137(32):10048–10051, 2015.

[277] Edoardo Mosconi and Filippo De Angelis. Mobile Ions in Organohalide Perovskites: Interplay of Electronic Structure and Dynamics. *ACS Energy Lett.*, 1:182–188, 2016.

[278] Yanqi Luo, Parisa Khoram, Sarah Brittman, Zhuoying Zhu, Barry Lai, Shyue Ping Ong, Erik C. Garnett, and David P. Fenning. Direct Observation of Halide Migration and its Effect on the Photoluminescence of Methylammonium Lead Bromide Perovskite Single Crystals. *Adv. Mater.*, 29:1703451, 2017.

[279] Hongliang Shi and Mao Hua Du. Shallow Halogen Vacancies in Halide Optoelectronic Materials. *Phys. Rev. B*, 90:174103, 2014.

[280] Jun Kang. Effects of Band Edge Positions on Defect Structure in Lead Halide Perovskites: A Case Study on the Br Vacancy in $CsPbBr_3$. *Phys. Rev. Mater.*, 4:085405, 2020.

[281] Michael W. Swift and John L. Lyons. Deep Levels in Cesium Lead Bromide from Native Defects and Hydrogen. *J. Mater. Chem. A*, 9:7491–7495, 2021.

[282] Julius Koettgen, Tobias Zacherle, Steffen Grieshammer, and Manfred Martin. Ab Initio Calculation of the Attempt Frequency of Oxygen Diffusion in Pure and Samarium Doped Ceria. *Phys. Chem. Chem. Phys.*, 19:9957–9973, 2017.

[283] Michael Häfner and Thomas Bredow. Mobility of F Centers in Alkali Halides. *J. Phys. Chem. C*, 125:9085–9095, may 2021.

[284] M. Saiful Islam. Ionic Transport in ABO_3 Perovskite Oxides: a Computer Modelling Tour. *J. Mater. Chem.*, 10:1027–1038, 2000.

[285] Henry Wu, Tam Mayeshiba, and Dane Morgan. High-Throughput Ab-Initio Dilute Solute Diffusion Database. *Sci. Data*, 3:160054, 2016.

[286] Ravi Agarwal and Dallas R. Trinkle. Ab Initio Magnesium-Solute Transport Database Using Exact Diffusion Theory. *Acta Mater.*, 150:339–350, 2018.

[287] Ronghan Chen, Zhenming Xu, Yuechuan Lin, Buyao Lv, Shou Hang Bo, and Hong Zhu. Influence of Structural Distortion and Lattice Dynamics on Li-Ion Diffusion in $Li_3OCl_{1-x}Br_x$ Superionic Conductors. *ACS Appl. Energy Mater.*, 4:2107–2114, 2021.

[288] Ji Hyun Cha, Jae Hoon Han, Wenping Yin, Cheolwoo Park, Yongmin Park, Tae Kyu Ahn, Jeong Ho Cho, and Duk Young Jung. Photoresponse of $CsPbBr_3$ and Cs_4PbBr_6 Perovskite Single Crystals. *J. Phys. Chem. Lett.*, 8:565–570, 2017.

[289] Paifeng Luo, Yugang Zhou, Shengwen Zhou, Yingwei Lu, Chenxi Xu, Wei Xia, and Lin Sun. Fast Anion-Exchange from $CsPbI_3$ to $CsPbBr_3$ via Br_2-Vapor-Assisted Deposition for Air-Stable All-Inorganic Perovskite Solar Cells. *Chem. Eng. J.*, 343:146–154, 2018.

[290] Subas Muduli, Padmini Pandey, Gayathri Devatha, Rohit Babar, Thripuranthaka M, Dushyant C Kothari, Mukul Kabir, Pramod P Pillai, and Satishchandra Ogale. Photoluminescence Quenching in Self-Assembled $CsPbBr_3$ Quantum Dots on Few-Layer Black Phosphorus Sheets. *Angew. Chem.*, 130:7808–7812, 2018.

[291] L. Bányai and A. Aldea. Master Equation Approach to the Hopping Transport Theory. *Fortschritte der Phys.*, 27:435–462, 1979.

[292] Dallas R Trinkle. Diffusivity and Derivatives for Interstitial Solutes: Activation Energy, Volume, and Elastodiffusion Tensors. *Philos. Mag.*, 96:2714–2735, 2016.

[293] Atsushi Togo and Isao Tanaka. Spglib: A Software Library for Crystal Symmetry Search. *arXiv*, page 1808.01590v1, 2018.

[294] Roger A. De Souza and David N. Mueller. Electrochemical Methods for Determining Ionic Charge in Solids. *Nat. Mater.*, 10:1038, 2020.

[295] Luca Bertoluzzi, Rebecca A Belisle, Kevin A Bush, Rongrong Cheacharoen, Michael D. McGehee, and Brian C. O'Regan. In Situ Measurement of Electric-Field Screening in Hysteresis-Free PTAA/$FA_{0.83}Cs_{0.17}Pb(I_{0.83}Br_{0.17})_3$/$C_{60}$ Perovskite Solar Cells Gives an Ion Mobility of 3×10^{-7} $cm^2/(Vs)$, 2 Orders of Magnitude Faster than Reported for Metal-Oxide-Contacted Perovskite C. *J. Am. Chem. Soc.*, 140:12775–12784, 2018.

[296] Susanne T. Birkhold, Jake T. Precht, Rajiv Giridharagopal, Giles E. Eperon, Lukas Schmidt-Mende, and David S. Ginger. Direct Observation and Quantitative Analysis of Mobile Frenkel Defects in Metal Halide Perovskites Using Scanning Kelvin Probe Microscopy. *J. Phys. Chem. C*, 122:12633–12639, 2018.

[297] Cheng Li, Antonio Guerrero, Sven Huettner, and Juan Bisquert. Unravelling the Role of Vacancies in Lead Halide Perovskite Through Electrical Switching of Photoluminescence. *Nat. Commun.*, 9:5113, 2018.

[298] Monojit Bag, Lawrence A. Renna, Ramesh Y. Adhikari, Supravat Karak, Feng Liu, Paul M. Lahti, Thomas P. Russell, Mark T. Tuominen, and D. Venkataraman. Kinetics of Ion Transport in Perovskite Active Layers and Its Implications for Active Layer Stability. *J. Am. Chem. Soc.*, 137:13130–13137, 2015.

[299] Alessandro Senocrate, Igor Moudrakovski, Gee Yeong Kim, Tae-youl Yang, Giuliano Gregori, Michael Grätzel, and Joachim Maier. The Nature of Ion Conduction in Methylammonium Lead Iodide: A Multimethod Approach. *Angew. Chem. , Int. Ed.*, 56:7755–7759, 2017.

[300] Moritz H. Futscher, Ju Min Lee, Lucie McGovern, Loreta A. Muscarella, Tianyi Wang, Muhammad Irfan Haider, Azhar Fakharuddin, Lukas Schmidt-Mende, and Bruno Ehrler. Quantification of Ion Migration in $CH_3NH_3PbI_3$ Perovskite Solar Cells by Transient Capacitance Measurements. *Mater. Horizons*, 6:1497–1503, 2019.

[301] Sebastian Reichert, Jens Flemming, Qingzhi An, Yana Vaynzof, Jan Frederik Pietschmann, and Carsten Deibel. Ionic-Defect Distribution Revealed by Improved Evaluation of Deep-Level Transient Spectroscopy on Perovskite Solar Cells. *Phys. Rev. Appl.*, 13:034018, 2020.

[302] Biao Li, Chenxia Kan, Pengjie Hang, Yanjun Fang, Lijian Zuo, Lihui Song, Yiqiang Zhang, Deren Yang, and Xuegong Yu. Understanding the Influence of Cation and Anion Migration on Mixed-Composition Perovskite Solar Cells via Transient Ion Drift. *Phys. Status Solidi - Rapid Res. Lett.*, 15:1–7, 2021.

[303] Dennis Kemp and Roger A. De Souza. Nonlinear Ion Mobility at High Electric Field Strengths in the Perovskites $SrTiO_3$ and $CH_3NH_3PbI_3$. *Phys. Rev. Mater.*, 5:105401, 2021.

[304] Yonggang Wang, Xujie Lü, Wenge Yang, Ting Wen, Liuxiang Yang, Xiangting Ren, Lin Wang, Zheshuai Lin, and Yusheng Zhao. Pressure-Induced Phase Transformation, Reversible Amorphization, and Anomalous Visible Light Response in Organolead Bromide Perovskite. *J. Am. Chem. Soc.*, 137:11144–11149, 2015.

[305] Xujie Lü, Yonggang Wang, Constantinos C. Stoumpos, Qingyang Hu, Xiaofeng Guo, Haijie Chen, Liuxiang Yang, Jesse S. Smith, Wenge Yang, Yusheng Zhao, Hongwu Xu, Mercouri G. Kanatzidis, and Quanxi Jia. Enhanced Structural Stability and Photo Responsiveness of $CH_3NH_3SnI_3$ Perovskite via Pressure-Induced Amorphization and Recrystallization. *Adv. Mater.*, 28:8663–8668, 2016.

[306] Adam Jaffe, Yu Lin, Christine M. Beavers, Johannes Voss, Wendy L. Mao, and Hemamala I. Karunadasa. High-Pressure Single-Crystal Structures of 3D Lead-Halide Hybrid Perovskites and Pressure Effects on Their Electronic and Optical Properties. *ACS Cent. Sci.*, 2:201–209, 2016.

[307] Adam Jaffe, Yu Lin, Wendy L. Mao, and Hemamala I. Karunadasa. Pressure-Induced Metallization of the Halide Perovskite $(CH_3NH_3)PbI_3$. *J. Am. Chem. Soc.*, 139:4330–4333, 2017.

[308] Gang Liu, Lingping Kong, Jue Gong, Wenge Yang, Ho Kwang Mao, Qingyang Hu, Zhenxian Liu, Richard D. Schaller, Dongzhou Zhang, and Tao Xu. Pressure-Induced Bandgap Optimization in Lead-Based Perovskites with Prolonged Carrier Lifetime and Ambient Retainability. *Adv. Funct. Mater.*, 27:1604208, 2017.

[309] Bijaya B. Karki and Gaurav Khanduja. A Computational Study of Ionic Vacancies and Diffusion in $MgSiO_3$ Perovskite and Post-Perovskite. *Earth Planet. Sci. Lett.*, 260:201–211, 2007.

[310] M. W. Ammann, J. P. Brodholt, and D. P. Dobson. DFT Study of Migration Enthalpies in $MgSiO_3$ Perovskite. *Phys. Chem. Miner.*, 36:151–158, 2009.

[311] R. D. King-Smith and David Vanderbilt. Theory of Polarization of Crystalline Solids. *Phys. Rev. B*, 47:1651–1654, 1993.

[312] Raffaele Resta. Macroscopic Polarization in Crystalline Dielectrics: The Geometric Phase Approach. *Rev. Mod. Phys.*, 66:899–915, 1994.

[313] David Vanderbilt and R. D. King-Smith. Electric Polarization as a Bulk Quantity and its Relation to Surface Charge. *Phys. Rev. B*, 48:4442–4455, 1993.

[314] Nicola A. Spaldin. A Beginners Guide to the Modern Theory of Polarization. *J. Solid State Chem.*, 195:2–10, 2012.

[315] Kate Wright and Geoffrey D. Price. Computer Simulation of Defects and Diffusion in Perovskites. *J. Geophys. Res. Solid Earth*, 98(B12):22245–22253, dec 1993.

[316] Raied Al-Hamadany, J. P. Goss, P. R. Briddon, Shahin A. Mojarad, A. G. O'Neill, and M. J. Rayson. Impact of Tensile Strain on the Oxygen Vacancy Migration in $SrTiO_3$: Density Functional Theory Calculations. *J. Appl. Phys.*, 113:224108, 2013.

[317] Raied Al-Hamadany, J. P. Goss, P. R. Briddon, Shahin A. Mojarad, Meaad Al-Hadidi, A. G. O'Neill, and M. J. Rayson. Oxygen Vacancy Migration in Compressively Strained $SrTiO_3$. *J. Appl. Phys.*, 113:024108, 2013.

[318] Q. Yang, J. X. Cao, Y. Ma, Y. C. Zhou, L. M. Jiang, and X. L. Zhong. Strain Effects on Formation and Migration Energies of Oxygen Vacancy in Perovskite Ferroelectrics: A First-Principles Study. *J. Appl. Phys.*, 113:184110, 2013.

[319] Li Yong Gan, Salawu Omotayo Akande, and Udo Schwingenschlögl. Anisotropic O Vacancy Formation and Diffusion in $LaMnO_3$. *J. Mater. Chem. A*, 2:19733–19737, 2014.

[320] Tam Mayeshiba and Dane Morgan. Strain Effects on Oxygen Migration in Perovskites. *Phys. Chem. Chem. Phys.*, 17:2715–2721, 2015.

[321] Jianqi Xi, Haixuan Xu, Yanwen Zhang, and William J. Weber. Strain Effects On Oxygen Vacancy Energetics in $KTaO_3$. *Phys. Chem. Chem. Phys.*, 19:6264–6273, 2017.

[322] Ran Gao, Abhinav C.P. Jain, Shishir Pandya, Yongqi Dong, Yakun Yuan, Hua Zhou, Liv R. Dedon, Vincent Thoréton, Sahar Saremi, Ruijuan Xu, Aileen Luo, Ting Chen, Venkatraman Gopalan, Elif Ertekin, John Kilner, Tatsumi Ishihara, Nicola H. Perry, Dallas R. Trinkle, and Lane W. Martin. Designing Optimal Perovskite Structure for High Ionic Conduction. *Adv. Mater.*, 32:1905178, 2020.

[323] Isabella Poli, Jenny Baker, James McGettrick, Francesca De Rossi, Salvador Eslava, Trystan Watson, and Petra J. Cameron. Screen Printed Carbon $CsPbBr_3$ Solar Cells with High Open-Circuit Photovoltage. *J. Mater. Chem. A*, 6:18677–18686, 2018.

[324] Jie Lei, Fei Gao, Haoxu Wang, Juan Li, Jiexuan Jiang, Xin Wu, Rongrong Gao, Zhou Yang, and Shengzhong (Frank) Liu. Efficient Planar $CsPbBr_3$ Perovskite Solar Cells by Dual-Source Vacuum Evaporation. *Sol. Energy Mater. Sol. Cells*, 187:1–8, 2018.

[325] Jingchen Hua, Xi Deng, Cheng Niu, Fuzhi Huang, Yong Peng, Wangnan Li, Zhiliang Ku, and Yi bing Cheng. A Pressure-Assisted Annealing Method for High Quality $CsPbBr_3$ Film Deposited by Sequential Thermal Evaporation. *RSC Adv.*, 10:8905–8909, 2020.

[326] Jungjin Yoon, Hyangki Sung, Gunhee Lee, Woohyung Cho, Namyoung Ahn, Hyun Suk Jung, and Mansoo Choi. Superflexible, High-Efficiency Perovskite Solar Cells Utilizing Graphene Electrodes: Towards Future Foldable Power Sources. *Energy Environ. Sci.*, 10:337–345, 2017.

[327] Tangyue Xue, Gangshu Chen, Xiaotian Hu, Meng Su, Zengqi Huang, Xiangchuan Meng, Ze Jin, Jiale Ma, Yiqiang Zhang, and Yanlin Song. Mechanically Robust and Flexible Perovskite Solar Cells via a Printable and Gelatinous Interface. *ACS Appl. Mater. Interfaces*, 13:19959–19969, 2021.

[328] Cheng Wang, Lin Ma, Deqiang Guo, Xin Zhao, Zilin Zhou, Dabin Lin, Fangteng Zhang, Weiren Zhao, Jiahua Zhang, and Zhaogang Nie. Balanced Strain-Dependent

Carrier Dynamics in Flexible Organic-Inorganic Hybrid Perovskites. *J. Mater. Chem. C*, 8:3374–3379, 2020.

[329] Avi Mathur, Hua Fan, and Vivek Maheshwari. Soft Polymer-Organolead Halide Perovskite Films for Highly Stretchable and Durable Photodetectors with Pt-Au Nanochain-Based Electrodes. *ACS Appl. Mater. Interfaces*, 13:58956–58965, 2021.

[330] Tam T. Mayeshiba and Dane D. Morgan. Factors Controlling Oxygen Migration Barriers in Perovskites. *Solid State Ionics*, 296:71–77, 2016.

[331] Mohamed Boubchir and Hafid Aourag. Materials Genome Project: Mining the Ionic Conductivity in Oxide Perovskites. *Mater. Sci. Eng. B Solid-State Mater. Adv. Technol.*, 267:114984, 2021.

[332] J. A. Kilner and R. J. Brook. A Study of Oxygen Ion Conductivity in Doped Non-Stoichiometric Oxides. *Solid State Ionics*, 6:237–252, 1982.

[333] M. Mogensen, D. Lybye, N. Bonanos, P. V. Hendriksen, and F. W. Poulsen. Factors Controlling the Oxide Ion Conductivity of Fluorite and Perovskite Structured Oxides. *Solid State Ionics*, 174:279–286, 2004.

[334] Roger A. De Souza and Manfred Martin. An Atomistic Simulation Study of Oxygen-Vacancy Migration in Perovskite Electrolytes Based on $LaGaO_3$. *Monatshefte fur Chemie*, 140:1011–1015, 2009.

[335] Marcel Schie, Rainer Waser, and Roger A. De Souza. A Simulation Study of Oxygen-Vacancy Behavior in Strontium Titanate: Beyond Nearest-Neighbor Interactions. *J. Phys. Chem. C*, 118:15185–15192, 2014.

[336] Ronald L. Cook and Anthony F. Sammells. On the Systematic Selection of Perovskite Solid Electrolytes for Intermediate Temperature Fuel Cells. *Solid State Ionics*, 45:311–321, 1991.

[337] Anthony F. Sammells, Ronald L. Cook, James H. White, Jeremy J. Osborne, and Robert C. MacDuff. Rational Selection of Advanced Solid Electrolytes for Intermediate Temperature Fuel Cells. *Solid State Ionics*, 52:111–123, 1992.

[338] R.D. Shannon. Revised Effective Ionic Radii and Systematic Studies of Interatomie Distances in Halides and Chaleogenides. *Acta Crystallogr.*, 32:751, 1976.

[339] Ronald L. Cook, Jeremy J. Osborne, James H. White, Robert C. MacDuff, and Anthony F. Sammells. Investigations on $BaTh_{0.9}Gd_{0.1}O_3$ as an Intermediate Temperature Fuel Cell Solid Electrolyte. *J. Electrochem. Soc.*, 139:L19–L20, 1992.

[340] Roger A. De Souza, M. Saiful Islam, and Ellen Ivers-Tiffée. Formation and Migration of Cation Defects in the Perovskite Oxide $LaMnO_3$. *J. Mater. Chem.*, 9:1621–1627, 1999.

[341] Roger A. De Souza and Joachim Maier. A Computational Study of Cation Defects in $LaGaO_3$. *Phys. Chem. Chem. Phys.*, 5:740–748, 2003.

[342] Alison Jones and M. Saiful Islam. Atomic-Scale Insight into $LaFeO_3$ Perovskite: Defect Nanoclusters and Ion Migration. *J. Phys. Chem. C*, 112:4455–4462, 2008.

[343] Peter R. Spackman, Michael J. Turner, Joshua J. McKinnon, Stephen K. Wolff, Daniel J. Grimwood, Dylan Jayatilaka, and Mark A. Spackman. CrystalExplorer: A Program for Hirshfeld Surface Analysis, Visualization and Quantitative Analysis of Molecular Crystals. *J. Appl. Crystallogr.*, 54:1006–1011, 2021.

[344] Egor Ospadov, Jianmin Tao, Viktor N. Staroverov, and John P. Perdew. Visualizing Atomic Sizes and Molecular Shapes with the Classical Turning Surface of the Kohn–Sham Potential. *Proc. Natl. Acad. Sci. U. S. A.*, 115:E11578–E11585, 2018.

[345] Aaron D. Kaplan, Stewart J. Clark, Kieron Burke, and John P. Perdew. Calculation and interpretation of classical turning surfaces in solids. *npj Comput. Mater.*, 7:25, 2021.

[346] Dong Xia Zhao, Chun Yu Yan, Zun Wei Zhu, Le Zhang, Yi Ming Jiang, Rui Gong, and Zhong Zhi Yang. An Intrinsic Criterion of Defining Ionic or Covalent Character of AB-type Crystals Based on the Turning Boundary Radii Calculated by an ab Initio Method. *Mol. Phys.*, 116:969–977, 2018.

[347] Dong Xia Zhao, Jian Zhao, and Zhong Zhi Yang. Partitioning a Molecule into the Atomic Basins and the Resultant Atomic Charges from Quantum Chemical Topology Analysis of the Kohn-Sham Potential. *J. Phys. Chem. A*, 124:5023–5032, 2020.

[348] Khuong P. Ong, Teck Wee Goh, Qiang Xu, and Alfred Huan. Structural Evolution in Methylammonium Lead Iodide $CH_3NH_3PbI_3$. *J. Phys. Chem. A*, 119:11033–11038, 2015.

[349] Khuong P. Ong, Teck Wee Goh, Qiang Xu, and Alfred Huan. Mechanical Origin of the Structural Phase Transition in Methylammonium Lead Iodide $CH_3NH_3PbI_3$. *J. Phys. Chem. Lett.*, 6:681–685, 2015.

[350] Keith P. McKenna. Electronic Properties of {111} Twin Boundaries in a Mixed-ion Lead Halide Perovskite Solar Absorber. *ACS Energy Lett.*, 3:2663–2668, 2018.

[351] Lucy D. Whalley, Jonathan M. Skelton, Jarvist M. Frost, and Aron Walsh. Phonon Anharmonicity, Lifetimes, and Thermal Transport in $CH_3NH_3PbI_3$ from Many-Body Perturbation Theory. *Phys. Rev. B*, 94:220301, 2016.

[352] Arthur Marronnier, Heejae Lee, Bernard Geffroy, Jacky Even, Yvan Bonnassieux, and Guido Roma. Structural Instabilities Related to Highly Anharmonic Phonons in Halide Perovskites. *J. Phys. Chem. Lett.*, 8:2659–2665, 2017.

[353] Marcelo A. Carignano, S. Assa Aravindh, Iman S. Roqan, Jacky Even, and Claudine Katan. Critical Fluctuations and Anharmonicity in Lead Iodide Perovskites from Molecular Dynamics Supercell Simulations. *J. Phys. Chem. C*, 121:20729–20738, 2017.

[354] Arthur Marronnier, Guido Roma, Soline Boyer-Richard, Laurent Pedesseau, Jean Marc Jancu, Yvan Bonnassieux, Claudine Katan, Constantinos C. Stoumpos, Mercouri G. Kanatzidis, and Jacky Even. Anharmonicity and Disorder in the Black Phases of Cesium Lead Iodide Used for Stable Inorganic Perovskite Solar Cells. *ACS Nano*, 12:3477–3486, 2018.

[355] Jonathan Lahnsteiner and Menno Bokdam. Anharmonic Lattice Dynamics in Large Thermodynamic Ensembles with Machine-Learning Force Fields: $CsPbBr_3$, a Phonon Liquid with Cs Rattlers. *Phys. Rev. B*, 105:024302, 2022.

[356] M. J.L. Sangster and A. M. Stoneham. Calculation of Absolute Diffusion Rates in Oxides. *J. Phys. C Solid State Phys.*, 17:6093–6104, 1984.

[357] Aron Walsh, C. Richard A. Catlow, Alastair G.H. Smith, Alexey A. Sokol, and Scott M. Woodley. Strontium Migration Assisted by Oxygen Vacancies in $SrTiO_3$ from Classical and Quantum Mechanical Simulations. *Phys. Rev. B - Condens. Matter Mater. Phys.*, 83:220301(R), 2011.

[358] Haiwu Zhang, Amr H.H. Ramadan, and Roger A. De Souza. Atomistic Simulations of Ion Migration in Sodium Bismuth Titanate (NBT) Materials: Towards Superior Oxide-Ion Conductors. *J. Mater. Chem. A*, 6:9116–9123, 2018.

[359] Henrik J. Heelweg and Roger A. De Souza. Metadynamics simulations of strontium-vacancy diffusion in $SrTiO_3$. *Phys. Rev. Mater.*, 5:013804, 2021.

[360] Yuchuan Shao, Yanjun Fang, Tao Li, Qi Wang, Qingfeng Dong, Yehao Deng, Yongbo Yuan, Haotong Wei, Meiyu Wang, Alexei Gruverman, Jeffery Shield, and Jinsong Huang. Grain Boundary Dominated Ion Migration in Polycrystalline Organic-Inorganic Halide Perovskite Films. *Energy Environ. Sci.*, 9:1752–1759, 2016.

[361] Jae S. Yun, Jan Seidel, Jincheol Kim, Arman Mahboubi Soufiani, Shujuan Huang, Jonathan Lau, Nam Joong Jeon, Sang Il Seok, Martin A. Green, and Anita Ho-Baillie. Critical Role of Grain Boundaries for Ion Migration in Formamidinium and Methylammonium Lead Halide Perovskite Solar Cells. *Adv. Energy Mater.*, 6:1600330, 2016.

[362] Nga Phung, Amran Al-Ashouri, Simone Meloni, Alessandro Mattoni, Steve Albrecht, Eva L. Unger, Aboma Merdasa, and Antonio Abate. The Role of Grain Boundaries on Ionic Defect Migration in Metal Halide Perovskites. *Adv. Energy Mater.*, 10:1903735, 2020.

[363] Lucie McGovern, Isabel Koschany, Gianluca Grimaldi, Loreta A Muscarella, and Bruno Ehrler. Grain Size Influences Activation Energy and Migration Pathways in $MAPbBr_3$ Perovskite Solar Cells. *J. Phys. Chem. Lett.*, 12:2423–2428, mar 2021.

[364] Bohee Hwang, Chungwan Gu, Donghwa Lee, and Jang Sik Lee. Effect of Halide-Mixing on the Switching Behaviors of Organic-Inorganic Hybrid Perovskite Memory. *Sci. Rep.*, 7:43794, 2017.

[365] Chundan Lin, Siyuan Li, Wansong Zhang, Changjin Shao, and Zhenqing Yang. Effect of Bromine Substitution on the Ion Migration and Optical Absorption in $MAPbI_3$ Perovskite Solar Cells: The First-Principles Study. *ACS Appl. Energy Mater.*, 1:1374–1380, 2018.

[366] Aleksandra Oranskaia, Jun Yin, Osman M. Bakr, Jean Luc Brédas, and Omar F. Mohammed. Halogen Migration in Hybrid Perovskites: The Organic Cation Matters. *J. Phys. Chem. Lett.*, 9:5474–5480, 2018.

[367] Jie Xing, Qi Wang, Qingfeng Dong, Yongbo Yuan, Yanjun Fang, and Jinsong Huang. Ultrafast Ion Migration in Hybrid Perovskite Polycrystalline Thin Films under Light and Suppression in Single Crystals. *Phys. Chem. Chem. Phys.*, 18:30484–30490, 2016.

[368] Dane W. DeQuilettes, Wei Zhang, Victor M. Burlakov, Daniel J. Graham, Tomas Leijtens, Anna Osherov, Vladimir Bulović, Henry J. Snaith, David S. Ginger, and Samuel D. Stranks. Photo-Induced Halide Redistribution in Organic-Inorganic Perovskite Films. *Nat. Commun.*, 7:11683, 2016.

[369] Tae-Youl Yang, Giuliano Gregori, Norman Pellet, Michael Grätzel, and Joachim Maier. The Significance of Ion Conduction in a Hybrid Organic-Inorganic Lead-Iodide-Based Perovskite Photosensitizer. *Angew. Chem.*, 127:8016–8021, 2015.

[370] Xun Xiao, Jun Dai, Yanjun Fang, Jingjing Zhao, Xiaopeng Zheng, Shi Tang, Peter Neil Rudd, Xiao Cheng Zeng, and Jinsong Huang. Suppressed Ion Migration along the In-Plane Direction in Layered Perovskites. *ACS Energy Lett.*, 3:684–688, 2018.

[371] Xiaojian Zhu, Jihang Lee, and Wei D. Lu. Iodine Vacancy Redistribution in Organic–Inorganic Halide Perovskite Films and Resistive Switching Effects. *Adv. Mater.*, 29:1700527, 2017.

[372] Soohyun Bae, Seongtak Kim, Sang Won Lee, Kyung Jin Cho, Sungeun Park, Seunghun Lee, Yoonmook Kang, Hae Seok Lee, and Donghwan Kim. Electric-Field-Induced Degradation of Methylammonium Lead Iodide Perovskite Solar Cells. *J. Phys. Chem. Lett.*, 7:3091–3096, 2016.

[373] Wenke Zhou, Yicheng Zhao, Xu Zhou, Rui Fu, Qi Li, Yao Zhao, Kaihui Liu, Dapeng Yu, and Qing Zhao. Light-Independent Ionic Transport in Inorganic Perovskite and Ultrastable Cs-Based Perovskite Solar Cells. *J. Phys. Chem. Lett.*, 8:4122–4128, 2017.

[374] Hui Yu, Haipeng Lu, Fangyan Xie, Shuang Zhou, and Ni Zhao. Native Defect-Induced Hysteresis Behavior in Organolead Iodide Perovskite Solar Cells. *Adv. Funct. Mater.*, 26:1411–1419, 2016.

[375] Edoardo Mosconi, Daniele Meggiolaro, Henry J. Snaith, Samuel D. Stranks, and Filippo De Angelis. Light-Induced Annihilation of Frenkel Defects in Organo-Lead Halide Perovskites. *Energy Environ. Sci.*, 9:3180–3187, 2016.

[376] Himchan Cho, Christoph Wolf, Joo Sung Kim, Hyung Joong Yun, Jong Seong Bae, Hobeom Kim, Jung Min Heo, Soyeong Ahn, and Tae Woo Lee. High-Efficiency Solution-Processed Inorganic Metal Halide Perovskite Light-Emitting Diodes. *Adv. Mater.*, 29:1700579, 2017.

[377] Un Gi Jong, Chol Jun Yu, Gum Chol Ri, Andrew P. McMahon, Nicholas M. Harrison, Piers R.F. Barnes, and Aron Walsh. Influence of Water Intercalation and Hydration on Chemical Decomposition and Ion Transport in Methylammonium Lead Halide Perovskites. *J. Mater. Chem. A*, 6:1067–1074, 2018.

Appendix A

Appendix

A.1 Organic Cation Perovskites

A.1.1 Organic Cation Perovskites; Bromide Perovskites

Material	**E_a (eV)**	Theo/Exp	**Source**
$MAPbBr_3$	0.168 $\pm$ 0.043	Experimental (J-V curves)	[120]
$MAPbBr_3$	0.2/0.22 (V^+_{Br})	Computational (NEB DFT-MD)	[120]
$MAPbBr_3$	0.09 (V_{Br})	Computational (DFT)	[254]
$MAPbBr_3$	0.227 (Br^-)	Computational (DFT)	[278]
$MAPbBr_3$	0.23	Comp (DFT)	[364]
$MAPbBr_3$	1.14 (Br^-_i) 1.41 V^+_{Br}	Theo DFT	[365]
$MAPbBr_3$	0.27 (V_{Br}) 0.34 (I_{Br})	Computational (DFT)	[366]
$FAPbBr_3$	0.33 (V_{Br}) 0.24 (I_{Br})	Computational (DFT)	[366]

Table A.1: Overview of bromide ion migration in $MAPbBr_3$ and $FAPbBr_3$.

A.1.2 Organic Cation Perovskites; Iodide Perovskites

Material	**E_a (eV)**	Comp/Exp	**Source**
$MAPbI_3$	0.50 (large grain film, dark) 0.14 (large grain film, 0.25 sun) 0.27 (small grain film, dark) 0.08 (small grain film, 0.25 sun) 1.05 (single crystal, dark) 0.47 (single crystal, 0.25 sun)	Exp Conductivity	[367]
$MAPbI_3$	0.19 $\pm$ 0.05	Experimental (PL)	[368]
$MAPbI_3$	0.43 (dark)	Exp (Impedance)	[369]
$MAPbI_3$	0.08 (V_I / I_i)	Comp (DFT)	[254]
$MAPbI_3$	0.58 (V_I^+	Comp (DFT)	[87]
$MAPbI_3$	0.6–0.68 (dark)	Exp (photocurrent relaxation)	[87]
$MAPbI_3$	0.32–0.33 (V_I / V_I^+ / I_i^- / I_i)	Comp (DFT)	[276]
$MAPbI_3$	0.342	Comp (DFT)	[29]
$MAPbI_3$	0.30	Comp (DFT)	[364]
$MAPbI_3$	0.83 (single crystal, dark) 0.33 (single crystal, 0.25 sun)	Exp Conductivity	[370]
$MAPbI_3$	0.17 (dark)	Exp Resistance switching	[371]
$MAPbI_3$	0.29 (dark) $\pm$ 0.06	Exp Transient ion drift	[300]
$MAPbI_3$	0.31 (forward sweep, light) 0.23 (reverse sweep, light)	Exp Staircase voltage	[28]
$MAPbI_3$	0.19 (dark)	Exp (dark current decay)	[372]
$MAPbI_3$	0.62 (0.1 mW/cm^2) 0.07 (25 mW/cm^2)	Exp Conductivity	[373]
$MAPbI_3$	0.14 (stoichiometric) 0.18 (excess MAI) 0.10 (excess PbI_2)	Exp Normalised current decay	[374]
$MAPbI_3$	0.14	Exp PL decay (light)	[375]
$MAPbI_3$	0.06 (I_i^0) 0.08 (I_i^-) 0.05 (I_i^-) (e/h excited state) 0.15 (V_I^0) 0.09 (V_I^+) 0.15 (V_I^+) (e/h excited state)	Theo ab-initio MD	[375]
$MAPbI_3$	0.25 (I_i^-) 0.53 (V_I^+)	Theo DFT	[365]
$MAPbI_3$	0.28 (V_I^+)	Computational(NEB DFT-MD)	[120]
$FAPbI_3$	0.42–0.55 (V_I / V_I^+)	Comp (DFT)	[276]

Table A.2: Overview of iodide ion migration in $MAPbI_3$ and $FAPbI_3$ for both experimental and theoretical studies.

A.2 Inorganic Cation Perovskites

A.2.1 Inorganic Cation Perovskites; Bromide Perovskites

Material	**E_a (eV)**	Theo/Exp	**Source**
$CsPbBr_3$	0.25	Experimental (Impedance)	[115]
$CsPbBr_3$	0.27 (V^+_{Br})	Computational(NEB DFT-MD)	[120]
$CsPbBr_3$	0.28	Experimental (PL)	[121]
$CsPbBr_3$	0.3	Theoretical (MD)	[121]
$CsPbBr_3$	0.49	Experimental (NMR)	[117]
$CsPbBr_3$	0.09	Exp (Hysteresis)	[376]
$CsPbBr_3$	0.17 (intrinsic region) 0.7 (extrinsic region)	Exp conductivity	[116]
$CsPbBr_3$	0.162 (current decay) 0.228 (current buildup)	Exp transient current	[118]
$CsPbBr_3$	0.33 (V^+_{Br})	Computational (DFT)	[70]

Table A.3: Overview of bromide ion migration parameters.

A.2.2 Inorganic Cation Perovskites; Iodide Perovskites

Material	**E_a (eV)**	Theo/Exp	**Source**
$CsPbI_3$	0.29 (V^+_I)	Computational(NEB DFT-MD)	[120]
$CsPbI_3$	0.35 (V^+_I)	Computational (DFT)	[70]

Table A.4: Overview of iodide ion migration in $CsPbI_3$.

A.2.3 Comparison between I- and Br-based LHPs

$APbI_3$	**$APbBr_3$**	**A**	**Source**
0.08	0.09	MA	[254]
0.55	0.58	MA	[377]
0.22 (water-intercalated)	0.29 (water-intercalated)	MA	[377]
0.44 (mono-hydrated)	0.47 (mono-hydrated)	MA	[377]
0.28	0.2	MA	[120]
0.25 / 0.53 (I^-_i / V^+_I)	1.14 / 1.41 (Br^-_i / V^+_{Br})	MA	[365]
0.35	0.33	Cs	[120]

Table A.5: Overview of (all computational) studies looking at halide migration in both $APbI_3$ and $APbBr_3$ systems.